TIME-DEPENDENT MHD WAVE COUPLING IN NON-UNIFORM MEDIA

Ian R. Mann

A Thesis Submitted for the Degree of PhD
at the
University of St Andrews

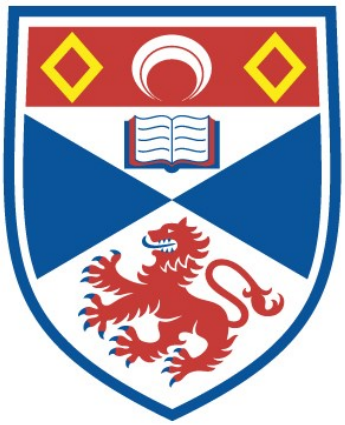

1996

Time-Dependent MHD Wave Coupling in Non-Uniform Media.

Ian R. Mann

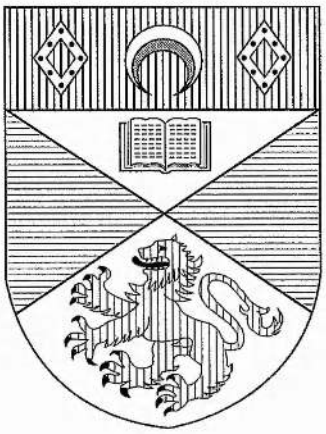

Thesis submitted for the degree of Doctor of Philosophy
of the University of St. Andrews.

25th September 1995

ProQuest LLC.
789 East Eisenhower Parkway
P.O. Box 1346
Ann Arbor, MI 48106 – 1346

B904.

Declaration

1. I, Ian Robert Mann, hereby certify that this thesis has been composed by myself, that it is a record of my own work, and that it has not been accepted in partial or complete fulfilment of any other degree or professional qualification.

   Signed .... Date 25/9/95

2. I was admitted to the Faculty of Science of the University of St. Andrews under Ordinance General No. 12 in October 1992 and as a candidate for the degree of Ph.D. in October 1993.

3. I hereby certify that the candidate has fulfilled the conditions of the Resolution and Regulations appropriate to the Degree of Ph.D.

   Signature of Supervisor .... ..Date 14/9/95

4. In submitting this thesis to the University of St. Andrews I understand that I am giving permission for it to be made available for use in accordance with the regulations of the University Library for the time being in force, subject to any copyright vested in the work not being affected thereby. I also understand that the title and abstract will be published, and that a copy of the work may be made and supplied to any bona fide library or research worker.

To

Grandad Lee

(1910-1994)

A kind and generous man, fondly missed.

Acknowledgements

First, I would like to thank my supervisor, Dr. Andrew Wright, for all the help and encouragement (and the odd game of golf) which he has given me over the past three years. Without his advice, this thesis would not have been possible. I am also indebted to Paul Cally for the suggestion of the eigenvalue problem method, and for the discussions and collaboration leading to Mann, Wright and Cally (1995).

I would also like to thank all the members of the solar group, for useful discussions, many coffees, and the odd "funny" (that includes you Graham R.). In particular, I am grateful to Dr. Alan Hood for discussions about Chapter 6, and to Prof. Bernard Roberts for his waves sub-group.

Most grateful thanks must go to my Mum and Dad, who have always supported me (both emotionally and financially) throughout my university career.

I cannot finish these "thank yous" without mentioning the friends I've made in St. Andrews during the past three years - cheers, it's been great. In particular (in no particular order), I should mention: the dept. "footy boys" (and girls), the golf "grudge match", my flatmates (who've managed to put up with me), St. Andrews University Breakaway club for escapes to the hills, my officemate Cesar, Graham F. for tinnies and a two-wheeler, Al for the odd "epic" climb and his impressions of Delia Smith, Skye for being there, and everyone who has ever gone for a quick pint on the way home!

I am also grateful to PPARC for financial support, and to Darren McDonald for proof reading this thesis.

Energy is contagious
Enthusiasm spreads
Tides respond to lunar gravitation
Everything turns in synchronous relation

Laughter is infectious
Excitement goes to my head
Winds are stirred by planets in rotation
Sparks ignite and spread new information

Respond, vibrate, feedback, resonate ...

From Chain Lightning, on the album Presto,
by Rush, Atlantic/Anthem, 1989.

Abstract

This thesis studies the time dependent evolution of MHD waves in cold, fully compressible non-uniform plasmas. We used a 1-D box model (e.g., Southwood (1974)) to study wave mode coupling, and concentrate upon developing an understanding of the underlying physics that governs waves in the Earth's magnetosphere.

We begin by discussing the form of the (often singular) governing eigenmodes of the system, and subsequently use these eigenmodes as a basis with which to construct the solution to a variety of initial value problems. We consider a detailed analysis of both the widths and the internal length scales developed by cavity mode driven field line resonances (FLRs), and compare our results to observations presented in the literature. We find that (especially asymptotically in time) the coupled waves derive their dominant characteristics from the form of undriven decoupled toroidal Alfvén eigenmodes. Ideal numerical solutions show that fine spatial scales are developed across the background magnetic field, and we demonstrate that this is accurately estimated as the decoupled phase mixing length $L_{ph} = 2\pi/\omega'_A t$, where $\omega'_A = d\omega_A/dx$. We also discuss the likely ionospheric and kinetic modifications to our theory.

Later, we consider the evolution of poloidal Alfvén waves having large azimuthal wavenumber (λ). We find that the $\lambda \rightarrow \infty$ decoupled poloidal Alfvén wave evaluation (Dungey, 1967) is modified for finite λ, approaching decoupled toroidal field line oscillations for large t. We define a poloidal lifetime τ, when toroidal and poloidal displacements become equal, and demonstrate that this is when the phase mixing length is equal to $2\pi/\lambda$. We examine numerically the poloidal Alfvén wave evolution for $\lambda \gg k_z$, and $k_z \gtrsim \lambda$, when $k_x(x, t = 0) \ll \lambda$ or k_z. We interpret the $\lambda \gg k_z$ results (applicable to the Earth's magnetosphere) in the context of poloidal Alfvén wave observations, and compare our study to the numerical analysis of Ding et al. (1995).

We conclude the thesis by undertaking an asymptotic derivation of the large λ solutions by using the method of multiple time scales. We find our analytic solutions are in excellent agreement with those determined numerically.

A central result of the thesis is the importance and dominance of the phase mixing length for time dependent solutions, irrespective of the value of λ.

Contents

1 Introduction. **1**

1.1 Brief History of Solar Terrestrial Interactions. 1
1.2 Magneto-Hydrodynamic Waves. 4
1.2.1 MHD Equations. 4
1.2.2 Uniform Plasma MHD Wave Solutions. 8
1.2.3 Applicability of MHD to Waves in the Magnetosphere. 12
1.3 Brief Morphology of the Earth's Magnetosphere. 15
1.4 ULF Waves in the Magnetosphere. 17
1.5 Outline of the Thesis. 21

2 Governing Equations and Numerical Model. **23**

2.1 Model Magnetosphere. 23
2.2 Governing Equations. 24
2.3 Numerical Solution of the Governing Equations. 26
2.4 Accuracy of Numerical Matrix Eigenvalue Solutions. 30
2.4.1 Numerical "Energy" Invariant. 30
2.4.2 Orthogonality of Numerical Eigenvectors. 33
2.4.3 Further Checks on the Decoupled $\lambda = 0$ Numerical Eigenmodes. . . 35
2.4.4 Verification of Coupled Wave ($\lambda \neq 0$) Temporal Evolution Results. . 35

3 MHD Normal Modes. **38**

3.1 Introduction. 38
3.2 Decoupled ($\lambda = 0$) Normal Modes. 39
3.2.1 Homogeneous Background Plasma. 40
3.2.2 Inhomogeneous Background Plasma. 41
3.3 Runge-Kutta Numerical Integration of Decoupled Fast Eigenmodes. 47
3.4 Mathieu Function Decoupled Fast Eigenmode Analysis. 49
3.4.1 Introduction to Mathieu Functions. 50
3.4.2 Mathieu Functions of the 1st Kind. 52
3.4.3 Mathieu Function Series Solution For Decoupled Fast Eigenmodes. . 54
3.4.4 Calculation of Mathieu Function Solutions. 54
3.4.5 Mathieu Function Stability Diagram. 56
3.5 Coupled ($\lambda \neq 0$) Normal Modes. 59

3.5.1 Introduction. 59
3.5.2 $\lambda \sim O(1)$ Normal Modes. 62
3.5.3 Large λ Normal Modes. 71
3.5.4 $\lambda \to \infty$ Normal Modes. 73

4 Temporal Evolution of Resonant Waves. 76
4.1 Introduction. 76
4.2 Compressible Verses Incompressible Plasma Resonant Absorption. 78
4.3 Observations of Magnetospheric FLRs. 79
4.4 Numerical Results. 82
4.4.1 Fast and Alfvén Mode Interaction. 83
4.4.2 Temporal Evolution of Resonance Energy Widths. 84
4.4.3 Fast Cavity Mode Coupling Rates. 91
4.4.4 Phase Mixing Lengths. 91
4.4.5 Asymptotic State of Coupled Waves. 98
4.5 Discussion 102
4.5.1 Overall Pulsation Energy Widths. 102
4.5.2 Magnetospheric Perturbation Widths ΔX_ξ. 103
4.5.3 FLR Characteristics. 106
4.6 Conclusions. 108

5 Large λ Numerical Poloidal Wave Evolution. 112
5.1 Introduction. 112
5.2 High λ Magnetospheric ($k_z \ll \lambda$) Poloidal Pulsations. 114
5.2.1 Review of Magnetospheric Observations. 114
5.2.2 Basic Governing Equation Analysis. 116
5.2.3 Numerical Results. 117
5.2.4 Discussion. 125
5.3 Evolution of $k_z \gtrsim \lambda$ Azimuthally Small Scale Waves. 138
5.3.1 Numerical $k_z \gtrsim \lambda$ Results. 139
5.3.2 Fast Wave Refraction Bounce Period. 145
5.4 Conclusions. 148

6 Asymptotic Poloidal Alfvén Wave Solutions. 150
6.1 Introduction. 150
6.2 Multiple Time-Scales Analysis. 150
6.2.1 Zeroth Order Solution. 153
6.2.2 First Order Solution. 153
6.2.3 Second and Higher Order Solutions. 155
6.3 Comparison of Asymptotic and Numerical Results. 155
6.4 Conclusions. 160

7 Summary and Suggestions for Future Work. 161
7.1 Thesis Summary. 161
7.2 Possible Future Work. 163
7.2.1 Further Analysis of ULF Wave Satellite Data. 163
7.2.2 Inclusion of Ionospheric Conductivity in FLR Studies. 164
7.2.3 Reflectivity of Radial Magnetospheric Boundaries. 165
7.2.4 Non-Monotonic Radial Alfvén Speed Studies. 166
7.2.5 Poloidal Alfvén Waves in a Dipole Geometry. 166
7.2.6 Kinetic and Electron Inertia Effects at Alfvén Resonances. 167

A Mathieu Function Fast Eigenmode Solutions. 169
A.1 Recursion Relations Necessary to Calculate se_{2n+2}. 169
A.2 Calculation of Fundamental Fast Eigenmode. 171
A.3 Calculation of Higher Harmonic Fast Eigenmodes. 173

B Poloidal Alfvén Wave Multiple Scales Equation. 175

Bibliography 177

Chapter 1

Introduction.

1.1 Brief History of Solar Terrestrial Interactions.

The subject of this thesis is the study of ultra-low frequency (ULF) magnetic waves in the Earth's uppermost atmosphere. Historically, the connection between solar and terrestrial activity (such as aurora) has often been tenuous. The earliest transient changes to the Earth's magnetic field were detected by George Graham (1724). Graham, a watchmaker by trade and a Fellow of the Royal Society, built several accurate compasses which he used to record changes in the direction of magnetic north on the timescales of hours, days, and months. He offered no explanation for the changes, but was confident that they were a real effect and were not caused by local magnetic materials. It wasn't until after Schwabe's discovery of the 11 year sunspot cycle in 1843, that these transient magnetic field variations were correlated with the periodicity of sunspot number. This provided the first direct solar terrestrial link. Interestingly, since the relationship between auroras and magnetic disturbances had previously been determined, this also linked the auroras with a solar energy source (see Chapman (1970) for a review of the history of auroral observations).

From sunspot observations, it was known that the sun rotated with a 27 day period. In 1904, Maunder interpreted an observed 27 day recurrence tendency of auroral and magnetic disturbances as a further indication of a solar-terrestrial connection. He proposed that gas streams were emitted by solar active regions and that these subsequently caused the terrestrial disturbances. This flow is now known to originate in regions of open solar magnetic field to form the "solar wind". Chapman and Ferraro (1930), concluded that such a neutral stream of ionised particles would be prevented from entering the Earth's

atmosphere by it's magnetic field, and hence that the field would create a "cavity" in the flow of the solar wind. This cavity is now called the magnetosphere (after Gold (1959)) and was defined as the region "above the ionosphere in which the magnetic field of the Earth has a dominant control over the motion of gas and fast charged particles".

A year earlier, Parker (1958) developed a model which showed how the outer atmosphere of the Sun (the solar corona) would continually expand outwards to form the solar wind. The sunward boundary of the magnetosphere (the magnetopause) lies $\sim 10.8R_E$ (where R_E is the Earth's radius) from the Earth, and on the nightside the magnetosphere is stretched out by the solar wind to form a comet-like tail (the magnetotail). The magnetotail has a detected wake up to $\sim 1000R_E$ downstream. In the tail the reversal of stretched field lines, from the northern and southern hemispheres, creates the tail current sheet which carries a current flowing from dawn to dusk. In Figure (1.1) we show an artists impression of the solar wind and the magnetosphere.

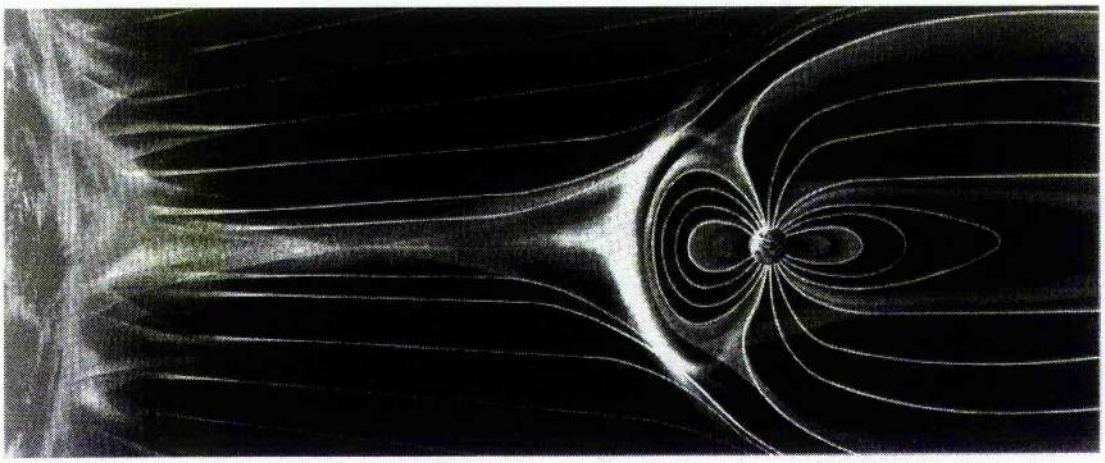

Figure 1.1: Artists impression of the solar wind incident upon the Earth's magnetosphere (not to scale).

The magnetopause, however, is not totally impenetrable. The interaction of the solar wind and the magnetosphere was independently modelled by Dungey (1961) and Axford and Hines (1961). Dungey proposed that it was possible for the magnetic field of the solar wind to connect to the Earth's magnetic field. By a method known as magnetic reconnection, the solar wind magnetic fields could thread through the magnetopause, and

hence drive the observed large scale circulation pattern which was known to exist inside the magnetosphere. In the model of Axford and Hines, a viscous interaction of the solar wind and the magnetosphere causes particle diffusion across the magnetopause, and results in the observed convection pattern. Both of these processes are now believed to occur (Cowley, 1982), and the Sun is believed to be ultimately responsible, via the solar wind, for the energisation of the magnetosphere. Consequently, the solar wind ultimately forms the energy source for magnetospheric waves.

In this thesis, we are interested in ULF magnetic oscillations (known as micropulsations - or simply pulsations) inside the magnetosphere. These pulsations are often quite sinusoidal, have well defined frequencies, and can be easily measured using ground based magnetometers. The first recorded observation of quasi-sinusoidal ULF waves was that of Stewart (1861), who reported waves with a period of a few minutes (see Hughes (1994) and references therein). Magnetospheric ULF waves are now regularly observed by chains of ground based magnetometers, *in situ* by satellites, and seen by radar which detect the flows they cause in the ionosphere (the collisional, highly conducting atmospheric layer which exists at heights of $\sim 90-300$km, and which separates the magnetosphere from lower atmospheric layers).

Dungey (1954) first proposed that pulsations were the result of Alfvén waves standing on geomagnetic field lines. It is now believed that although most waves have ionospheric displacement nodes, if the ends of an oscillating field line are situated in ionospheric regions having widely differing conductivities, then quarter wavelength standing modes are possible. These have one approximately nodal and one anti-nodal displacement boundary condition (e.g., Allan and Knox (1979) and Allan (1983)).

To model ULF waves we utilise a model in which the magnetospheric plasma is treated as a single fluid, permeated by a magnetic field, and which uses both the equations of fluid dynamics (modified by the inclusion of the Lorentz force) and Maxwell's equations of electromagnetism. This approach is known as magneto-hydrodynamics (MHD). Since the magnetosphere represents an inhomogeneous plasma system, this thesis studies the properties of MHD waves in non-uniform plasmas.

1.2 Magneto-Hydrodynamic Waves.

In this section we consider the governing equations of MHD, examine the wave modes of oscillation which these equations support, and briefly discuss the applicability of MHD to the plasma populations which exist in the Earth's magnetosphere.

1.2.1 MHD Equations.

MHD is the study of (assumed) continuous fluid media (in this case a plasma) in the presence of magnetic fields. Consequently, the description of MHD utilises a combination of the (usually) classical fluid equations with the electro-magnetic field equations of Maxwell (see for example Boyd and Sanderson (1969)).

We begin our description of MHD with Maxwell's equations,

$$\nabla_{\wedge}\mathbf{B} = \mu_0\mathbf{j} + \frac{1}{c^2}\frac{\partial \mathbf{E}}{\partial t} \tag{1.1}$$

$$\nabla.\mathbf{B} = 0 \tag{1.2}$$

$$\nabla_{\wedge}\mathbf{E} = -\frac{\partial \mathbf{B}}{\partial t} \tag{1.3}$$

$$\nabla.\mathbf{E} = \frac{\rho^*}{\epsilon_0} \tag{1.4}$$

where $\mathbf{B}$ is the magnetic field, $\mathbf{E}$ the electric field, $\mathbf{j}$ the current density, ρ^* the electric charge density, μ_0 the magnetic permeability and ϵ_0 the permittivity of free space (in the magnetosphere $\mu \approx \mu_0$ and $\epsilon \approx \epsilon_0$), and c $(= 1/\sqrt{\mu_0\epsilon_0})$ is the (vacuum) speed of light.

We now need to consider a form of Ohm's law to link $\mathbf{E}$, $\mathbf{B}$ and $\mathbf{v}$ with $\mathbf{j}$. Plasma moving in the presence of a magnetic field is subject to an electric field $\mathbf{v}_{\wedge}\mathbf{B}$, in addition to the electric field $\mathbf{E}$ which would act on a plasma at rest. Hence we have the following equation for the total current density

$$\mathbf{j} = \sigma(\mathbf{E} + \mathbf{v}_{\wedge}\mathbf{B}) \tag{1.5}$$

where σ is the electrical conductivity.

When analysing waves in plasmas where the conductivity is assumed to be infinite, we have the ideal MHD limit whereby the magnetic field can be considered to be frozen into the plasma (Alfvén's frozen flux theorem). In this limit, equation (1.5) becomes

$$\mathbf{E} + \mathbf{v}_\wedge \mathbf{B} = 0 \tag{1.6}$$

which is known as the ideal Ohm's law.

We will be considering non-relativistic wave propagation, so that

$$V_0 = \frac{L_0}{t_0} \ll c \tag{1.7}$$

where V_0 is a characteristic velocity, with L_0 and t_0 characteristic length and times respectively. Following Siscoe (1983), we can compare the magnitude of the second term on the RHS of equation (1.1) with the LHS, to obtain

$$\frac{|c^{-2}\partial \mathbf{E}/\partial t|}{|\nabla_\wedge \mathbf{B}|} \approx \frac{c^{-2}E_0/t_0}{B_0/L_0} \approx \frac{c^{-2}V_0 B_0/t_0}{B_0/L_0} \approx \frac{V_0^2}{c^2} \tag{1.8}$$

where E_0 and B_0 are typical values of $\mathbf{E}$ and $\mathbf{B}$, and where $E_0 \approx V_0 B_0$ (from equation (1.6)). Hence, in a non-relativistic plasma, the second term on the RHS can be considered negligible, so that

$$\nabla_\wedge \mathbf{B} = \mu_0 \mathbf{j}. \tag{1.9}$$

Taking the divergence of the reduced form of equation (1.1), (i.e., equation (1.9)), we obtain $\nabla.\mathbf{j} = 0$ and hence all currents in MHD can be expected to flow in closed circuits. Similarly, combining equation (1.9) with equations (1.2), (1.3) and (1.5) we obtain the Induction Equation

$$\frac{\partial \mathbf{B}}{\partial t} = \nabla_\wedge(\mathbf{v}_\wedge \mathbf{B}) + \eta \nabla^2 \mathbf{B} \tag{1.10}$$

where the magnetic diffusivity $\eta = 1/\mu_0\sigma$. The first term on the RHS of this equation describes the advection of fluid magnetic field by fluid motion, whereas the second term on the RHS represents the diffusion of $\mathbf{B}$ through the plasma.

We can also consider the charge densities and quasi-neutrality of non-relativistic plasmas with the following analysis. Considering orders of magnitude in equation (1.4), we have

$$\frac{\rho^*}{\epsilon_0} \approx \frac{E_0}{L_0} \approx \frac{V_0 B_0}{L_0} \tag{1.11}$$

where we have again used the relation $E_0 \approx V_0 B_0$. Now, to evaluate the quasi-neutrality of the plasma we can consider the dimensionless parameter ρ^*/en, where e is the magnitude of the plasma particles charge (i.e., they are assumed to be protons and electrons), and n is the particle number density. We can hence write

$$\frac{\rho^*}{en} \approx \frac{\epsilon_0 V_0 B_0}{enL_0} \tag{1.12}$$

and using equation (1.9) we have

$$\frac{B_0}{L_0} \approx \mu_0 J_0 \approx \mu_0 ne\,|\mathbf{v_i} - \mathbf{v_e}| \tag{1.13}$$

where $\mathbf{v_i}$ and $\mathbf{v_e}$ are ion and electron velocities. Assuming $V_0 \approx v_i$, we have (after Siscoe (1983))

$$\frac{\rho^*}{en} \approx \frac{1}{c^2} v_i\,|\mathbf{v_i} - \mathbf{v_e}| \ll 1 \tag{1.14}$$

so that in non-relativistic plasmas charge neutrality is strongly obeyed, and $\rho^* \approx 0$. Consequently, there is no build up of significant space charges in MHD.

We now turn our attention to the fluid equations, which complete the MHD description. We regard the plasmas being considered as continuous fluids, and hence neglect both kinetic and two fluid plasma effects which may occur due to the presence of two differently charged species (ions and electrons), and as a result of their energy distribution functions. The first fluid equation we consider is the (mass) continuity equation

$$\frac{\partial \rho}{\partial t} + \nabla.(\rho \mathbf{v}) = 0 \tag{1.15}$$

where ρ is the mass density of the fluid. The second fluid equation we consider is the equation of motion for a non-viscous plasma

$$\rho \frac{D\mathbf{v}}{Dt} = -\nabla P + \rho \mathbf{g} + \mathbf{j}_\wedge \mathbf{B} \tag{1.16}$$

where P is the pressure, $\rho \mathbf{g}$ represents the gravitational force on a fluid element, $\mathbf{j}_\wedge \mathbf{B}$ is the Lorentz force and D/Dt is the convective derivative given by

$$\frac{D}{Dt} = \frac{\partial}{\partial t} + \mathbf{v}.\nabla. \tag{1.17}$$

Neglecting gravity, and assuming that the plasma is cold (i.e., β (the ratio of thermal / magnetic pressure) = 0), we have

$$\rho \frac{D\mathbf{v}}{Dt} = \mathbf{j} \wedge \mathbf{B}. \tag{1.18}$$

Standard MHD analyses in warm plasmas often need to consider the absorption of energy by a fluid element. We can consider a heat equation of the form

$$\frac{Ds}{Dt} = -\frac{k_B \mathcal{L}}{mP} \tag{1.19}$$

where s is the entropy, k_B is Boltzmann's constant, m is the mean particle mass, and $\mathcal{L}$ is a loss/gain function describing the net effect of thermal conduction, Joule dissipation, radiative losses and any external heat input in a fluid element.

In an adiabatic system $\mathcal{L} = 0$, so that there is no heat flow into or out of the fluid element in time, and hence its entropy remains constant. Since $s = P/\rho^\gamma$, in an adiabatic system we have

$$\frac{D}{Dt}\left(\frac{P}{\rho^\gamma}\right) = 0. \tag{1.20}$$

It is also interesting to note that the adiabatic equation can be written as $P/\rho^\gamma = \alpha$, where α is a constant of the motion. For adiabatic variations it is not necessary for all fluid elements to have the same α, only that a particular fluid element retains constant α along a streamline. If α is the same constant for all fluid elements, then the flow is isentropic (Siscoe, 1983).

In space plasmas, we normally consider particles with three degrees of freedom, so that $\gamma = 5/3$. We can use the relationship between P and ρ to define the temperature T of the plasma. With $\gamma = 5/3$, we obtain the ideal gas law

$$P = nk_B T \tag{1.21}$$

where $n(= \rho/m)$ is the particle number density (see Siscoe (1983) for a more detailed discussion). If we restrict ourselves to a consideration of cold plasmas, then we can neglect equations (1.19-1.21).

We can summarise the relevant non-relativistic ideal MHD equations as

$$\nabla_{\wedge}\mathbf{B} = \mu_0\mathbf{j} \tag{1.22}$$

$$\nabla.\mathbf{B} = 0 \tag{1.23}$$

$$\nabla_{\wedge}\mathbf{E} = -\frac{\partial \mathbf{B}}{\partial t} \tag{1.24}$$

$$\nabla.\mathbf{E} = 0 \tag{1.25}$$

$$\mathbf{E} + \mathbf{v}_{\wedge}\mathbf{B} = 0 \tag{1.26}$$

$$\frac{\partial \rho}{\partial t} + \nabla.(\rho\mathbf{v}) = 0 \tag{1.27}$$

$$\rho\frac{D\mathbf{v}}{Dt} = -\nabla P + \mathbf{j}_{\wedge}\mathbf{B} \tag{1.28}$$

$$\frac{D}{Dt}\left(\frac{P}{\rho^{\gamma}}\right) = 0 \tag{1.29}$$

which can be combined, in the cold plasma case, to give

$$\frac{\partial \rho}{\partial t} + \nabla.(\rho\mathbf{v}) = 0 \tag{1.30}$$

$$\rho\frac{D\mathbf{v}}{Dt} = (\nabla_{\wedge}\mathbf{B})_{\wedge}\frac{\mathbf{B}}{\mu_0} \tag{1.31}$$

$$\frac{\partial \mathbf{B}}{\partial t} = \nabla_{\wedge}(\mathbf{v}_{\wedge}\mathbf{B}) \tag{1.32}$$

along with the solenoidal constraint $\nabla.\mathbf{B} = 0$.

1.2.2 Uniform Plasma MHD Wave Solutions.

The form of the ideal MHD equations described above can be used to infer the properties of wave modes which may propagate in an MHD plasma. To illustrate the characteristics of these wave modes, we derive the uniform warm plasma dispersion relations for the three types of wave modes which exist - namely fast, slow and Alfvén waves. In a homogeneous plasma these modes are decoupled from each other; however, when a non-uniformity is introduced they become coupled.

If we assume that the background magnetic field is uniform and lies purely in the $\hat{\mathbf{z}}$ direction ($\mathbf{B_0} = B_0\hat{\mathbf{z}}$), that the background pressure and density are uniform, and linearise about a stationary background equilibrium, equations (1.22) and (1.28) can be combined, and along with equation (1.32) can be written as

$$\frac{\partial \mathbf{b}}{\partial t} = \nabla_{\wedge}(\mathbf{v}_{\wedge}\mathbf{B_0}) = B_0\frac{\partial \mathbf{v}}{\partial z} - B_0\Delta \tag{1.33}$$

and

$$\rho_0\frac{\partial \mathbf{v}}{\partial t} = -\nabla P_1 + \mu_0^{-1}\left[B_0\frac{\partial \mathbf{b}}{\partial z} - \nabla(\mathbf{B_0}.\mathbf{b})\right] \tag{1.34}$$

where P_1, $\mathbf{v}$ and $\mathbf{b}$ are the linearised pressure, velocity and magnetic field respectively, and $\Delta = \nabla.\mathbf{v}$ (Cowling, 1976).

For adiabatic motions, equation (1.20) can be used to obtain

$$P_1 = \gamma P_0\left(\frac{\rho_1}{\rho_0}\right) = c_s^2\rho_1 \tag{1.35}$$

where ρ_1 is the linearised density perturbation and c_s is the sound speed. Using the (mass) continuity equation we obtain

$$\frac{\partial^2 \mathbf{v}}{\partial t^2} = c_s^2\nabla\Delta + v_A^2\left[\frac{\partial}{\partial z}\left(\frac{\partial \mathbf{v}}{\partial z} - \hat{\mathbf{z}}\Delta\right) - \nabla\left(\frac{\partial v_z}{\partial z} - \Delta\right)\right] \tag{1.36}$$

where $v_A = (B_0^2/\mu_0\rho_0)^{\frac{1}{2}}$ is the Alfvén speed (Cowling, 1976). Taking the $\hat{\mathbf{z}}$ component, and the divergence, of this equation results in the following two equations

$$\frac{\partial^2 v_z}{\partial t^2} = c_s^2\frac{\partial \Delta}{\partial z} \tag{1.37}$$

and

$$\frac{\partial^2 \Delta}{\partial t^2} = c_s^2\nabla^2\Delta + v_A^2\nabla^2\left(\Delta - \frac{\partial v_z}{\partial z}\right) \tag{1.38}$$

(Cowling, 1976; Roberts, 1985; Roberts, 1991).

Now if $\Delta = \nabla.\mathbf{v} = 0$ (i.e., the disturbance is incompressible) equation (1.37) gives $v_z = 0$, equation (1.27) and (1.35) give $P_1 = \rho_1 = 0$, and equation (1.36) becomes

$$\frac{\partial^2 \mathbf{v}}{\partial t^2} = v_A^2\frac{\partial^2 \mathbf{v}}{\partial z^2}. \tag{1.39}$$

This equation describes Alfvén waves in a homogeneous medium. Alfvén waves propagate without disturbing the thermal pressure or the (mass) density of the plasma, are driven by magnetic tension alone, and are analogous to waves travelling on stretched strings. If we

assume disturbances of the form $\mathbf{v} \sim \exp i\,[\omega t - (k_x x + k_y y + k_z z)]$, we obtain the Alfvén wave dispersion relation

$$\omega^2 = v_A^2 k_z^2 \tag{1.40}$$

where k_x, k_y and k_z are the components of the Alfvén wavevector $\mathbf{k}$. Consequently, the Alfvén waves' group velocity $(\partial\omega/\partial\mathbf{k})$ lies purely in the $\hat{\mathbf{z}}$ direction (independent of the direction of propagation of the waves' phase fronts $\mathbf{k}$) and the waves can only transport energy along the magnetic field lines.

The second case to consider is when $\Delta \neq 0$. Here, (1.37) and (1.38) can be combined to give a single equation for Δ

$$\frac{\partial^4 \Delta}{\partial t^4} - (v_A^2 + c_s^2)\frac{\partial^2}{\partial t^2}(\nabla^2 \Delta) + v_A^2 c_s^2 \frac{\partial^2}{\partial z^2}(\nabla^2 \Delta) = 0 \tag{1.41}$$

(Lighthill, 1960; Cowling, 1976; Roberts, 1985; Roberts, 1991). Again assuming disturbances of the form $\exp i\,[\omega t - (k_x x + k_y y + k_z z)]$ we obtain the dispersion relation

$$\omega^4 - (c_s^2 + v_A^2)k^2\omega^2 + c_s^2 v_A^2 k_z^2 k^2 = 0 \tag{1.42}$$

where $k = (k_x^2 + k_y^2 + k_z^2)^{\frac{1}{2}}$. This has the solution

$$\omega^2 = \frac{k^2}{2}\left\{(c_s^2 + v_A^2) \pm \left[c_s^4 + v_A^4 - 2c_s^2 v_A^2 \cos 2\theta\right]^{\frac{1}{2}}\right\} \tag{1.43}$$

where $k_z = k\cos\theta$, and hence θ represents the angle between $\mathbf{k}$ and $\mathbf{B_0}$. The positive and negative solutions of this dispersion relation correspond to the fast and slow magneto-acoustic waves respectively. Fast waves can be considered to be analogous to sound waves modified by the presence of the magnetic field. They are driven by both tension and pressure forces, and have thermal and magnetic pressure variations which are in phase. Slow waves are also driven by both tension and pressure forces, but have thermal and magnetic pressure variations which are out of phase. This phase difference is often used to distinguish the fast and slow wave modes from each other. Slow waves are similar to sound waves in an organ pipe - the magnetic field lines giving the rigidity to the flux tube.

In the left hand panel of Figure (1.2) we sketch the reciprocal normal surface for fast, slow and Alfvén waves for a case where $v_A > c_s$ (i.e., a low β plasma). This diagram shows how far a plane wave phase front would travel from the origin in a unit time in

the direction of $\mathbf{n}$ ($\mathbf{n}$ represents the normalised wavevector $\mathbf{n} = \mathbf{k}/(k_x^2 + k_y^2 + k_z^2)^{\frac{1}{2}}$). The strong solid horizontal arrow shows the direction of $\mathbf{B_0}$, and by symmetry (perpendicular to $\mathbf{B_0}$) the 3-D phase front propagation can be visualised as surfaces of rotation about $\mathbf{B_0}$. In terms of the phase speed, the fast mode propagates almost isotropically, whilst the slow and Alfvén modes are constrained so that their phase fronts cannot propagate perpendicular to $\mathbf{B_0}$. The Alfvén modes have circular reciprocal normal surfaces.

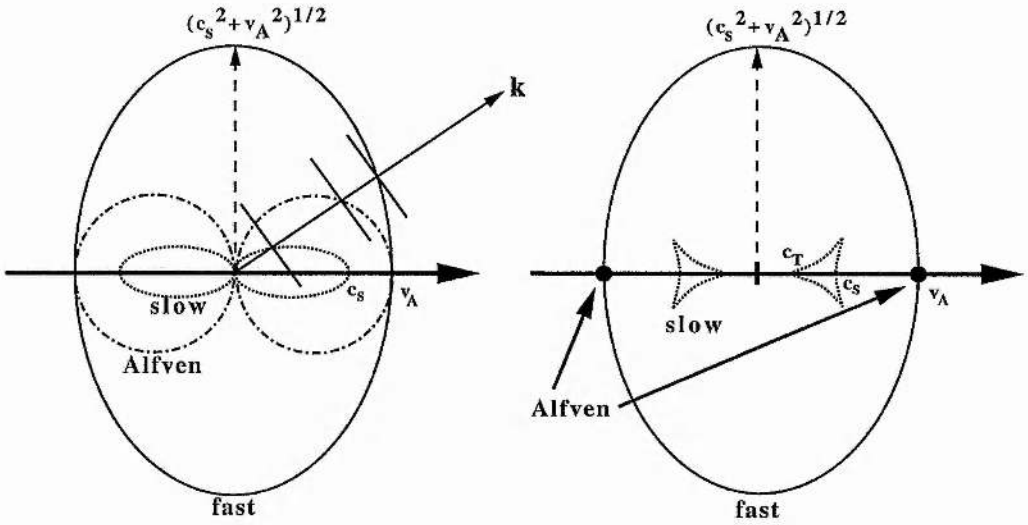

Figure 1.2: Left hand panel: The phase speed of fast, slow and Alfvén waves in a homogeneous plasma as a function of θ, the angle between the waves wavevector ($\mathbf{k}$) and $\mathbf{B_0}$. Right-hand panel: Wave group velocity as a function of θ.

In the right hand panel of Figure (1.2), we sketch the group velocity ray surfaces, again for fast, slow and Alfvén waves. These surfaces can be calculated by taking the envelope of the plane phase fronts for each mode (illustrated by the three phase front lines drawn perpendicular to $\mathbf{k}$ in the first panel). Whilst in terms of group velocities, the fast mode maintains its near isotropic propagation (exactly isotropic when $c_s = 0$), the anisotropic nature of the slow and Alfvén modes is enhanced. The Alfvén mode only propagates energy exactly parallel to $\mathbf{B_0}$ at the Alfvén speed, whilst the slow mode generates a group velocity cusp which is almost field guided. Interestingly, whilst slow modes with $\mathbf{k}$ parallel to $\mathbf{B_0}$ have a group velocity ($= c_s$) which is also parallel to $\mathbf{B_0}$, waves with $\mathbf{k}$ exactly perpendicular to $\mathbf{B_0}$ have a group velocity which is also parallel to $\mathbf{B_0}$, given by

$c_T = c_s v_A/(c_s^2 + v_A^2)^{\frac{1}{2}}$.

The unusual behaviour of the slow waves is further illustrated by the interesting fact that for the wave propagation perpendicular to $\mathbf{B_0}$ (albeit small), the group velocity occurs in a direction opposite to k. Hence, the slow waves direct energy perpendicular to $\mathbf{B_0}$ using phase fronts which actually travel anti-parallel to the direction of energy propagation! (Goedbloed, 1983). In a cold plasma $c_s^2 = 0$, so that the slow wave has $\omega = 0$ and hence no longer propagates. In this limit the fast mode has the dispersion relation

$$\omega^2 = k^2 v_A^2 \tag{1.44}$$

and propagates energy isotropically at the Alfvén speed (i.e., $\partial\omega/\partial k_\alpha(\alpha = x, y, z) = \pm v_A$). The propagation characteristics of fast and Alfvén waves in uniform plasmas are clearly quite different. When the waves are coupled in non-uniform media, the behaviour becomes more complex; however, the uniform results provide a useful benchmark for the interpretation of the inhomogeneous results.

In Figure (1.3), we sketch the directions of the fields of (a) Alfvén and (b) fast waves relative to $\mathbf{k}$ and $\mathbf{B_0}$. The Alfvén wave can be seen to be incompressible in a uniform cold plasma, since k is perpendicular to v. Moreover, the magnetic field is not compressed since $\mathbf{b}$ is perpendicular to $\mathbf{B_0}$. The fast wave, however, is clearly compressible as it has a component b_z parallel to $\mathbf{B_0}$ and $\mathbf{k}.\mathbf{v} \neq 0$. This important distinction between the behaviour of fast and Alfvén wave modes can still be usefully employed in the non-uniform case to analyse wave behaviour. The direction of the other vectors follows from the form of the governing MHD equations (Dungey, 1967; Southwood and Hughes, 1983).

When a non-uniformity is introduced the distinct separation of modes into fast, slow and Alfvén waves is lost. The three modes can become coupled to each other, and their resonant interactions form an active current research topic. In Chapter 4, we consider the resonant interaction of fast and Alfvén waves in a cold inhomogeneous plasma environment.

1.2.3 Applicability of MHD to Waves in the Magnetosphere.

In section (1.2), we made assumptions whereby the resistivity (the ideal assumption) and the viscosity of the plasma were neglected. We similarly assumed $\beta \ll 1$ so that thermal pressure could be neglected in comparison with magnetic pressure, and hence set $c_s^2 = 0$. These are reasonable assumptions for the sparse density plasma populations which

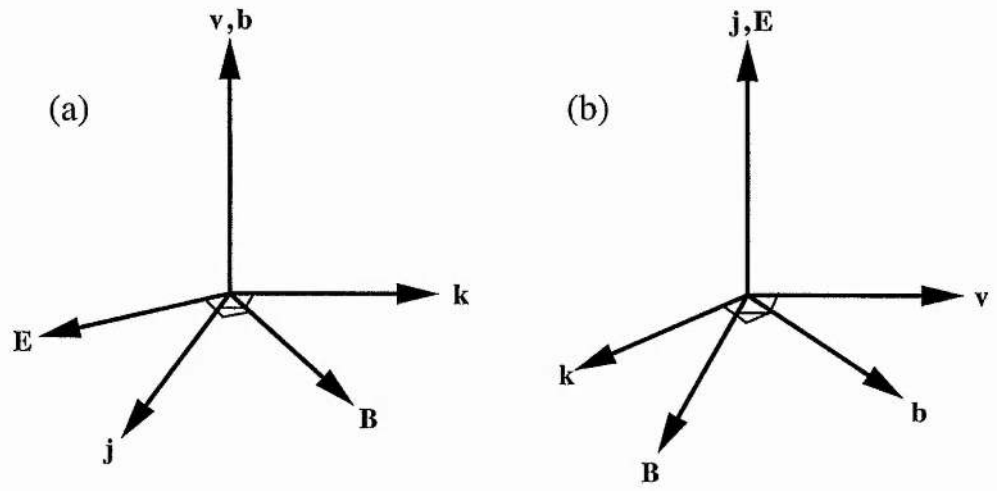

Figure 1.3: Relationship between $\mathbf{B_0}$, $\mathbf{k}$ and the field vectors for (a) Alfvén and (b) fast waves in a homogeneous plasma. After Dungey (1967).

exist in most of the Earth's magnetosphere, and are self- consistent with the single fluid MHD description. However, the assumption that the magnetospheric plasma can behave as a single continuous fluid (single fluid MHD) needs careful consideration. The single fluid model can be modified to incorporate two or more interacting fluids, to better approximate the constituent plasma species (ions and electrons) where necessary. We will however confine ourselves to a single fluid discussion here.

Firstly, since we are treating the fluid as a continuum, the length-scales of variations described by MHD need to strictly be much larger than typical internal (kinetic) plasma length-scales, such as the ion gyro-radius (r_L). For typical pulsations, the wave scales can be $\sim$ several Earth radii (R_E) and the criteria is usually satisfied (we discuss this further in Chapter 4). Similarly, the periods of the waves which we want to describe should be very much greater than the particle gyro-periods. For ULF waves this condition is usually satisfied.

Secondly, since we are implicitly assuming that the plasma is in a stable (thermodynamic) equilibrium (i.e, it has a Maxwellian distribution function), we can strictly only use MHD to describe waves with timescales much longer than particle collision times, and with length-scales much longer than mean free paths. (Note that non-Maxwellian velocity distributions can resonantly drive pulsations, in a manner similar to Landau damping - Southwood and Kivelson (1981) and Southwood and Kivelson (1982) for examples of the

theory, and Hughes et al. (1978) for observations of pulsations driven by energetic particle populations). Unfortunately, in the magnetosphere the plasma is very sparse and the time between particle collisions is very long. In fact to a good approximation the collision frequency is so low that the plasma can be treated as collisionless. Strictly, this means that MHD theory should not be applied to the study of magnetospheric pulsations.

However, as discussed by Cowling (1976), the presence of the magnetic field in the plasma can be invoked to tie the charged particle populations together sufficiently that a one fluid continuum approximation remains valid. The reason is that the motions of charged particles in a collisionless plasma, permeated by a magnetic field, consist predominantly of a spiralling of the particles about the background magnetic field ($\mathbf{B_0}$). This introduces a coupling of particles through the action of the magnetic field, rather than through collisions. This effect can be considered to be playing the role of collisions by providing a perpendicular interaction length.

The particles can also experience acceleration parallel to the magnetic field, by forces which act parallel to $\mathbf{B_0}$, and they experience slow drifts perpendicular to $\mathbf{B_0}$ when acted on by perpendicular forces. In low energy plasmas, the perpendicular drifts are dominated by the electric field drift. This acts independent of the sign of electric charge, and causes both electrons and ions to drift with the velocity of the field. In this way, the collisionless plasma can be viewed as being very nearly frozen to the field lines. Despite the fact that no equivalent behaviour exists for parallel motions, the single fluid continuum approximation remains a valid approximation in collisionless plasmas, and can be used to determine results which agree with observations better than might be expected (see Cowling (1976) for more details). Consequently, we can apply MHD to the fast and Alfvén wave modes which are known to propagate in the magnetosphere.

Unfortunately, the compressible MHD description of slow waves in a collisionless plasma is of questionable validity, since the slow wave phase speed is of the same order as the ion thermal speed. This can result in strong Landau damping of the waves, so that MHD fails to accurately describe the wave evolution. The fast mode is much better described by MHD since its phase speed is always greater than the Alfvén speed (Southwood and Hughes, 1983; Southwood, 1985). Since we restrict ourselves to a cold plasma description, the shortfalls of MHD in describing slow modes in a collisionless plasma should not concern us.

1.3 Brief Morphology of the Earth's Magnetosphere.

As we have previously discussed, the solar wind is ultimately the dominant energy source for magnetospheric pulsations. However, how such waves evolve will depend on the local background plasma conditions. In this section, we discuss how the solar wind interacts with the magnetosphere to generate it's known morphology (see Vasyliunas (1983) for a detailed review).

Since the solar wind flow at the Earth is supersonic (actually supersonic, super-Alfvénic and super-fast) it generates a standing collisionless shock up stream of the magnetopause at a standoff distance from the Earth of $\sim 15R_E$. This is known as the *bow shock*. Solar wind plasma is thermalised by this shock, and the subsequently sub-fastmagnetosonic flows form the region called the *magnetosheath* as they flow around the magnetosphere. On the magnetopause (the boundary between magnetospheric and solar wind magnetic fields) surface currents are driven, as shown in the schematic diagram of Figure (1.4).

With Dungey's open model for the solar wind/magnetospheric magnetic fields, plasma can enter the magnetosphere directly through the *cusp*. This plasma is believed to experience strong magnetic mirror forces which carry it back up the field lines, to be swept downstream by magnetospheric convection to form the *plasma mantle*. At lower latitudes, magnetosheath plasma can similarly cross the magnetopause to form the *low latitude boundary layer*.

Inside the magnetosphere itself, various plasma population regions are generated. Above the ionosphere, and up to a height of $\sim 5R_E$, a relatively cold plasma population ($\leq$ 1eV) of ions and electrons co-rotates with the Earth and it's atmosphere to form the *plasmasphere*. The plasmasphere is threaded by permanently closed magnetic field lines, and its plasma is believed to be in diffusive equilibrium with the ionosphere. Consequently, the ionosphere is the main source of plasmaspheric particles.

Continuing radially outwards, the next plasma region consists of plasma flux tubes which are involved in the magnetospheric convection being driven by the solar wind. Closed field lines are advected in a sunward direction around the flanks of the magnetosphere and are believed to become reconnected with solar wind magnetic fields near the nose of the magnetosphere (Dungey, 1961). After reconnection, the solar wind carries these flux tubes across the polar cap, and into the magnetotail. In the tail the flux tubes drift towards the magnetic neutral line and are thought to again become closed as they reconnect at an X-

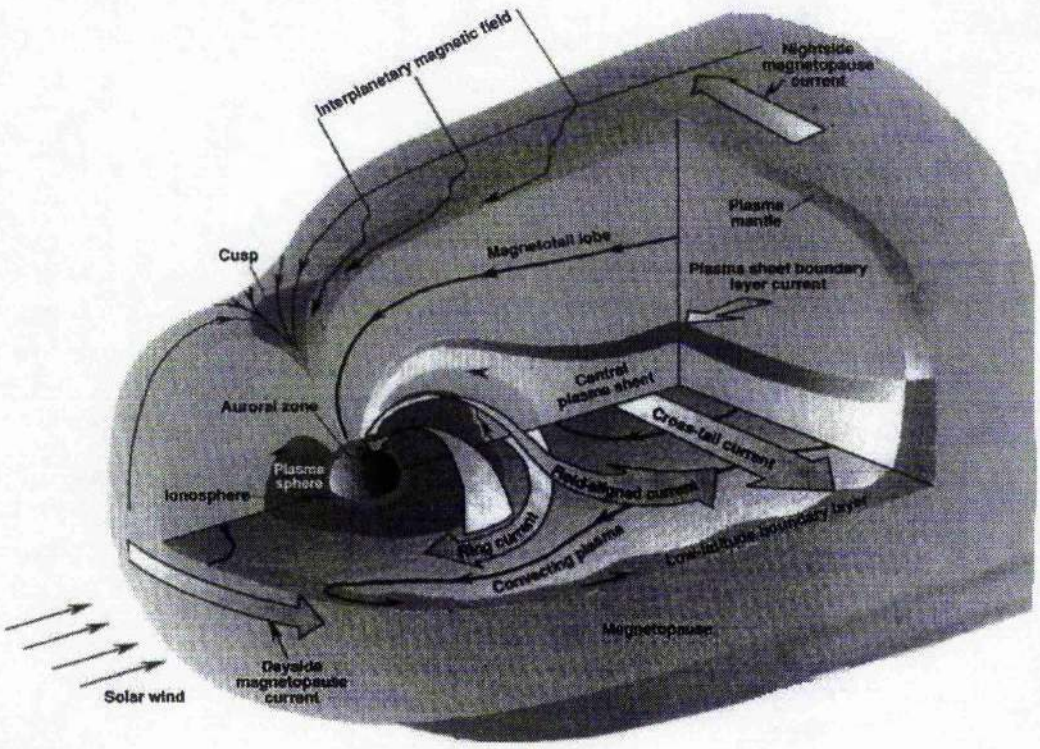

Figure 1.4: Cut-away schematic diagram of the Earth's magnetosphere. (From Rice University's space weather homepage: http://rigel.rice.edu/~dmb/spwea.html)

type magnetic neutral point in the tail current sheet. The closed field lines which are formed are again advected towards the nose, and the cycle continues. This plasma region is known as the *plasmatrough*, and consists of highly energetic particles ($\sim 1 - 10$keV). These particles mirror between the endpoints of the field lines, generating the radiation belts (after Van Allen and Frank (1959)). Since these high energy particles experience drifts dominated by both gradient and curvature drifts, positive and negative charges drift in opposite directions and establish the *ring current* which circles the Earth in the plasmatrough.

Over the polar cap itself, ionospheric plasma can stream out along magnetic field lines and into the *magnetotail lobes*. On the nightside, the lobes are populated by both this

streaming ionospheric plasma, and by mantle plasma (from the solar wind) which drifts towards the centre of the tail. Following reconnection at the neutral point, this plasma is energised by neutral line acceleration, and compression as the flux tubes move Earthwards. This generates the *plasmasheet* and ultimately these energetic particles are the source of the energetic ring current particle population. Clearly, the plasmasheet is a very energetic and active part of the magnetosphere, and it is believed to play an important role in the large scale disruptions of the magnetosphere known as *sub-storms*.

The magnetospheric convection pattern also sets up large scale current systems, which occur as a result of transverse momentum being transferred along magnetic field lines (for example ionospheric drag on field lines being convected across the polar cap (Southwood and Hughes, 1983)). These currents can be generated by Alfvén waves which propagate to transfer momentum along the field lines.

The existence of different magnetospheric plasma regions, having different field strengths and particle number densities, can create plasma boundaries. These can either separate wave propagation regions or even support waves themselves - for example allowing the propagation of surface wave modes. In the next section we review the types of ULF waves which have been observed in different magnetospheric regions, and briefly outline their likely energy sources.

1.4 ULF Waves in the Magnetosphere.

Magnetospheric ULF waves (having frequencies $\sim$ 1Hz - 1mHz) are classified into into two basic types, continuous, representing quasi-sinusoidal waves lasting for several cycles or more, and irregular, meaning pulsations which are either short lived or broadband. These classes are sub-divided according to period, with a number specifying a particular waveband. Consequently, pulsations have come to be classified as Pc1-5, or Pi1 and 2, as shown in Table 1.1.

Usually, no particular source mechanism is implied by a particular classification, the exception being Pi2 pulsations which have come to be synonymous with waves generated by the magnetospheric reorganisation of sub-storms. In this thesis, we are interested in pulsations primarily in the Pc3-5 wavebands. For reviews of the MHD theory of pulsations see Southwood and Hughes (1983), Hughes (1983), Southwood (1985), Wright (1994b), and for a historical review see Hughes (1994).

Continuous Pulsations		Irregular Pulsations	
Type	Period range (sec)	Type	Period range (sec)
Pc 1	0.2-5.0	Pi 1	1-40
Pc 2	5-10	Pi 2	40-150
Pc 3	10-45		
Pc 4	45-150		
Pc 5	150-600		

Table 1.1: The classification of ULF pulsations.

Various energy sources are believed to be responsible for exciting different types of pulsations. The occurrence of Pc3 waves, for example, has been correlated with the orientation of the interplanetary magnetic field (IMF) (see Hughes (1994) and references therein). For IMF angles $\lesssim 50^{o}$ to the Sun-Earth line, waves are observed by ground-based magnetometers. For larger angles, they are not. These Pc3 pulsations are driven by upstream waves, themselves generated by an ion-cyclotron instability in ions reflected by the bow shock. This reflection only occurs when the IMF is approximately normal to the shock front, and in this case the waves can be advected by the solar wind through the bow shock and the magnetopause, and into the magnetosphere where they excite pulsations.

With the advent of modern technology, computers allowed high resolution digital measurements to be made with ground based magnetometer chains. Results from these studies showed that despite pulsations being excited over a range of latitudes (having different local natural Alfvén periods), the pulsations often had monochromatic oscillation frequencies, with one particular latitude displaying an amplitude peak. This lead to the field line resonance (FLR) concept, whereby a single driving frequency resonantly excites a dominant response at one particular latitude.

Polarisation studies of FLRs revealed a characteristic polarisation reversal about local noon, indicating that the solar wind was most probably the source of the waves (Samson et al., 1971). Independently, Southwood (1974) and Chen and Hasegawa (1974a) proposed that the solar wind excited travelling Kelvin-Helmholtz (KH) vortices on the magnetopause, and that these surface waves would excite pulsations inside the magnetosphere where their frequency matched that of the local Alfvén frequency. However, observations of the azimuthal phase velocity of FLRs predicted magnetosheath speeds greatly in excess of those typically observed. Moreover, KH surface waves should have phase speeds which

are less than the sheath velocity, and this introduces an even greater discrepancy.

Kivelson and Southwood (1985) subsequently proposed that the magnetosphere as a whole could resonate at it's global eigenfrequencies. This removed the excessively high velocities required by the KH models, although KH may still be a viable mechanism when the sheath velocity is large. These ideas were put on a firm theoretical foundation by both analytical and numerical models (Kivelson and Southwood, 1985; Kivelson and Southwood, 1986; Allan et al., 1986b; Inhester, 1987; Krauss-Varban and Patel, 1988; Zhu and Kivelson, 1988; Lee and Lysak, 1989; Lee and Lysak, 1991; Fujita and Patel, 1992; Wright, 1992b). Observations by Samson et al. (1991a) and Walker et al. (1992) show that there is a preference for high latitude FLRs to be observed at specific frequencies. They identify these Pc5 frequencies to be the lowest harmonic fast eigenfrequencies. Unfortunately, the cavity produced by the magnetopause and a predicted magnetospheric turning point produce frequencies which are in general too high to match those regularly seen (in particular the lowest eigenfrequency). Harrold and Samson (1992) subsequently proposed that the outer boundary might be provided by the bow shock, rather than the magnetopause, as this produces lower frequencies, and is likely to be a better wave reflector.

In situ satellite observations of cavity modes, having spatially monochromatic compressional signals, have proved difficult to find. A statistical study by Anderson et al. (1989), using the AMPTE/CCE data, failed to detect either waves with cavity mode characteristics, or resonances which were localised in latitude. However, as discussed by Hughes (1994), the failure to observe localised resonances may in part be due to the fact that the AMPTE/CCE data emphasises waves with frequencies $\gtrsim 10$ mHz. This is higher than the Pc5 FLR frequencies often observed on the ground by magnetometers at latitudes covering the AMPTE/CCE orbit. AMPTE/CCE did observe Pc3/4 pulsations with latitude dependent frequencies, corresponding to local field line eigenfrequencies. It is possible that these waves were driven by cavity eigenmodes, since if the frequencies ($\sim$ mHz) seen by Samson et al. (1991a) are the lowest order cavity modes, and because the cavity modes are governed by three mode numbers, then at frequencies $\gtrsim 10$ mHz the cavity mode spectrum could become so densely packed that it approximates a continuum (Hughes, 1994).

A study by Crowley et al. (1987) (see also Crowley et al. (1989)) used radar observations to infer the ionospheric conductivity at the location of an FLR, and hence the expected wave damping. The decay of the pulsations occurred over a longer timescale than that predicted by the observed ionospheric conductivity. This was interpreted as evidence

that the pulsation was being continually driven by a cavity mode during their observations. This, along with the constancy of the FLR frequencies seen by Samson et al. (1991a) and Walker et al. (1992), is probably the best evidence currently available to support the definite existence of cavity modes.

Further extensions to the cavity model have been made by recognising the fact that the outer magnetosphere (between the magnetopause and the plasmapause) is probably better modelled by a waveguide which remains open downtail (Samson et al., 1992a; Walker et al., 1992). Simulations within waveguides reveal that the fast waveguide modes do not possess the cavity model feature of regular oscillations with constant period over a range of L shells (Rickard and Wright, 1995). This could explain why AMPTE/CCE failed to observe the monochromatic compressional signals expected in a cavity. Indeed, further analysis of the AMPTE/CCE data, completed by Engebretson and Anderson (1995), despite failing to detect standing outer magnetospheric Pc5 cavity modes, did find evidence of travelling monochromatic compressional waves which may be the signature of waveguide modes. Theory by Wright (1994a), and simulations by Rickard and Wright (1994) and Rickard and Wright (1995) show that in a waveguide, it is the low azimuthal wavenumber (m) waves (where m is the azimuthal wavenumber, normalised in units of R_E^{-1} - typically $m \lesssim 10$) which excite FLRs: consequently low m cavity models can still be utilised as an approximation with which to study FLR behaviour.

Statistical studies of the occurrence distributions of ULF waves in the magnetosphere using AMPTE/CCE (Anderson et al., 1990) and ISEE (Cao et al., 1994) data show that monochromatic, fundamental Pc5 waves (consistent with FLR's) are often ($\approx$ 70% probability) seen at the flanks. Since Anderson et al. (1990) fail to see localised resonances, they argue that the observed latitude dependent frequency oscillations result from KH instabilities on the magnetopause. However, as we have previously discussed, the frequency resolution of the AMPTE/CCE data set may make low frequency Pc5 resonances hard to observe. Also, once a cavity/waveguide mode has decayed and driven an FLR, the transient toroidal oscillation at the driving frequency will become dominated by the local Alfvén frequency response, and if the fast mode spectrum is sufficiently dense, observations could approximate the observed continuum. It remains to be resolved why monochromatic signals are so consistently observed with ground based magnetometers, although this may be the result of spatial integration effects (Poulter and Allan, 1985).

Similarly, it is possible that outer magnetospheric cavity modes can tunnel past

the Alfvén speed barrier generated by the plasmapause to drive plasmaspheric FLRs. Indeed, numerical studies by Allan et al. (1986a) and Zhu and Kivelson (1989) show how the magnetosphere may be better approximated by two cavities, both of which may support global compressional eigenmodes, and drive FLR's. These FLR's may have frequencies in the Pc3/4 range. Magnetometer observations by Ziesolleck et al. (1993) show evidence for the existence of plasmaspheric FLR's, Yumoto et al. (1994) found some evidence for global plasmasphere oscillations, and Samson et al. (1995) found evidence of Pc3-4 oscillations having discrete frequency spectra fine structure consistent with the harmonics of modes excited between the magnetopause and a turning point within the plasmasphere.

In Chapter 4, we consider the temporal development of FLR's as driven by a model cavity eigenmode. The cavity eigenmode can be considered to represent either an outer magnetospheric, or a plasmaspheric cavity mode. We investigate the temporal development of the widths of FLR's in an ideal plasma, and compare them to detailed observations reported in the literature.

Radially polarised (poloidal) ULF waves were also reported by Anderson et al. (1990). Their observations are consistent with waves driven by a drift-bounce resonance mechanism (see e.g., Southwood and Kivelson (1981) and Southwood and Kivelson (1982)). These pulsations are believed to be generated by particles mirroring along field lines, drifting in azimuth, and resonantly exciting high m poloidal ULF waves. Other satellite studies have observed waves of this type (Singer et al., 1982; Hughes and Grard, 1984; Takahashi et al., 1984; Takahashi et al., 1990). In Chapters 5 and 6, we consider an MHD evolution of high m poloidal waves in an inhomogeneous plasma.

1.5 Outline of the Thesis.

This thesis is concerned with the temporal evolution of MHD waves in the inhomogeneous plasma of the Earth's magnetosphere. In Chapter 2 we outline the governing equations and the numerical model utilised to study these waves, and discuss the methods used to ensure that the scheme was converging to the correct solution.

Many previous inhomogeneous MHD wave studies have concentrated on the normal modes of the system (Kivelson and Southwood, 1986; Zhu and Kivelson, 1988; Krauss-Varban and Patel, 1988). In Chapter 3 we discuss the details of the normal modes generated by our code, for both homogeneous and inhomogeneous plasmas, for decoupled ($\lambda = 0$) and

for coupled, high and low λ, wave modes (λ being the "azimuthal" wavenumber).

Chapter 4 concentrates on the temporal development of FLR's driven by low λ cavity eigenmodes. We derive some analytical results for the evolution of the overall resonance width, and for the fine displacement scales developed in our ideal MHD model. We also consider the modifications to the ideal model implied by the introduction of a conducting ionosphere, and by kinetic plasma effects.

In Chapters 5 and 6, we turn to a consideration of the evolution of large λ poloidal Alfvén waves. Chapter 5 considers numerical results for low and high field aligned harmonic studies. We find that asymptotically in time, the poloidal waves approach a purely toroidal polarisation state, consisting of decoupled field line oscillations. In Chapter 6, we derive an analytic representation for this polarisation rotation, by utilising the asymptotic method of multiple time scales. Chapter 7 concludes the thesis and discusses the possibilities for future research.

Chapter 2

Governing Equations and Numerical Model.

2.1 Model Magnetosphere.

To study the problem of coupled MHD wave modes in an inhomogeneous plasma, we choose to adopt a box model for the magnetosphere (e.g., Southwood (1974)) - see Figure (2.1). In this model we assume that the magnetic field is uniform, straight, and lies purely in the $\hat{\mathbf{z}}$ direction between ionospheric endpoints (i.e., $\mathbf{B_0} = B_0\hat{\mathbf{z}}$). We impose a density profile $\rho(x)$ to define an inhomogeneous Alfvén velocity profile in the $\hat{\mathbf{x}}$ (radial or L-shell) direction, with the $\hat{\mathbf{y}}$ direction completing the triad and representing the "azimuthal" direction of the model magnetosphere.

We assume that the ionospheric boundaries are perfectly conducting, so that plasma displacements are zero there (i.e., $\xi(z = 0, z_0) = 0$). Similarly, boundaries in the $\hat{\mathbf{x}}$ direction are provided by assuming large Alfvén speed gradients so that incident waves have zero normal velocity components ($\xi_x(x = 0, L_x) = 0$) and hence are perfectly reflected. We also assume that the magnetospheric plasma is cold, i.e., magnetic forces dominate thermal pressure forces, so that the plasma β (the ratio thermal/magnetic pressures) is zero.

In this cold plasma, there is no linearised displacement $\xi_z = 0$ since there is no component of the $\mathbf{j}_\wedge\mathbf{B}_0$ force acting in the $\hat{\mathbf{z}}$ direction. Assuming periodic boundary conditions in the $\hat{\mathbf{y}}$ direction, we choose the plasma displacements to vary as

$$\xi = (\xi_x(x,t), \xi_y(x,t), 0)e^{i\lambda y} \sin k_z z. \tag{2.1}$$

Here the factor $\sin k_z z$ yields a standing wave solution between the perfectly reflecting northern and southern ionosphere, and λ specifies the azimuthal variation of the waves.

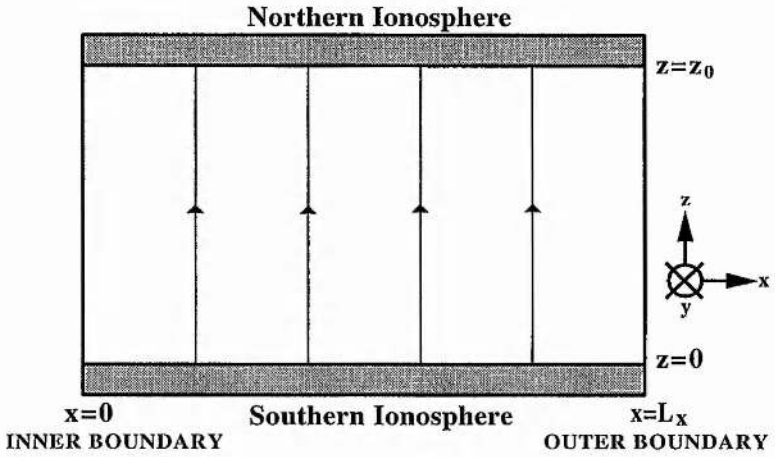

Figure 2.1: The box model magnetosphere adopted for this numerical study. The edges of the simulation box in $\hat{\mathbf{x}}$, (at $x = 0, L_x$) are provided by boundaries with large Alfvén speed gradients.

2.2 Governing Equations.

To study the properties of ideal wave coupling, we neglect viscous and resistive dissipation in the body of the magnetosphere, and adopt an ideal MHD description so that

$$\mathbf{E} + \mathbf{v}_\wedge \mathbf{B} = 0. \tag{2.2}$$

In the cold plasma limit, we neglect thermal pressure forces. In this limit, slow mode waves cannot propagate, leaving only fast and Alfvén waves as possible modes. With $\mathbf{B_0} = B_0\hat{z}$, linearising about a stationary background equilibrium (i.e., $\mathbf{v}_0 = 0$), and prescribing $\rho_0 = \rho_0(x)$ the relevant MHD equations become

$$\frac{\partial \rho_1}{\partial t} + \mathbf{v_1}.\nabla\rho_0 + \rho_0(\nabla.\mathbf{v_1}) = 0 \tag{2.3}$$

$$\rho_0 \frac{\partial \mathbf{v_1}}{\partial t} = (\nabla \wedge \mathbf{b}) \wedge \frac{\mathbf{B_0}}{\mu_0} \tag{2.4}$$

$$\frac{\partial \mathbf{b}}{\partial t} = \nabla \wedge (\mathbf{v_1} \wedge \mathbf{B_0}) \tag{2.5}$$

along with the solenoidal constraint

$$\nabla . \mathbf{b} = 0. \tag{2.6}$$

(Note that $\nabla . \mathbf{B_0} = 0$ is satisfied by the chosen equilibrium magnetic field).

Equation (2.3) (the (mass) continuity equation) simply defines an evolution equation for ρ_1, which is fully determined by both the velocity and the compressibility of the waves (i.e., v_1 and $\nabla . \mathbf{v_1}$). Consequently, we can combine equations (2.4) and (2.5) to give equations for the velocity components v_x and v_y. Integrating (2.5) with respect to time prescribes a plasma displacement ξ, given by $\mathbf{b} = \nabla \wedge (\xi \wedge \mathbf{B_0})$. Substituting this equation into (2.4), and equating x and y components gives the two coupled equations

$$\frac{1}{v_A^2(x)} \frac{\partial^2 \xi_x}{\partial t^2} + k_z^2 \xi_x - \frac{\partial^2 \xi_x}{\partial x^2} = i\lambda \frac{\partial \xi_y}{\partial x} \tag{2.7}$$

and

$$\frac{1}{v_A^2(x)} \frac{\partial^2 \xi_y}{\partial t^2} + k_z^2 \xi_y + \lambda^2 \xi_y = i\lambda \frac{\partial \xi_x}{\partial x} \tag{2.8}$$

where the Alfvén speed $v_A(x) = (B_0^2/\mu_0 \rho_0(x))^{\frac{1}{2}}$.

If we choose $\lambda = 0$ or ∞, these two equations decouple (Dungey, 1967). For $\lambda = 0$ they essentially describe the evolution of the fast mode (ξ_x) (equation (2.7)), and the Alfvén mode (ξ_y) (equation (2.8)). When $\lambda \to \infty$, $\xi_y \to 0$ and ξ_x describes a decoupled poloidal Alfvén wave. When $\lambda \neq 0$ or ∞ the wave modes are coupled together. If λ is small, energy initially in the fast mode may resonantly mode convert to Alfvén wave energy on localised field lines. In this case, energy initially resident in the fast mode will asymptotically become localised in a narrow resonant Alfvén layer, where the fast mode frequency matches the local Alfvén speed, until it is lost through various dissipation mechanisms (Radoski, 1974). We discuss this further in Chapter 4. When λ is large (but not infinite), then the well known $\lambda \to \infty$ decoupled poloidal Alfvén wave solution is modified, experiencing a polarisation rotation from poloidal to toroidal. We discuss this in Chapters 5 and 6.

2.3 Numerical Solution of the Governing Equations.

In our numerical model, we normalise all lengths to the radial extent of the model magnetospheric box, and velocities to the Alfvén speed at the centre of the box. In all the subsequent equations, all quantities have been normalised and hence normalised k_z defines the (constant) field line length. We use Fourier series expansions to solve for the spatial and temporal evolution of the coupled wave modes in a compressible plasma (c.f. the incompressible study of Cally (1991)).

To satisfy the boundary conditions on ξ_x in the $\hat{\mathbf{x}}$-direction, we write this displacement as a half-range Fourier sine series (e.g., Cally (1991))

$$\xi_x = \sum_{m=1}^{\infty} a_m(t) \sin(\pi m x). \tag{2.9}$$

The form of equations (2.7) and (2.8), suggest that ξ_y be expanded in a cosine series,

$$i\xi_y = \frac{1}{2} b_0(t) + \sum_{m=1}^{\infty} b_m(t) \cos(\pi m x). \tag{2.10}$$

We can now follow a similar procedure to that of Cally (1991), and by assuming a time dependence of $\exp(-i\omega t)$ can write the solutions to the coupled equations (2.7) and (2.8) as a single generalised matrix eigenvalue problem. To employ this method we adopt a model for the monotonically decreasing magnetospheric Alfvén velocity profile given by

$$v_A^{-2}(x) = A^2 - B^2 \cos(\pi x). \tag{2.11}$$

Substituting the half range Fourier series expansions for ξ_x and ξ_y into equations (2.7) and (2.8) and using standard trigonometric identities, we gain two further coupled equations for $a_m(t)$ and $b_m(t)$, given by

$$-\frac{B^2}{2}\ddot{a}_{m-1}(t) + A^2\ddot{a}_m(t) - \frac{B^2}{2}\ddot{a}_{m+1}(t) + (k_z^2 + (\pi m)^2)a_m(t) + \lambda\pi m b_m(t) = 0 \tag{2.12}$$

$$-\frac{B^2}{2}\ddot{b}_{m-1}(t) + A^2\ddot{b}_m(t) - \frac{B^2}{2}\ddot{b}_{m+1}(t) + (k_z^2 + \lambda^2)b_m(t) + \lambda\pi m a_m(t) = 0 \tag{2.13}$$

Assuming perturbations of the form $e^{-i\omega t}$, equations (2.12) and (2.13) can be written as the generalised matrix eigenvalue problem,

$$\omega_n^2 \mathbf{R^2 X_n} = \mathbf{M^2 X_n} \tag{2.14}$$

where $\mathbf{X_n}$ represents an eigenvector, and ω_n^2 its corresponding eigenvalue. By writing $\mathbf{X}$ in the form

$$\mathbf{X} = \begin{bmatrix} b_0 \\ a_1 \\ b_1 \\ a_2 \\ b_2 \\ \vdots \end{bmatrix} \tag{2.15}$$

and using the term $\frac{1}{2}b_0(t)$ in the expansion for ξ_y, we obtain two symmetric matrices $\mathbf{R^2}$ and $\mathbf{M^2}$. We find $\mathbf{R^2}$ is penta-diagonal and $\mathbf{M^2}$ is tri-diagonal (both being Hermitian) as shown below.

$$\mathbf{R^2} = \begin{bmatrix} A^2/2 & 0 & -B^2/2 & 0 & 0 & \cdots \\ 0 & A^2 & 0 & -B^2/2 & 0 & \cdots \\ -B^2/2 & 0 & A^2 & 0 & -B^2/2 & \cdots \\ 0 & -B^2/2 & 0 & A^2 & 0 & \cdots \\ 0 & 0 & -B^2/2 & 0 & A^2 & \cdots \\ \vdots & \vdots & \vdots & \vdots & \vdots & \searrow \end{bmatrix} \tag{2.16}$$

$$\mathbf{M^2} = \begin{bmatrix} \frac{(k_z^2+\lambda^2)}{2} & 0 & 0 & 0 & 0 & 0 & 0 & \cdots \\ 0 & (k_z^2+\pi^2) & \lambda\pi & 0 & 0 & 0 & 0 & \cdots \\ 0 & \lambda\pi & (k_z^2+\lambda^2) & 0 & 0 & 0 & 0 & \cdots \\ 0 & 0 & 0 & (k_z^2+(2\pi)^2) & 2\pi\lambda & 0 & 0 & \cdots \\ 0 & 0 & 0 & 2\pi\lambda & (k_z^2+\lambda^2) & 0 & 0 & \cdots \\ 0 & 0 & 0 & 0 & 0 & (k_z^2+(3\pi)^2) & 3\pi\lambda & \cdots \\ 0 & 0 & 0 & 0 & 0 & 3\pi\lambda & (k_z^2+\lambda^2) & \cdots \\ \vdots & \vdots & \vdots & \vdots & \vdots & \vdots & \vdots & \searrow \end{bmatrix} \tag{2.17}$$

Truncating the summations (equations (2.9) and (2.10)) to a finite number of Fourier modes ($m = N$) yields for the decoupled ($\lambda = 0$) case N Fast modes and $N + 1$

Alfvén modes (i.e. a $(2N+1)$ by $(2N+1)$ matrix eigenvalue problem). Thus in general, we obtain numerically $2N+1$ eigenfrequencies ω_n^2, and $2N+1$ corresponding eigenvectors, representing the coupled wave modes. We employ the NAG libraries generalised matrix eigenvalue problem solver for banded real symmetric matrices - routines F02FHF and F02SDF. In routine F02SDF, we use the convergence criteria for matrices with elements of widely differing magnitudes, since some of the entries in $\mathbf{M^2}$ are $\propto m^2$ (this corresponds to setting the parameter $D(1) = -1$ in the NAG library routine. See NAG library documentation for more details).

Writing α_{mn} as the components of a solution matrix, having the solution eigenvectors as its columns, we get a general solution for both $\xi_x(x,t)$ and $\xi_y(x,t)$ in the form

$$\xi_x(x,t) = \sum_{m=1}^{N} a_m(t) \sin(\pi m x) \tag{2.18}$$

where

$$a_m(t) = \sum_{n=1}^{2N+1} \alpha_{m_x n} \left[c_n \cos(\omega_n t) + d_n \sin(\omega_n t)\right] \tag{2.19}$$

and $m_x = 2m$. And similarly,

$$i\xi_y(x,t) = \frac{1}{2} b_0(t) + \sum_{m=1}^{N} b_m(t) \cos(\pi m x) \tag{2.20}$$

where

$$b_0(t) = \sum_{n=1}^{2N+1} \alpha_{1n} \left[c_n \cos(\omega_n t) + d_n \sin(\omega_n t)\right] \tag{2.21}$$

and

$$b_m(t) = \sum_{n=1}^{2N+1} \alpha_{m_y n} \left[c_n \cos(\omega_n t) + d_n \sin(\omega_n t)\right] \tag{2.22}$$

where $m_y = 2m + 1$.

The components of the column vectors $\mathbf{c}$ and $\mathbf{d}$ (i.e. c_n and d_n) are determined by the initial conditions at $t = 0$. In general we have the equations

$$\alpha \mathbf{c} = \mathbf{e} \tag{2.23}$$

and

$$\alpha \mathbf{\Omega} \mathbf{d} = \dot{\mathbf{e}} \tag{2.24}$$

where

$$\mathbf{c} = \left[\; c_1, c_2, c_3, \cdots, c_n \; \right]^{\mathbf{T}} \tag{2.25}$$

$$\mathbf{d} = \left[\; d_1, d_2, d_3, \cdots, d_n \; \right]^{\mathbf{T}} \tag{2.26}$$

$$\mathbf{\Omega} = \left[\; \omega_1, \omega_2, \omega_3, \cdots, \omega_n \; \right]^{\mathbf{T}} \tag{2.27}$$

and

$$\mathbf{e} = \left[\; b_0(t=0), a_1(t=0), b_1(t=0), \cdots, a_n(t=0), b_n(t=0) \; \right]^{\mathbf{T}} \tag{2.28}$$

$$\dot{\mathbf{e}} = \left[\; \dot{b}_0(t=0), \dot{a}_1(t=0), \dot{b}_1(t=0), \cdots, \dot{a}_n(t=0), \dot{b}_n(t=0) \; \right]^{\mathbf{T}}. \tag{2.29}$$

We can solve for $\mathbf{c}$ and $\mathbf{d}$ by using LU decomposition in equations (2.23) and (2.24) (NAG routine F04ATF), and use them to solve equation (2.14). Using equations (2.18-2.22) gives the full solution for $\xi_x(x,t)$ and $\xi_y(x,t)$ which are used to reconstitute the solution of an initial value problem across the box for all times until energy reaches the finest Fourier mode scale, that is, until a_N or $b_N \neq 0$.

This numerical method is novel and has several advantages over more standard finite differencing schemes. Notably, by taking a sufficiently large number of Fourier modes, and following the propagation of energy toward finer scales (primarily through the phase mixing process - see section (2.4.4), and Chapter 4), we can ensure that at any time the structure of the waves is being fully resolved. Our code allows us to compute the resolved wave structures at any time simply by calculating the Fourier summation. This removes the usual finite difference code problems in calculating long timescale evolutions, whereby the disturbance must be calculated at every previous time-step.

The summations for ξ_x and ξ_y can also be written in terms of a sum over spatial modes. We can write,

$$\xi_x(x,t) = \sum_{n=1}^{2N+1} \left[c_n \cos(\omega_n t) + d_n \sin(\omega_n t) \right] \phi_{nx}(x) \tag{2.30}$$

where $\phi_{nx}(x)$ is the spatial mode in the $\hat{\mathbf{x}}$ direction given by

$$\phi_{nx}(x) = \sum_{m=1}^{N} \alpha_{m_x n} \sin(\pi m x) \qquad (m_x = 2m) \tag{2.31}$$

and

$$i\xi_y(x,t) = \sum_{n=1}^{2N+1} \left[c_n \cos(\omega_n t) + d_n \sin(\omega_n t)\right] \phi_{ny}(x) \tag{2.32}$$

where

$$\phi_{ny}(x) = \alpha_{1n}/2 + \sum_{m=1}^{N} \alpha_{m_y n} \cos(\pi m x) \tag{2.33}$$
$$(m_y = 2m + 1).$$

These "normal" modes $\phi_{nx}(x)$ and $\phi_{ny}(x)$ correspond to the singular Barston (1964) eigenmodes for a compressible plasma. We should note that for coupled modes, both sets of spatial modes $\phi_{nx}(x)$ and $\phi_{ny}(x)$ exist for all values of n from 1 to $(2N + 1)$. We examine the structure of these modes in Chapter 3.

2.4 Accuracy of Numerical Matrix Eigenvalue Solutions.

To verify the accuracy of our numerical code, we employed various checks to ensure that the Fourier series expansions were converging to the correct solution.

2.4.1 Numerical "Energy" Invariant.

Following Bray and Loughhead (1974), we can derive an invariant quantity for our linear MHD waves based on considerations of kinetic and magnetic energy. Using the ideal, cold MHD equations (linearising about a static equilibrium) we can use equations (2.4) and (2.5) to generate the sum of kinetic and magnetic energy like terms. With the form of ξ specified by equations (2.9) and (2.10), we can see that components of the field variables will be complex and hence we consider terms of the form $\rho_0 \mathbf{v}^*.\mathbf{v}/2$ and $\mathbf{b}^*.\mathbf{b}/2\mu_0$, where a^* represents the complex conjugate of a. With our choice of ξ, we notice that

$$\mathbf{b}^*.\frac{\partial \mathbf{b}}{\partial t} = \mathbf{b}.\frac{\partial \mathbf{b}^*}{\partial t} \tag{2.34}$$

and

$$\mathbf{v}^*.\frac{\partial \mathbf{v}}{\partial t} = \mathbf{v}.\frac{\partial \mathbf{v}^*}{\partial t}. \tag{2.35}$$

Therefore, taking the dot product of $\mathbf{v}^*$ with equation (2.4), and the dot product of $\mathbf{b}^*$ with equation (2.5) yields

$$\rho_0 \frac{\partial}{\partial t} \frac{(\mathbf{v}^*.\mathbf{v})}{2} = \mathbf{v}^*.(\nabla \times \mathbf{b}) \times \frac{\mathbf{B_0}}{\mu_0} \tag{2.36}$$

and

$$\frac{\partial}{\partial t} \frac{(\mathbf{b}^*.\mathbf{b})}{2\mu_0} = \frac{\mathbf{b}^*}{\mu_0}.(\nabla \times (\mathbf{v} \times \mathbf{B_0})) \tag{2.37}$$

Combining these two equations and using standard vector identities, gives (after algebra)

$$\frac{\partial}{\partial t}\left(\frac{\rho_0}{2}(\mathbf{v}^*.\mathbf{v}) + \frac{(\mathbf{b}^*.\mathbf{b})}{2\mu_0}\right) + \nabla.\left(\frac{\mathbf{b}^*}{\mu_0}.(\mathbf{v} \times \mathbf{B_0})\right) = 0. \tag{2.38}$$

This equation is now in standard conservation form, i.e.,

$$\frac{\partial W}{\partial t} + \nabla.\mathbf{S} = 0. \tag{2.39}$$

By assuming that ξ_x is purely real, from the prescription in equation (2.9), we can write $\xi_x = \xi_{xr}$ (as $\xi_{xi} = 0$). Similarly, from the form of equations (2.7) and (2.8), we have the case where ξ_y is purely imaginary, i.e. $\xi_y = i\xi_{yi}$ (where $\xi_{xr}, \xi_{xi}, \xi_{yr}$ and ξ_{yi} are all purely real). Hence we have

$$\mathbf{v} = \frac{\partial \xi}{\partial t} = \begin{pmatrix} e^{i\lambda y} \sin(k_z z) \partial \xi_{xr}/\partial t \\ i e^{i\lambda y} \sin(k_z z) \partial \xi_{yi}/\partial t \\ 0 \end{pmatrix} \tag{2.40}$$

and

$$\mathbf{b} = B_0 e^{i\lambda y} \begin{pmatrix} k_z \cos(k_z z) \xi_{xr} \\ i k_z \cos(k_z z) \xi_{yi} \\ -\sin(k_z z)\left(\partial \xi_{xr}/\partial x - \lambda \xi_{yi}\right) \end{pmatrix} \tag{2.41}$$

Substituting these into equation (2.38), gives the flux

$$\mathbf{S} = -\frac{B_0^2}{\mu_0} \begin{pmatrix} \left(\partial \xi_{xr}/\partial x - \lambda \xi_{yi}\right) \sin^2(k_z z) \partial \xi_{xr}/\partial t \\ i\left(\partial \xi_{xr}/\partial x - \lambda \xi_{yi}\right) \sin^2(k_z z) \partial \xi_{yi}/\partial t \\ k_z \sin(k_z z) \cos(k_z z)\left(\xi_{xr} \partial \xi_{xr}/\partial t + \xi_{yi} \partial \xi_{yi}/\partial t\right) \end{pmatrix} \tag{2.42}$$

Considering the flux **S** out of our box model for the magnetosphere, we see that:

- S_x vanishes at $x = 0, 1$, as $\xi_{xr} = 0$ there $\forall t$. (i.e. $\partial \xi_{xr}/\partial t(x = 0, 1) = 0$).
- S_y is independent of y. Therefore the "energy" flux flowing out of the box in the positive $\hat{\mathbf{y}}$ direction exactly equals the flux flowing in from the negative $\hat{\mathbf{y}}$ direction.
- S_z vanishes at $z = 0, z_0$, where $\sin(k_z z_0) = 0$.

Therefore, no net flux of the derived quantity W flows into or out of our model box magnetosphere in time. We can therefore integrate W over the volume of the box V to gain

$$\frac{\partial}{\partial t}\int_V W dV + \int_V \nabla.\mathbf{S} dV = 0 \tag{2.43}$$

Knowing that the normal component of S vanishes at the boundaries of the box in x and z, and is independent of y, then using the divergence theorem

$$\int_V \nabla.\mathbf{S} dV = \int_\sigma \mathbf{N}.\mathbf{S} d\sigma, \tag{2.44}$$

where N is normal to the surface σ bounding the volume V, gives

$$\frac{\partial}{\partial t}\int_V W dV = 0. \tag{2.45}$$

Clearly $\int_V W dV$ is constant in time and represents an "energy" invariant which can be used to follow the temporal evolution of the waves in our box model magnetosphere. Completing the integration w.r.t. z analytically, and the integration w.r.t. x numerically, we can determine an invariant per unit y, $\int\int W dx dz$, which we then use to follow the temporal evolution of the numerical solution.

We can also prove analytically, starting from the governing equations (2.7) and (2.8), that this is in fact an invariant quantity. Substituting for ξ_x and ξ_y in terms of their Fourier series expansions, gives equations for $a_m(t)$ and $b_m(t)$. Multiplying these equations by $\dot{a}_m(t)$ and $\dot{b}_m(t)$ respectively, allows us to substitute for terms in the expression $\partial/\partial t(\int\int W dx dz)$. All the terms in this expression can be equated to zero by using these two governing equations, and this confirms that the quantity is indeed mathematically invariant. In the numerical results which we present in this thesis, invariance was maintained to at least 1 part in 10^6 (usually much greater).

2.4.2 Orthogonality of Numerical Eigenvectors.

We can also consider the orthogonality of the numerically derived eigenvectors to check on the accuracy of the eigenvalue solver.

When $\lambda = 0$, the two wave polarisations decouple, and the generalised matrix eigenvalue problem (equation (2.14)) can be written as two separate eigenvalue problems involving only one wave polarisation. In this case, both these new eigenproblems can be re-written in the form of a simple eigenvalue problem (governed by a real symmetric matrix) by adjusting the eigenvectors (see Chapter 3). These derived symmetric matrices will have real eigenvalues, and a set of real eigenvectors which form an orthogonal set (Wylie, 1960). Similarly, the decoupled ξ_x equation (equation (2.7) with $\lambda = 0$) is in standard Sturm-Liouville form and hence the ξ_x eigenfunctions will be orthogonal under the weighting of $\rho(x)$ (Arfken, 1985), i.e.,

$$\int \phi_{nx}\rho(x)\phi_{mx}dx = 0 \tag{2.46}$$

for $n \neq m$.

However, when $\lambda = 0$, despite the fact that the two polarisations become decoupled, we can obtain a check on the code by keeping both the fast and Alfvén parts together in the generalised eigenvalue problem (equation (2.14)). If we re-cast the eigenvalue problem in terms of a new eigenvector $\mathbf{Y}$,

$$\mathbf{Y} = \mathbf{MX}, \tag{2.47}$$

with (for $\lambda = 0$) $\mathbf{M^2}$ being diagonal, and the matrix $\mathbf{M}$ having entries $M_{m,m} = \sqrt{M^2_{m,m}}$, equation (2.14) can be re-written in terms of a simple eigenvalue problem governed by a Hermitian matrix. In this way, we have

$$\mathbf{M^{-1}R^2M^{-1}Y} = \frac{1}{\omega^2}\mathbf{Y} = \mu^2\mathbf{Y} \tag{2.48}$$

i.e.,

$$\mathbf{HY} = \mu^2\mathbf{Y} \tag{2.49}$$

where $\mathbf{H} = \mathbf{M^{-1}R^2M^{-1}}$, $\mu^2 = 1/\omega^2$, and $\mathbf{Y}$ represents the required set of orthogonal eigenvectors.

We verified the accuracy of the code by numerically solving equation (2.14) and checking that each of the modified eigenvectors $\mathbf{Y}$ (calculated from $\mathbf{MX} = \mathbf{Y}$) were orthogonal to each other (i.e., $\mathbf{Y_n}.\mathbf{Y_{n'}} = 0$ for $n \neq n'$). When $n = 9$ (i.e., $N = 4$) all the adjusted eigenvectors $\mathbf{Y}$ were orthogonal to at worst 1 part in 10^{14}. Increasing the value of n maintained the accuracy of the eigenvector routine, and hence the orthogonality of the adjusted eigenvectors.

When $\lambda \neq 0$, the generalised eigenvalue problem in equation (2.14) can be written in the form

$$\omega_n^2 \mathbf{X_n} = \mathbf{R^{-2}M^2X_n}. \tag{2.50}$$

Unfortunately, the matrix $\mathbf{R^{-2}M^2}$ is not Hermitian, even though when $\lambda \neq 0$ both $\mathbf{M^2}$ and $\mathbf{R^2}$ are symmetric. We used the symbolic computation package *Maple* to check whether $\mathbf{R^{-2}}$ was Hermitian, for small values of n. It turns out that for $n = 9$ (the case we tried) $\mathbf{R^{-2}}$ is symmetric, but the banded character of the matrix is destroyed so that it is no longer sparse. In theory it would be possible to solve this new simple (rather than generalised) eigenvalue problem governed by the matrix $\mathbf{R^{-2}M^{-2}}$. However, the difficulty (even numerically) which would be involved in inverting $\mathbf{R^2}$, and the fact that the attractive sparse character of the governing matrices would be lost, make this a very inefficient way to solve the governing equations. It was for this reason that we chose to remain with the problem as described by equation (2.14), especially since the matrix $\mathbf{R^{-2}M^2}$ (which is not symmetric) doesn't have orthogonal eigenvectors either.

This means that we cannot verify the results of the eigenvalue solver directly, for $\lambda \neq 0$, using orthogonality. We do however obviously have other checks available to us such as following the "energy" invariant. It is known that for any generalised eigenvalue problem involving two symmetric matrices, a Hermitian matrix $\mathbf{G}$ can be found that is similar to $\mathbf{R^{-2}M^2}$. $\mathbf{G}$ will have eigenvalues which are real (as expected for ideal MHD), and which will be identical to the eigenvalues of $\mathbf{R^{-2}M^2}$. Consequently, we know that the eigenvalues of our coupled wave problem will be real as required (Stoer and Bulirsch, 1980). The corresponding eigenvectors will be linearly independent (as for any non-singular $n \times n$ matrix), but will not necessarily be orthogonal.

2.4.3 Further Checks on the Decoupled $\lambda = 0$ Numerical Eigenmodes.

We can also verify that the decoupled ($\lambda = 0$) numerical eigenmodes ϕ_{nx} and ϕ_{ny} match up with both known analytical formulae, and with results derived using alternative numerical schemes.

In Chapter 3, section (3.2), we consider a reference analytical solution for the decoupled Alfvén eigenmodes, derived using known analytical results for the eigenvalues and eigenvectors of symmetric tri-diagonal matrices. We also solve for the decoupled fast eigenmodes first by using a Runge-Kutta numerical integration scheme, with a shooting method for ω_n (see section (3.3)), and second by using an analogy with Mathieu's equation (see section (3.4)). Each method verifies the accuracy of the eigenvalue solver which we subsequently use to solve for the temporal evolution of the coupled MHD waves.

2.4.4 Verification of Coupled Wave ($\lambda \neq 0$) Temporal Evolution Results.

i) Short Duration Simulations.

We were able to check the early time results from our code by comparing them to results produced by a finite difference scheme, developed independently during the study of another wave problem (G.J. Rickard, *Personal Communication*, (1993)). This gave us confidence that our early time results were converging to the correct solution.

ii) Long Duration Simulations.

To ensure that we successfully resolve the linear MHD waves in simulations which are run over long timescales, we need to make sure any fine scales developed in the system are correctly resolved by the Fourier series. We require a sufficiently large number of Fourier series harmonics (N) so that all physical length scales are correctly reconstructed by the Fourier series approximations.

In an inhomogeneous plasma, waves which are evolving can generate increasingly fine scales in time by a process known as phase mixing (Burghes et al., 1969; Radoski, 1974; Heyvaerts and Priest, 1983). We can illustrate this process by the following simple analysis. In a plasma with an inhomogeneous background Alfvén frequency profile, undriven standing decoupled toroidal Alfvén waves will cause each field line to oscillate with its own natural background frequency. To leading order, these waves (with a low value of λ) can be described by

$$\xi_y(x,t) \sim A(x) \exp i\omega_A(x)t. \tag{2.51}$$

At this order, and in the ideal limit, each field line decouples from the adjacent field lines and oscillates at its own natural frequency given by $\omega_A(x)$. Consequently, oscillations which are initially in phase (at $t = 0$ say) drift out of phase with each other in time and generate phase mixing fine scales in the $\hat{\mathbf{x}}$ direction. Looking for a solution of the form $\xi_y \sim \xi_{y0} \exp ik_x x$, where $k_x = k_x(x,t)$, we can take

$$\frac{\partial}{\partial x} \sim ik_x = i\omega_A'(x)t + \frac{A'(x)}{A(x)} \tag{2.52}$$

and hence as $t \to \infty$

$$k_x \approx \omega_A'(x)t \tag{2.53}$$

where $'$ represents d/dx.

This allows the definition of the phase mixing length (the length-scale developed at any time t, based on these decoupled Alfvén oscillations) as

$$L_{ph} = \frac{2\pi}{k_x(t)} = 2\pi \left(\omega_A'(x)t\right)^{-1}. \tag{2.54}$$

This length can be used to estimate the finest scales developed by the coupled MHD waves at any time t_N, and this gives a lower limit on the number of Fourier mode harmonics N (and hence the size of the eigenvalue problem $(2N+1)$) which will be needed to resolve the waves until this time. Considering $m\pi \approx k_x$, we find that the number of modes required is

$$N \sim \omega_A'(x)t_N/\pi. \tag{2.55}$$

In fact, we can consider the phase mixing process to be a cascade towards smaller and smaller length-scales. At early times, the low m Fourier harmonics will be sufficient to describe the wave disturbances, whilst at later times as $t \to t_N$, the highest Fourier harmonics (with the finest scales) will be needed to accurately describe the waves. In reality, the code will need several more than N wave modes to describe the waves at a time t_N, since to construct an accurate Fourier approximation at this time will require several additional Fourier harmonics.

By using equation (2.55), we have an estimate of the size of the matrix which will be required to describe the MHD waves over a given finite time. This can be verified *a posteriori* by following the evolution of the "energy" invariant (described in section (2.4.1)) in time.

The behaviour of the "energy" invariant in time reveals interesting properties about the eigenvalue solver. For example, when $\lambda = 0$ and the initial conditions comprise only the first ξ_x Fourier mode at rest, the invariance is maintained for all times. Hence the eigenvectors can be used to describe the evolution of this initial condition up to *any* time. This can be understood because the fast and Alfvén waves are decoupled, and hence increasingly fine scales are not generated in time. When $\lambda \neq 0$, however, the invariance of the code can degenerate with time. In general, if the initial evolution conserves energy for a given value of N (with better invariance obtained for larger N), we find that the invariance starts to be lost after a finite time. This time is $\sim t_N$. By this time, we can be confident energy is reaching the highest Fourier modes (so that a_N or b_N become non-zero) and hence that the waves are no longer being accurately described. In this case, the simulations must be re-run with a larger matrix.

There are also cases, run with certain parameter values, which fail to show strong invariance (to many significant figures) over any finite period of time. In these situations, the eigenvalue routine struggles to generate suitably independent eigenvectors. Errors in the reconstruction of any disturbance (by using these eigenvectors) occurs as a result. This shortfall is revealed by the failure of the invariant (constructed using a combination of the eigenvectors) to remain constant.

Chapter 3

MHD Normal Modes.

3.1 Introduction.

In this chapter we consider the spatial form of the inhomogeneous MHD wave normal modes $\phi_{nx}(x)$ and $\phi_{ny}(x)$, each of which oscillate at their characteristic frequency ω_n throughout the plasma. Firstly, in section (3.2), we describe the features of the numerical $\lambda = 0$ fast and Alfvén wave normal modes. In this limit, since the waves are decoupled, the fast modes are non-singular in x, whilst the Alfvén modes exist as a set of decoupled harmonic oscillators each having a frequency $\omega_A(x)$. We subsequently discuss some analytical solutions which exist for the decoupled wave case. In sections (3.3) and (3.4), we go on to consider Runge-Kutta and Mathieu function methods and use them to derive decoupled fast eigenmode solutions.

In section (3.5), we analyse coupled wave modes, having $\lambda \neq 0$. In this case the distinction between fast and Alfvén waves on the grounds of compressibility or incompressibility is no longer appropriate. Instead, both ξ_x and ξ_y wave polarisations become important for all modes. A fast or Alfvénic $\lambda = 0$ mode may retain its dominant compressibility characteristic for small values of λ, and this can be useful in interpreting the results from time-dependent coupled wave studies, for example when a "fast" wave drives an "Alfvén" resonance. When $\lambda \neq 0$, both the modes $\phi_{nx}(x)$ and $\phi_{ny}(x)$ may be singular as a result of the Alfvén resonance. Hence they cannot be described as normal modes in the usual sense (Barston, 1964; Sedláček, 1971a; Cally, 1991). We examine the detailed nature of these modes and the form of their singularities. We conclude the chapter by discussing the form of large λ eigenmodes.

3.2 Decoupled ($\lambda = 0$) Normal Modes.

As we have previously mentioned, when $\lambda = 0$ or ∞ wave modes polarised in the $\hat{\mathbf{x}}$ and $\hat{\mathbf{y}}$ directions oscillate independently, and hence ξ_x and ξ_y become decoupled. In this section we consider the structure of the $\lambda = 0$ modes. Assuming a dependence of $\exp -i\omega t$, then equation (2.7) can be written as

$$\frac{\partial^2 \xi_x}{\partial x^2} + \left(K^2 - k_z^2\right) \xi_x = 0 \tag{3.1}$$

where $K^2 = \omega^2 / v_A^2(x)$, and equation (2.8) as

$$\left(\omega_A^2(x) - \omega^2\right) \xi_y = 0. \tag{3.2}$$

Equation (3.1), when subject to suitable boundary conditions (e.g., $\xi_x(x = 0, 1) = 0$) is in standard Sturm-Liouville from. Hence the fast eigenfunctions ϕ_{nx} can be expected to be non-singular and can be determined by solving the eigenvalue problem for ω. Equation (3.2) has Dirac delta function solutions $\delta\left(\omega_A^2(x) - \omega^2\right)$ for the Alfvén modes, each having eigenfrequencies determined by $\omega^2 = \omega_A^2(x)$. Consequently, each polarisation oscillates independently of the other in meridian (for ξ_x) and "azimuthal" (for ξ_y) planes. The normal mode solutions ($\phi_{nx}(x)$ and $\phi_{ny}(x)$) can reveal interesting properties about wave behaviour in an inhomogeneous plasma environment. By understanding the decoupled waves, we can go on to interpret the more complicated coupled wave phenomena.

When $\lambda = 0$, the governing eigenvalue problem (2.14) can be split into two entirely separate generalised eigenvalue problems - one for each of the $\hat{\mathbf{x}}$ and $\hat{\mathbf{y}}$ polarisations. We can define two new eigenvectors $\mathbf{X_X}$ and $\mathbf{X_Y}$

$$\mathbf{X_X} = \begin{bmatrix} a_1 \\ a_2 \\ a_3 \\ \vdots \\ a_N \end{bmatrix} \tag{3.3}$$

and

$$\mathbf{X_Y} = \begin{bmatrix} b_0 \\ b_1 \\ b_2 \\ b_3 \\ \vdots \\ b_N \end{bmatrix} \tag{3.4}$$

which represent eigenvector solutions to the two eigenvalue problems defined by the pairs of matrices $\mathbf{M_X^2}$, $\mathbf{R_X^2}$ and $\mathbf{M_Y^2}$, $\mathbf{R_Y^2}$ respectively. Consequently, we can solve for the purely decoupled wave normal modes, which are now given by ϕ_{nX} and ϕ_{nY}, simply by solving each eigenvalue problem separately. When $\lambda = 0$, the matrix $\mathbf{M^2}$ (and hence $\mathbf{M_X^2}$ and $\mathbf{M_Y^2}$) become diagonal.

3.2.1 Homogeneous Background Plasma.

As a preliminary study, we can consider the wave normal modes which exist in a uniform plasma by setting $B^2 = 0$ in equation (2.11). In this limit $\mathbf{R^2}$ (and hence $\mathbf{R_X^2}$ and $\mathbf{R_Y^2}$) as well as $\mathbf{M^2}$ (i.e., $\mathbf{M_X^2}$ and $\mathbf{M_Y^2}$) become diagonalised. The solutions to these eigenproblems are analytic.

The solution eigenvectors $\mathbf{X_{nY}}$ (for ξ_y) are found to be degenerate, with all their eigenfrequencies given by

$$\omega_{nY}^2 = \frac{k_z^2}{A^2} = k_z^2 v_A^2 \tag{3.5}$$

(where v_A is a constant). The corresponding wave normal modes are given by a summation over the eigenvectors (equation (2.33)) which results in

$$\phi_{0Y}(x) = 1/2 \tag{3.6}$$

$$\phi_{nY}(x) = \cos \pi n x \quad (n \geq 1). \tag{3.7}$$

The ξ_x eigensolutions are not degenerate, having eigenfrequencies given by

$$\omega_{nX} = \frac{k_z^2 + (n\pi)^2}{A^2}, \tag{3.8}$$

with the corresponding eigenfunctions given by

$$\phi_{nX}(x) = \sin n\pi x. \tag{3.9}$$

Clearly these ϕ_{nX} solutions are global, and exist throughout the plasma.

3.2.2 Inhomogeneous Background Plasma.

i) Numerical Matrix Eigenvalue Results.

Introducing an inhomogeneous background Alfvén velocity profile, by choosing $B^2 \neq 0$, removes the degeneracy of the ϕ_{nY} eigenfunctions. As we shall see, the frequencies of these normal modes span the imposed background Alfvén frequency profile $\omega_{A1} \leq \omega_{nY} \leq \omega_{A2}$, where ω_{A2} and ω_{A1} are given by $k_z v_A(x = 0, 1)$. In the truncated eigenvalue problem, the eigenfunctions approximate the Alfvén continuum. As the size of the eigenvalue problem matrices are increased the mode spectrum becomes increasingly densely packed. As $N \rightarrow \infty$, the discrete spectrum approaches a continuum. The corresponding continuum eigenfunctions, rather than being global in nature in the $\hat{\mathbf{x}}$ direction, are localised in $\hat{\mathbf{x}}$ around the position defined by $\omega_{nY}^2 = k_z^2 v_A^2(x)$. With a truncated matrix, the derived eigenmodes are Fourier approximations to the Dirac delta function continuum eigenmode solutions. We can also calculate the inhomogeneous ξ_x eigenfunctions ϕ_{nX}. These eigenmodes, however, retain their global x character (for $\lambda = 0$), although they no longer have a simply sinusoidal x dependence, because of the background plasma inhomogeneity.

Using the method described in section (2.3), we numerically calculated the modes ϕ_{nX} and ϕ_{nY}. The eigenvalue routine we used produced eigenfunctions which were ordered in terms of the magnitude of their eigenfrequency. Since the ($\lambda = 0$) fast and Alfvén eigenmodes oscillate in perpendicular directions and are purely decoupled, when the "full" eigenvectors $\mathbf{X_n}$ are calculated (from equations (2.14) and (2.15)) they produce eigenvectors with $2N + 1$ entries. The $2N + 1$ eigenmodes, which correspond to the $2N + 1$ eigenfrequencies, either produce purely ξ_x or ξ_y motions. These solutions can be identified with either a fast (compressional) or an Alfvén (incompressible) MHD wave mode respectively. The routine produced N fast modes (with non-zero entries only in positions corresponding to the eigenvectors $\mathbf{X_X}$) and $N + 1$ Alfvén modes (having non-zero entries corresponding to $\mathbf{X_Y}$). All other entries are zero within numerical accuracy.

For coupled wave modes (with $\lambda \neq 0$ or ∞), the distinction between Alfvén and fast modes cannot be made. Eigenmodes which were previously either fast with an $\hat{\mathbf{x}}$

polarisation, or Alfvén with a $\hat{\mathbf{y}}$ polarisation, become coupled and the distinction between them on the grounds of compressibility or polarisation can no longer be used. Both modes have both polarisations, although the eigenmodes may still retain a dominant Alfvénic or compressible character. Strictly, in these coupled situations neither fast nor Alfvén waves exist, and we return to this point in section (3.5).

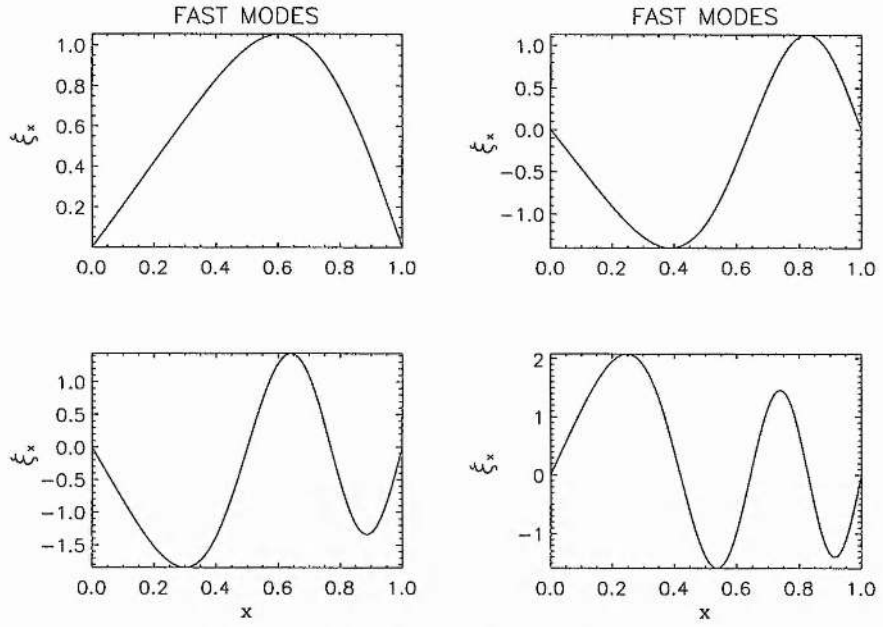

Figure 3.1: The first four decoupled ($\lambda = 0$) fast eigenmodes $\phi_{nx}(x)$ - from the fundamental (first harmonic) up to the fourth harmonic. Parameters $A^2 = 1.0$, $B^2 = 0.9$, $k_z = 2.0$ and $N = 50$ were chosen to illustrate the form of the eigenmodes. Note that the normalisation employed produces eigenvectors which have their largest entry as unity.

In Figure (3.1) we plot the first four numerical decoupled fast eigenmodes. These modes are global in character, and involve a compression of plasma in the x direction. Increasing the size of the eigenvalue problem increases the number of fast eigenmode harmonics which are produced (N of them). The numerical eigenvalue routine also calculates the fast eigenfrequencies (ω_n^2) for a given value of N, their accuracy being determined in general by the size of the matrix N.

In Figure (3.2) we plot Alfvén eigenmodes for both $N = 50$, in the first column, and for $N = 200$ in the second column. An increase in N enhances the resolution of the Fourier series expansions used to describe the wave modes, and hence improves the Fourier

approximations to the continuum Alfvén (Dirac delta) eigenfunctions - as is clearly shown in Figure (3.2). Similarly, an increase in N increases the density of the Alfvén eigenfrequencies

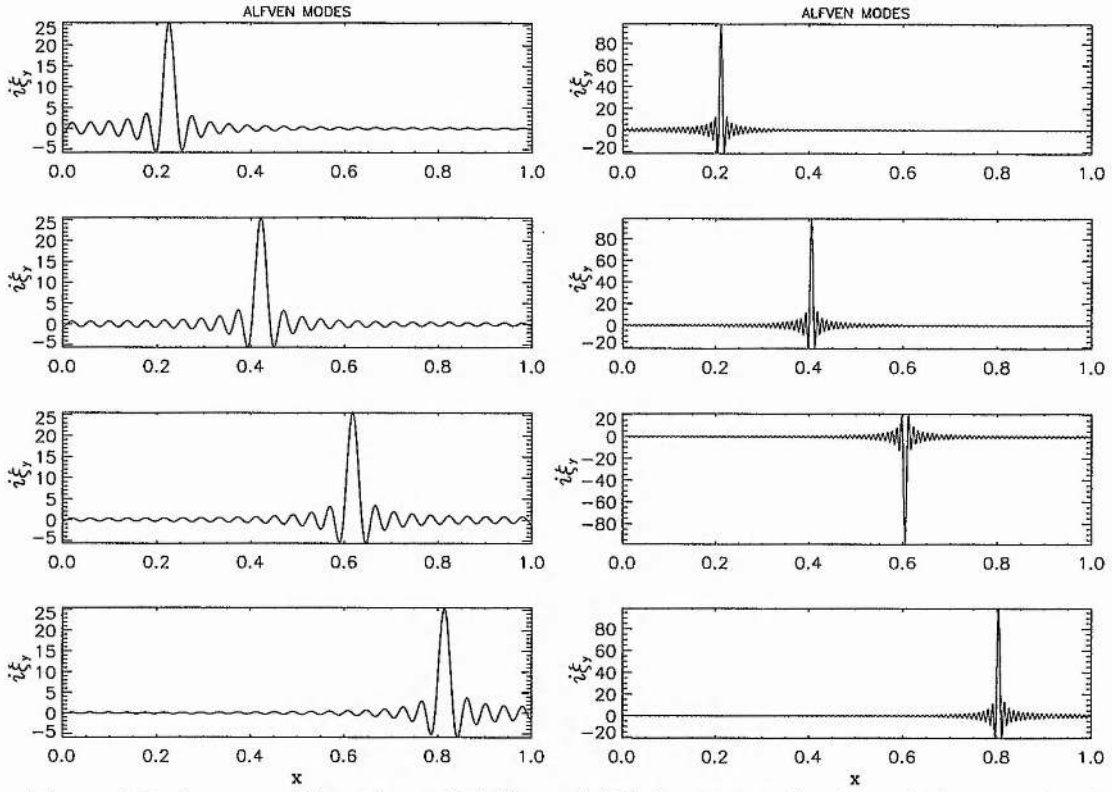

Figure 3.2: A range of four decoupled ($\lambda = 0$) Alfvén eigenmodes ϕ_{ny} which span the Alfvén continuum. $N = 50$ in the first column, and $N = 200$ in the second. Again parameters $A^2 = 1.0$, $B^2 = 0.9$, and $k_z = 2.0$ were chosen.

in ω space, whilst they continue to span the continuum $\omega_{A1} \leq \omega_{nY} \leq \omega_{A2}$.

ii) Analytic Matrix Eigenmode Analysis ($\mathbf{B^2 \neq 0}$).

a) Alfvén Eigenmodes.

Here, we consider an analytic approximation to the $\phi_{nY}(x)$ decoupled Alfvén eigenfunctions. When $B^2 \neq 0$, the matrix $\mathbf{R^2_Y}$ becomes tri-diagonal whilst $\mathbf{M^2_Y}$ remains diagonal. $\mathbf{R^2_Y}$ has entries

$$R^2_{Y1,1} = A^2/2$$

$$\begin{aligned} R^2_{Y\,m,m} &= A^2 \\ R^2_{Y\,m-1,m} &= R^2_{Y\,m,m+1} = -B^2/2 \end{aligned}$$

and $\mathbf{M^2_Y}$ has entries

$$\begin{aligned} M^2_{Y\,1,1} &= k_z^2/2 \\ M^2_{Y\,m,m} &= k_z^2. \end{aligned}$$

We can compare this actual problem to a reference matrix system based on a tri-diagonal matrix $\mathbf{P_{ref}}$ of the form

$$\mathbf{P_{ref}} = \begin{bmatrix} \alpha & \beta & 0 & 0 & 0 & 0 & \cdots \\ \gamma & \alpha & \beta & 0 & 0 & 0 & \cdots \\ 0 & \gamma & \alpha & \beta & 0 & 0 & \cdots \\ 0 & 0 & \gamma & \alpha & \beta & 0 & \cdots \\ 0 & 0 & 0 & \gamma & \alpha & \beta & \cdots \\ \vdots & \vdots & \vdots & \vdots & \vdots & \vdots & \searrow \end{bmatrix}. \tag{3.10}$$

An analytical solution exists for the eigenvalues and eigenvectors of $\mathbf{P_{ref}}$. The eigenvalues are given by

$$\lambda_{Ps} = \alpha + 2\sqrt{\beta\gamma}\cos(s\pi/(N+1)) \quad s = 1, 2 \ldots N \tag{3.11}$$

for an N by N system (e.g., Smith (1985)).

Changing a single entry in the matrix $\mathbf{R^2_Y}$ and a single entry in $\mathbf{M^2_Y}$ allows the generalised eigenvalue problem to be re-written as a simple eigenvalue problem in terms of the reference matrix $\mathbf{P_{ref}}$. The modified reference system has an analytical solution, and we will denote this approximate solution by using a tilde notation. By modifying $\mathbf{R^2_Y}$ so that $\tilde{R}^2_{Y\,1,1} = A^2$ (where $\tilde{M}$ represents a reference matrix), and $\mathbf{M^2_Y}$ so that $\tilde{M}^2_{Y\,1,1} = k_z^2$, we can replace the (diagonal) reference matrix $\tilde{\mathbf{M}}^{\mathbf{2}}_{\mathbf{Y}}$ by the scalar k_z^2, to gain

$$\tilde{\omega}^2 \tilde{\mathbf{R}}^{\mathbf{2}}_{\mathbf{Y}} \mathbf{X_Y} = k_z^2 \mathbf{X_Y} \tag{3.12}$$

and hence

$$\tilde{\mathbf{R}}^{\mathbf{2}}_{\mathbf{Y}} \mathbf{X_Y} = \frac{k_z^2}{\tilde{\omega}^2} \mathbf{X_Y}. \tag{3.13}$$

This is a symmetric eigenvalue problem and hence its eigenfrequencies are real (as expected for an ideal MHD formulation). Comparing $\tilde{\mathbf{R}}^{\mathbf{2}}_{\mathbf{Y}}$ with $\mathbf{P_{ref}}$, then clearly $\beta = \gamma = -B^2/2$, and $\alpha = A^2$. Since changing the background Alfvén velocity to a monotonically increasing (rather than decreasing) profile, by changing the sign of $x \rightarrow -x$ (i.e, $B^2 \rightarrow -B^2$) produces the same Alfvén frequency span, we can infer from the reference system an analytic set of approximate eigenvalues given by

$$\tilde{\lambda}_s = \frac{k_z^2}{\tilde{\omega}_s^2} = A^2 - B^2 \cos\left(\frac{s\pi}{N+1}\right) \qquad s = 1, 2 \ldots N \tag{3.14}$$

again for an N by N matrix. These reference eigenvalues span the Alfvén continuum ($A^2 - B^2 < \tilde{\lambda}_s < A^2 + B^2$) and hence

$$k_z^2 v_{A1}^2 < \tilde{\omega_A}^2 < k_z^2 v_{A2}^2 \tag{3.15}$$

where v_{A1} and v_{A2} are the Alfvén speeds at the extremes of the inhomogeneity.

The eigenvectors of this reference system are also known analytically (Smith, 1985) to be given by

$$\mathbf{X_{nY}} = \left[\sin\tfrac{n\pi}{(N+1)}, \sin\tfrac{2n\pi}{(N+1)}, \sin\tfrac{3n\pi}{(N+1)}, \cdots, \sin\tfrac{(N+1)n\pi}{(N+1)} \right]^T. \tag{3.16}$$

Substituting the $N+1$ by $N+1$ matrix version of these eigenvectors into equation (2.33) allows the construction of reference ξ_y eigenfunctions $\tilde{\phi}_{nY}$. In Figure (3.3) we show the functions $\tilde{\phi}_{nY}$ for $N = 50$ and $N = 200$. These reference eigenfunctions can be compared with the corresponding numerical matrix eigenvalue eigenfunctions shown in Figure (3.2). The singular nature of the decoupled toroidal Alfvén wave eigenfunctions is maintained in the reference problem, as is clearly shown in Figure (3.3). The reference matrix and the numerical results show good agreement, with any discrepancies resulting from the modification of the (1,1) $\mathbf{R^2_Y}$ and $\mathbf{M^2_Y}$ matrix entries in the reference system.

b) Fast (ξ_x) Eigenmodes.

We can also consider the solution to the decoupled ξ_x inhomogeneous eigenvalue problem, by using the matrices $\mathbf{R^2_X}$ and $\mathbf{M^2_X}$. Here

$$M^2_{Xm,m} = k_z^2 + (m\pi)^2$$

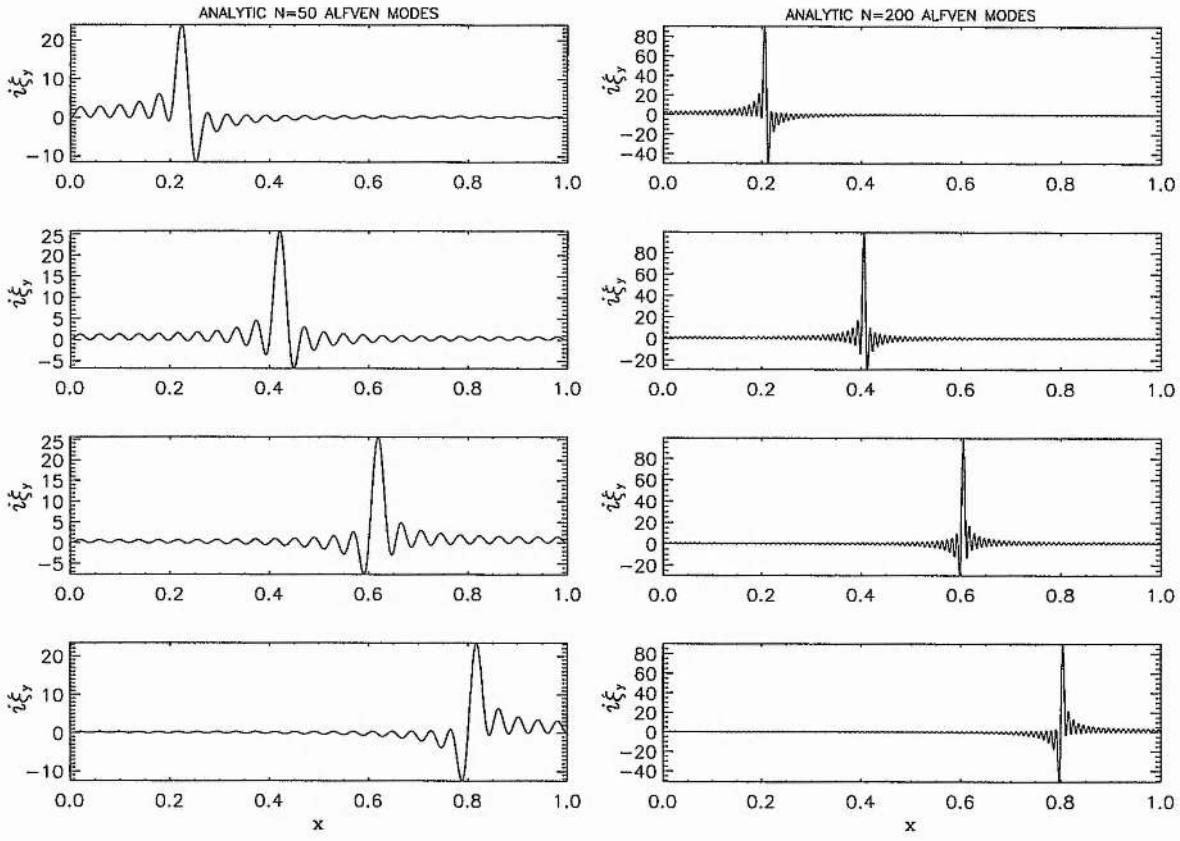

Figure 3.3: In this Figure we plot a range of four decoupled ($\lambda = 0$) reference Alfvén eigenmodes $\tilde{\phi}_{ny}$ which are the same harmonics as shown in Figure (3.2). Again $N = 50$ is the first column, and $N = 200$ is the second column, with parameters $A^2 = 1.0$, $B^2 = 0.9$, and $k_z = 2.0$.

whilst

$$\begin{aligned} R^2_{Xm,m} &= A^2 \\ R^2_{Xm-1,m} &= R^2_{Xm,m+1} = -B^2/2. \end{aligned}$$

Inverting the matrix $\mathbf{M_X^2}$ (which is diagonal), we can again rewrite the equation for eigenvectors as a simple eigenvalue problem. Writing this in terms of a new eigenvector $\mathbf{Z_X} = \mathbf{M_X X_X}$, where $\mathbf{M_X}$ has the elements $M_{Xm,m} = (k_z^2 + m^2\pi^2)^{\frac{1}{2}} = M_{Xm}$ (i.e., $\mathbf{M_X M_X} = \mathbf{M_X^2}$ (both $\mathbf{M_X^2}$ and $\mathbf{M_X}$ being diagonal)), we gain

$$\omega^2 \mathbf{R}_\mathbf{X}^2 \mathbf{M}_\mathbf{X}^{-1} \mathbf{Z}_\mathbf{X} = \mathbf{M}_\mathbf{X} \mathbf{Z}_\mathbf{X} \tag{3.17}$$

and hence

$$\mathbf{F}_\mathbf{X} \mathbf{Z}_\mathbf{X} = \nu^2 \mathbf{Z}_\mathbf{X} \tag{3.18}$$

where $\mathbf{F}_\mathbf{X} = \mathbf{M}_\mathbf{X}^{-1} \mathbf{R}_\mathbf{X}^2 \mathbf{M}_\mathbf{X}^{-1}$ and $\nu^2 = 1/\omega^2$. Since $\mathbf{M}_\mathbf{X}^{-1} \mathbf{M}_\mathbf{X} = \mathbf{I}$, then $M^{-1}_{Xm,m} = 1/M_{Xm,m}$. Consequently, the matrix $\mathbf{F}_\mathbf{X}$ is a symmetric tri-diagonal having entries

$$\begin{aligned} F_{Xm,m} &= A^2/M_{Xm}^2 \\ F_{Xm-1,m} &= -B^2/(2M_{Xm-1}M_{Xm}) \\ F_{Xm,m+1} &= -B^2/(2M_{Xm}M_{Xm+1}). \end{aligned}$$

The solution to this problem will produce real eigenvalues (again as expected for ideal MHD). However, to calculate these eigenvalues and eigenvectors, without resorting to numerics, would require a known analytic solution.

3.3 Runge-Kutta Numerical Integration of Decoupled Fast Eigenmodes.

Assuming a dependence of $\exp(-i\omega t)$, equation (2.7) (with $\lambda = 0$) can be written as

$$\frac{d^2\xi_x}{dx^2} + \left(\frac{\omega^2}{v_A^2} - k_z^2 \right) \xi_x = 0. \tag{3.19}$$

This can be solved numerically by using a Runge-Kutta numerical integration scheme. Writing this equation as two first order equations

$$\frac{d\xi_x}{dx} = y \tag{3.20}$$

and

$$\frac{dy}{dx} = -\left(\frac{\omega^2}{v_A^2} - k_z^2 \right) \xi_x, \tag{3.21}$$

subject to the boundary conditions $\xi(x = 0, 1) = 0$, we can use a standard Fourth order Runge-Kutta integration technique on this first order system to integrate from the boundary

at $x = 0$ to the boundary at $x = 1$. Employing a shooting method, we can find the eigenvalues (ω_n^2) and hence the eigenfunctions ($\phi_{nX}(x)$) of the decoupled fast modes (Abramowitz and Stegun, 1972). We compare the Runge-Kutta harmonics to those derived using the eigenvalue solver (again for $A^2 = 1.0$, $B^2 = 0.9$ and $k_z = 2.0$), in Table (3.1). Whilst we can calculate the decoupled eigenfrequencies to a known accuracy with the Runge-Kutta routine, the accuracy of the eigenvalue results is dependent on the value of N. However, to 6 significant figures the values of the first 5 fast eigenfrequencies (i.e., ω_n) are identical for $N = 10$ and $N = 100$. Clearly, the eigenvalue routine very accurately calculates the solution eigenfrequencies, even when N is quite small. However, the eigenfunctions having $n \sim N$ will have some errors associated with them because of the truncation of the Fourier series expansions.

Fast Mode Harmonic	Runge-Kutta Eigenfrequency	Comparison Matrix Eigenfrequency
1	3.57462	3.57462
2	6.82306	6.82305
3	10.16271	10.16271
4	13.52518	13.52516
5	16.89436	16.89435

Table 3.1: Runge-Kutta decoupled fast mode eigenfrequencies calculated with 5.10^4 x integration steps, with an iteration error on ω_n of $\sim \Delta\omega/\omega < 10^{-10}$. These are compared to the matrix eigenvalue results for $N = 100$ - although to 6 significant figures these eigenfrequencies are identical to those calculated with $N = 10$.

With the Runge-Kutta integration routine, we also investigated the range of parameters A^2, B^2 and k_z for which the decoupled fast mode harmonics lie within the Alfvén continuum. Since the eigenvalues of the coupled low λ waves are only weakly dependent on λ (Zhu and Kivelson, 1988), we can use the Runge-Kutta decoupled eigenvalues to choose suitable parameter ranges with which to investigate the resonant coupling of fast and Alfvén waves (see Chapter 4).

Due to normalisation, we have $A^2 = 1$. We selected $B^2 = 0.9$ so that the Alfvén continuum spanned a reasonable range of natural frequencies, without making the maximum frequency $\omega_{A2}^2 = k_z^2/(A^2 - B^2)$ orders of magnitude greater than $\omega_{A1}^2 = k_z^2/(A^2 + B^2)$ (as would be the case for $B^2 = 0.99$ for example). With the Runge-Kutta algorithm, we

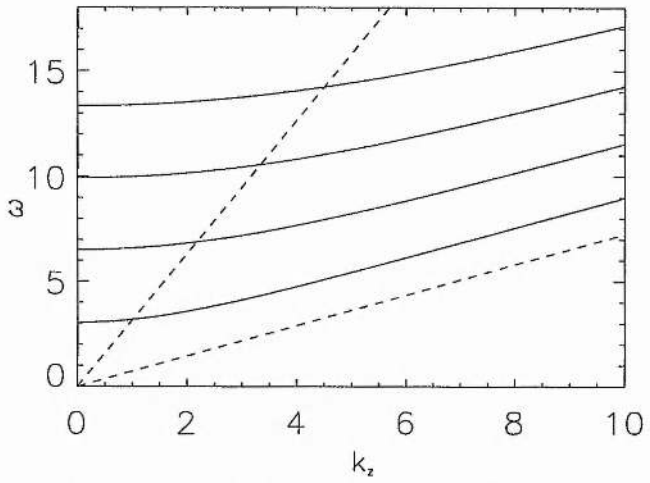

Figure 3.4: The first four decoupled fast eigenfrequencies as a function of k_z (the solid curves). Also plotted are the limits of the Alfvén continuum for each value of k_z (dashed lines). Where the fast eigenfrequencies lie inside the continuum we can expect Alfvén resonances to be driven when the condition $\lambda = 0$ is relaxed (Kivelson and Southwood, (1986)).

calculated how many fast mode resonances we would expect for various values of k_z (i.e., which decoupled fast modes have frequencies within the Alfvén continuum). A few sample results are shown in Table (3.2). Similarly, in Figure (3.4), we plot the k_z dependence of the decoupled fast eigenmode harmonics and the frequency span of the Alfvén continuum from ω_{A1} to ω_{A2}.

In Chapter 4, we examine fast and Alfvén wave resonant coupling by choosing parameters $A^2 = 1.0$, $B^2 = 0.9$, and $k_z = 2.0$. This ensures that only the fundamental fast mode lies within the Alfvén continuum, and allows the investigation of a case where only a single resonance is driven. The subsequent investigation of the physics of this mode coupling is also reported in Chapter 4.

3.4 Mathieu Function Decoupled Fast Eigenmode Analysis.

In addition to the numerical integration presented in the previous section, we can also analyse the decoupled fast mode equation in terms of Mathieu functions (McLachlan, 1947; Arscott, 1964; Abramowitz and Stegun, 1972). This is possible because we have chosen an Alfvén speed profile which consists of the monotonically decreasing part of the $\cos \pi x$

k_z	ω_{A1}	ω_{A2}	Number Of Resonances.
1.0	0.725	3.162	0
2.0	1.451	6.324	1
3.0	2.176	9.487	2
4.0	2.902	12.649	3
5.0	3.627	15.811	4

Table 3.2: Examples of the number of resonant fast eigenfrequencies which lie within the Alfvén continuum for various values of k_z. The first mode to enter the continuum is the fundamental, followed by the second harmonic etc.

function. This means that the governing decoupled ($\lambda = 0$) O.D.E. for ξ_x perturbations is one with periodic coefficients, and one which can be written in the form of Mathieu's equation.

If we had chosen an arbitrary density profile containing more Fourier components, we would still have had a differential equation with periodic coefficients. This could have been solved using Floquet theory, however this would have removed the sparsity of the governing matrices - see section (2.3).

3.4.1 Introduction to Mathieu Functions.

The canonical form of Mathieu's equation is

$$\frac{d^2y}{dz^2} + (a - 2q\cos(2z))y = 0. \tag{3.22}$$

Assuming solutions of the form $\exp -i\omega t$, and substituting for v_A^{-2} from equation (2.11), we find that the decoupled ($\lambda = 0$) form of equation (2.7) can be written as

$$\frac{d^2\xi_x}{dx^2} + \left[(\omega^2A^2 - k_z^2) + \omega^2B^2\cos\pi x\right]\xi_x = 0. \tag{3.23}$$

Transforming the variables $2z = \pi x$ and $y = \xi_x$, this equation becomes identical to equation (3.22), with the parameters a and q given by

$$a = \frac{4}{\pi^2}(\omega^2A^2 - k_z^2); \qquad q = -\frac{2\omega^2B^2}{\pi^2}. \tag{3.24}$$

In general, solutions to Mathieu's equation can be either stable or unstable in z, depending on the values of the two parameters a and q.

Linear, second order O.D.E.'s with periodic coefficients can be analysed using Floquet theory (Bender and Orszag, 1978). This is illustrated by the following simple analysis. Consider a general solution to Mathieu's equation which is constructed from two linearly independent solutions $y_1(z)$ and $y_2(z)$, so

$$y(z) = Py_1(z) + Qy_2(z). \tag{3.25}$$

Since Mathieu's equation is invariant under the transformation $z \rightarrow z + \pi$, then $y_1(z+\pi)$ and $y_2(z+\pi)$ must also be solutions. These can be written in terms of $y_1(z)$ and $y_2(z)$ so that

$$y_1(z+\pi) = \alpha y_1(z) + \beta y_2(z) \tag{3.26}$$

$$y_2(z+\pi) = \gamma y_1(z) + \delta y_2(z). \tag{3.27}$$

Writing

$$y(z+\pi) = Py_1(z+\pi) + Qy_2(z+\pi) \tag{3.28}$$

then

$$y(z+\pi) = Ry_1(z) + Sy_2(z) \tag{3.29}$$

where $R = P\alpha + Q\gamma$ and $S = P\beta + Q\delta$, so that

$$\begin{pmatrix} R \\ S \end{pmatrix} = \begin{bmatrix} \alpha, \gamma \\ \beta, \delta \end{bmatrix} \begin{pmatrix} P \\ Q \end{pmatrix} \tag{3.30}$$

Choosing $\begin{pmatrix} P \\ Q \end{pmatrix}$ to be an eigenvector of the matrix $\begin{bmatrix} \alpha, \gamma \\ \beta, \delta \end{bmatrix}$, then denoting it's eigenvalue by η we have $R = \eta P$ and $S = \eta Q$, so that

$$y(z+\pi) = \eta y(z). \tag{3.31}$$

This implies that we can write the solution for $y(z)$ as $e^{\mu z}\phi(z)$, where $\eta = e^{\pi\mu}$ and $\phi(z)$ is a π periodic function so that $\phi(z+\pi) = \phi(z)$.

The parameter η is determined by the coefficients a and q in Mathieu's equation, and hence we expect stable solutions to be found where $\mathrm{Re}(\mu) \leq 0$, and unstable ones if $\mathrm{Re}(\mu) > 0$. Since Mathieu's equation is invariant under the transformation $z \rightarrow -z$, then for both $e^{\mu z}\phi(z)$ and $e^{-\mu z}\phi(z)$ to not be exponentially growing, then we require $\mu = 0$ for stable solutions.

It can be shown (see for example Arscott (1964) and references therein) that if the two solutions to the above equation η_1 and η_2 are equal, then they have the values ± 1, and hence the solutions are stable. Solutions of this form (with equal μ roots) correspond to the four "basically-periodic" integral Mathieu functions of the first kind, which have periodicities of either π or 2π, and are either even or odd. For a given value of q, these "basically periodic" solutions only exist for a given (infinite) set of discrete characteristic numbers a_n, which can be shown to be real and different (see Arscott (1964), Chapter 2). In the terms of our previous analysis of decoupled fast eigenmodes, the values of a_n determine the eigenfrequencies (ω_n^2) of the fast MHD wave mode harmonics.

3.4.2 Mathieu Functions of the 1st Kind.

These "basically periodic" functions are called Mathieu functions of the first kind. We will concentrate on the functions of integral order which are usually denoted by $ce_{2n}(z,q), ce_{2n+1}(z,q), se_{2n+1}(z,q), se_{2n+2}(z,q)$. If we take the case $q = 0$, we recover the simple harmonic oscillator equation

$$\frac{d^2y}{dz^2} + ay = 0. \tag{3.32}$$

Writing the general form of the characteristic number a as a power series in q so that

$$a = m^2 + \alpha_1 q + \alpha_2 q^2 + \alpha_3 q^3 + \ldots \tag{3.33}$$

then equation (3.32) has pairs of solutions when $q = 0$ given by $\sin mz$, $\cos mz$; $m = 1, 2, 3, \ldots$ (the positive signs taken by convention). Note that these α_n are different from the α_{mn} entries in the numerical solution matrix α, which has as its columns the solution eigenvectors of the inhomogeneous plasma. These $q = 0$ Mathieu solutions are analogous to the homogeneous ξ_x eigenfunctions which we derived for the uniform background plasma case in section (3.2.1), and which when subject to the boundary conditions $\xi_x(x = 0, 1) = 0$ gave the solutions as $\sin \pi n x$.

For cases where $q \neq 0$, we can take the same power series for a, and similarly expand the solution functions $y(z)$ as power series in q. For example, the solution for the Mathieu function giving the solution $\cos z$ when $q = 0$ would be taken as

$$y(z) = \cos z + qc_1(z) + q^2c_2(z) + q^3c_3(z) + \cdots \tag{3.34}$$

where α_n (in equation (3.33)) and the functions $c_n(z)$ are to determined. These expansions clearly illustrate how setting $q \neq 0$ distorts the $q = 0$ trigonometric function eigenmodes. This can be understood when we consider that $q \neq 0$ represents fast eigenmodes in a non-uniform background plasma distribution. Unfortunately, the problem with this series formulation is that the expansions only converge for small values of $|q|$, and hence are generally of limited use (in the only study of convergence known to the author, a convergence criteria for ce_0 was found to be $|4q|^2 < 1$ (see Arscott (1964) and references therein)). However, the expansions for a may be convergent for a wider range of q (again, see e.g., Arscott (1964)). For this case it has been proven that the range of convergence is certainly $|q| > 1$, and hence the expansions may be of more use if they are used to determine characteristic numbers (i.e., ω_n).

In general however, Mathieu's equation is solved for the "basically-periodic" integral Mathieu functions of the first kind by using expansions in terms of trigonometric functions. These expansions are usually written as

$$ce_{2n}(z,q) = \sum_{r=0}^{\infty} A_{2r}^{(2n)} \cos 2rz \tag{3.35}$$

$$ce_{2n+1}(z,q) = \sum_{r=0}^{\infty} A_{2r+1}^{(2n+1)} \cos(2r+1)z \tag{3.36}$$

$$se_{2n+1}(z,q) = \sum_{r=0}^{\infty} B_{2r+1}^{(2n+1)} \sin(2r+1)z \tag{3.37}$$

$$se_{2n+2}(z,q) = \sum_{r=0}^{\infty} B_{2r+2}^{(2n+2)} \sin(2r+2)z \tag{3.38}$$

which have the characteristic numbers a_{2n}, a_{2n+1}, b_{2n+1} and b_{2n+2} respectively. The functions ce_{2n}, ce_{2n+1} and se_{2n+1}, se_{2n+2} are either even or odd, and are 2π or π periodic respectively. Similarly, each of these functions has n zeros in the interval $0 \leq z \leq \pi/2$.

For the fast eigenmodes, we require solutions which are subject to the boundary conditions $\xi_x(x = 0, 1) = 0$, i.e., they are periodic with an x period of 2. Consequently, we

are interested in Mathieu function solutions which are π periodic in z, and are odd with respect to $z = 0$, i.e., the functions se_{2n+2}.

3.4.3 Mathieu Function Series Solution For Decoupled Fast Eigenmodes.

The problem of finding the decoupled fast eigenmodes using the Mathieu function formulation becomes one of simply calculating the characteristic numbers b_{2n+2} and their corresponding expansion coefficients $B_{2r+2}^{(2n+2)}$.

Firstly, we need to consider the normalisation which we will adopt for the Mathieu functions. By convention, when $q = 0$ the Mathieu functions are taken to revert to the source trigonometric function having the same harmonic number as the Mathieu function. The standard form of normalisation is taken to be

$$\sum_{r=0}^{\infty} \left(B_{2r+2}^{(2n+2)}\right)^2 = 1. \tag{3.39}$$

This allows all of the $B_{2r+2}^{(2n+2)}(n \neq r)$ to be related to $B_{2r+2}^{(2n+2)}(n = r)$ and normalised accordingly. Hence when $q = 0$, then $B_{2r+2}^{(2n+2)}(n = r) = 1$ and $B_{2r+2}^{(2n+2)}(n \neq r) = 0$ so that the trigonometric functions have an amplitude of $+1$.

However, this normalisation is in essence simply a convention. Since the numerical matrix eigenvalue routine which we have discussed in section (2.3) produces eigenvectors which are normalised so that their largest entry is unity, then we choose to renormalise our Mathieu functions in exactly the same way. This means we simply rescale the coefficients so that the largest element $B_{2r+2}^{(2n+2)}$ will be equal to 1. To calculate $B_{2r+2}^{(2n+2)}$ and b_{2n+2}, we use the continued fraction method of McLachlan (1947) which is described in Appendix A.

3.4.4 Calculation of Mathieu Function Solutions.

In this section we calculate the values of the Mathieu function characteristic numbers a and the expansion coefficients B_{2r+2} for the fundamental fast mode and several harmonics. We choose values of $A^2 = 1.0$, $B^2 = 0.9$ and $k_z = 2.0$ to facilitate a comparison with the numerical matrix eigenvalue results from section (3.2.2).

To calculate each harmonic solution we input the parameter q - calculated on the basis of equation (3.24), with omega taken from high accuracy Runge-Kutta numerical integrations, as described in section (3.3). The methods described in Appendix A allow

the calculation of the values of b_{2n+2} corresponding to the input values of q, and their respective eigenfunction expansion parameters $B_{2r+2}^{(2n+2)}$. These can be compared directly to the numerical matrix eigenfrequencies, and to the normal mode expansion coefficients which make up the entries in the eigenvector solution matrix α_{mn}. In this way, we can verify independently that not only are the eigenfrequencies being calculated correctly by the eigenvalue solver (which we previously checked using the Runge-Kutta routine), but also that the correct form of the Fourier series expansions for the fast normal modes is being generated (i.e., that the eigenvectors are also reliable).

Note that since we are interested here in verifying the results from the numerical matrix eigenvalue calculation, just because we are using a "known" value of ω to determine the input value of q does not render the Mathieu function analysis invalid.

i) Calculation of Characteristic Numbers.

To ensure that the Mathieu function routines were working correctly, we used the Runge-Kutta calculated values of ω to input q, and hence found the expected Mathieu function solution characteristic numbers using this same accurate value of ω. When these were compared with the values calculated using the Mathieu routines, good agreement was found - see Table (3.3) below.

Harmonic, n	Input RK ω	Expected RK b_{2n+2}	Mathieu b_{2n+2} $r^\star = 10$
1	3.5746223	3.5575588	3.5575548
2	6.8230629	17.246563	17.246561
3	10.1627130	40.236967	40.236927
4	13.5251813	72.517809	72.517638

Table 3.3: Comparison of the first four harmonic Mathieu function calculated characteristic numbers b_{2n+2}, with those b_{2n+2} expected on the basis of $a = 4(\omega^2 A^2 - k_z^2)/\pi^2$, using the value of ω (the second column) from the Runge-Kutta integration.

ii) Calculation of Coefficients $B_{2r+2}^{(2n+2)}$.

Using the values of the characteristic numbers from the previous section, we calculated the expansion coefficients and compared them to those derived using the matrix

eigenvalue solver. The results are presented in Table (3.4). Again, we can see that the accuracy of the matrix eigenvalue results depends on the value of N - whilst that of the Mathieu analysis depends on the choice of r^* - the r value used to truncate the continued fraction used in calculating the coefficients $B_{2r+2}^{(2n+2)}$ (see Appendix A). Table (3.4) shows results for a small value of $r^* = 10$. As N increases, the eigenvalue results approach those of the Mathieu analysis. However, we should note that the accuracy of the eigenvalue routine is remarkable, even when $N = 7$ (final column). When, for instance $N = 10$, the accuracy of the derived eigenvectors matches those for $N = 100$ to an accuracy of ~ 8 decimal places.

Since the normalisation of the Mathieu functions neglects the high r elements, which will exist for the numerical eigenvectors (derived with sufficient N), then $B_{2r+2}^{(2n+2)}$ with large r (i.e., those with the smallest magnitude) will have some small errors associated with the neglect of the $r > r^*$ coefficients. Consequently, only the first 8 elements of $B_{2r+2}^{(2n+2)}$, out of 11, are shown. Similarly, truncation in r introduces errors into the continued fraction iterative determination of both a and $B_{2r+2}^{(2n+2)}$ (see Appendix A).

3.4.5 Mathieu Function Stability Diagram.

As we have previously discussed, solutions to Mathieu's equation can either be stable or unstable, depending on the parameters q and a. For equal roots of equation (3.31) (i.e., equal η) then we obtain the four sets of "basically periodic" integral Mathieu functions of the first kind. The solutions for the characteristic numbers of these functions are shown in Figure (3.5).

By considering the cold background plasma distribution which we have imposed in our MHD wave study, we clearly have a situation whereby $A^2/B^2 =$ a constant. Since $q = -2\omega^2 B^2/\pi^2$ and $a = 4(\omega^2 A^2 - k_z^2)/\pi^2$, then we can substitute for the value of ω^2 in the equation for a to gain

$$a = -\frac{2A^2}{B^2} q - \frac{4k_z^2}{\pi^2}. \tag{3.40}$$

This equation describes a straight line in the q-a diagram having a gradient $-2A^2/B^2$ and a y (i.e., a) intercept of $-4k_z^2/\pi^2$. Since the q-a diagram is symmetric about $q = 0$, then we can consider this line in the standard $+q$ $+a$ quadrant (plotted as a dot-dash line in this Figure). Where this line crosses the stable "basically periodic" Mathieu function solution curves b_{2n+2} locates the position of the fast eigenmode harmonics on this diagram. These

Harmonic, n	r value	Mathieu $B_{2r+2}^{(2n+2)}$ ($r^* = 10$)	Eigenvector $B_{2r+2}^{(2n+2)}$ $N = 100$	Eigenvector $B_{2r+2}^{(2n+2)}$ $N = 7$
1	0	1.0	1.0	1.0
	1	0.1898569	0.18985679	0.18985678
	2	1.3675761E-02	1.3675743E-02	1.36757433E-02
	3	5.2777344E-04	5.2777240E-04	5.27772401E-04
	4	1.2758117E-05	1.2758084E-05	1.27580840E-05
	5	2.1174277E-07	2.1174207E-07	2.11742066E-07
	6	2.5644212E-09	2.5644108E-09	2.56412428E-09
	7	2.3674959E-11	2.3674659E-11	-
	8	1.7218323E-13	1.7202671E-13	-
2	0	-0.6409584	-0.64095688	-0.64095688
	1	1.0	1.0	1.0
	2	0.4941451	0.49414343	0.49414342
	3	9.1452887E-02	9.1452314E-02	9.14523137E-02
	4	9.4481602E-03	9.4480746E-03	9.44807423E-03
	5	6.3489975E-04	6.3489225E-04	6.34888792E-04
	6	3.0207658E-05	3.0207219E-05	3.01559811E-05
	7	1.0752904E-06	1.0752744E-06	-
	8	2.9710284E-08	2.9780154E-08	-
3	0	-0.5198053	-0.51980484	-0.51980478
	1	1.0	1.0	1.0
	2	-0.7669189	-0.76692046	-0.76692115
	3	-0.8274923	-0.82749206	-0.82749085
	4	-0.2770185	-0.27701809	-0.27701389
	5	-5.1428355E-02	-5.1428208E-02	-5.14150926E-02
	6	-6.2858869E-03	-6.2858616E-03	-6.21753284E-03
	7	-5.5196866E-04	-5.5196581E-04	-
	8	-3.6767660E-05	-3.6767430E-05	-
4	0	0.4033701	0.40336760	0.40322251
	1	-0.8284135	-0.82841021	-0.82815647
	2	1.0	1.0	1.0
	3	-0.2661569	-0.26616223	-0.26715007
	4	-0.9320486	-0.93204743	-0.93145314
	5	-0.5016175	-0.50161458	-0.49829016
	6	-0.1427141	-0.14271279	-0.13476827
	7	-2.6600173E-02	-2.6599838E-02	-
	8	-3.5776270E-03	-3.5775729E-03	-

Table 3.4: Comparison of the first four harmonic Mathieu function $B_{2r+2}^{(2n+2)}$ ($r^* = 10$), with the numerical fast eigenvectors for $N = 100$ and $N = 7$.

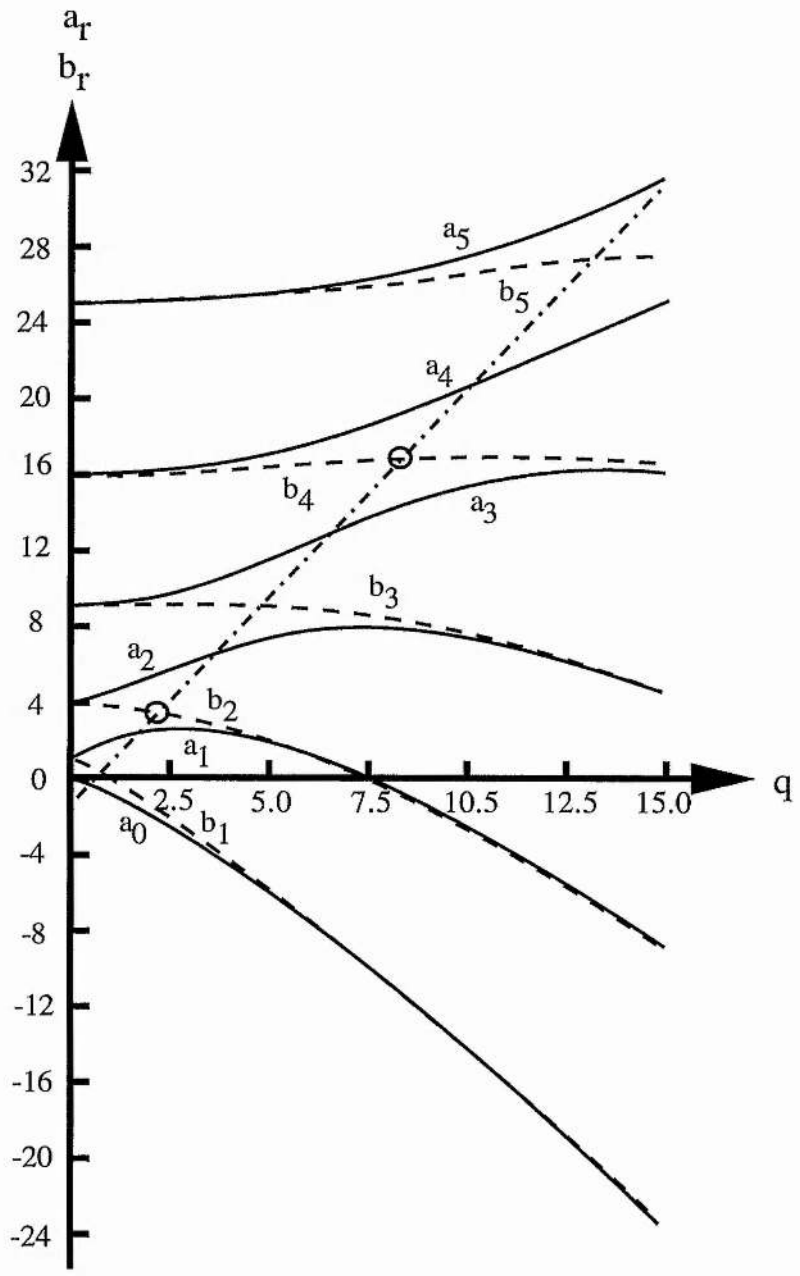

Figure 3.5: The form of the "basically periodic" first order Mathieu functions of integral order. Where the functions b_{2r+2} cross the dot-dash line defines the fast eigenmode harmonics. Here we show the first two harmonics i.e., b_2 and b_4. In the regions between the "basically periodic" function curves, solutions are unstable between b_n and a_n, and stable between a_n and b_{n+1}. Obviously, the basically periodic solutions are stable (Adapted from Abramowitz and Stegun, (1972)).

correspond to points defined by the fast mode eigenfrequencies $\omega = \omega_n$, and are highlighted by over-plotted circles at their points of intersection.

3.5 Coupled ($\lambda \neq 0$) Normal Modes.

3.5.1 Introduction.

Once we choose $\lambda \neq 0$, then fast and Alfvén wave eigenmodes become coupled. They form hybrid modes which are neither purely compressible nor incompressible. In particular, both the $\phi_{nx}(x)$ and $\phi_{ny}(x)$ modes may become singular, as were the $\phi_{ny}(x)$ modes when $\lambda = 0$. These modes, despite being singular, oscillate with their eigenfrequency ω_n throughout the plasma.

Historically, singularities of this form have caused some confusion. In the early papers which investigated these types of singular eigenvalue equations (in the areas of hydrodynamics, magnetohydrodynamics, astrophysics and plasma physics) some concern was voiced about the existence of singularities in the eigenfunctions at positions within the domain of interest (see the extensive review by Adam (1986)). The solution to the "apparent" paradox of these singular normal modes is two-fold. Firstly, in any real system the singularities will be resolved by dissipation mechanisms such as friction, viscosity or resistivity. Secondly, and more interestingly, in dissipation-less systems (such as ideal MHD) the existence of singular eigenmodes should not be interpreted as a surprising feature of the equations (in fact they should, as pointed out by Boyd (1981) in his study of Sturm-Liouville eigenproblems with an interior pole, be expected to be as common as "kittens from cats" !). The point is that despite the fact that the equations (after a Fourier transform in time) produce singular eigenmodes, when these Fourier transform solutions are inverse Fourier transformed (by performing an integral Fourier superposition) they produce solutions to the governing equations which are well behaved (Barston, 1964; Adam, 1986). In fact, it is well known that many well behaved functions have Fourier transforms which are not well behaved - for instance Dirac delta functions.

In an early study of this type, Barston (1964) considered the problem of electrostatic oscillations in cold inhomogeneous plasmas. His equations are in fact identical to those governing the incompressible inhomogeneous MHD wave problem (Uberoi, 1972) (with the local plasma frequency $\omega_p^2(x)$ replaced by the local Alfvén frequency $\omega_A^2(x)$). Hence his

results have an interesting relation to our problem (although the plasma which we consider is compressible). Barston (1964) found that the eigenvalue spectrum of his problem was real and continuous, consisting of modes with $\omega^2 = \omega_p^2(x)$ for each particular value of x, and which were not degenerate if a monotonically increasing $\omega_p(x)$ profile was adopted. For values of ω which lie inside the inhomogeneous background plasma frequency spectrum, the eigenfunctions of these modes are singular - being in general composed of a logarithmic singularity and a step function at the x position defined by $\omega^2 = \omega_p^2(x)$. On performing the Fourier inversion, Barston (1964) found a well behaved solution to his initial value problem for the electrostatic potential perturbation, which asymptotically (as $t \to \infty$) behaves like

$$\psi(x,t) \sim t^{-1} \exp\left(i\omega_p(x)t\right). \tag{3.41}$$

These oscillations represent the non-collective (Barston) modes of the inhomogeneous plasma. We should point out that Barston (1964) considers the case of an embedded inhomogeneity, whereby the inhomogeneous region is matched onto homogeneous regions which extend to $|x| \to \infty$. In our box model, we have imposed perfectly reflecting boundaries in x at the edges of the inhomogeneous regions - the isolated inhomogeneity in the terminology of Cally (1991). We also note that for an isolated inhomogeneity in an incompressible plasma, the step function part of the singular eigenmodes is suppressed, leaving only the logarithmic singularity (Cally, 1991).

There is also another approach to solving the coupled MHD wave problem. This entails employing a Laplace (rather than a Fourier) transform to solve the initial value problem (Sedláček, 1971a; Sedláček, 1971b; Goedbloed, 1983). It is well known that in the limit of a discontinuity in plasma density, there exists a well behaved collective (surface wave) solution which oscillates with a frequency independent of x determined by an average of the frequencies on either side of the discontinuity. Sedláček was lead to attempt the continuous inhomogeneous problem by asking the question "what happens to these collective modes as the discontinuity is smoothed to an inhomogeneous profile ?", as will exist in any real physical system.

Although the normal modes method of Barston (1964) is mathematically simpler to use, the Laplace transform method reveals some interesting new properties of the inhomogeneous plasma waves. The method involves constructing the Green's function for the governing differential equation. This turns out to be a multi-valued function of complex ω,

with branch point singularities on the real ω axis, which correspond to the Barston (1964) eigenmodes.

An analytic continuation of the Green's function, however, into the adjacent $n = \pm 1$ Riemann sheets (across the branch cuts), reveals simple poles with complex frequencies which are independent of x position. Whilst these modes do not correspond to new normal modes of the system (since their poles are off the principal (physical) Riemann sheet) they do have some physical significance. They represent collective modes which oscillate with a position independent complex frequency, and which decay in time due to their imaginary frequency component γ (these modes are often called "quasi-modes" or global modes). As the width of the inhomogeneous region is reduced ($ka \rightarrow 0$, where k is the wavenumber of the waves and a is the half-width of the inhomogeneous region), so that the system again approaches the discontinuous case, these simple poles on the $n = \pm 1$ sheets approach the real frequency axis. Ultimately, they coalesce there and recreate the surface modes which existed when $ka = 0$. (Note that in fact there are also an infinite number of other poles off the principal Riemann sheet. These additional quasi-modes lie further from the branch cuts, and as $ka \rightarrow 0$ move away from the principal sheet as their frequency $|\omega| \rightarrow \infty$ (Sedláček, 1971a)).

The complex frequencies of these quasi-modes occur despite the governing system being Hermitian. The frequencies of the true eigenmodes (the Barston (1964) modes), however, remain purely real (as they should). In fact, the quasi-modes can be generated by a summation over the Barston (1964) modes of the system, as in fact could any disturbance. We should note that from a numerical point of view, a very large number of these singular modes would be required if they are to be used as a basis with which to generate an accurate approximation to any perturbation. The number of these modes would be very much greater than for example the number of Fourier modes which would be required if they were to be used as an alternative basis. We have used this fact to employ Fourier series to obtain numerical solutions to the coupled wave problem - as described in Chapter 2.

There has been some confusion in the literature about the complex frequency of the quasi-modes, as discussed by Lee (1980) and Adam (1986). In particular, in some instances the damping rate of the quasi-modes has been interpreted as a dissipative (i.e., non-ideal) heating rate of an ideal plasma! (e.g., Wentzel (1979)). As Lee points out, this seems to have stemmed from the discussions in Chen and Hasegawa (1974c) and Hasegawa and Chen (1974) which incorrectly identify the rate of absorption of Alfvén waves at the

resonance as a plasma heating rate. Rae and Roberts (1981) point out that the correct interpretation for the imaginary frequency in ideal MHD, is to identify it as the timescale for the re-organisation of the quasi-modes energy into the energy stored at the resonance. Budden (1961) also discusses this point in the context of the singular equations which occur in the context of radio wave absorption in the ionosphere. Similarly, the reader is referred to Hasegawa and Uberoi (1982), chapters 3 and 4 for a discussion of resonant absorption in incompressible inhomogeneous plasmas.

Since the quasi-modes are not strictly normal modes of the plasma, we do not discuss them further in this chapter, however they are very important in the discussions of the resonant absorption of wave energy considered in Chapter 4.

3.5.2 $\lambda \sim O(1)$ Normal Modes.

With $\lambda \sim O(1)$, then those eigenmodes (which when $\lambda = 0$ were fast modes) having frequencies (ω_n) inside the Alfvén continuum can couple to previously Alfvénic modes with frequencies $\sim \omega_n$. In this way, these coupled modes become singular ("improper") eigenmodes. The singularities are a manifestation of the wave coupling which is an integral part of the structure of the inhomogeneous plasma waves, and which is paramount in generating the phenomena of resonant absorption. Fast waves which have frequencies outside the continuum remain well behaved and non-singular.

i) Analytic Solutions for Singular Normal Modes.

The standard treatment of the singularities which appear in the coupled wave problem involves assuming a dependence of $\exp(-i\omega t)$ and combining equations (2.7) and (2.8) to generate a single equation for the linear compressible magnetic field component b_z. This generates the equation

$$\frac{d^2 b_z}{dx^2} - \frac{dK^2/dx}{K^2 - k_z^2}\frac{db_z}{dx} + \left(K^2 - k_z^2 - \lambda^2\right) b_z = 0 \tag{3.42}$$

where $K^2(x) = \omega^2/v_A^2(x)$ (Kivelson and Southwood, 1986). If we assume that the density varies linearly with x in the vicinity of the resonance then we can take

$$K^2 - k_z^2 = \alpha^2 (x - x_w) \tag{3.43}$$

and

$$K^2 - k_z^2 - \lambda^2 = \alpha^2 (x - x_\lambda) \tag{3.44}$$

to generate the equation, given in terms of an operator L, as

$$L(b_z) = \frac{d^2 b_z}{dx^2} - \frac{1}{(x - x_w)} \frac{db_z}{dx} + \alpha^2 (x - x_\lambda) b_z = 0 \tag{3.45}$$

which has a regular singular point at $x = x_w$ (Kivelson and Southwood, 1986).

Using a standard Frobenius method (Bender and Orszag, 1978) we can follow Southwood (1974) and solve this equation. We find a regular solution of the form

$$b_z = \sum_{n=0}^{\infty} a_n (x - x_w)^{n+r}. \tag{3.46}$$

Equating terms in powers of $(x - x_w)^r$ generates the indices $r = 0$ or 2 for $a_0 \neq 0$. We find that $a_1 = 0$, and generate a regular solution given by

$$R(x) = (x - x_w)^2 + \frac{\lambda^2}{8}(x - x_w)^4 - \frac{\alpha^2}{15}(x - x_w)^5 + O(x - x_w)^6. \tag{3.47}$$

A second independent (and in this case singular) solution can be found again by using standard Frobenius techniques, however these solutions are in general more difficult to obtain. With $r_1 = 2$ and $r_2 = 0$, we have the case where $r_1 - r_2 = N$, and N is an integer. This second solution is found from the equation

$$S(x) = \sum_{n=1}^{\infty} c_n (x - x_w)^{n+r_2} - \frac{\partial}{\partial r} R(x)|_{r=r_1} \tag{3.48}$$

(Bender and Orszag, 1978) so that

$$S(x) = \sum_{n=0}^{\infty} c_n (x - x_w)^{n+r_2} - R(x) \ln(x - x_w) - \sum_{n=0}^{\infty} b_n (x - x_w)^{n+r_1} \tag{3.49}$$

where $b_n = \frac{\partial}{\partial r} a_n(r)|_{r=r_1}$ and c_n represent the coefficients of a regular Frobenius solution to the inhomogeneous equation

$$L\left[\frac{\partial}{\partial r}\left(\sum_{n=0}^{\infty} c_n (x - x_w)^{r_2+n}\right)\right] = 2a_0 (x - x_w)^{r_2+N-2}. \tag{3.50}$$

When $n = N$ in equation (3.50), we find a relation between a_0 and $c_o, c_1, \ldots, c_{N-1}$; in this case $a_0 = -\frac{\lambda^2}{2} c_0$. The values of c_0 and c_N are arbitrary, and we take $c_0 = 1$ and $c_N = 0$

(solutions with different values of c_N just introduce different multiples of $R(x)$ into the final solution).

This generates the second independent (singular) solution as

$$S(x) = \left[1 - \frac{\alpha^2}{3}(x - x_w)^3 - \frac{\alpha^2\lambda^2}{3}(x - x_w)^5 + O(x - x_w)^6\right]$$
$$+\frac{\lambda^2}{2}R(x)\ln(x - x_w) + \frac{\lambda^2}{2}\left[-\frac{3\lambda^2}{32}(x - x_w)^4 + \frac{8\alpha^2}{15^2}(x - x_w)^5 + O(x - x_w)^6\right] \quad (3.51)$$

These expansion solutions agree with the solutions of Speziale and Catto (1977), for the analogous equation they used to study the interactions of lasers and plasmas. They also agree with the solutions of Kivelson and Southwood (1986) and Zhu and Kivelson (1988) for their magnetospheric pulsation studies (note that in Zhu and Kivelson (1988), their normalisation means that $\alpha^2 = \omega^2$).

In order to find a full solution, these two linearly independent solutions must be combined so that they satisfy the boundary conditions, and connect across the singularity at $x = x_w$. By considering a solution of the form

$$b_z = [A_1 R(x) + B_1 S(x)]\, H(x - x_w) + [A_2 R(x) + B_2 S(x)]\, H(x_w - x) \quad (3.52)$$

where $H(x)$ is the Heaviside function (Lighthill, 1958), a relationship between A_1, B_1, A_2 and B_2 can be determined across the singularity (Goedbloed, 1983). Substituting for the small function $b_z = A_1 R(x) H(x - x_w)$ into equation (3.45) shows that this combination is also a solution to the governing equations. Similarly, $A_2 R(x) H(x_w - x)$ is a solution - independent of $A_1 R(x) H(x - x_w)$, i.e., $A_1 \neq A_2$. However, neither of the large solution functions $B_1 S(x) H(x - x_w)$ and $B_2 S(x) H(x_w - x)$ satisfy equation (3.45), and both leave a quantity $\propto \delta(x - x_w) \neq 0$ (where δ is the Dirac delta function). Consequently $B_1 = B_2$. The full solution can hence be written in the form

$$b_z = AR(x) + BR(x)H(x - x_w) + CS(x) \quad (3.53)$$

where the discontinuity (the Heaviside function) is apparent, the logarithmic singularity is contained within the function $S(x)$, and A,B and C are determined by the boundary conditions and an arbitrary normalisation.

The step (Heaviside) part of the solution can also be demonstrated by considering the continuation of the singular solution across the resonance layer. The function $\ln(x-x_w)$ (the solution for $x > x_w$) becomes $\ln(x_w-x)+i\pi$, when $x < x_w$. This introduces a Heaviside contribution of $i\pi R(x)/2$ into the solution (Kivelson and Southwood, 1986).

The existence of the singular solution (where we have assumed a dependence of $\exp(-i\omega t)$) clearly shows that we can expect the coupled wave normal modes to similarly show singular behaviour. Note that despite being logarithmically singular, $S(x)$ is finite at $x = x_w$. However, the solutions for ϕ_{nx} and ϕ_{ny} are infinite at $x = x_w$. Their solutions can be determined from the form of the b_z eigenmodes, so that

$$\xi_x = \frac{\partial b_z/\partial x}{\alpha^2(x - x_w)} \tag{3.54}$$

and

$$\xi_y = \frac{-i\lambda b_z}{\alpha^2(x - x_w)} \tag{3.55}$$

(Kivelson and Southwood, 1986). Consequently, ϕ_{nx} retains a Heaviside discontinuity and an infinite logarithmic singularity (since $R(x) \sim (x - x_w)^2$ and $S(x) \sim 1 + (x - x_w)^2 \ln(x - x_w)$). ϕ_{ny} contains no Heaviside discontinuous contribution (but retains continuous terms like $(x - x_w)^2 H(x - x_w)$), and has a leading order $1/(x - x_w)$ singularity.

We can further illustrate the singular behaviour of the ξ_x and ξ_y eigenmodes with the following simple analysis. If we consider the wave displacement component ξ_x, then by again assuming a dependence of $\exp(-i\omega t)$, and combining the equations (2.7) and (2.8), we can generate the equation

$$\frac{\partial^2 \xi_x}{\partial x^2} - \lambda^2 \frac{\partial K^2/\partial x}{(K^2 - k_z^2)\left[K^2 - k_z^2 - \lambda^2\right]} \frac{\partial \xi_x}{\partial x} + \left(K^2 - k_z^2 - \lambda^2\right) \xi_x = 0 \tag{3.56}$$

(Rankin et al., 1993; Mann et al., 1995). When $\lambda = 0$, this equation reverts to equation (3.19), which is clearly non-singular. A similar equation to (3.56) was derived for the electric field E_y (which corresponds to a plasma displacement ξ_x) by Southwood (1974). As Southwood points out, equation (3.56) has two regular singularities at the points where $K^2 = k_z^2$ and $K^2 = k_z^2 + \lambda^2$. The first of these corresponds to the Alfvén resonance, where ω matches the local natural Alfvén frequency $\omega_A(x)$, and generates singular ξ_x wave fields. However the second regular singular point corresponds to the approximate turning point

of the waves and hence the wave modes are non-singular and well behaved at this position (see also Radoski (1974) for the case of waves in a hemi-cylindrical geometry). Taking a Taylor expansion of the function $K^2 - k_z^2$ around the resonance position $x = x_w$, then we find

$$\frac{\partial^2 \xi_x}{\partial x^2} + \frac{1}{(x - x_w + i\epsilon)} \frac{\partial \xi_x}{\partial x} - \lambda^2 \xi_x = 0 \tag{3.57}$$

(Chen and Hasegawa, 1974c; Rankin et al., 1993) where

$$\epsilon = -2k_{zi}k_{zr} / \left. \frac{dK^2}{dx} \right|_{x=x_w}. \tag{3.58}$$

Here k_{zi} represents a small imaginary component of the field aligned wavenumber k_z, which is associated with the dissipation due to the resistivity of the ionospheric boundaries. Assuming a complex wavenumber of this form is often invoked in magnetospheric studies to resolve the singularity (we discuss this further in Chapter 4). In ideal MHD (and assuming infinitely conducting ionospheric boundaries) the singularities will not be resolved and $\epsilon = k_{zi} = 0$.

Equation (3.57) has the leading order solution

$$\xi_x \sim \ln(x - x_w + i\epsilon). \tag{3.59}$$

Using equation (2.8), we have the relation

$$i\xi_y = \frac{\lambda}{(K^2 - k_z^2 - \lambda^2)} \frac{\partial \xi_x}{\partial x} \tag{3.60}$$

so that to leading order around the resonance

$$i\xi_y \sim -\frac{1}{\lambda} \frac{\partial \xi_x}{\partial x} \sim -\frac{1}{\lambda(x - x_w + i\epsilon)}. \tag{3.61}$$

Hence we expect that to leading order, the numerical ξ_x and ξ_y normal modes (for $\lambda \sim O(1)$) will have a logarithmic singularity and a $1/x$ singularity respectively (the discontinuity (Heaviside function) arises at $O(1)$ in ϕ_{nx}, coming from the function $H(x - x_w)\frac{dR(x)}{\partial x}/(x - x_w)$ in terms of the analysis in equation (3.53) (since $R(x) \sim (x - x_w)^2$)).

It has recently been suggested that the singularities which occur in equations of this type are an artefact of the simplified geometries which had been assumed, in this case a box model (Hansen and Goertz, 1992). Hansen and Goertz (1992) suggested that in

more complicated media, such as those which will occur in nature, the resonance would no longer exist. However it has recently been shown that the calculations of Hansen and Goertz (1992) are in error (Thompson and Wright, 1994). In fact, the Frobenius expansion method described here has now been successfully generalised and applied to the partial differential equations which occur in more complicated geometries, and it has been proved that the singularities are robust features of totally general curvilinear geometries consisting of potential background magnetic fields (Wright and Thompson, 1994; Federov et al., 1995). Consequently, we expect the Alfvén resonances to persist in nature, and hence that resonant absorption at these singularities may be invoked to explain pulsations in the curved geometry of the magnetosphere, or proposed as a possible solution to the solar coronal heating problem.

We can summarise the analytical properties of the ideal singular eigenmodes as follows:

- To leading order b_z eigenmodes have finite valued logarithmic singularities $\sim (x - x_w)^2 \ln(x - x_w)$.
- ϕ_{nx} and ϕ_{ny} have infinite singularities.
- To leading order $\phi_{nx} \sim \ln(x - x_w)$.
- To leading order $\phi_{ny} \sim 1/(x - x_w)$.
- ϕ_{nx} has a higher order discontinuous (Heaviside) solution generated by $R'(x)H(x - x_w)/(x - x_w) \sim H(x - x_w)$.
- ϕ_{ny} has no Heaviside discontinuity across the resonance (higher order terms $x^N H(x - x_w)$ $(N \geq 1)$ remain continuous).
- Neither of the coupled ϕ_{ny} or ϕ_{nx} eigenmodes contain leading order Dirac delta function contributions (higher order terms in ϕ_{nx} such as $(x - x_w)^N \delta(x - x_w) = 0$ (for $N \geq 1$)).

ii) Numerical $\lambda \sim O(1)$ Normal Modes.

We choose $\lambda = 1$ here, and investigate the form of the wave modes for various values of k_z.

a) Non-Resonant Modes.

In this case, all the decoupled fast eigenfrequencies lie outside the Alfvén continuum, as defined by $\omega_A(x) = k_z v_A(x)$. Consequently, we expect the resonant position x_w to lie outside the simulation domain of $0 \leq x \leq 1$. In Figure (3.6), we plot the spatial form of three of the previously Alfvénic (continuum) modes for $k_z = 0.5$, $A^2 = 1.0$, $B^2 = 0.9$ and $N = 100$. Their strongly Alfvénic nature is illustrated by the fact that $\xi_y \gg \xi_x, b_z$. Both the logarithmic nature of the $\phi_{nx}(x)$ eigenmodes, and the approximation to the $1/x$ singular nature of the $\phi_{ny}(x)$ modes, are apparent. The logarithmic structure of $\phi_{nx}(x)$ compares well with the incompressible study of Cally (1991). Note that these modes are no longer incompressible, but contain a well behaved (finite and continuous) b_z component, as illustrated in the bottom row of this Figure. The small scale oscillations in the form of b_z are numerical and originate from combining the Fourier approximations to the singular $\phi_{nx}(x)$ and $\phi_{ny}(x)$ in the equation for normalised $b_z = -(i\lambda\xi_y + \partial\xi_x/\partial x)$.

In Figure (3.7), we plot the coupled form of those modes which when decoupled were the first three fast harmonics, for the same parameters. The modes have the expected non-singular and global x nature, since their eigenfrequencies lie outside the continuum, however, they now have a significant $\phi_{ny}(x)$ component. We should note here that the number of b_z nodes for small λ is a suitable diagnostic with which to determine the harmonic number of these globally structured modes.

We next plot three "continuum" (localised) eigenmodes, in Figure (3.8), now for $k_z = 1.0$. The mode shown in the third column still shows the expected logarithmic behaviour in $\phi_{nx}(x)$, however in the first and second columns the discontinuity is becoming apparent. Indeed, in the central column the discontinuity is clearly superposed onto the logarithmic singularity in $\phi_{nx}(x)$. In general, the coefficients A, B and C in equation (3.53) determine the extent to which particular modes have logarithmic or discontinuous features.

For this case (where $k_z = 1.0$) the fundamental decoupled fast eigenfrequency ($\omega = 3.1893$) lies just outside the continuum (c.f. $\omega_{A2} = 3.162$), at a position predicted to be given by $\cos \pi x = 1.0019$. Examining the modes $n = 102, 103, 104$ for $k_z = 1.0$ (not shown) (i.e., the first three fast harmonics) shows them to remain non-singular (in the same

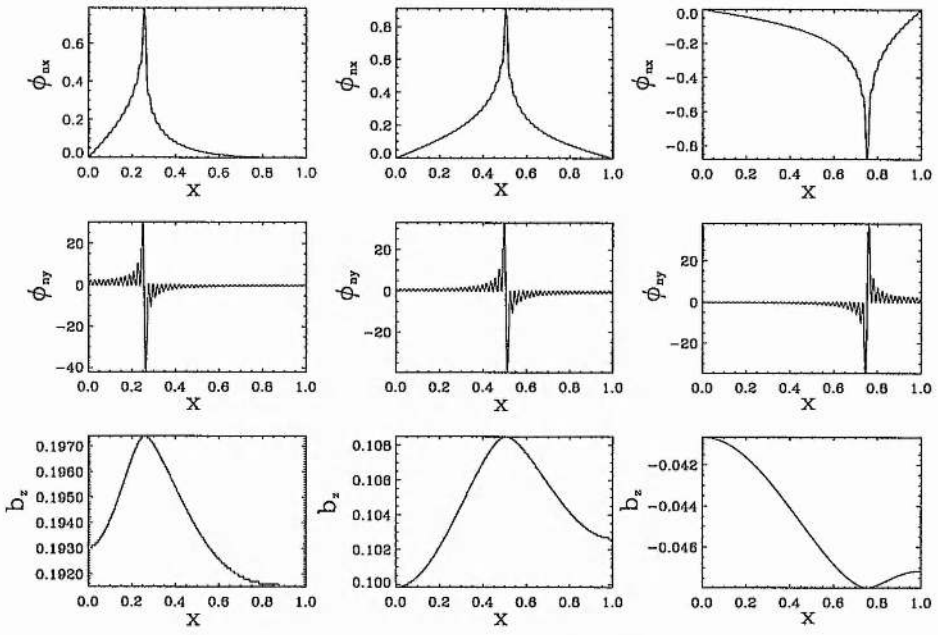

Figure 3.6: The continuum eigenmodes for $n = 25, 50, 75$ with $\lambda = 1.0$ and $k_z = 0.5$, for a 201 square matrix eigenvalue problem (i.e., $N = 100$).

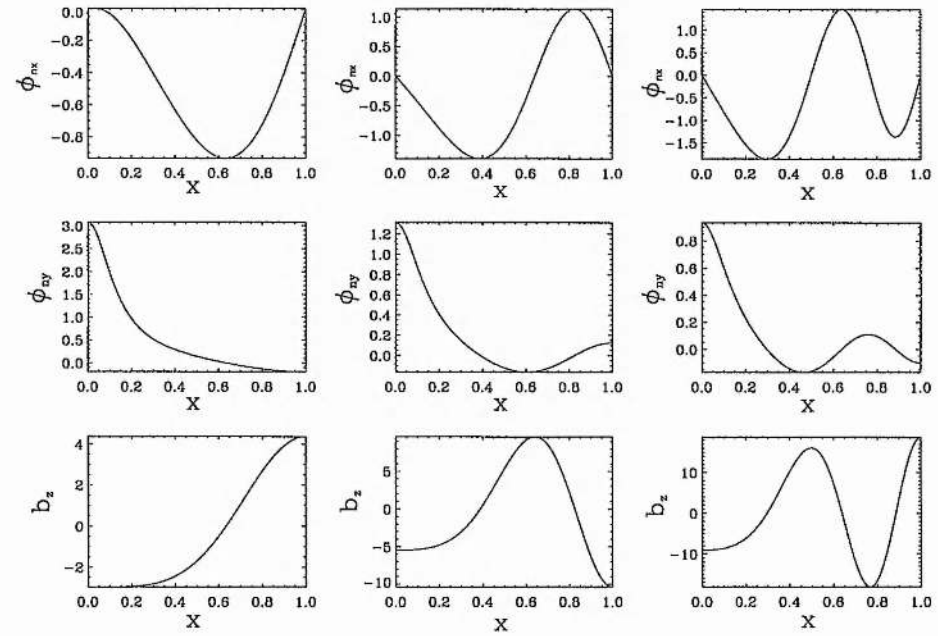

Figure 3.7: The discrete, global eigenmodes for $n = 102, 103, 104$ with $\lambda = 1.0$ and $k_z = 0.5$, for a 201 square matrix eigenvalue problem (i.e., $N = 100$).

way as the modes in Figure (3.7)). However, despite all the decoupled fast eigenfrequencies lying outside the continuum, there are still $N+1$ singular (Barston) modes.

b) Resonant Modes.

In Figure (3.9), we plot the form of the "resonant" fundamental eigenmodes for $k_z = 2.0$, again for $A^2 = 1.0$, $B^2 = 0.9$ and $N = 100$. Based on the decoupled fast eigenfrequency, we expect the resonance to be located at the position $x = 0.22$, where $n \sim 79$. In this Figure we have plotted the modes $n = 78, 80, 82$ which surround the "exact" resonance location (the mode $n = 79$ has the same form as the modes shown).

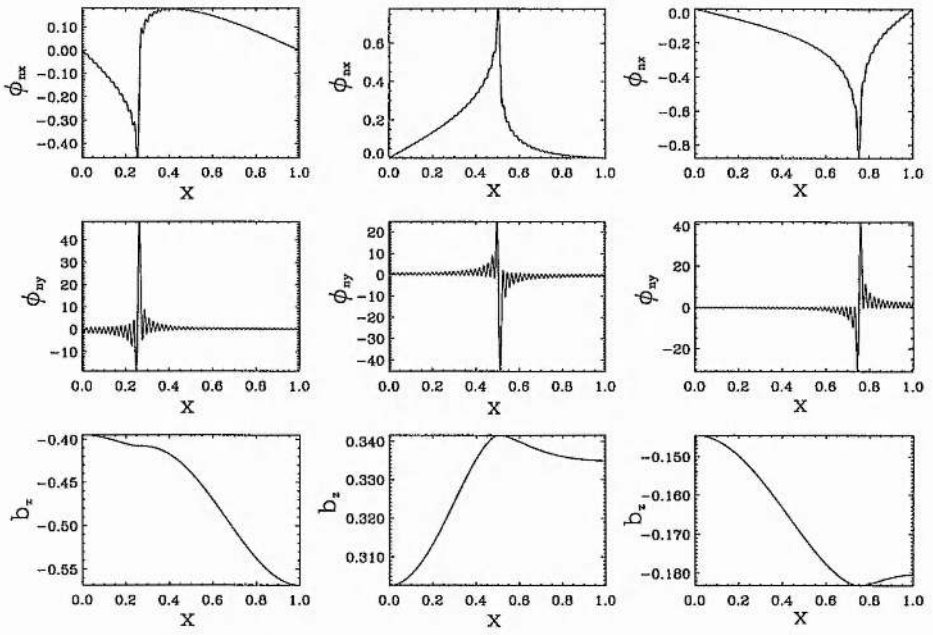

Figure 3.8: The localised (continuum) eigenmodes for $n = 25, 50, 75$ with $k_z = 1.0$, $A^2 = 1.0$, $B^2 = 0.9$, and $\lambda = 1.0$, for a 201 square matrix eigenvalue problem (i.e., $N = 100$).

The logarithmic and the Heaviside singular form of the $\phi_{nx}(x)$ mode is clearly shown, as is the Fourier approximation to the $1/x$ singular behaviour of the $\phi_{ny}(x)$ modes. Since the discontinuity is associated with generating a Poynting flux of energy which propagates into the resonance from both sides (Zhu and Kivelson, 1988), it is not surprising that this feature is particularly apparent in those modes which surround the resonant location.

Continuum modes with $n \ll 80$ in general have only a small discontinuous component, and strongly resemble the logarithmic Barston-like modes shown in Figure (3.6). The higher harmonic "fast" eigenmodes remain well behaved.

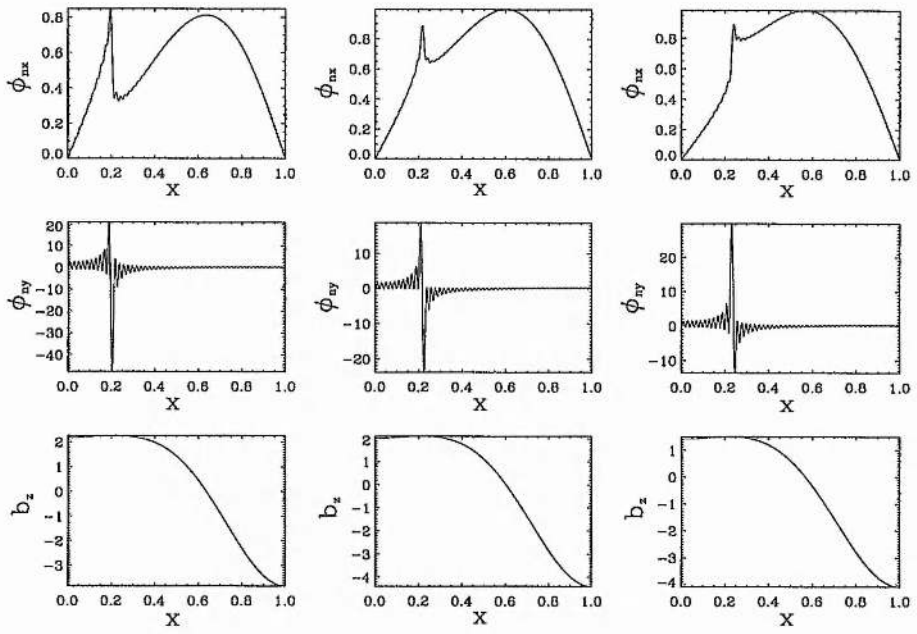

Figure 3.9: The coupled resonant eigenmodes around the exact resonance location $x = 0.22$. The modes $n = 78, 80, 82$ are shown for $k_z = 2.0$, and with $N = 100$.

For cases with larger values of k_z, the higher harmonic "fast" eigenfrequencies enter the continuum, and similarly begin to display the discontinuity and resonant characteristics around these new higher harmonic resonant locations x_w. Those "fast" eigenmodes whose frequencies remain outside the continuum retain their non-singular behaviour.

3.5.3 Large λ Normal Modes.

As λ increases, the turning point of the "fast" modes moves towards higher x, and the frequency of the modes increases (although ω_n is only weakly dependent on λ (Zhu and Kivelson, 1988; Walker et al., 1992; Wright, 1994a)). For example, with $k_z = 2.0$, $A^2 = 1.0$, $B^2 = 0.9$ and $\lambda \geq 10$, the fundamental "fast" eigenfrequency moves out of the Alfvén continuum.

In Figure (3.10) we plot the form of the 1st, 2nd and 10th harmonics for $\lambda = 50$, $A^2 = 1.0$, $B^2 = 0.9$ and $k_z = 2.0$. Note that for large values of λ there is some ambiguity in the definition of the "fast" mode harmonic number. In this case we have defined the harmonic number by the number of anti-nodes in ξ_x, rather than the number of b_z nodes, and plotted the modes $n = 101, 102, 110$. This seems a sensible distinction since the $n = 101$

mode is clearly a compressible mode (the first column in this Figure), but is one which only has a b_z node as $x \to 0$. This is in contrast to the first column of Figure (3.7) for $\lambda = 1.0$, and $k_z = 0.5$. There, the $n = 102$ mode was defined to be the first "fast" harmonic. In this large λ case, the eigenvalue routine calculates 100 "Alfvénic" modes (with low b_z), and 101 "fast" modes (high b_z). This is the opposite distinction from the low λ eigenmodes, where 101 continuum modes were generated.

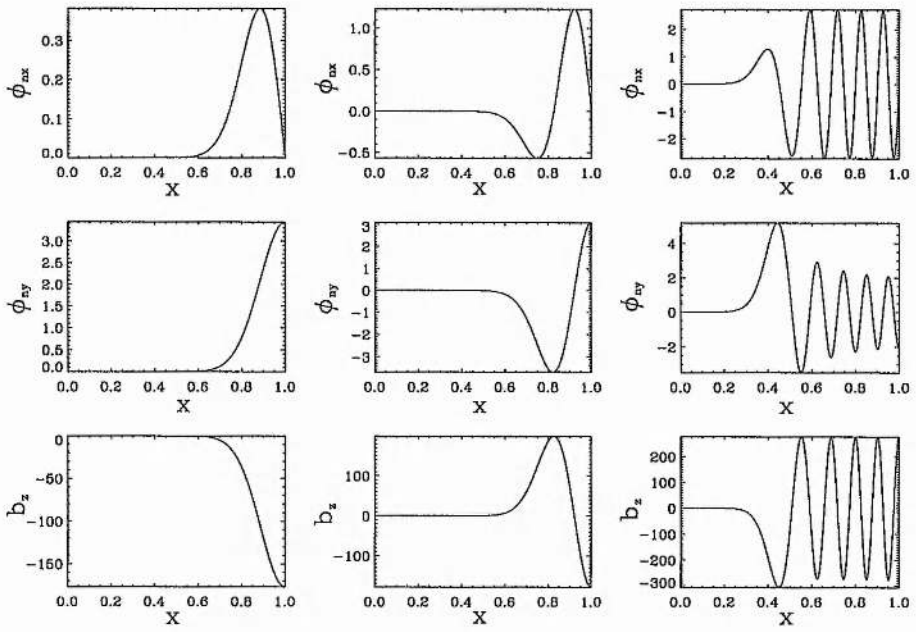

Figure 3.10: The first, second and tenth "fast" (large b_z) eigenmodes for $\lambda = 50$ and $N = 100$.

In Figure (3.11) we plot the "Alfvénic" eigenmodes for $n = 25, 50, 75$ for the same parameters. These continuum modes are seen to be still clearly singular. Now the ϕ_{nx} modes adopt a more Dirac delta function like character (probably generated by a localised logarithmic term) and have no apparent discontinuity. This most likely occurs as a result of all the 'fast" eigenfrequencies being far removed from the continuum, and hence removing the discontinuity associated with resonance absorption. The ϕ_{ny} modes retain their $1/x$ dependence, and despite the singular behaviour of ϕ_{nx} and ϕ_{ny}, the form of b_z remains smooth and non-singular. It is also interesting to note that the continuum modes are beginning to exhibit non-resonant decoupled field line oscillation behaviour, in accord with the decoupled $\lambda \to \infty$ modes described by Dungey (1967) and Radoski (1967)

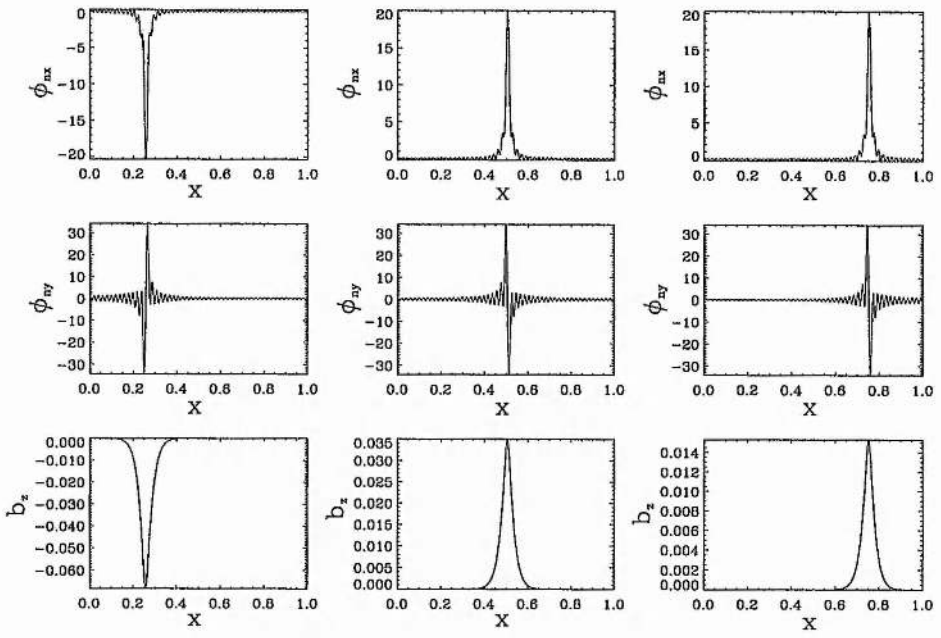

Figure 3.11: The $n = 25, 50, 75$ continuum (low b_z) modes for $\lambda = 50$ and $N = 100$.

3.5.4 $\lambda \to \infty$ Normal Modes.

As $\lambda \to \infty$, the governing equations (2.7) and (2.8) approach an asymptotic limit whereby the poloidal (ξ_x) component of the waves looses its global eigenmode character and is governed by the decoupled local poloidal Alfvén frequency of each field line. For the case of the box geometry which we have assumed, both the local poloidal (ξ_x) and toroidal (ξ_y) natural Alfvén frequencies are identical - $\omega_A(x)$. In more complicated geometries, such as a dipole, the scale factors of the background field introduce an asymmetry into these two eigenfrequencies.

For $\lambda \to \infty$, the poloidal waves can be expected to oscillate with $\omega_A(x)$, and to experience phase mixing (we discussed this for the case of toroidal, low λ waves in section (2.4.3)) (Dungey, 1967; Radoski, 1967). This behaviour can be illustrated by taking the $\lambda \to \infty$ limit of equation (2.8), to give the asymptotic result that

$$\frac{\partial \xi_x}{\partial x} + i\lambda \xi_y = -b_z \sim \frac{1}{\lambda} \tag{3.62}$$

Substituting this result into equation (2.7) gives the simple equation

$$\frac{1}{v_A^2(x)}\frac{\partial \xi_x}{\partial x} + k_z^2 \xi_x = 0 \tag{3.63}$$

which has the $\lambda \to \infty$ poloidal phase mixing solution given by

$$\xi_x \sim A\exp(i\omega_A(x)t) + B\exp(-i\omega_A(x)t) \tag{3.64}$$

i.e., independent field line oscillations at the local $\omega_A(x)$.

In Figure (3.12) we plot the form of the $n = 25, 50, 75$ ($N = 100$) modes for $\lambda = 10000$ and $A^2 = 1.0$, $B^2 = 0.9$ and $k_z = 2.0$. These eigenmodes are now dominated by poloidal (ξ_x) motions, they are localised in x, and are essentially incompressible. The

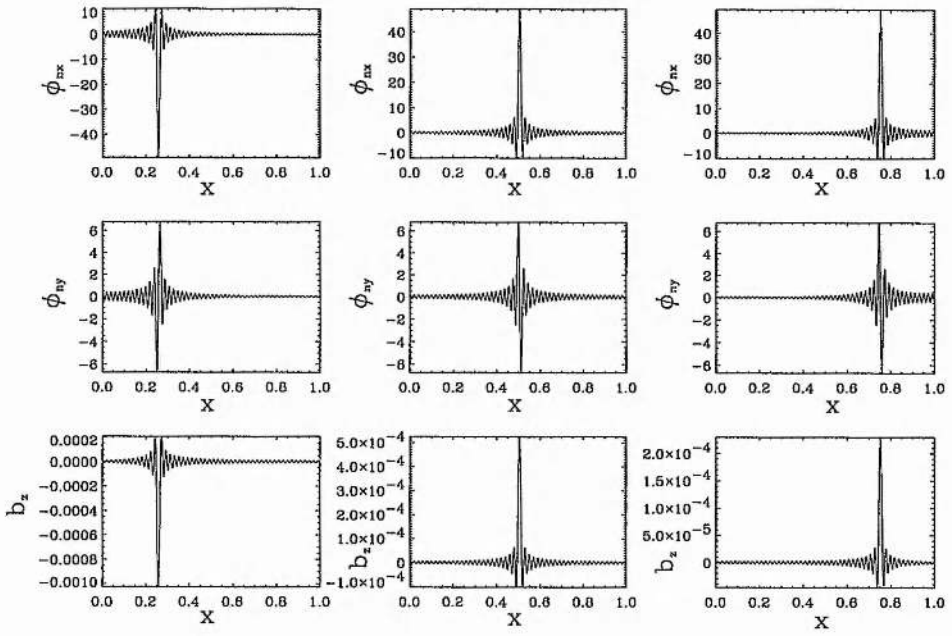

Figure 3.12: The $n = 25, 50, 75$ continuum modes for $\lambda = 10000$ and $N = 100$. These modes have small b_z and are essentially Alfvénic.

eigenmodes for $n = 125, 150, 175$ are shown in Figure (3.13), for the same parameters. In contrast, these modes are dominated by toroidal (ξ_y) motions, and since $\lambda \to \infty$ they are very strongly compressible ($b_z = -(\partial \xi_x/\partial x + i\lambda \xi_y)$) and have very high eigenfrequencies determined by $\omega^2(x) \approx \lambda^2 v_A^2(x)$. Increasing λ still further (towards ∞) continues this trend towards generating a set of purely incompressible $b_z \sim 0$ poloidal wave eigenmodes oscillating as decoupled field lines (c.f. Dungey (1967) and Radoski (1967)) and a set of

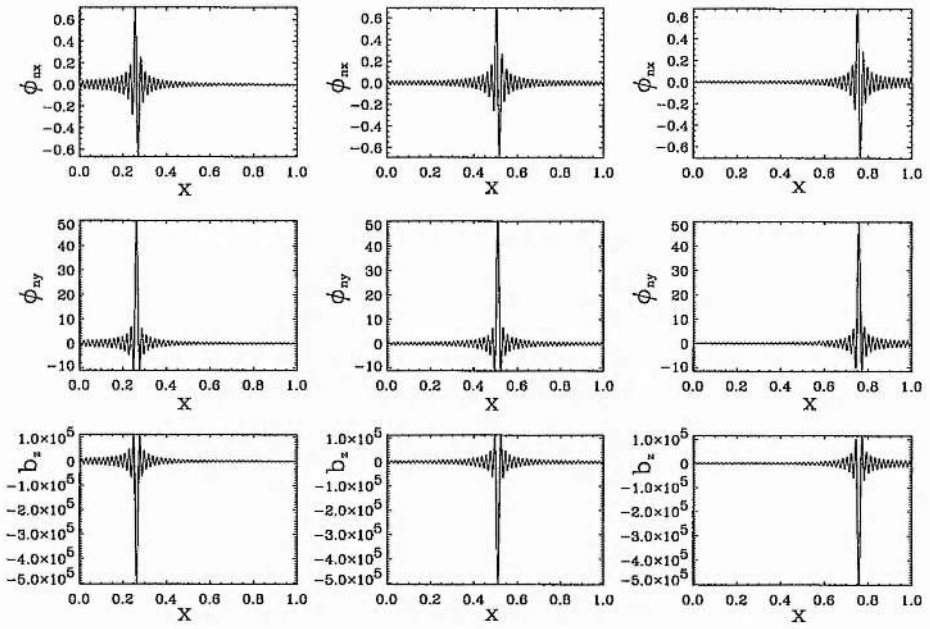

Figure 3.13: The $n = 125, 150, 175$ high b_z modes for $\lambda = 10000$ and $N = 100$.

$b_z \sim \infty$ eigenmodes.

The localised form of these Alfvénic type modes (and the continuum eigenmodes in section (3.5.3)) has interesting consequences for the temporal evolution of initially large λ poloidally polarised waves in inhomogeneous plasmas. This is discussed in detail in Chapters 5 and 6.

Chapter 4

Temporal Evolution of Resonant Waves.

4.1 Introduction.

In this chapter[1] we consider the temporal evolution of the resonant coupling between fast and Alfvén waves. As we have discussed in the previous chapter, with the prescription for plasma displacements given in equation (2.1), when the "azimuthal" wavenumber $\lambda \neq 0$ or ∞, the decoupled fast and Alfvén waves become inexorably coupled to each other.

Here, we are interested in determining the time dependent behaviour of an inhomogeneous plasma which has an Alfvén frequency continuum $\omega_A(x)$ and which contains the eigenfrequency of a $\lambda = 0$ decoupled discrete fast eigenmode. When $\lambda \neq 0$, and is $O(1)$, compressional energy which initially resides in the ξ_x displacements can resonantly drive Alfvénic oscillations on those field lines around positions defined by $\omega_n = \omega_A(x)$.

The evolution of these inhomogeneous plasma systems has been subjected to much theoretical (both analytical and numerical) study in the contexts of solar coronal heating (e.g., Poedts et al. (1990)), laboratory fusion plasma heating (e.g., Hasegawa and Chen (1974) and Hasegawa and Chen (1976)) and in describing magnetic pulsations in the Earth's magnetosphere (e.g., Southwood (1974) and Kivelson and Southwood (1986)). Many important physical mechanisms are at work in these inhomogeneous systems, and we briefly

[1]Based on Mann, I.R., A.N. Wright, and P.S. Cally, "Coupling of Magnetospheric Cavity Modes to Field Line Resonances: A Study of Resonance Widths", *J. Geophys. Res.* , (1995), in press.

discuss them here.

As we have mentioned in Chapter 3, these systems are generally governed by singular differential equations (Barston, 1964; Sedláček, 1971a; Adam, 1986), having singularities which may be associated with the accumulation of energy at a resonance, and the generation of the fine scales which are necessary if they are to be utilised as solar or laboratory plasma heating mechanisms. In general, the accumulation of energy at a resonance is referred to as resonant absorption. In the resonant absorption process, the plasma is driven with a monochromatic driving frequency ω_d. In the laboratory, this usually takes the form of an external antenna (e.g., see Poedts et al. (1990)), whilst in the solar coronal loop case the plasma is driven at the loop photospheric footpoints by some assumed dominant part of the frequency spectrum of granular or super-granular motions. In the magnetosphere, the original work on resonant absorption proposed that Kelvin-Helmholtz vortices travelling on the magnetopause surface would couple to field lines having the same natural frequency, deep within the magnetosphere. This explained the ground magnetometer observations of pulsations having a localised structure in latitude (Southwood, 1974; Chen and Hasegawa, 1974a; Chen and Hasegawa, 1974b).

In addition to resonances being driven by evanescent (surface) waves, or by incident travelling fast waves driven from an external plasma boundary, it was subsequently realised that in a plasma system with strongly reflecting boundaries, standing global wave modes could be set up. Kivelson et al. (1984) first proposed that this could occur in the Earth's magnetosphere. These global modes would be excited by the incident solar wind, and adopt a standing nature between an outer boundary (often assumed to be the magnetopause) and a turning point in the body of the magnetosphere (these are analogous to the global, low λ, dominantly ξ_x eigenmodes discussed in Chapter 3). If these modes have frequencies which lie inside the natural Alfvén frequency continuum, then they can resonantly drive pulsations (Kivelson and Southwood, 1985). In an entirely analogous way, global modes can become trapped (ducted) inside solar coronal loops (flux tubes) and similarly drive resonances which then heat the coronal plasma (e.g., Steinolfson and Davila (1993)).

Recently, the importance of this global mode behaviour has been stressed further by Wright and Rickard (1995). In their study, they drove an inhomogeneous plasma system with a random external driver. The effect of the global (cavity) modes was to filter the incident broadband spectrum so that the internal plasma response was dominated by the global mode eigenfrequencies ω_g. These global modes could then drive resonances at the

frequency ω_g in an entirely similar way to the monochromatically driven studies (having a driving frequency ω_d), the only difference being that ω_g need not be the dominant driving frequency. Hence the well known results from monochromatic normal mode studies can be expected to be equally valid in the more natural randomly driven situation.

The inhomogeneous coupled system which we are considering clearly has singular eigenmodes, as discussed in Chapter 3, whilst the physical wave fields remain well behaved in time. It is interesting to note that the growth of energy at the resonance in time can be considered purely in terms of the independent oscillations of the individual singular eigenmodes which were used to construct the displacements corresponding to the initial conditions. Instead of viewing the system as being one whereby fast waves drive Alfvén waves (as is often the case in the magnetospheric literature, using the terminology of the decoupled wave modes as the reference point), you can equally well view the evolution of the resonant interactions in a purely mathematical way. Here, the combined oscillations of the eigenmodes "reveal" the energy at the resonant location as each of the eigenmodes oscillates with its frequency ω_n.

In this chapter, we consider the temporal evolution of an undriven inhomogeneous plasma cavity. The results which we present could be applied to many of the inhomogeneous plasma systems which we have just mentioned, although we choose to interpret them in the context of magnetospheric pulsations.

4.2 Compressible Verses Incompressible Plasma Resonant Absorption.

As a prelude to our compressible plasma results, in this section we briefly discuss the relationship between resonant absorption in compressible and incompressible plasmas. Both these cases are governed by similar singular differential equations; both can exhibit phase mixing; and both possess quasi-mode behaviour whereby global mode energy is accumulated at a resonance.

In an incompressible plasma, the only modes of oscillation which are available in an isolated inhomogeneity are the Barston modes. Consequently, an initial disturbance such as $\xi_x = \sin \pi x$ will phase mix in time (see Cally (1991) section 2). The oscillations maintain a constant total energy (the plasma is ideal and hence has no dissipation present), however

energy is propagated towards finer and finer scales. Asymptotically in time, their ξ_x amplitude decays as t^{-1}, due to the logarithmic singularities which exist in the governing Barston eigenmodes (Barston, 1964; Cally, 1991). In the incompressible case the perturbations ξ_x and ξ_y are decoupled, and a solution for ξ_y can be found from the ξ_x solution by using the relation $\nabla.\mathbf{v} = 0$. Hence, $ik_y\xi_y = -\partial\xi_x/\partial x$, and the amplitude of the incompressible ξ_y oscillations asymptotically approaches a constant (Uberoi, 1995).

In a compressible plasma, however, ξ_x motions can have compressional normal modes which have a global nature, existing across the entire x domain. Consequently, in a system where all the global eigenfrequencies lie outside the continuum, an initial condition such as $\xi_x = \sin \pi x$ can be synthesised from the first few global eigenmode harmonics, and these subsequently simply oscillate in time. In this case, the initial conditions are generated from non-singular eigenmodes and hence no phase mixing results. If some of the global eigenfrequencies lie inside the continuum, then the initial global mode energy may be accumulated at the resonance. This absorption is due to the singularities in the coupled global eigenmodes, and can be considered to be due to the singular eigenmodes being used to re-constitute the initial conditions. The ξ_x logarithmic singularities (in $\phi_{nx}(x)$) allow phase mixing in ξ_x to proceed in time around the resonant location, and for their amplitude to decay as in the imposed incompressible studies of Cally (1991) - see section (4.4.5). Initial conditions comprising of purely ξ_y motions exhibit phase mixing in time, however they are not subject to the t^{-1} decay which the incompressible ξ_x phase mixed solutions experience.

Clearly, the solution to the initial value problem in compressible inhomogeneous plasmas has a variety of interesting features which are not present in the incompressible case.

4.3 Observations of Magnetospheric FLRs.

Magnetic pulsations are regularly observed by both space-borne and ground-based magnetometers, in the form of Ultra-Low Frequency (ULF) waves standing on magnetic field lines. The Doppler signatures of these pulsations are also often observed by HF radar at the ionospheric footpoints of oscillating field lines.

Dungey (1954) and Dungey (1967) first suggested that pulsations were standing Alfvén waves on dipolar field lines (toroidal modes). He also identified fast poloidal compressional waves, which should propagate across the background magnetic field, and

subsequently completed the first decoupled studies of these modes. As we have previously noted, Southwood (1974) and Chen and Hasegawa (1974a) then independently presented the first attempts at a full theoretical analysis of the coupled pulsation problem, whereby waves were driven by Kelvin-Helmholtz vortices travelling on the magnetopause. Models of this type, however, often require excessively high magnetosheath velocities to explain the observed pulsations (Hughes, 1994).

Later treatments invoked global fast magnetospheric modes, driven by sudden impulses in the solar wind, to drive pulsations (Kivelson et al., 1984; Kivelson and Southwood, 1985). This phenomenon has been subjected to much theoretical and numerical modelling (Kivelson and Southwood, 1986; Allan et al., 1986b; Inhester, 1987; Kivelson and Southwood, 1988; Zhu and Kivelson, 1988; Lee and Lysak, 1989; Wright, 1992b) and has been used to predict the frequencies of the cavity mode harmonics, and hence the frequencies of the observed driven nightside/early morning Pc5 Field Line Resonances (Samson et al., 1992b; Samson et al., 1992a; Harrold and Samson, 1992; Walker et al., 1992; Ruohoniemi et al., 1991). However, a little known paper by Radoski (1976), considered the coupling of cavity modes to Alfvén resonances numerically well before 1985. His early paper predicted many quantitative features which are now well known, his work has many similarities to the discussions in this Chapter, and the interested reader is referred to it.

Recent papers by Wright (1994a), Rickard and Wright (1994), and Rickard and Wright (1995) have considered the propagation of compressional modes down a waveguide. The waveguide models an open magnetospheric cavity where energy can propagate downtail. They conclude that compressional waves, with a low azimuthal wavenumber k_y, will propagate only slowly downtail, whilst high k_y modes propagate away quickly downtail. These low k_y modes will thus be able to act as long lived and coherent drivers for Alfvén resonances, and hence cavity models, using a small k_y prescription, may still provide a good approximation for modelling coupled pulsation phenomena even when the cavity is open. After all, a waveguide solution may be synthesised from a sum over cavity solutions with suitable k_y values.

Much work has been completed on ULF waves in the Earth's magnetosphere over the last 30 years and readers are referred to the reviews by Southwood and Hughes (1983), Hughes (1983), Hughes (1994), and Wright (1994b) for further details. Both the "Kelvin-Helmholtz" and the "cavity/waveguide" mechanisms may be responsible for coupling solar wind energy into ULF pulsations, the dominant one at any time probably depending upon

solar wind and magnetosheath conditions. It is probably impossible to explain all data with solely one of these mechanisms. Here we concentrate upon the cavity model. We use numerical and analytical modelling to address the time-dependent growth of pulsations and the question of Field Line Resonance (FLR) widths.

The latitudinal extent of FLRs is important for two reasons. Whilst Pc5 pulsations observed by ground based magnetometers show frequencies corresponding to theoretically predicted cavity mode frequencies, satellite observations often show several pulsation packets with finite width in L-shell, which suggests that they might have been driven by a broadband source, such as a solar wind impulse incident on the magnetosphere. If cavity modes do drive these pulsations, then theory must explain how they can drive Alfvén waves with a finite frequency bandwidth. Satellite observations show that Pc5 ULF pulsations often occur in spatially (L-shell) confined wave packets with typical widths which can be as small as $\sim 0.5R_E$ (Mitchell et al., 1990; Lin et al., 1992). Magnetometer observations of low latitude pulsations inside the plasmasphere also found widths as small as 0.2 R_E (Ziesolleck et al., 1993), which were believed to be driven by tunnelling global modes (Allan et al., 1986a; Zhu and Kivelson, 1989). Radar measurements of high latitude FLRs found equatorial resonance widths of $\sim 0.5R_E$ using the STARE radar (Walker et al., 1979), and ionospheric widths of $\lesssim$ 45 km, mapping to an equatorial width of $\sim 0.35R_E$, using the Goose Bay HF radar (Walker et al., 1992).

Also, if pulsation scales can narrow to kinetic scale lengths (including where single fluid MHD breaks down), then mode conversion from the MHD wave mode to kinetic Alfvén or electron inertia waves may occur. Previous numerical models by Inhester (1987) and Rankin et al. (1993) found that kinetic effects could be important within the lifetime of pulsations, and hence excitation of these wave modes might explain observations of auroral arcs which show that their electron precipitation can be modulated at the frequency of a coexisting FLR (Samson et al., 1991b; Samson et al., 1992b; Xu et al., 1993). Walker et al. (1992) suggest resonances can be excited so that they take on what they call a "packet structure" in time. Here the amplitude of the resonance grows over several cycles in response to the cavity mode driver, then decays due to dissipation once this forcing is removed. For these kinetic/two fluid effects to become important, small scales must be reached within the lifetime of this packet.

Pulsations may be damped by a variety of mechanisms, and this can be important both in determining their lifetimes, and in generating finite latitudinal widths. The

dominant pulsation energy dissipation mechanism is generally considered to be ionospheric. FLRs drive strong field aligned currents (FACs) which are closed by Pedersen currents flowing in the ionosphere. These Pedersen currents then damp the pulsations by resistive dissipation at the ionosphere. However, for dayside and active nightside conductivities, this dissipation may be small and allow the FLRs to be relatively long lived ($\sim 10 - 30$ cycles).

Using our numerical model (as described in Chapter 2) we investigate both the pulsation energy density widths developed by FLRs in space, and whether sufficiently small latitudinal scales can be developed within FLRs so that kinetic effects become important.

4.4 Numerical Results.

To fully investigate the coupling of magnetospheric cavity modes to FLRs we choose $\lambda \neq 0$. The boundaries of the simulation domain at $x = 0, 1$ (see Figure (2.1)) are again perfectly reflecting, and could correspond to various cavities such as those between the plasmapause and the magnetopause (in the plasmatrough), or the Earth and the plasmapause (in the plasmasphere), or a combination of the two. We take the initial conditions to be the state where only the first ξ_x Fourier mode is excited and at rest, and where no energy resides in the Alfvén continuum (i.e. set $a_1(0) = 1, a_{m\neq 1}(0) = 0$ and $b_m(0) = \dot{a}_m(0) = \dot{b}_m(0) = 0$, where $\dot{a}_m$ denotes da_m/dt). We select values of the parameters $A^2 = 1.0$, $B^2 = 0.9$ and $k_z = 2.0$ so that only the fundamental fast cavity mode eigenfrequency lies within the Alfvén continuum, and so that the Alfvén resonance occurs well within the magnetospheric box. This allows the resonance growth to be studied without the edges of the box significantly altering its structure. With these chosen parameters, the fundamental cavity eigenmode has a normalised angular frequency $\omega \approx 3.574$. The higher harmonic cavity eigenfrequencies lie outside the Alfvén continuum.

As the system evolves, energy from this initial state couples to the Alfvén continuum and excites the field lines resonant with the fundamental fast cavity mode. Asymptotically in time, the energy which is initially resident in the fast mode will ultimately reside in narrow resonant Alfvén fields (Radoski, 1974). By varying the parameter λ, the strength of the coupling between the two wave modes is altered, with maximum coupling occurring at some low azimuthal wave number (Kivelson and Southwood, 1986; Zhu and Kivelson, 1988).

4.4.1 Fast and Alfvén Mode Interaction.

For small values of λ, the displacements ξ_x and ξ_y are the dominant components for the fast and Alfvén modes respectively, and this provides a useful distinction for discussing our results. We find that the fundamental cavity mode has approximately 16% of its amplitude in the second Fourier mode, as well as around 1% in the third. Hence its major amplitude component ($\sim 83\%$) corresponds to the fundamental Fourier mode. By imposing the above initial conditions (comprising of only this Fourier mode) and choosing $\lambda = 1.0$, we can approximate a strongly coupled fundamental cavity eigenmode driver. There will, of course, also be small components of higher cavity eigenmodes present which will not be resonantly coupled to the Alfvén continuum.

Figure (4.1) shows snapshots of the driven ξ_y perturbations at two times. In response to the fast mode driver, a driven field line resonance grows at the expected position ($x \approx 0.22$), where $\omega_A(x) = 3.574$. This figure also shows how the resonance width narrows

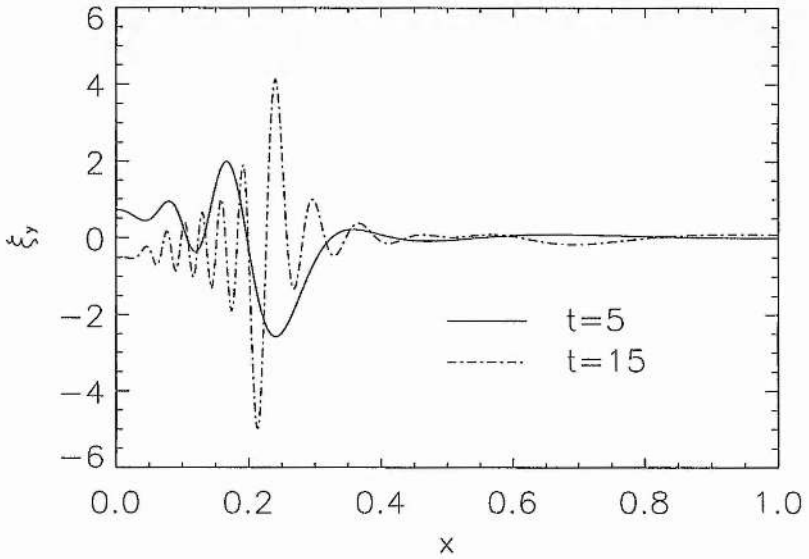

Figure 4.1: The development of ξ_y perturbations at the resonance in response to the fundamental x Fourier mode driver, for $\lambda = 1.0$. The solid line shows the ξ_y perturbations at $t = 5$, and the dotted-dashed line at $t = 15$. The growth in amplitude and the narrowing of scales in x, due to phase mixing, are clearly shown.

whilst the Alfvén oscillations grow in amplitude at the resonant field line. At both of these times, the resonance is already clearly showing a localised structure in x.

To further illustrate this temporal evolution, we use equation (2.38) and plot the

energy density in the system as a function of both x and time (See Figure (4.2)). The plot shows the growth of the Alfvén resonance in response to the initial fast mode. As this system evolves in time, a fast mode pulse propagates backwards and forwards across the box. This pulse sets up a standing global cavity eigenmode confined to large x, as expected (between the magnetopause and the turning point), and both couple energy into the Alfvén resonance.

The energy envelope of the driven resonance is narrow, centred on $x \approx 0.22$, and its width decreases in time. Simultaneously, the amplitude of the fast cavity mode decreases as it is mode converted to Alfvén waves, driving a resonance with increasing amplitude. Ultimately, the resonant amplitude saturates, once all the fundamental cavity mode energy has been transferred. The remaining fast mode energy, confined to large x, continues to oscillate but does not drive FLRs. This remnant fast mode energy represents the proportion of the initial ξ_x Fourier mode which existed in cavity eigenmodes other than the fundamental, and whose eigenfrequencies lie outside the Alfvén continuum.

4.4.2 Temporal Evolution of Resonance Energy Widths.

From Figure (4.2), it is clear that the energy width of the resonance narrows in time. Previous theoretical studies have concentrated on the expected temporal asymptotic resonance width. Considering the fast mode to have a complex frequency with an imaginary component ω_{fi}, Southwood and Allan (1987) postulated that the Alfvén wave response would be of the form

$$\xi_y \sim \xi_{y0}\left[\exp(i(\omega_{fr} + i\omega_{fi})t) - \exp(i\omega_A(x)t)\right]. \tag{4.1}$$

Using a Taylor expansion for $\omega_A(x)$, they derived a resonance width ΔX of

$$\Delta X \sim \omega_{fi}\left(\frac{d\omega_A(x_r)}{dx}\right)^{-1}. \tag{4.2}$$

At $x = x_w$ this gives,

$$\xi_y = \xi_{y0}[1 - \exp(-\omega_{fi}t)]\exp(i\omega_{fr}t). \tag{4.3}$$

Thus at the resonance, the Alfvén waves which are represented by ξ_y, grow on a timescale of $\tau_{fi} = {\omega_{fi}}^{-1}$, whilst the driving cavity mode represented by ξ_x decays.

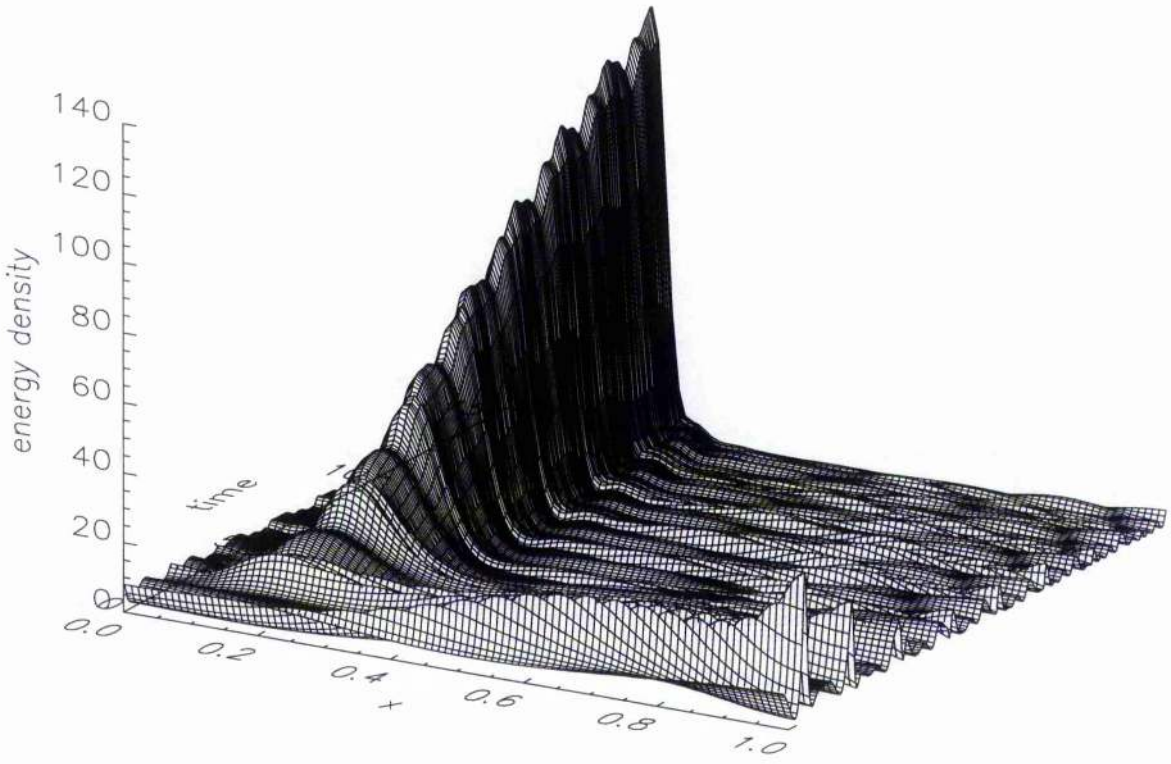

Figure 4.2: Surface plot of the energy density (arbitrary units) of the wave modes as a function of both x and time (up to t=15) for a strong coupling case with $\lambda = 1.0$. The initial fast mode $\xi_x = \sin x$ perturbation sends a fast mode pulse propagating across the box in the x direction. This fast mode energy becomes ducted at large x (in the low Alfvén speed region), but is quickly damped as it drives a large amplitude Alfvén resonance around $x = 0.22$. The energy width of the resonance is seen to narrow in time as it is driven by the fast mode.

From this analysis, just off resonance, the ξ_y response would be expected to show beating between the driver frequency ω_{fr} and the natural Alfvén frequency of the oscillating field lines $\omega_A(x)$. This beating would occur on a timescale much shorter than τ_{fi}. On timescales longer than τ_{fi}, the driving cavity mode has decayed. Hence the Alfvén oscillations should then settle down to vibrate with their natural frequency $\omega_A(x)$ (Allan and Poulter, 1989).

We can continue this analysis further by examining the temporal evolution of this width. As we have discussed in Chapter 3, by assuming an $e^{-i\omega t}$ dependence, equations (2.7) and (2.8) can be combined to give a single equation for ξ_x - equation (3.56). The usual procedure for solving equation (3.56) involves adopting a field aligned wavenumber k_z, which has both real and imaginary components. This has the required effect of removing the singularity, and allows for Poynting flux to be driven towards the ionospheres to represent dissipative losses there. Specifying $k_z = k_{zr} + ik_{zi}$ then equation (3.56) can then be written, in the vicinity of the resonance, as equation (3.57) (see Chapter 3).

A problem exists with this formulation, as noted by Kivelson and Southwood (1988) : the field aligned currents of an Alfvén wave are closed by Pedersen currents in the ionosphere, and thus k_{zi} is determined by Σ_P - the height integrated Pedersen conductivity. The fast mode interacts with the ionosphere in a different fashion to the Alfvén wave, typically being better reflected and having a smaller k_{zi}. Thus a problem arises in a coupled fast-Alfvén wave solution - it is impossible to choose a single value for k_{zi} which is appropriate near the resonance (dominated by Alfvénic perturbations), and away from the resonance (dominated by the fast mode). In the literature, k_{zi} is chosen to be that corresponding to the Alfvén wave in all studies we are aware of.

Alfvén waves naturally drive field aligned currents and by imposing an imaginary k_z, the damping of these Alfvén waves by currents flowing in the resistive ionospheres can be readily modelled. However, imposing the same boundary conditions on the fast mode waves forces them to similarly drive large Pedersen currents. This would cause the fast modes to become damped directly by Joule dissipation, when in fact they shouldn't be significantly damped by this mechanism. This is because the Pedersen currents driven by the fast modes are several orders of magnitude less than those driven by Alfvén waves. In fact the fast mode electric field should be subject to the boundary condition $E_M \approx 0$, where E_M represents the wave electric field at the ionosphere (Kivelson and Southwood, 1988).

In order to avoid potentially unrealistic effects, we choose to adopt a more phys-

ical picture for "damping" the fast mode. In an entirely analogous way, we remove the singularity in equation (3.56) by adopting a complex frequency rather than a complex k_z. This represents the oscillating cavity mode naturally, which is decreasing in amplitude as it couples to the Alfvén resonance (c.f. the quasi-modes discussed in Chapter 3 - see Barston (1964), and Sedláček (1971a)). If we assume that $K^2(x)$ $(= \omega^2/v_A^2(x))$ is complex, due to the complex cavity mode frequency, we can write

$$\omega_f = \omega_{fr} - i\omega_{fi}, \tag{4.4}$$

with the negative sign so that the $e^{-i\omega t}$ dependence "damps" the cavity mode. This assumes that the entire fast mode will decay uniformly as it drives the Alfvén resonance, which should be a particularly good approximation when λ is small (Wright, 1992a). This gives equation (3.57), with the damping now defined by

$$\epsilon = \frac{-2\omega_{fi}\omega_{fr}}{v_A^2(x)\,(dK^2(x)/dx)}. \tag{4.5}$$

With this approach, the cavity mode is damped due to coupling to the Alfvén resonance rather than direct ionospheric dissipation. We can hence consider the width of the Alfvén resonance, in the absence of ionospheric dissipation, to be determined by which field lines the cavity mode actually drives.

This interpretation is similar to that considered by Hollweg (1987) and Hollweg and Yang (1988). In their analysis, they considered the width of a resonance which would be driven by a surface wave whose frequency lay within the Alfvén continuum generated by an inhomogeneous Alfvén speed profile. By defining the surface waves lifetime as t_d, they considered that waves would be driven on a particular field line if the driving surface wave oscillations and the local Alfvén frequency of oscillation remained in phase for the lifetime of the surface wave. Using (essentially arbitrary) criteria of $\pi/2$ for the permitted phase difference which develops, then for an Alfvén wave to be resonantly driven they require

$$|kv_A(x) - \omega|\, t_d \leq \pi/2. \tag{4.6}$$

Expanding $v_A(x)$ in a Taylor series about the resonance, the resonance width is given by

$$\Delta X \sim \pi(k_z v_A'(x) t_d)^{-1} = \pi(\omega_A'(x) t_d)^{-1}. \tag{4.7}$$

This is entirely analogous to considering the cavity mode resonance width to be given by $\omega_{fi}(\omega'_A(x_w))^{-1}$ (equation (4.2)), since $t_d \sim 1/\omega_{fi}$ (Southwood and Allan, 1987).

However, to calculate the temporal evolution of this resonance width, we can examine the frequency bandwidth of the cavity mode driver at any time τ_0 by taking the Fourier transform of the ξ_x time history, to give $F(\omega)$

$$\begin{aligned} F(\omega) &= \int_0^{\tau_0} f(t)e^{-i\omega t}dt = \int_0^{\tau_0} \xi_{x0}e^{-\omega_{fi}t}e^{i(\omega_{fr}-\omega)t}dt \\ &= \xi_{x0}\left[\frac{\exp\left[i(\omega_{fr}-\omega)-\omega_{fi}\right]\tau_0 - 1}{\left[i(\omega_{fr}-\omega)-\omega_{fi}\right]}\right]. \end{aligned} \tag{4.8}$$

(Bracewell, 1986). To remove the phase effects of $F(\omega)$, we can consider the bandwidth of the driver in terms of energy or power (i.e. in terms of displacements squared). We can thus write

$$\begin{aligned} P(\omega) &= [F(\omega)]^* F(\omega) \\ &= \frac{\xi_0^2}{[\omega_{fi}^2 + (\omega_{fr}-\omega)^2]}(1 + e^{-2\omega_{fi}\tau_0} - 2e^{-\omega_{fi}\tau_0}\cos[(\omega_{fr}-\omega)\tau_0]) \end{aligned} \tag{4.9}$$

where $[F(\omega)]^*$ represents the complex conjugate of $F(\omega)$. Hence we have an analytic expression for the frequency spectrum in energy of the driving fast cavity mode.

Two different width regimes exist for the function $P(\omega)$:

i) Short Times ($\tau_0 \ll 1/\omega_{fi}$)

$$P(\omega) = \frac{4\xi_0^2}{[\omega_{fi}^2 + (\omega_{fr}-\omega)^2]}\sin^2[\frac{(\omega_{fr}-\omega)}{2}\tau_0]. \tag{4.10}$$

If $\omega_{fr} \gg \omega_{fi}$ then

$$P(\omega) \simeq \xi_0^2\tau_0^2\mathrm{sinc}^2\left((\frac{\omega_{fr}-\omega}{2})\tau_0\right) \tag{4.11}$$

where the sinc function (familiar from Fourier optics) is defined by $\mathrm{sinc}(x) = \sin(x)/x$.

ii) Asymptotic times ($\tau_0 \gg 1/\omega_{fi}$)

$$P(\omega) = \frac{\xi_0^2}{[\omega_{fi}^2 + (\omega_{fr}-\omega)^2]}. \tag{4.12}$$

This is a Lorentzian profile, and has a Full Width at Half Maximum (FWHM) of $\Delta\omega = 2\omega_{fi}$.

In terms of the above analysis, the energy width of the resonance region will be determined by the frequency bandwidth of $P(\omega)$. By calculating the FWHM frequency bandwidth $\Delta\omega$ at any time τ_0, we can predict the physical energy width of the resonance ΔX_E at this time using the relation

$$\Delta X_E(\tau_0) = (\Delta\omega(\tau_0)/\omega_A{}'(x_w)) \tag{4.13}$$

where $' = d/dx$.

Considering the spectrum of individual plasma displacements by taking the square root of $P(\omega)$, suggests that the asymptotic FWHM of the FLRs, seen in terms of their fields, will be a factor of $\sqrt{3}$ greater than ΔX_E. We can denote this length by L_{fi}. This difference between displacement and energy FWHM can be seen clearly in our numerical results, shown later.

Consequently, we can predict the temporal evolution of ΔX_E which we expect to see in our numerical model. We do this by solving the transcendental equation for $\Delta\omega$ using the function $P(\omega)$, inserting the value of ω_{fr} (the fundamental cavity mode eigenfrequency, calculated using the Runge-Kutta routine (see section (3.3)) and a value for ω_{fi}.

Using the approximation that all fast mode oscillations can be described by a single complex frequency (see equation (4.4)), and energy conservation, we infer that the Alfvén energy (calculated on the basis of $\rho\dot{\xi}_y^2/2 + b_y^2/(2\mu_0)$), integrated across the entire magnetospheric box, would grow as

$$E_A(t) = E_{A0}(1 - \exp(-2\omega_{fi}t)). \tag{4.14}$$

Consequently, plotting $\ln\left(\frac{E_{A0}-E_A(t)}{E_{A0}}\right)$ against t, allows ω_{fi} to be calculated from the gradient.

The width calculated by the above ad-hoc method, ΔX_E, can then be compared to the widths measured directly from the results of the numerical solution - see Figure (4.3). In this Figure, we plot as solid lines the overall energy width of the resonance measured using the results from our numerical code, and show the width evolution which we expect on the basis of this Fourier analysis as dashed lines. This clearly shows how the energy width decreases as time evolves, and ultimately saturates to a constant value determined by the damping rate of the fast cavity mode. At early times the width is $\propto 1/\tau_0$, and is independent of ω_{fi}.

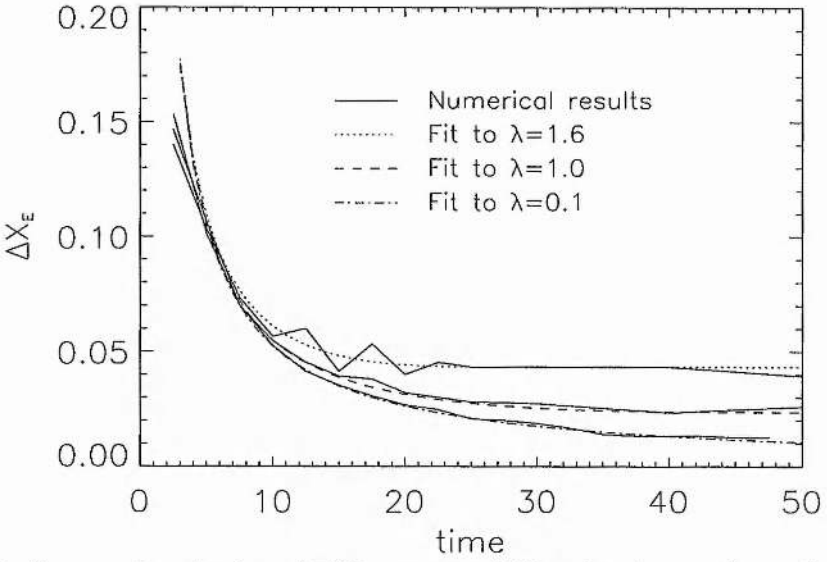

Figure 4.3: Temporal evolution of FLR energy widths. As time evolves, the energy width of the resonances ΔX_E in space is seen to narrow due to phase mixing, and asymptotically approaches the width due to the damping rate of the driving fast mode ω_{fi}. The solid lines show the widths as measured from the results of our numerical solution, and the dashed lines show the fit to these results based on our Fourier analysis where we assume the driving fast mode to have the form $\xi_x = \xi_{x0} \exp[-i(\omega_{fr} - i\omega_{fi})t]$.

It is clear that this simple analysis, whereby we assume that the energy width of the resonance is governed by the frequency bandwidth of the driver, matches our numerical results excellently. This is a new result, which predicts that the overall widths in L-shell of pulsations in the Earth's magnetosphere will evolve and narrow in time. Satellites crossing these L-shells should observe relatively broad resonances soon after a cavity mode has started to deposit its energy at the resonance. Observations of well established FLRs, long after the cavity mode has driven the resonance, should have a narrower saturated width given by equation (4.12). As stated above, these asymptotic widths will be determined by the damping rate of the cavity mode, which in the real magnetosphere will depend not only on their coupling rate to Alfvén waves (in our model governed by ω_{fi}), but also other cavity mode losses such as propagation downtail, into the polar cap, or out through non-perfectly reflecting boundaries such as the magnetopause.

We believe that analysis using this procedure can give valuable insight into why resonances adopt specific widths, and perhaps provide an important analytic tool when

considering the various driving mechanisms which have been proposed for exciting magnetospheric pulsations.

4.4.3 Fast Cavity Mode Coupling Rates.

Clearly, with our box model for the magnetosphere and within the framework of ideal MHD, the loss of energy from the cavity mode occurs only as a result of coupling to an Alfvén resonance. In a realistic magnetosphere, with additional fast mode energy losses, ω_{fi} may be slightly larger than the value adopted here. Once a suitable value of ω_{fi} has been estimated, the frequency bandwidth of the fast mode is determined. Consequently, this coupling rate has an important role to play in determining the energy widths adopted by resonances.

Using the method for obtaining ω_{fi} previously described, we can follow Kivelson and Southwood (1986) and Zhu and Kivelson (1988), and plot ω_{fi} verses the parameter $\lambda^2/\omega^{\frac{4}{3}}$ (we choose this parameter as our ordinate to facilitate comparison with previous studies which assumed a linear density profile and where a transformation to yield the equations of Budden (1961) generates the variable $\lambda^2/\omega^{\frac{4}{3}}$. See also Forslund et al. (1975)). For our study, we find that the maximum coupling rate occurs when our normalised (dimensionless) $\lambda = \lambda_{max} = 1.6$, which corresponds to $\lambda^2/\omega^{\frac{4}{3}} \approx 0.5$ (See Figure (4.4)). This gives a damping of $\omega_{fi}/\omega_{fr} = 0.06$, which means that the fast mode would damp on a timescale $\tau_{fi} = 2.65$ Alfvén periods. Consequently, resonances excited by this rapidly damped fast mode can develop narrow overall energy widths on the timescale of a few driving periods, as was suggested necessary by Walker et al. (1992).

Zhu and Kivelson (1988) found that using their box geometry with density proportional to x, the maximum coupling occured when the parameter $\lambda^2/\omega^{\frac{4}{3}} = 0.5$. Qualitatively our results agree well with their analysis (any differences being attributable to the different density profiles).

4.4.4 Phase Mixing Lengths.

From the analysis in the previous section, it is clearly possible for cavity modes to drive FLRs with a finite width in L-shell, encompassing resonant field lines with a range of natural Alfvén frequencies, as seen in satellite data (Mitchell et al., 1990; Lin et al., 1992).

It is well known that the coupling of fast and Alfvén MHD wave modes has many

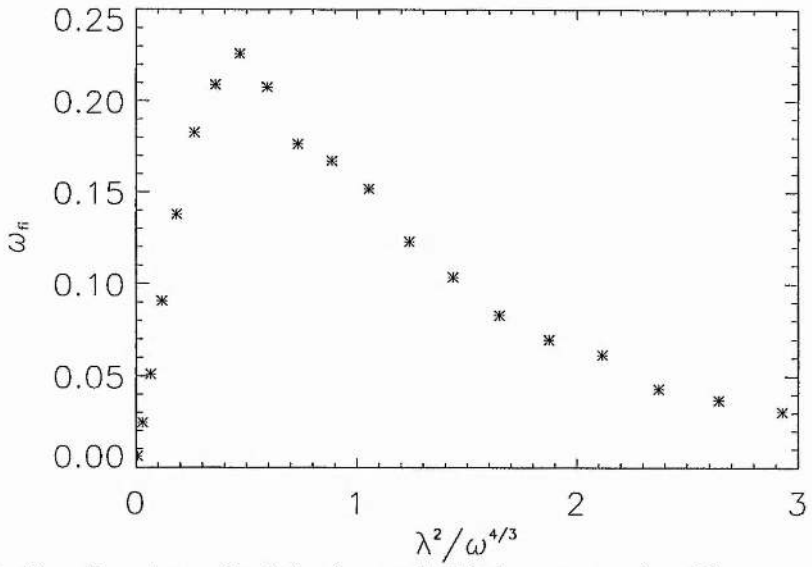

Figure 4.4: Coupling strength of the fast and Alfvén wave modes. We measure the coupling rate of the fast mode by ω_{fi}, and plot it against the parameter $\lambda^2/\omega^{\frac{4}{3}}$ using the results from our numerical code. Maximum coupling occurs where $\lambda \approx 1.6$. The coupling strength decreases on either side of the maximum giving the asymptotic decoupled limits at $\lambda = 0, \infty$.

analogies to the behaviour of a classical driven harmonic oscillator (see Wright (1992b); and Steinolfson and Davila (1993) for the case of cavity modes excited in solar coronal loops). Consequently, exactly on resonance where the real part of the cavity mode frequency matches the local Alfvén frequency ($\omega_{fr} = \omega_A(x)$), we expect to observe monotonic growth of Alfvén oscillations on a timescale of $\tau_{fi} = \omega_{fi}^{-1}$. Off resonance however (but still within $\Delta\omega$), we expect a beating Alfvén wave response due to the frequency mis-match between the cavity mode and the now slightly different natural Alfvén frequency of this particular field line. On timescales longer than τ_{fi}, once the driving cavity mode has decayed, the Alfvén oscillations should then settle down to vibrate with their own natural frequency $\omega_A(x)$ (Allan and Poulter, 1989).

Figures (4.5) and (4.6) reproduce this expected behaviour both on and just off-resonance using our numerical model. This response compares well with the previously published results of Allan and Poulter (1989) and Wright (1992b) for the magnetospheric case, and those of Poedts et al. (1990) and Steinolfson and Davila (1993) for the coronal loop case.

As a consequence of the inhomogeneous background natural Alfvén frequency in

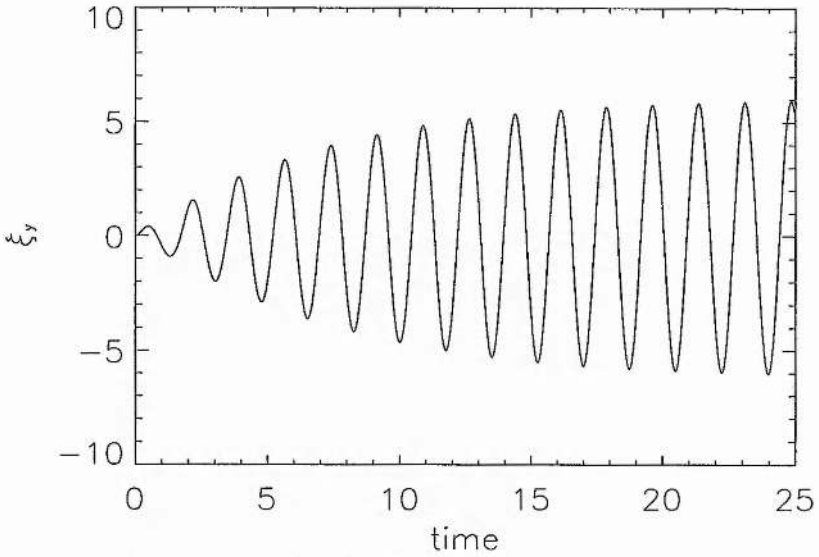

Figure 4.5: Growth of ξ_y perturbations in time exactly on resonance, at the position $x = 0.22$ for $\lambda = 1.0$, which represents a quite strong coupling case. The resonant amplitude grows smoothly to a maximum value which is attained once all the fundamental cavity mode energy has been transferred to the resonance.

the $\hat{\mathbf{x}}$ direction, we expect the perturbations within these radial pulsation packets, which are initially excited in phase, to drift out of phase with each other in time. This process is called phase mixing (Burghes et al., 1969; Heyvaerts and Priest, 1983) - see also section (2.4.4) (ii). Phase mixing continually reduces the scale length of the disturbance in time, and we can define the length scale reached after a time t as the phase mixing length $L_{ph}(t)$.

Considering an ideal solution of the form $\xi_y(x,t) = A(x)\exp(i\omega_A(x)t)$ and assuming that $\partial/\partial y = 0$, we can differentiate with respect to x to gain the local wavenumber $k_x(x)$. This gives $k_x(x) \approx \omega_A'(x)t$ (where $'$ denotes d/dx) and allows us to define $L_{ph}(t) = 2\pi\left(\omega_A(x)'t\right)^{-1}$; see equation (2.54).

Although the decoupled oscillation of each field line relies upon $\partial/\partial y = 0$, we shall see from our numerical model, that even when $\partial/\partial y \neq 0$ the scalelength of the solution in x is still dominated by the decoupled phase mixing length. This continual narrowing of spatial scales in time can be thought of as a wave propagating in modenumber space towards higher harmonics. Cally (1991) considered the speed of propagation of the outermost wavefront in this modenumber space for an incompressible plasma, and the concept is discussed in greater detail in Cally and Sedláček (1994).

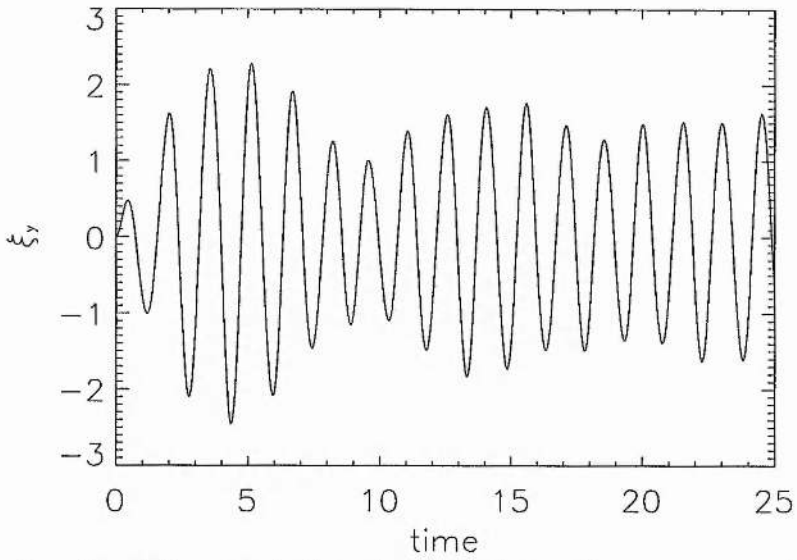

Figure 4.6: Growth of ξ_y perturbations in time at an off resonance position, again for $\lambda = 1.0$, showing the expected beating between the driving cavity mode frequency ω_{fr} and the natural Alfvén frequency $\omega_A(x)$, here at $x = 0.17$.

As finer scales develop, the Alfvén oscillations (ξ_y), develop very high gradients of $\partial\xi_y/\partial x$, associated with very strong field aligned currents j_z given by

$$j_z = (\nabla \times \hat{\mathbf{b}})_z = \left(\frac{\partial b_y}{\partial x} - \frac{\partial b_x}{\partial y}\right) = B_0 k_z \cos k_z z \left(\frac{\partial \xi_y}{\partial x} - i\lambda\xi_x\right), \tag{4.15}$$

where j_z is normalised. Figure (4.7) shows snapshots of the spatial structure of the energy density, the resonant Alfvén perturbation described by ξ_y, and the derived field aligned current for two chosen values of λ at one single time, $t = 45$.

The first column in Figure (4.7) shows results for a small value of λ (here taken as 0.1), where $t < \tau_{fi} \approx 330$. The system evolves so that at this time, the resonance energy width ΔX_E is small and of the order of L_{ph}, as are the displacement scales within the resonance. An almost singular resonance is excited with little obvious fine ξ_y structure visible beneath the energy envelope. This compares well with the full non-linear FLR resonance width results published by Rankin et al. (1993). In their model, they drive their resonances externally from an outer boundary with a ramped and then constant amplitude incident fast mode. We would expect this driver to be almost monochromatic and drive a very narrow resonance. Some small finite width is developed in their scheme due to

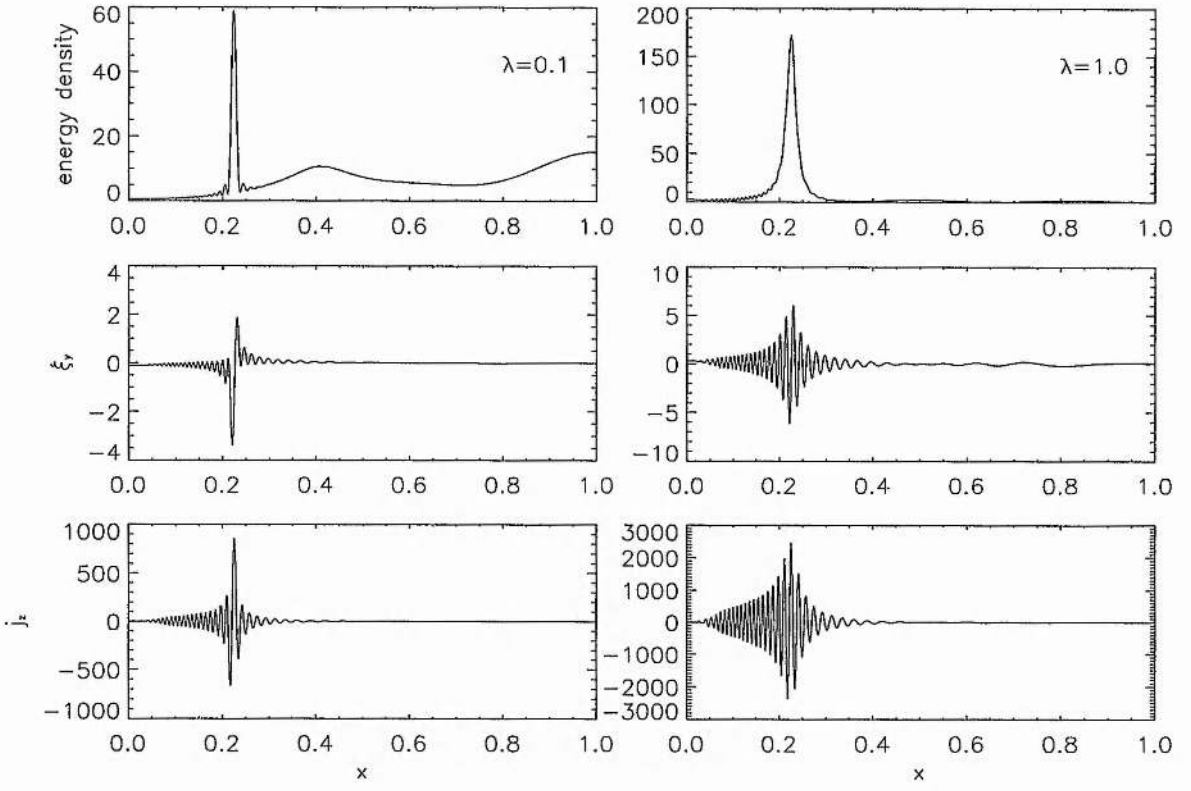

Figure 4.7: Energy density, ξ_y perturbation and j_z as a function of x at the time $t = 45$. Left Column: The $\lambda = 0.1$ case, where the coupling of the fast and Alfvén modes is weak. For this case $t < \tau_{fi} \approx 330$. Significant energy still resides in the fast mode at high x, both the energy and ξ_y have narrow widths $\sim L_{ph}$. Strong field aligned currents j_z have already been established at this time. Right column: The $\lambda = 1.0$ case, representing stronger coupling. This is a case where $t > \tau_{fi} \approx 7$. Here the energy width is broad and has saturated at the asymptotic width. However, the ξ_y has developed fine scales through phase mixing inside the energy envelope. In the second column, more energy has been transferred to the resonance and it has driven extremely strong field aligned currents (FAC's).

dissipation and non-linear processes which they included in their numerical code.

The second column of Figure (4.7), on the other hand, shows perturbations excited with a rather larger value of $\lambda = 1.0$, where $t > \tau_{fi}(\lambda) = 7$. In this case, the anticipated j_z and ξ_y fine scale spatial oscillations are clearly seen inside the now much broader energy envelope ΔX_E.

We can now see why the displacements show the two types of behaviour seen in Figure (4.7). For small coupling rates (here the $\lambda = 0.1$ case), the value of ω_{fi} is small and the time $\tau_{fi}(\lambda)$ is large (~ 330). Consequently, the energy envelope is still narrowing at $t = 45$, and has a width of order the phase mixing length (i.e., $\propto 1/t$).

For the stronger coupling rate, shown in the second column of Figure (4.7) ($\lambda = 1.0$), the energy width ΔX_E is wide, and this is reached in the now short time $\tau_{fi}(\lambda) \approx 7$. Now, $t \gg \tau_{fi}$, and the phase mixing length L_{ph} is much smaller than the overall pulsation width. Consequently, fine structure is revealed inside the resonance envelope.

If magnetospheric pulsations have lifetimes longer than τ_{fi}, they have time to evolve (phase mixing) fine structure within their energy envelope. Realistic spatial pulsation packets in the magnetosphere may contain several spatial oscillations and satellites crossing these pulsation packets might see oscillations from both crossing oscillations in space, as well as the temporal oscillation of the field lines (c.f. the AMPTE/CCE results of Anderson et al. (1989)).

We can further examine the existence of the two apparently different resonance time regimes shown in Figure (4.7) by considering the temporal evolution of the field aligned current j_z at the resonance (see Figure (4.8)) (Wright, 1994b). On timescales shorter than τ_{fi}, then FAC's grow proportional to t^2. This is because the amplitude of ξ_y is growing proportional to t (see Figure (4.5)) and the scale width of the perturbations δx is narrowing as t^{-1}. Considering the form of j_z in equation (4.15), shows that for times $t < \tau_{fi}$, j_z will grow $\propto t^2$. On timescales longer than τ_{fi}, then the resonant ξ_y amplitude has saturated and j_z only grows because of the continual reduction of scales through phase mixing (L_{ph}) - hence j_z only grows proportional to t. We note of course, that in the real magnetosphere, the ionosphere will damp these pulsations on a timescale determined by the Pedersen conductivity, which we denote as τ_I. On timescales longer than τ_I, then these ideal results need to be re-examined.

Ideal phase mixing means that the ξ_y perturbation scales continually narrow in time. Following Cally (1991), we can plot a diagram of the magnitude of the coefficients b_m

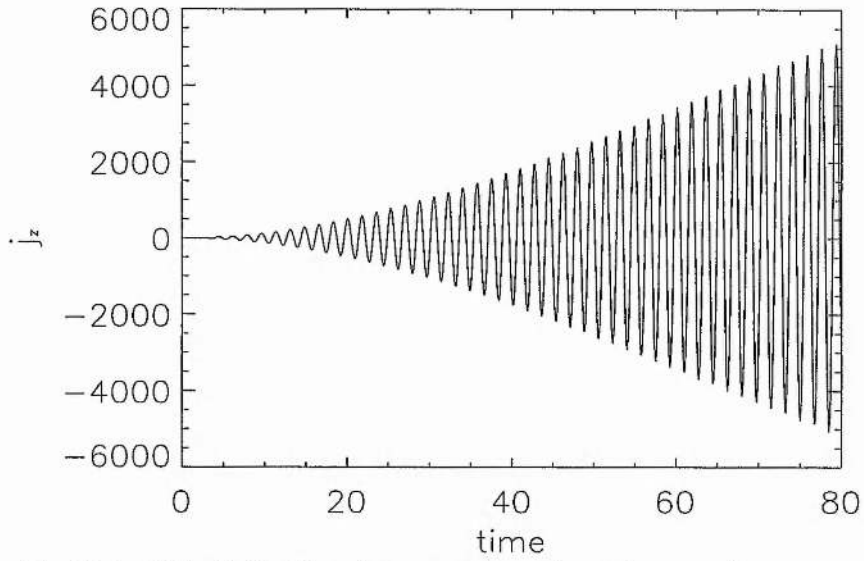

Figure 4.8: Plot of the field aligned current j_z against time, at the resonant position $x = 0.22$, for $\lambda = 0.3$. This shows the expected t^2 growth at times $t < \tau_{fi}$, and then the growth only proportional to t for times $t > \tau_{fi}$, once the ξ_y amplitude at the resonance has saturated. For this value of λ, $\tau_{fi} \approx 65$.

(i.e. the ξ_y Fourier amplitudes) as a function of time. In the incompressible work of Cally (1991), a clear pulse was seen propagating in wave number space towards higher Fourier harmonics (and hence smaller spatial scales) in time. Figure (4.9) shows the magnitude of the coefficients b_m at two times, and a similar (if less smooth) picture of this propagation is revealed for the ξ_y components in our compressible case. The difference is probably a result of the finite time taken for the cavity mode to deposit energy at the resonance.

We can estimate the finest scales which may be generated by phase mixing by considering the maximum magnitude of the natural Alfvén frequency gradient $|\omega_A'|_{max}$, and then using

$$k_{x,max} = m_{max}\pi = |\omega_A'|_{max}\, t \tag{4.16}$$

to give

$$m_{max} = \frac{1}{\pi}|\omega_A'|_{max}\, t. \tag{4.17}$$

This predicts an increase in m between two times as $\Delta m = (|\omega_A'|_{max})\Delta t$. Hence between

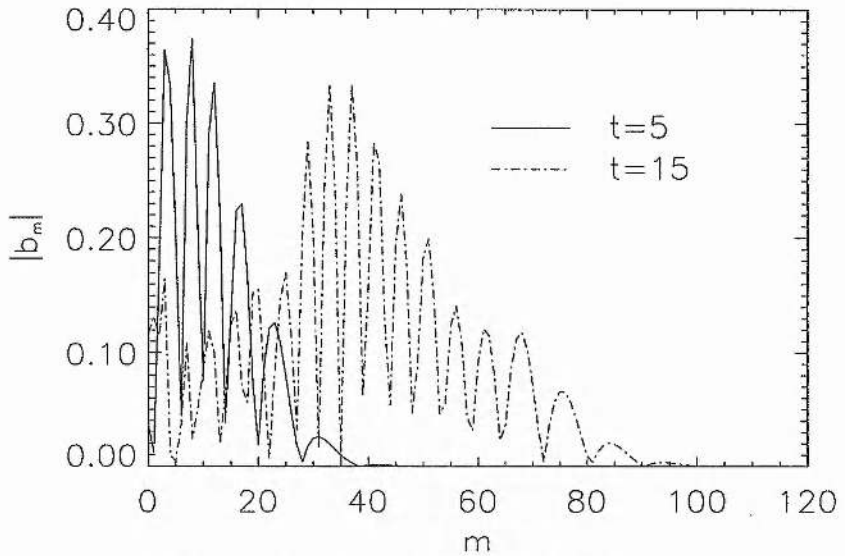

Figure 4.9: The magnitude of the components $b_m(t)$ in the Fourier series expansion for $\xi_y = b_0(t)/2 + \sum_{m=1}^{N} b_m(t)\cos(\pi m x)$, plotted at two times, for $\lambda = 1.0$. We can clearly see a wave pulse propagating in wavenumber space (m) towards higher harmonics and hence finer scales, due to phase mixing. The solid line represents an early time ($t = 5$) and the dashed line a later time ($t = 15$).

$t = 5$ and 15, the foremost wavefront should advance by a Δm of 51, in good agreement with the results shown in Figure (4.9). (Note that we have used this argument to choose sufficient Fourier modes to ensure that the wave evolution is being fully resolved - see section (2.4.4) (ii)).

In the real magnetosphere, pulsations can be damped by a variety of mechanisms, such as ohmic dissipation in the ionosphere. This can damp the pulsation, as well as creating finite widths. If pulsations generate sufficiently fine scales in space, then they can mode convert to kinetic or two fluid wave modes which may broaden the resonance (Rankin et al., 1993). These dissipation mechanisms may limit the extent to which realistic pulsations will phase mix, and hence limit the finest radial scales which they will develop. We discuss these effects and compare our results to other studies in section (4.5).

4.4.5 Asymptotic State of Coupled Waves.

In our study of the absorption of energy thus far, we have seen that the "fast" mode (compressional) energy of the initial global oscillations may be concentrated at the resonance

location $\omega_A(x_w)$. Since, for small values of λ, the global compressional oscillations are dominated by ξ_x perturbations, and the Alfvénic (essentially incompressible) disturbances at the resonance are dominated by a ξ_y polarisation, then we can see that this represents an asymptotic polarisation rotation in the evolution of coupled wave modes from poloidal to toroidal.

This concept was first discussed by Radoski (1974). In his paper he considered how an arbitrary MHD wave disturbance would evolve in time in a cylindrical magnetospheric model comprising a cold, compressible inhomogeneous plasma. By examining the coupled ($\lambda \neq 0$ or ∞) toroidal and poloidal wave equations, Radoski (1974) found two apparent resonances, however only the well known Alfvén resonance (where $\omega = \omega_A(r)$) was found to actually produce singular wave fields.

Since the asymptotic behaviour of the wave fields is governed by the singularities in their Fourier transforms, Radoski (1974) found that completing a Fourier superposition of the singular terms arising from the Alfvén resonances implied that the poloidal wave fields would decrease $\propto 1/t$. Similarly, the toroidal wave fields tended (in an ideal plasma) to a non-decaying oscillating function having the same form as the decoupled ($\lambda = 0$) toroidal Alfvén waves.

This is clearly in accord with our numerical results. In figure (4.10) we plot the growth of the toroidal, and the decay of the combined poloidal (ξ_x and b_x) and compressional (b_z), x integrated wave energy densities as a function of time for $A^2 = 1.0$, $B^2 = 0.9$, $k_z = 2.0$ and $\lambda = 1.0$. The polarisation rotation is obvious, with the oscillations being due to the fundamental global mode eigenfrequency. The non-zero poloidal/compressional energy which remains after the resonant transfer of energy to the toroidal state corresponds to those higher harmonic modes whose eigenfrequencies lie outside the Alfvén continuum.

We can further examine this polarisation rotation by looking at the long timescale evolution of the perturbations around the resonant locations using our numerical code. Radoski (1974) predicts that not only will the waves asymptote to a toroidal state, but also that the compressional component of the magnetic field $b_z \rightarrow 0$, i.e., the waves become purely incompressible decoupled toroidal oscillations. This implies that asymptotically, around the resonance, the small amplitude components of ξ_x (which are necessary to maintain $\nabla.\mathbf{b} = 0$ (with $b_z = 0$)) should decay in time. This was considered analytically by Wright (1992b). He found that to leading order at the resonance $\nabla.\mathbf{v} = 0$, and hence $b_z = 0$ to leading order. Consequently,

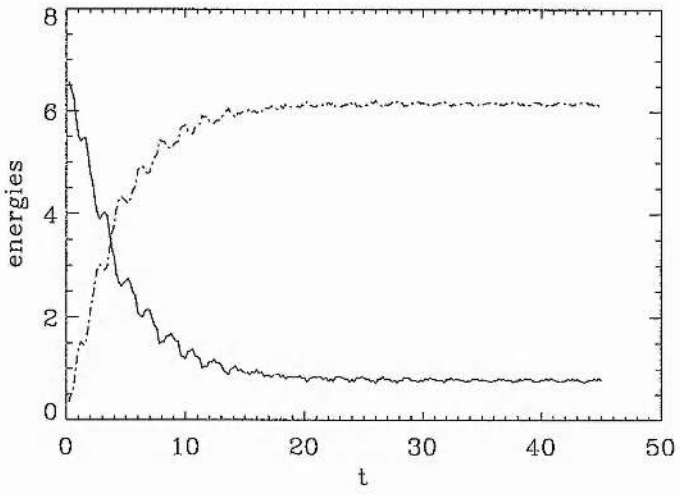

Figure 4.10: Combined poloidal and compressional $(1/(2\mu_0)(b_x^2 + b_z^2) + 1/2\rho(x)v_x^2)$ (solid line) and the toroidal $(1/(2\mu_0)b_y^2 + 1/2\rho(x)v_y^2)$ (dashed line) x integrated energy densities as a function of time. The transfer of energy from the global compressional mode to the essentially Alfvénic toroidal oscillations at the resonance are apparent.

$$\frac{\partial \xi_x}{\partial x} + i\lambda\xi_y = 0. \tag{4.18}$$

In Figure (4.11) we plot the amplitude of the wave perturbations around the resonant location, at two times, for the single ξ_x Fourier mode initial condition, with $A^2 = 1.0$, $B^2 = 0.9$ and $k_z = 2.0$. The fine scale, phase mixed, oscillations in ξ_y are clearly shown, as are the much smaller amplitude fine scale ξ_x oscillations (which are super-imposed upon the remnant non-resonant fast mode perturbations).

Considering equation (4.18), we expect the length-scale to decay proportional to t^{-1} as a result of phase mixing. To maintain the incompressible nature of the waves, we expect the amplitude of ξ_x to decay $\propto t^{-1}$. In Figure (4.12), we plot the amplitude of these fine scale oscillations plotted as a function of t^{-1}, sampled at periods of the fundamental cavity mode eigenfrequency so that the amplitudes are all shown at the same phase. Good agreement with the t^{-1} decay is found.

This analysis of the essentially incompressible waves which exist around the resonance can be compared to those of Barston (1964) and Cally (1991) in fully incompressible plasmas. The numerical study of Cally (1991) found the ξ_x decay proportional to t^{-1} pre-

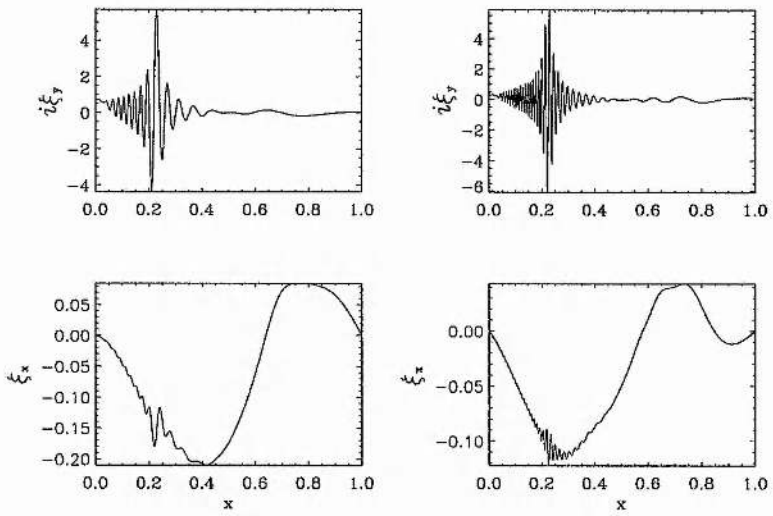

Figure 4.11: The first column shows the $i\xi_y$ and ξ_x perturbations at $t = 20$, whilst the second column shows $t = 45$, both for the case where the fundamental global mode drives a resonance around $x = 0.22$. The small scale ξ_x perturbations around $x = 0.22$ required to keep $\nabla.\mathbf{b} = 0$ and $b_z \approx 0$ are clearly shown.

dicted by Barston (1964). This asymptotic decay occurs as a result of the logarithmic singularities which exist in the governing Barston eigenmodes of the system. In our compressible model, the eigenmodes $\phi_{nx}(x)$ which have been used to reconstruct the initial ξ_x conditions also possess logarithmic singularities. Since the asymptotic behaviour of the Fourier transform of these normal modes (i.e., their behaviour in time) is governed by their singularities, then we might expect the ξ_x amplitude around the resonant location to decay $\propto t^{-1}$, as we have seen.

Consequently, our numerical results support the conclusions of Radoski (1974), with both the global mode poloidal disturbances decaying exponentially, as well as the localised ξ_x disturbances around the resonance decaying $\propto t^{-1}$. This means that the coupled waves approach an asymptotic state consisting of purely decoupled toroidal field line oscillations at the local natural Alfvén frequency $\omega_A(x)$.

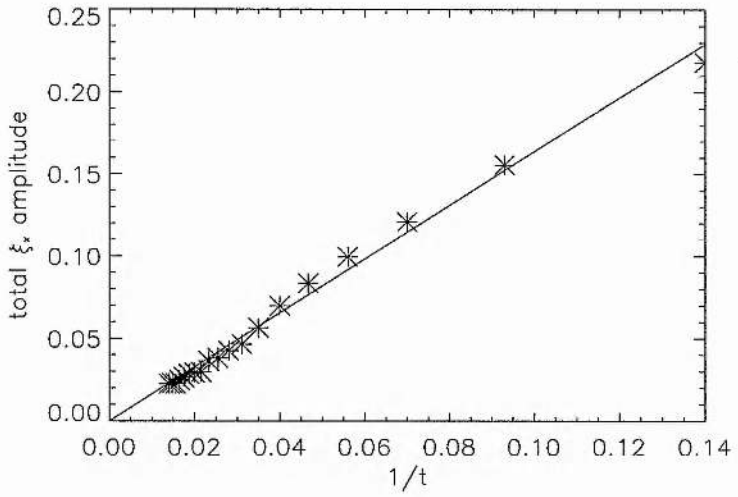

Figure 4.12: The peak to peak amplitude of the small scale ξ_x phase mixed oscillations at $x = 0.22$ are plotted as asterisks as a function of $1/t$. The basic linear trend is apparent (shown as a best fit straight line), with the discrepancies probably due to the super-imposed oscillations of the non-resonant global eigenmodes present in the initial conditions.

4.5 Discussion

4.5.1 Overall Pulsation Energy Widths.

We can now compare the asymptotic resonance widths (ΔX_E) developed in our numerical model with the overall pulsation widths which have been observed in the terrestrial magnetosphere.

We use equation (4.13), and follow Anderson et al. (1989) (and references therein) by adopting their dipole magnetic field geometry. By assuming a fast mode damping parameter of $\omega_{fi}/\omega_{fr} = 0.06$ (to illustrate a typical coupling strength), then we expect the asymptotic values of ΔX_E to be $\sim 0.2R_E$ at $L = 4$ (assumed to be inside the plasmasphere), and at $L = 7$ (in the outer magnetosphere) $\sim 0.4R_E$. For a less strongly coupled cavity mode, these widths would be reduced.

Resonance widths seen in radar data are of $\sim 0.5R_E$ (Walker et al., 1979), and $\sim 0.35R_E$ (Walker et al., 1992). Walker et al. (1992) note that their observation was at the limiting ionospheric resolution of their radar (~ 45 km), and hence that the real width of the FLR which they observed could have been narrower than the inferred width of $\sim 0.35R_E$.

Similarly, the satellite observations of Mitchell et al. (1990), showed pulsations (which they believed to have been driven by a cavity mode) with a width of $\sim 0.5 R_E$. These widths are clearly of the order predicted by our numerical code.

4.5.2 Magnetospheric Perturbation Widths ΔX_ξ.

We now discuss the likely dominant damping mechanisms for magnetospheric pulsations. By considering this damping, we can determine whether pulsations are sufficiently long lived that the phase mixing structure within the energy envelope can develop.

Allan and Poulter (1989) concluded that it would take $\sim$ 100's of periods or more for dissipative phase mixing to damp out magnetospheric pulsations. Consequently, it is unlikely to be an important pulsation damping mechanism. Kelvin-Helmholtz instabilities can be driven in regions of high velocity shear, which may be generated by phase mixing within Alfvén resonances. These instabilities could be important for both widening the resonance region and for damping the pulsations. However, this will be a non-linear effect, so is not present in our linear analysis. (See Browning and Priest (1984), for a discussion of the Kelvin-Helmholtz stability of phase mixed Alfvén wave fields.)

The dominant mechanism for dissipating pulsation energy is usually regarded as ionospheric Joule heating. The energy dissipated by this mechanism clearly depends on the conductivity of the ionosphere, which is modelled using the height integrated Pedersen conductivity, Σ_P, of the assumed thin sheet ionosphere. We have discussed the different ionospheric boundary conditions which are applicable to decoupled cavity modes and Alfvén waves. We have argued that even for coupled modes, assuming two different boundary conditions provides a good approximation, and hence that the overall width of an FLR can be understood in terms of the frequency bandwidth of the cavity mode, rather than being due to direct ionospheric dissipation. However, once the Alfvén waves have been driven by the cavity mode, they have a finite lifetime based on this ionospheric damping. To incorporate the effects of ionospheric dissipation into our dynamic analysis in terms of phase mixing, we can consider the following theory.

i) Steady State Analysis.

The standard treatment in the literature for the case of continually driven pulsations, finds the standard steady harmonic ($\exp -i\omega t$) solution to the coupled wave problem

by considering a single complex k_z ($\omega_{fi} = 0, k_{zi} \neq 0$). These "normal" mode solutions oscillate with a real frequency ω_{fr}, and maintain a constant amplitude as the energy input from the driver at the external boundary is dissipated at the resonance.

The leading order solution for ξ_x modes can be written as $\xi_x \sim \ln(x - x_w + i\epsilon)$, see equation (3.59), and the leading order solution for the ξ_y (i.e. Alfvén wave) resonant response is $i\xi_y \sim 1/\lambda(x - x_w + i\epsilon)$, see equation (3.61) (Southwood, 1974). Considering this function, we can write

$$|\xi_y| \sim \frac{1}{\lambda\left((x - x_r)^2 + \epsilon^2\right)^{\frac{1}{2}}} \tag{4.19}$$

and derive a perturbation FWHM ΔX_ξ of

$$\Delta X_\xi = 2\sqrt{3}\epsilon \tag{4.20}$$

where ϵ is calculated using a single complex value for k_z based simply on ionospheric dissipation (see equation (3.58)).

In order to estimate ϵ, we need a value for k_{zi}. For the case of undriven Alfvén waves, decaying due to Σ_P, we can consider the boundary condition at the ionosphere to be

$$\mathbf{b} \times \hat{\mathbf{z}} = \pm\mu_0\Sigma_P\mathbf{E} \tag{4.21}$$

with the positive sign at $z = z_0$, and the negative sign at $z = 0$ (Hughes, 1974; Hughes and Southwood, 1976; Hughes, 1983; Kivelson and Southwood, 1988). Combining this with Maxwell's equations, and assuming

$$b_y = b_0 e^{-i\omega t}[e^{+ik_z z} + e^{-ik_z z}], \tag{4.22}$$

to represent the fundamental Alfvén mode with a b_y node at the equator, we obtain (after Ellis and Southwood (1983))

$$k_{zi} = \frac{1}{z_0}\ln|R|^{-1} \tag{4.23}$$

where $R = (\Sigma_A - \Sigma_P)/(\Sigma_A + \Sigma_P)$ and represents the reflection coefficient of Alfvén waves incident on the ionosphere, and $\Sigma_A = (\mu_0 v_A)^{-1}$ represents the conductance associated with

the shear Alfvén wave. If $v_A \gg (\mu_0 \Sigma_P)^{-1}$ as is the case for the Earth, then this can be written as

$$k_{zi} = \frac{2}{\mu_0 \Sigma_P v_A z_0}. \tag{4.24}$$

With the above assumption $\Sigma_P \gg \Sigma_A$ (usual for the magnetosphere), we obtain the expected relationship for the real part of the fundamental field aligned wavenumber

$$k_{zr} = \frac{\pi}{z_0}. \tag{4.25}$$

In this calculation for undriven Alfvén modes, we have assumed that the complex ω and complex k_z can be related via the Alfvén dispersion relation

$$\omega_A^2 = k_z^2 v_A^2. \tag{4.26}$$

This is appropriate because the net-flux of energy into the ionosphere, due to complex k_z, also cause the damping which is represented by γ. However, the v_A used in equation (4.26) will be the Alfvén speed in the body of the magnetosphere (which in a 1-D box model is constant along magnetic field lines) whilst in order to model the damping of pulsations by the ionosphere, we are interested in the mismatch between Σ_P and Σ_A at the ends of field lines. This reveals a significant shortfall when trying to calculate ionospheric pulsation damping in a 1-D box since v_A is not a function of z. It would clearly be desirable to have a more detailed model which would include the reflection of Alfvén waves from magnetospheric inhomogeneities, e.g., $\partial v_A / \partial z$, and hence take account of the variation of v_A which exists in the Earth's magnetosphere. However, the estimate for k_{zi} given above is sufficient for our order of magnitude analysis.

We expect that a time-dependent solution will asymptote to this (ionospheric) width for large times, and now demonstrate how our dynamic analysis in terms of phase mixing may reproduce this result.

ii) Phase Mixing Analysis.

A steadily driven resonance ($\omega_{fi} = 0$) is best simulated in our model by a weak coupling case, $\lambda \to 0$ ($\omega_{fi} \to 0$). We choose to adopt a dynamic viewpoint of this situation in terms of a superposition of Alfvén waves: Alfvén waves with relatively large amplitude and spatial scale in x are continually being driven. The Alfvén waves excited at a given time

will phase mix more and more the longer they live; however, they also decay in amplitude and so become more insignificant. Thus, ionospheric dissipation limits the finest scales that can be achieved for significant amplitudes. If we assume that after an e-fold damping time τ_I (due to ionospheric dissipation) the Alfvén wave amplitude is no longer significant, we can determine the finest scales which the pulsation can develop. This is given by the limiting ionospheric phase mixing length, L_I

$$L_I \sim 2\pi \left(\tau_I \omega_A{}'(x)\right)^{-1}. \tag{4.27}$$

We can now write

$$\tau_I \sim 1/\gamma = \frac{\Sigma_P \mu_0 z_0}{2} \tag{4.28}$$

where γ represents the ionospheric damping rate of an undriven Alfvén wave component, and hence

$$\Delta X_\xi \approx L_I \sim 2\pi \left(\frac{\Sigma_P \mu_0 z_0}{2} \omega_A'(x)\right)^{-1}. \tag{4.29}$$

This predicts the finest wave scales which develop in a steadily driven pulsation to be $\propto (\Sigma_P z_0 \omega_A'(x))^{-1}$.

The steady harmonic ($\omega_{fi} = 0, k_{zi} \neq 0$) estimate for the resonance width of ξ_y from the previous sub-section (equations (4.20), (3.58) and (4.24)) gives

$$\Delta X_\xi = 2\sqrt{3} \left(\frac{\Sigma_P \mu_0 z_0}{2} \omega_A'(x)\right)^{-1}. \tag{4.30}$$

This again clearly gives the result $\Delta X_\xi \propto (\Sigma_P z_0 \omega_A'(x))^{-1}$. This analysis shows how our novel dynamic phase mixing treatment can reproduce more standard steady harmonic results. The two results differ by a factor ~ 2, but this is not totally unexpected because of the order of magnitude estimate of the ionospheric e-fold damping time. It is gratifying that an appropriate limit of our treatment, based on phase mixing, reproduces the expected result that ionospheric damping will limit the finest ξ_y perturbation scales which may be developed by a continually driven resonance.

4.5.3 FLR Characteristics.

We can also consider the effects of ionospheric dissipation on FLRs driven by single damped cavity modes (i.e., with $\omega_{fi} \neq 0$). If $\tau_I > \tau_{fi}$, then this introduces the possibility

that FLRs have fine phase mixing structure inside their overall width.

Fine scales which are created within a pulsations energy envelope will continue to narrow by phase mixing, whilst their amplitude decreases due to ionospheric dissipation. If the Alfvén waves gain their energy on timescales which are quick compared to τ_I, i.e., $\tau_I \gg \tau_{fi}$, then we can view the pulsation in two stages: the first, for times of order τ_{fi}, is essentially the ideal growth of the resonance; the second ($t \gg \tau_{fi}$) represents the undriven phase mixing decay of Alfvén waves due to Σ_P. Hence, we can calculate an ionospheric pulsation damping rate by considering the decay of undriven Alfvén waves. For FLRs driven by rapidly damped cavity modes, this should be reasonably accurate.

A numerical calculation of this ionospheric damping rate, in a dipole magnetospheric geometry, was completed by Newton et al. (1978). They found that for typical dayside (or active nightside) Σ_P, the damping decrement $\gamma/\omega_A(x_w) \sim 0.01$ (see for example their Figure (9) - with $L = 7$ and Σ_P = 10-20 mhos (9×10^{12} - 1.8×10^{13} esu), they calculate $\gamma/\omega_A(x_w) \sim 0.0075 - 0.018$). If we define the e-fold ionospheric damping time of the pulsations as τ_I, then this value of $\gamma/\omega_A(x_w)$ corresponds to $\tau_I = 15.9$ Alfvén wave periods. This is longer than τ_{fi} for pulsations driven by strongly coupled fast cavity modes, and therefore we would expect these dayside pulsations to develop the phase mixing fine structure within the resonance envelope. Similarly, using typical nightside conductivities of $\Sigma_P \sim$ 0.1-1 mho ($\sim 10^{11} - 10^{12}$ esu), Newton et al. (1978) found damping on the nightside can become extreme, having $\gamma/\omega_{fr} \gtrsim 0.1 - 1$. Clearly, this is probably not sufficient for perturbation fine structure to develop significantly beneath the pulsations energy envelope, even for rapidly damped cavity modes.

Consequently, satellites crossing dayside or active nightside FLRs may see oscillations in magnetic field components both from it going through spatial oscillations, as well as seeing the natural Alfvén oscillations of the local field lines in time. This implies that inbound and outbound satellites, which are crossing FLRs, may see different apparent frequencies. Frequency shifts of this form were seen in the AMPTE/CCE data presented by Anderson et al. (1989).

If $\tau_I \lesssim \tau_{fi}$, as is the case for the non-auroral region nightside, then pulsation fine structure of significant amplitude will not be created within the overall resonance envelope and pulsations will be rapidly damped by ionospheric dissipation. However, Crowley et al. (1987), used both EISCAT radar and ground based magnetometer data from observations of a Pc5 pulsation to determine both its observed damping decrement, and a theoretically

predicted damping rate calculated on the basis of ionospheric dissipation. Σ_P ($\sim 2-5$ mho) was inferred from the EISCAT data, and predicted damping greater than that observed. Crowley et al. (1987) argued that the FLRs amplitude was being enhanced by a cavity mode continuing to drive it during the period of observation. This would be a case where $\tau_I \lesssim \tau_{fi}$, and explains how pulsations with short τ_I may have longer lifetimes than those predicted on the basis of τ_I alone.

For sufficiently long lived pulsations, phase mixing can narrow to kinetic/two fluid length scales L_k (such as the ion gyro-radius, or the electron inertia length). These effects will become important, from a phase mixing viewpoint, if the pulsations live longer than τ_k,

$$\tau_k = 2\pi \left(\frac{d\omega_A}{dx} L_k \right)^{-1} . \tag{4.31}$$

Of course, we would also require that the pulsation still had a significant amplitude for these effects to be important. These kinetic/two fluid wave modes may broaden the resonance, and will limit the perturbation scales to $\sim L_k$ (Rankin et al., 1993).

To excite equatorial kinetic Alfvén waves, or electron inertia waves above the polar ionosphere, then pulsation length scales must narrow to $\sim$ 100's km - $\sim 0.05 - 0.1$ R_E (Rankin et al. (1993), and references therein). Again using the dipole magnetospheric model of Anderson et al. (1989) for the magnetospheric Alfvén frequencies and assuming $L = 7$, we find that $t_k \sim 35 - 70$ Alfvén periods. For those FLRs with $\tau_k < \tau_I$, then these wave modes will be triggered and consequently we agree with Inhester (1987), and Rankin et al. (1993), that kinetic/two fluid waves may be excited within the lifetimes of some long lived pulsations.

On timescales less than both τ_I and τ_k (typically > 10 periods), then we expect that our ideal MHD code will provide an accurate description of the evolution of a FLR.

4.6 Conclusions.

In this chapter we have presented the numerical results for the resonant coupling between fast and Alfvén waves in the box magnetosphere. Using this model, we examine the temporal evolution of FLR widths driven by fast cavity modes. Three regimes for pulsation evolution become apparent from this analysis.

Firstly, the overall energy density width developed by the resonance can be understood in terms of the frequency components of the driving cavity mode. The frequency bandwidth of this mode is governed by its damping rate and driving duration, and these determine the field lines which are actually being driven. The overall resonance energy width at any time is given by the spatial extent of these driven field lines. This width develops on a timescale $\tau_{fi} = \omega_{fi}{}^{-1}$, and approaches an asymptotic FWHM of $\Delta\omega_A = 2\omega_{fi}$. This is a new result, which means that at early times the overall energy width of a resonance will be broader than previously thought ($\propto 1/t$), and only at large times will it approach the expected asymptotic width.

Secondly, for perturbations which live longer than τ_{fi}, further fine structure can develop beneath this envelope. Phase mixing between adjacent field lines within the resonance continues to generate finer and finer perturbation scales. Thus, the finest possible scales at any time within an ideal magnetospheric pulsation will be governed by the phase mixing length $L_{ph}(t) = 2\pi\,(td\omega_A/dx)^{-1}$. If ionospheric dissipation is included, the Alfvén fields will damp exponentially in time as they phase mix.

Thirdly, for the case of continually driven pulsations ($\omega_{fi} \approx 0$), for example driven by a small λ cavity mode, then after a time τ_I the perturbation width will narrow to L_I (defined by equation (4.27)). At this point the phase mixing process will cease to produce any finer detectable scales within the pulsation, which will appear as a single coherently oscillating structure having width L_I.

If the phase mixing within pulsations can continue for a sufficiently long time, so that it reaches a kinetic/two fluid scale L_k (by experiencing only slow ionospheric damping), then kinetic/two fluid effects may also broaden the resonance fine scales and limit them to the order of L_k or more. For various values of τ_{fi}, τ_I, and τ_k, the regimes for pulsation behaviour can be summarised as shown in Table (4.1).

The combination of these features allows pulsation energy envelope widths to be created on the timescale of several cavity mode periods, as observed in data by Walker et al. (1992), and allows the resonances to naturally exhibit the spatially localised packet structure across L-shells which is also seen in data (Mitchell et al., 1990; Lin et al., 1992).

We find that pulsations can be expected to exhibit fine structure inside the energy envelope, so long as they are not damped on timescales shorter than τ_{fi}. By considering ionospheric damping as the likely dominant pulsation energy dissipation mechanism, we conclude that for both dayside, and active nightside pulsations whose footpoints lie in the

Timescales	Energy Width	ξ_y Scale Length	Description
$t < \tau_{fi}, \tau_I, \tau_k$	Decreases $\propto t^{-1}$ $\Delta X_E \approx L_{ph}(t)/\sqrt{3}$	Decreases $\propto t^{-1}$ $\Delta X_\xi \approx L_{ph}(t)$	No fine structure beneath the energy envelope.
$\tau_{fi} < t < \tau_I, \tau_k$	ΔX_E saturated $\Delta X_E \approx 2\omega_{fi}\,(d\omega_A/dx)^{-1}$	Decreases $\propto t^{-1}$ $\Delta X_\xi \approx L_{ph}(t)$	ξ_y has fine scale structure within the energy envelope.
$\tau_{fi}, \tau_I < t < \tau_k$	ΔX_E saturated $\Delta X_E \approx 2\omega_{fi}\,(d\omega_A/dx)^{-1}$	$\Delta X_\xi \approx L_{ph}(t)$, but its amplitude decays in time	Kinetic effects not important. ξ_y reduces due to ionospheric Σ_P.
$\tau_I < t < \tau_k, \tau_{fi}$ $\omega_{fi} \approx 0$ (continually driven)	ΔX_E saturated $\Delta X_E \sim L_I$	ΔX_ξ saturated $\Delta X_\xi \approx L_I$.	Kinetic effects not important. Pulsation maintains dominant scale $\Delta X_\xi \sim L_I$.
$\tau_{fi}, \tau_k < t < \tau_I$	ΔX_E saturated $\Delta X_E \approx 2\omega_{fi}\,(d\omega_A/dx)^{-1}$	ΔX_ξ saturated $\Delta X_\xi \sim L_k$	ξ_y fine structure saturates. Pulsation couples to kinetic/two-fluid plasma waves.

Table 4.1: Pulsation Behaviour Regimes.

auroral region, ionospheric damping can be sufficiently small so that this fine structure is created within the pulsation energy envelope.

Depending on the values of L_{fi}, L_I and L_k, we agree with both Inhester (1987), and Rankin et al. (1993) that in general it may be possible for some pulsations to live long enough so that sufficiently small scales can develop, and hence that mode conversion to kinetic or two fluid waves should be considered. Both kinetic Alfvén or electron inertia waves can accelerate particles parallel to the background magnetic field. Hence, it is possible that FLRs have an important role to play in modulating auroral emissions and perhaps in generating some types of auroral arcs (Samson et al., 1991b; Samson et al., 1992b; Xu et al., 1993).

Current radar observations show a limiting resolution of $\sim$ 45 km in the ionosphere (Walker et al., 1992). Thus, smaller scale observations will be necessary to further

investigate pulsation fine structure. If the electron precipitation in auroral arcs is in fact a direct result of FLR fields, then, as suggested by Rankin et al. (1993), optical auroral observations might be useful for determining their internal fine structure.

We should note that the MHD code we have employed should be accurate in describing the evolution of pulsations during their growth phase. Only as times of the order of τ_k or τ_I are approached, do kinetic or dissipative effects become important suggesting that the ideal MHD approximation in our model requires revision.

We have also examined the long timescale evolution of the coupled wave modes. Our results show that once the resonant global wave energy has been deposited at the resonance, the waves continue to evolve and generate fine scales via the phase mixing process. Asymptotically in time, these essentially incompressible oscillations at the resonance experience a further polarisation rotation, so that the small poloidal ξ_x perturbations, which exist to maintain $\nabla.\mathbf{b} = 0$ at the resonance, decay $\propto t^{-1}$. Consequently, our numerical results agree with the predictions of Radoski (1974) whereby the coupled waves should experience a damping of ξ_x perturbations, and a decay of b_z, until asymptotically (in an ideal plasma) the waves approach a state governed by purely decoupled toroidal motions at local Alfvén frequencies $\omega_A(x)$.

Chapter 5

Large λ Numerical Poloidal Wave Evolution.

5.1 Introduction.

In this Chapter[1], we consider the temporal evolution of waves with a large "azimuthal" wavenumber λ. In the asymptotic limit $\lambda \to \infty$, the ξ_x and ξ_y polarisations of waves in an inhomogeneous plasma decouple (Dungey, 1967). However, for finite values of λ, the asymptotic results are no longer strictly valid. It is this case which we numerically analyse in detail here. In Chapter 6, we go on to analytically derive some relevant large λ asymptotic results.

To study the temporal evolution of high λ waves, we again utilise the box model of Figure (2.1) (e.g., Southwood (1974)) and impose an inhomogeneous Alfvén velocity profile in the $\hat{\mathbf{x}}$ direction by choosing a density profile $\rho(x)$. The edges of the simulation box are assumed to be perfectly reflecting.

Linearising the cold ideal MHD equations (see Chapter 2), we can rewrite equations (2.7) and (2.8) as two new equations governed by decoupled Alfvén wave operators, coupled via the linearised compressional magnetic field b_z. This gives the following two coupled differential equations (where again all variables are normalised)

[1]Based on Mann, I.R. and A.N. Wright, "Finite Lifetimes of Ideal Poloidal Alfvén Waves", *J. Geophys. Res.*, (1995), in press.

$$\frac{1}{v_A^2(x)}\frac{\partial^2 \xi_x}{\partial t^2} + k_z^2 \xi_x = -\frac{\partial b_z}{\partial x} \tag{5.1}$$

$$\frac{1}{v_A^2(x)}\frac{\partial^2 \xi_y}{\partial t^2} + k_z^2 \xi_y = -i\lambda b_z. \tag{5.2}$$

The time integrated form of Faraday's law, combined with ideal hydromagnetic frozen flux condition ($\mathbf{E} + \mathbf{v}_\wedge \mathbf{B} = 0$) gives

$$b_z = -\left(\frac{\partial \xi_x}{\partial x} + i\lambda \xi_y\right). \tag{5.3}$$

If $\lambda = 0$ or ∞, these equations decouple (Dungey, 1954; Dungey, 1967). When $\lambda \to \infty$, b_z and $\xi_y \to 0$ and ξ_x describes decoupled poloidal Alfvén waves having the general solution

$$\xi_x(x,t) = G(x)e^{i\omega_A(x)t}, \tag{5.4}$$

where $\omega_A(x)$ is the natural Alfvén frequency of a field line; $\omega_A^2(x) = k_z^2 v_A^2(x)$. This solution describes how the poloidal oscillations of adjacent field lines, which are initially in phase at $t = 0$, drift out of phase with each other in time. Consequently, initially coherent $\lambda \to \infty$ poloidal Alfvén waves can be expected to generate fine scales in meridian planes as they phase mix (see Chapter 4; or Heyvaerts and Priest (1983), and Mann et al. (1995) for an analysis of the phase mixing of toroidal Alfvén waves).

In order to study the temporal evolution of large (but not infinite) λ waves, we solve the above equations using the generalised matrix eigenvalue method described in Chapter 2. From the prescription of ξ in equation (2.1), we can see that the real physical displacements ξ_x^P and ξ_y^P vary as $\cos \lambda y$ and $\sin \lambda y$ respectively, and hence that their real physical amplitudes can be extracted from our code as the variables ξ_x and $i\xi_y$. We impose a wave displacement at $t = 0$, and then follow the evolution of the wave fields in time.

In section (5.2), we consider the temporal evolution of standing high λ waves which have $k_z \ll \lambda$, and which can be applied to high m poloidal oscillations in the Earth's magnetosphere. In section (5.3) we consider the case whereby $k_z \gtrsim \lambda$, both are larger than $k_x(x, t = 0)$. With this latter ordering, the purely field guided nature of the waves is destroyed, and we examine their subsequent evolution. We end the chapter with some conclusions in section (5.4).

5.2 High λ Magnetospheric ($k_z \ll \lambda$) Poloidal Pulsations.

5.2.1 Review of Magnetospheric Observations.

As we discussed in Chapter 4, section (4.3), ultra-low frequency (ULF) magnetic pulsations in the Earth's magnetosphere are believed to have a standing nature in the magnetosphere between the ionospheric endpoints of magnetic field lines (Dungey, 1954). Continuous pulsations of this type, classified as Pc3, 4 or 5 (having periods of 10-45s, 45-150s, and 150-600s respectively), are regularly observed from both the ground by radars (e.g., STARE - Walker et al. (1979), EISCAT - Crowley et al. (1987), GOOSE BAY - Walker et al. (1992), Ruohoniemi et al. (1991)) and magnetometers (e.g., Samson et al. (1991a) and Ziesolleck et al. (1993)), and on both geostationary (e.g., Hughes et al. (1977), Hughes (1980), Takahashi et al. (1984)) and elliptically Earth orbiting satellites (e.g., ISEE - Singer et al. (1982), Hughes and Grard (1984) and Cao et al. (1994); AMPTE-CCE - Anderson et al. (1990) and Takahashi and Anderson (1992)).

In addition to classification in terms of periods, Pc waves have been statistically grouped in terms of their dominant magnetic field components and their polarisations by Anderson et al. (1990). By using the AMPTE-CCE data from L=5-9 and over all local times, Anderson et al. (1990) undertook a statistical study of ULF wave activity in an attempt to link different types of waves with their energy sources. ULF waves may have energy sources which are either internal or external to the magnetosphere.

As we discussed in Chapter 4, external energy sources, such as solar wind driven Kelvin-Helmholtz waves travelling on the magnetopause, can resonantly excite pulsations where their frequency matches the local natural Alfvén frequency (Southwood, 1974; Chen and Hasegawa, 1974a). Similarly, sudden solar wind impulses, incident upon the magnetospheric cavity, can excite cavity modes which resonantly drive pulsations (Kivelson et al., 1984; Kivelson and Southwood, 1985; Kivelson and Southwood, 1986; Allan et al., 1986b; Wright, 1992a; Wright and Rickard, 1995). Waves resonantly driven by these external sources tend to have low azimuthal wave numbers ($m \lesssim 10$), and are dominantly azimuthally polarised.

However, waves can also be driven by energy sources internal to the magnetosphere. For example, the drift bounce resonance mechanism can result in energetic particle populations exciting travelling ULF waves which have large azimuthal wavenumbers (Southwood,

1976; Southwood and Kivelson, 1981; Southwood and Kivelson, 1982; Chen and Hasegawa, 1988) as were observed by Hughes et al. (1978). Similarly, plasma instabilities such as the drift-Alfvén-ballooning mode may excite some types of ULF waves in plasmas with warm components (Chen and Hasegawa, 1991; Chan et al., 1994).

Takahashi et al. (1990) observed Pc5 waves with a period of 200s, and examined the modulation of particle fluxes in the presence of the wave. Their data showed field aligned flux modulations, and these were attributed to the waves having been driven by resonance with $\sim$ 100 keV ions. Drift-Bounce resonance mechanisms are thought to be responsible for exciting high m, second harmonic radially polarised Pc4-5 waves which are often observed by satellites, especially during times of quiet magnetic activity (Kokubun et al., 1989; Anderson et al., 1990; Engebretson et al., 1992; Takahashi and Anderson, 1992). These high m waves are difficult to observe using ground based magnetometers, as their signals are believed to be screened by the ionosphere (Hughes and Southwood, 1976); however satellite observations show them to be consistent with the poloidal guided mode discussed by Radoski (1967) and Dungey (1967).

In this section, we use our numerical code to study of these second harmonic radially polarised Pc4-5 waves (classified as R waves by Kokubun et al. (1989)). Satellite studies show them to occur at all local times (Kokubun et al., 1989; Anderson et al., 1990), with a peak occurrence in the afternoon. They typically occur at $L < 7$ on the dayside and at $L > 7$ on the nightside (Anderson et al., 1990); have a longitudinal extent ranging from 1.5hrs to 8hrs (Engebretson et al., 1992); and are typically localised in L-shell, having widths $\sim 0.2 - 1.6 R_E$ (Singer et al., 1982). We should point out that Storm-time Pc5 waves (Anderson et al., 1990) have similar characteristics to these waves. However, they often have a significant compressional component, are believed to be associated with magnetospheric storms and sub-storms, and are not the subject of the theoretical study presented here.

In low-β plasmas, at quiet times, the drift-bounce resonance mechanism may be responsible for the excitation of essentially Alfvénic Pc4-5 wave disturbances. Consequently, we examine the temporal evolution of high m guided poloidal Alfvén waves, which may have been driven by this mechanism. We find that poloidal Alfvén waves have a finite lifetime during which their dominant polarisation is poloidal. In fact, when they are oscillating in an inhomogeneous plasma, they experience a polarisation rotation from poloidal to toroidal, and asymptotically in time approach a purely toroidal polarisation state in agreement with the calculation of Radoski (1974), who suggested that the poloidal wave fields decay $\propto 1/t$

for large t. This is in contrast to the results of Ding et al. (1995), who studied the evolution of poloidal waves in a dipole geometry, and we comment on this discrepancy in the light of our study.

5.2.2 Basic Governing Equation Analysis.

We can examine the behaviour of the governing equations (5.1) and (5.2), by considering the following analysis. Equation (5.2) implies that with $k_z \sim O(1)$ and $v_A(x) \sim O(1)$, then $\ddot{\xi}_y \sim \xi_y$ and $b_z \sim \xi_y/\lambda$. Thus the left hand side of (5.3) is of order ξ_y/λ, which must be much less than the last term on the right hand side when λ is large. To leading order (5.3) is the balance of

$$\partial \xi_x/\partial x \sim -i\lambda \xi_y. \tag{5.5}$$

Thus if $\partial/\partial x \sim O(1)$, we find the ordering $\xi_y \sim \xi_x/\lambda$, $b_z \sim \xi_y/\lambda \sim \xi_x/\lambda^2$, when $\lambda \to \infty$ (strictly we require $\lambda \gg k_z$ and $\partial/\partial x$). If we set $b_z(x, t = 0) = 0$, so that $\partial \xi_x/\partial x|_{t=0} = -i\lambda \xi_y|_{t=0}$ exactly, we have the situation where the waves are initially incompressible. With large λ, so that ξ_x dominates ξ_y at $t = 0$, we have a model for a high m poloidal Alfvén wave.

For cases when $\partial \xi_x/\partial x$ is constant in time (i.e., the background $v_A(x) =$ a constant), the initial (dominantly poloidal) torsional Alfvén wave simply oscillates at the local Alfvén frequency, maintaining the displacements ξ_x^P and ξ_y^P in phase in time, and keeping the perturbation incompressible (i.e., $b_z(x, t) \sim 0$).

If however $v_A(x) = f(x)$, then to first order we expect ξ_x^P to phase mix according to equation (5.4). Looking for a solution of the form $\xi_x(t)e^{ik_x x}$, $(k_x = k_x(x, t))$, we find that

$$\frac{\partial}{\partial x} \sim ik_x = i\omega_A'(x)t + \frac{G'(x)}{G(x)} \tag{5.6}$$

and as $t \to \infty$

$$k_x \approx \omega_A'(x)t \tag{5.7}$$

where $' = d/dx$.

Equation (5.7) can be used to define the radial scale length of an initially uniform disturbance which will be generated at any time via phase mixing (as we have done in Chapter 4)

$$L_{ph} = \frac{2\pi}{k_x} \approx 2\pi \left(\omega'_A t\right)^{-1}. \tag{5.8}$$

Knowing that $b_z \sim 0$ for large λ, then equations (5.5) and (5.7) yield

$$\left|\frac{\xi_x}{\xi_y}\right| \sim \frac{\lambda}{\omega'_A t}. \tag{5.9}$$

We can interpret this equation in terms of phase mixing. As the initial poloidal disturbance phase mixes, then $\partial/\partial x$ increases until is no longer very much less than λ. When the disturbance phase mixes to a radial scale length $2\pi/\lambda$ (i.e., equal to the azimuthal scalelength), then the ordering $\partial/\partial x \ll \lambda$ is no longer true, and hence the decoupled poloidal Alfvén wave solution is not valid. The poloidal wave couples to ξ_y, and its amplitude decays. When the radial scale reaches $2\pi/\lambda$, we expect the toroidal amplitude to have grown to equal the poloidal one. This defines the poloidal lifetime τ,

$$\tau = \frac{\lambda}{\omega'_A}. \tag{5.10}$$

Hence, we might expect these waves (with $k_z \ll \lambda$) to phase mix in time, whilst experiencing a polarisation rotation from $\xi_x \rightarrow \xi_y$.

5.2.3 Numerical Results.

i) Poloidal wave Lifetimes.

In this section we model the temporal evolution of high λ poloidal waves by again imposing the monotonically decreasing Alfvén speed profile given by equation (2.11). We take an initial wave perturbation comprising of only a $\xi_x = \sin \pi x$ profile, so that $a_1(t = 0) = 1, a_{m\neq 1}(t = 0) = 0$ and $b_m(t = 0) = 0$. The plasma is initially at rest so that $\dot{a}_m(t = 0) = \dot{b}_m(t = 0) = 0$, where $\dot{a} = da/dt$, and hence the waves energy is initially purely magnetic and stored in the tension of the displaced magnetic field lines. Note however that $b_z(t = 0) \neq 0$ (although it is small). We select these initial conditions, having $\xi_y = 0$, to demonstrate the form of the toroidal (ξ_y) displacement driven by the initial poloidal motions. With the prescription of ξ given in equation (2.1), then simply imposing large λ generates waves with "azimuthally" fine scales.

In Figure (5.1), we plot the amplitude of the wave perturbations at 3 times, taking $k_z = 1$, $A^2 = 1.0$, $B^2 = 0.9$ and $\lambda = 50$, with $N = 100$. With these parameters, an energy

invariance of only 1 part in 500 is obtained (i.e., $\sim 0.2\%$) for times up to t_N (~ 40 with $N = 100$). This introduces the superposed small amplitude fine scale oscillations seen at large x in Figure (5.1). These features are numerical in origin and hence unphysical, and they demonstrate the effects of a failure by the eigenvalue routine to calculate the eigenvectors to sufficient accuracy. Simulations with even larger λ, e.g., 500, reduce the invariance further and time evolution results using these eigenvectors show even larger numerical errors at large x. This probably occurs as a result of the Fourier approximations used to calculate the strongly localised and singular nature of these very high λ eigenfunctions (see Figures (3.12) and (3.13) for example).

We note that in equation (5.10), the poloidal lifetime τ is a function of x, since $d\omega_A/dx$ is a function of x. The rows in Figure (5.1) show times of τ, 2τ and 3τ, where here τ ($= 6.26$) is defined at $x = 0.11$, the position of maximum $d\omega_A/dx$ (which was also used to define t_N). Note that at this position, the local natural Alfvén period T_A is only 2.46, and hence the poloidal lifetime occurs after only a few periods. At higher x however, $d\omega_A/dx$ is much smaller and τ is a much larger number of Alfvén periods.

On the basis of the theory in the previous section, we would expect the ξ_x and $i\xi_y$ amplitudes in the first row to be equal at $x = 0.11$, in good agreement with the Figure. Similarly, because the maximum values of $d\omega_A/dx$ lie at small x, we would expect the phase mixing of the solutions to show finer scales at smaller rather than larger x, as is observed.

Increasing the value of λ, allows the phase mixing of the waves to proceed at the same rate whilst increasing $\tau \propto \lambda$. In Figures (5.2) and (5.3) we plot the displacement amplitudes ξ_x and $i\xi_y$ for the same initial conditions, with λ increased to 500. As we have already noted, with this value of λ the invariance is poor. The figures are snapshots at an early time in the evolution, when $t = \tau/4$ - again defined at $x = 0.11$. At this time the amplitude envelope of ξ_x will still be $\sim \sin \pi x$ - shown as a dot-dashed line in Figure (5.2). At early times, equation (5.9) implies that the driven toroidal response should be given by

$$i\xi_y = \frac{d\omega_A}{dx}\frac{t}{\lambda}\xi_x \sim \frac{d\omega_A}{dx}\frac{t}{\lambda}\sin \pi x. \tag{5.11}$$

The dot-dash line in Figure (5.3) represents this predicted envelope, and the agreement with the theory is excellent, with the proviso that there is some small numerical error at large x.

Modifying the initial ξ_x displacement to consist of only the second harmonic

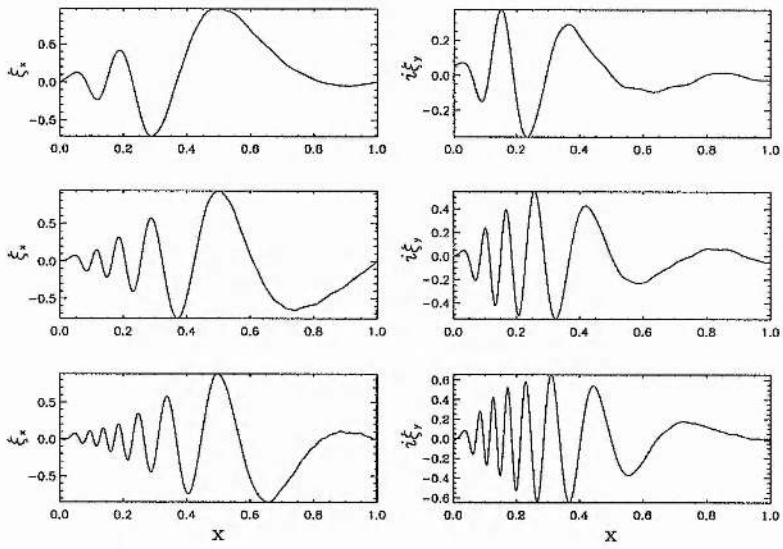

Figure 5.1: The rows of this figure show the amplitudes of ξ_x and $i\xi_y$ as a function of x, at times $t = \tau, 2\tau, 3\tau$ - where τ is defined at $x = 0.11$.

Fourier mode, changes the amplitude of the driven ξ_y envelope, and introduces extra nodes into the profile. Numerical results (not shown) reproduce the expected envelope, and hence we can be confident that the theory is correct.

However, since $d\omega_A/dx$ varies with x, it is not easy to quantify the exact timescales for poloidal oscillations to become toroidal. To illustrate τ further, we reduce the amplitude of B^2 to 0.1. Fortunately, this changes the nature of the governing eigenvalue problem, and greatly improves the energy invariance of the system. It also has the effect of making $d\omega_A/dx$ more symmetrical about $x = 0.5$, with the peak lying at $x = 0.432$. All the subsequent results shown in this and the following chapter retain energy invariance to around 1 part in 10^{10}. In Figure (5.4) we plot the amplitude of the wave displacements which develop due to the same initial conditions, with λ again taken to be 50. Solid lines show ξ_x, whilst dot-dash lines show $i\xi_y$. At $t = \tau$ (now defined at $x = 0.432$), the amplitudes of both polarisations can be seen to be equal, again in good agreement with our theory.

ii) Localised Magnetospheric Poloidal Wave Simulations.

Satellite observations of poloidal Alfvén waves show them to be spatially localised in the L-shell direction, having widths which are typically $\sim 1 - 2R_E$ (Hughes et al., 1977; Singer et al., 1982; Engebretson et al., 1992). Consequently, in this section we choose

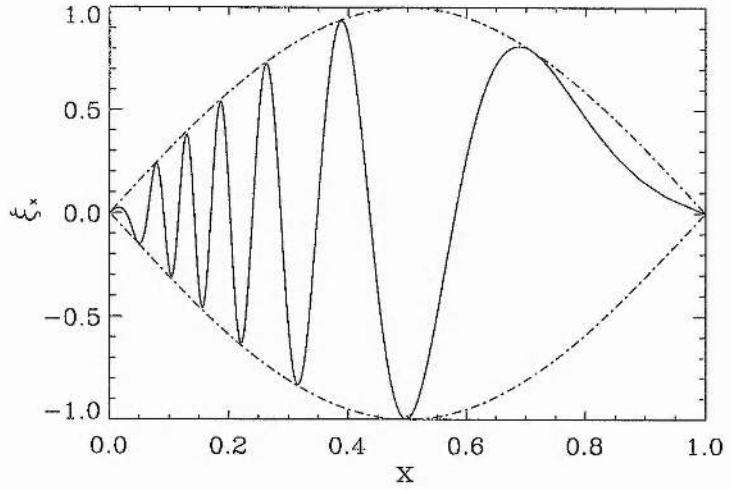

Figure 5.2: The amplitude of ξ_x displacements at $t = \tau/4$ as a function of x for $A^2 = 1.0$, $B^2 = 0.9$, $k_z = 1.0$ and $\lambda = 500$ - solid line. The dot-dash line shows the initial $\sin \pi x$ envelope.

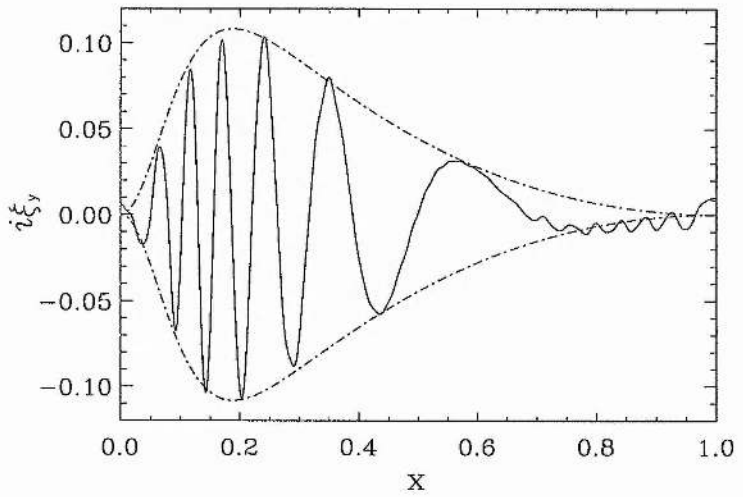

Figure 5.3: The amplitude of $i\xi_y$ displacements at $t = \tau/4$ as a function of x - solid line. The dot-dash line shows the predicted short timescales envelope described in the text.

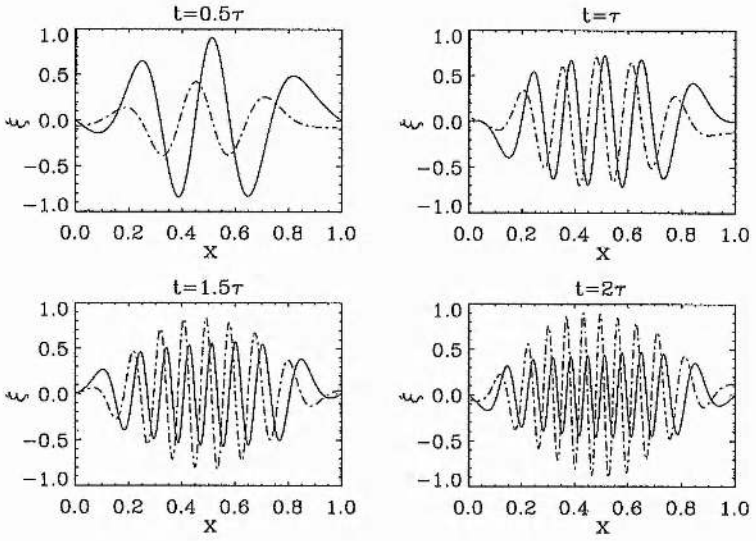

Figure 5.4: The amplitude of wave displacements at $t = 0.5\tau, \tau, 1.5\tau, 2\tau$ as a function of x. ξ_x is plotted as a solid line, whilst $i\xi_y$ is plotted as a dot-dash line.

our initial wave fields to be localised in the $\hat{\mathbf{x}}$ direction. Using the Fourier series expansions for ξ_x (see equation (2.9)), we now choose the coefficients $a_{m\leq 20}(t=0)$ to provide a Fourier approximation to the function

$$\xi_x(x, t=0) = \begin{cases} 0 & 0 \leq x < 0.65 \\ 1 - \sin(10\pi x) & 0.65 \leq x \leq 0.85 \\ 0 & 0.85 < x \leq 1.0 \end{cases} \tag{5.12}$$

to represent these localised waves. We selected the coefficients $b_{m\leq 20}(t=0)$ of the initial $i\xi_y(x, t=0)$ displacement so that the initial disturbance represents a torsional Alfvén wave with a purely field guided Poynting flux. This implies that the initial wave disturbance is incompressible, and linearly satisfies $b_z(x, t=0) = 0$ so that

$$\frac{\partial \xi_x(x, t=0)}{\partial x} + i\lambda \xi_y(x, t=0) = 0 \tag{5.13}$$

(note that increasing λ decreases the initial ξ_y displacement $\propto 1/\lambda$). The remaining coefficients ($21 \leq m \leq N$) are then taken to be zero (N is typically ~ 150). We again take $k_z = 1$, $A^2 = 1.0$ and $B^2 = 0.1$.

The variation with λ given in equation (2.1) implies that the initial twisted flux tubes comprising the torsional Alfvén waves are standing in the azimuthal direction. Ob-

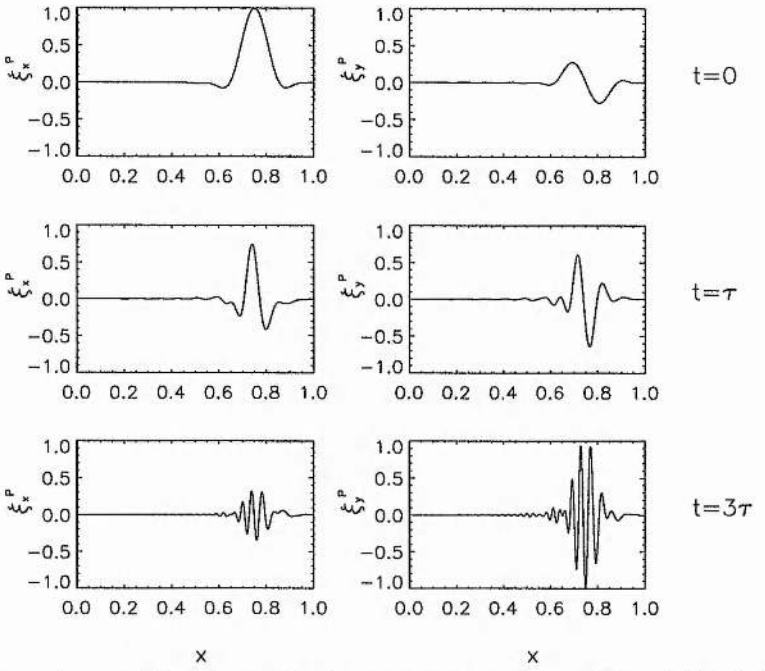

Figure 5.5: Snapshots of the physical plasma displacements ξ_x^P and ξ_y^P :(a) Initial displacements (t=0), (b) $t = \tau$, (c) $t = 3\tau$.

servations and theory show that drift-bounce resonance generated waves are generally propagating in the azimuthal direction (Southwood and Kivelson, 1982; Chen and Hasegawa, 1988; Takahashi et al., 1990). Since travelling waves can be synthesised from a summation of two standing waves, the conclusions from this numerical study should be applicable to the observed travelling waves.

In Figure (5.5), first row, we show the initial plasma displacements for $\lambda = 50$. In rows two and three, we show the displacements ξ_x^P and ξ_y^P at later times, also for $\lambda = 50$. The phase mixing of the wave fields in both the poloidal and toroidal directions are clearly visible. Also, by the time shown in the second row, the wave is no longer dominated by poloidal motions. In fact, at this time the amplitudes of the two polarisations are approximately equal - as expected when the time $t = \tau$. By the time shown in the third row ($t = 3\tau$), the wave polarisations have switched importance and the wave is again dominated by toroidal oscillations.

In order to further examine the polarisation rotation, we can consider the total

energy density of the waves. The total energy density (e_T) at any point within our simulation box is given by

$$e_T = \frac{1}{2}\rho(\dot{\xi}_x^2 + \dot{\xi}_y^2) + \frac{1}{2\mu_0}(b_x^2 + b_y^2 + b_z^2). \tag{5.14}$$

We choose to define the energy densities associated with the poloidal (e_p) and the toroidal (e_t) polarisations as

$$e_p = \frac{1}{2}\rho\dot{\xi}_x^2 + \frac{1}{2\mu_0}b_x^2 \tag{5.15}$$

$$e_t = \frac{1}{2}\rho\dot{\xi}_y^2 + \frac{1}{2\mu_0}b_y^2 \tag{5.16}$$

$$\tag{5.17}$$

and define the compressional energy density as

$$e_c = \frac{1}{2\mu_0}b_z^2. \tag{5.18}$$

However, e_c is initially zero, and remains small compared to e_p and e_t throughout all the high λ simulations which we consider in this section. In Figures (5.6) and (5.7), we plot e_p and e_t as a function of x and t. The decay of the poloidal oscillations, and the growth of the toroidal ones, are clearly shown. The waves are initially localised around $x = 0.75$, and the wave energy remains field guided and does not propagate away from this region. In Figure (5.7), the double peaked form of the initial ξ_y displacements (which removes compression form the initial waves) can be clearly seen near $t = 0$. As time evolves, the poloidal components drive the peak of toroidal energy centred on $x = 0.75$.

In Figure (5.8) we plot the $\hat{\mathbf{x}}$ integrated energy densities $E_p = \int_0^1 e_p dx$ and $E_t = \int_0^1 e_t dx$ as a function of time for $\lambda = 50$ (on this scale $E_c = \int_0^1 e_c dx$ is indistinguishable from the time axis). Again the polarisation rotation from initially poloidal, to asymptotically toroidal is apparent. The natural torsional Alfvén wave period (τ_A) at the centre of the initial disturbance (at $x = 0.75$) is 6.5 units. The time taken for E_t to equal E_p is the poloidal lifetime τ. Clearly, in this example $\tau \gg \tau_A$ and we consider this fact in section (5.2.4). In Chapter 6, we use this difference in timescales to utilise the method of multiple timescales in an analytical analysis.

In Figure (5.9) we plot the time taken for E_t to equal E_p as a function of λ. We have maintained the same initial ξ_x profile, and an identical $v_A(x)$. However, in order to

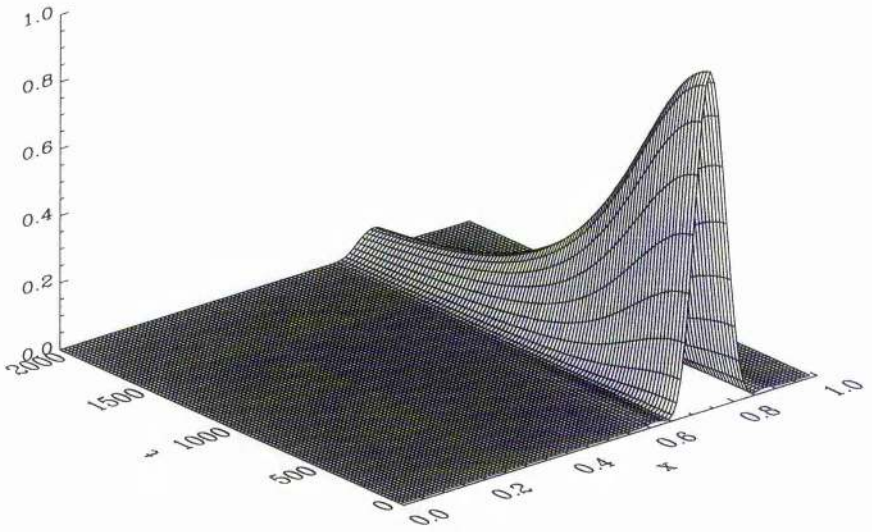

Figure 5.6: Time evolution of the poloidal energy density e_p as a function of x and t, for $A^2 = 1.0$, $B^2 = 0.1$, $k_z = 1.0$ and $\lambda = 50$. These values give $\tau \sim 498.7$ (at $x = 0.75$).

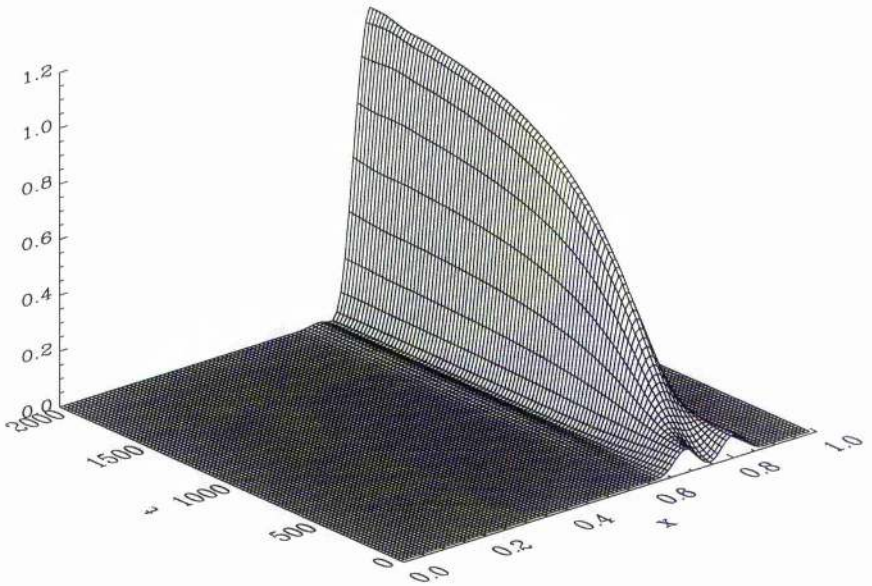

Figure 5.7: Time evolution of the toroidal energy density e_t as a function of x and t, for $A^2 = 1.0$, $B^2 = 0.1$, $k_z = 1.0$ and $\lambda = 50$.

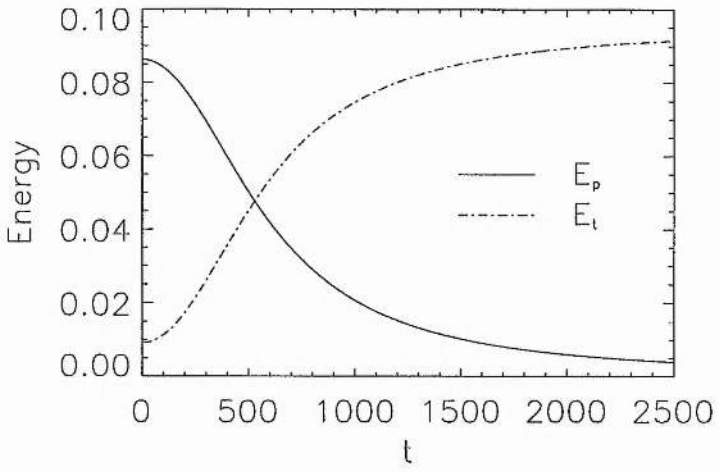

Figure 5.8: Time evolution of the $\hat{\mathbf{x}}$ integrated energy densities $E_p = \int_0^1 e_p dx$ and $E_t = \int_0^1 e_t dx$. The polarisation rotation from poloidal to toroidal is clearly shown.

satisfy the initial field guided Poynting flux condition the initial amplitude of ξ_y varies $\propto 1/\lambda$ (see equation (5.13)). The poloidal lifetime (on the basis of the integrated energy densities) is clearly proportional to λ. Using equation (5.10), we would expect the gradient of this graph to be given by $(\omega'_A)^{-1}$. For $A^2 = 1.0$, $B^2 = 0.1$, and $k_z = 1$, then at $x = 0.75$ we find that $(\omega'_A)^{-1} = 9.97$. This is in good agreement with the gradient in Figure (5.9) (defined using the energy densities) of 9.87.

5.2.4 Discussion.

i) Poloidal MHD Alfvén Wave Lifetimes.

The numerical results presented in the previous sections clearly suggest that large (but finite) λ MHD poloidal Alfvén waves excited in an inhomogeneous magnetosphere will have a finite lifetime with a poloidal polarisation, in accord with the theory in section (5.2.2). In particular, Figure (5.8) suggests that asymptotically in time these large λ waves will approach a purely toroidal polarisation state.

This concept was first discussed by Radoski (1974), and (as we have discussed in Chapter 4) he found that completing a Fourier superposition of the singular terms arising from the Alfvén resonances implied that the poloidal wave fields would decrease $\propto 1/t$,

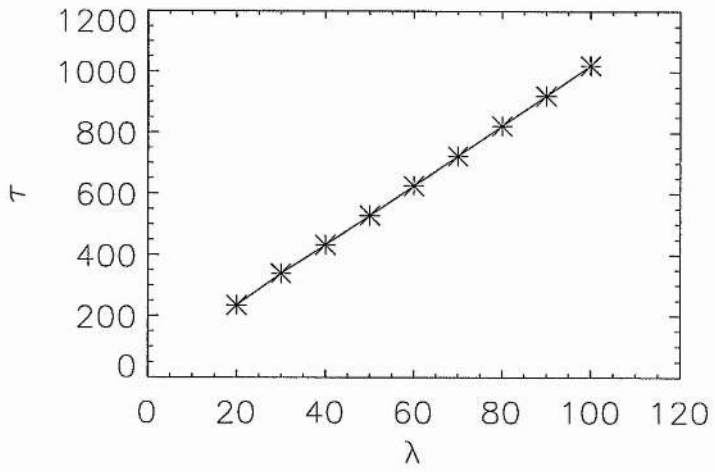

Figure 5.9: Plot of poloidal lifetime τ (calculated as the time when $E_t = E_p$) verses λ. Asterisks show simulation results using $20 \leq \lambda \leq 100$ (N.B. For $\lambda \lesssim 10$, the wave is no longer initially dominantly poloidal).

whereas the toroidal wave fields tended (in an ideal plasma) to a non-decaying oscillating function having the same form as the decoupled ($\lambda = 0$) toroidal Alfvén waves.

In our numerical model, we have introduced initially field guided torsional (dominantly poloidal) Alfvén waves and observed a similar polarisation rotation. Consequently, it appears that not only do low m compressional poloidal disturbances (fast MHD waves) decay into toroidal waves as they resonantly drive essentially Alfvénic waves at the Alfvén singularity (Chapter 4), but also large m magnetospheric ($k_z \ll \lambda$) poloidal waves (themselves essentially incompressible) approach a similar asymptotic state comprising waves with only a toroidal component.

We also investigated cases where the initial perturbation is not purely field guided. In the magnetosphere, $k_z \approx n\pi/L_z$, where L_z is the field line length. For low field aligned harmonics, we normally find $k_z \sim 1/L_z \ll \lambda$ (we consider cases where $k_z \gtrsim \lambda$ in section (5.3)). If we consider the wave field solenoidal constraint, $\nabla.\mathbf{b} = \mathbf{0}$, then we expect

$$k_x b_x + k_y b_y + k_z b_z = 0. \tag{5.19}$$

Hence with k_x given by equation (5.7), b_z can be non zero and still satisfy $k_z b_z \ll k_x b_x, k_y b_y$. Hence, the polarisation rotation from $b_x \rightarrow b_y$ (or $\xi_x \rightarrow \xi_y$) will still occur as a result of

$k_x b_x \sim -k_y b_y$ since k_x steadily increases according to equation (5.7).

This was verified by our numerical simulations (not shown), and is encouraging as it implies that so long as $k_z \ll \lambda$ (as is the case for these waves in the magnetosphere) the polarisation rotation previously discussed will be a robust feature of the wave evolution, and does not require a stringent field guided energy condition.

We note that although b_z is small compared to ξ_x and ξ_y (or b_x and b_y) it is the small b_z that is responsible for coupling the ξ_x and ξ_y equations (5.1) and (5.2) and causes the drift from radial to azimuthal polarisation. Although b_z is a small perturbation, it is the gradient λb_z or $\partial b_z/\partial x$ that is important, and this will be of a higher order than b_z. In Chapter 6 we derive an analytic poloidal Alfvén wave lifetime by using the method of multiple timescales. This approach is made possible because of the ordering $b_z \sim 1/\lambda$.

ii) Magnetospheric Poloidal Alfvén Wave Evolution.

The numerical model we have used here is a simple box model comprising straight field lines, and is one which allowed a 1-D $\hat{\mathbf{x}}$ (radial) time dependent wave solution to be determined. In more complex geometries, such as dipole magnetic fields (Radoski, 1967; Dungey, 1967), the ordering of the field aligned magnetic field component $b_{||} \sim \xi_y/\lambda$ is still valid. Radoski (1967) considered the case of $m \gg 1$ and obtained a guided poloidal mode where

$$\frac{\partial h_L E_L}{\partial \phi} = \frac{\partial h_\phi E_\phi}{\partial L}, \tag{5.20}$$

where L represents the radial, and ϕ the azimuthal co-ordinates in the dipole geometry, with h_L and h_ϕ scale factors given by $h_L = a\cos^3\theta/(1+3\sin^2\theta)^{\frac{1}{2}}$ and $h_\phi = La\cos^3\theta$. The field lines are described by $r = La\cos^2\theta$ (a is the Earth's radius (R_E) and θ is dipole latitude). In an entirely analogous way to the straight field case, we can expect that as phase mixing occurs in an initially poloidal disturbance, the wave polarisation will rotate from poloidal to toroidal so as to keep $b_{||}$ small.

If we adopt the dipole magnetic field toroidal Alfvén wave periods considered by Anderson et al. (1989), (neglecting variations with local time) then

$$\omega_A(L) = \frac{CL^{-a}}{\sqrt{L-1}} \tag{5.21}$$

where L is the McIllwain parameter, the equatorial plasma density varies as L^{-q}, $a = (7-q)/2$, and C is a constant. Choosing $q = 4$, a typical L value of $L = 7$, waves with $100s$ period and $m = 100$, then (at the equator) $\tau \sim 760s \sim 13$ minutes. This provides an estimate of the time before ideal poloidal pulsations become dominantly toroidal.

In the real magnetosphere, both the poloidal and toroidal wave components will be damped by driving Pedersen currents in the resistive ionospheric boundaries. A numerical calculation of the ionospheric damping rate of second harmonic poloidal pulsations in a dipole geometry was completed by Newton et al. (1978). They found that for typical dayside height integrated Pedersen conductivities $\Sigma_P \sim 10-20$ mhos (9×10^{12} - 1.8×10^{13} esu), at $L = 7$, the damping decrement $\gamma/\omega_r \sim 0.005-0.003$ (see for example the top of their Figure (5) - which corresponds to fixed end second harmonic poloidal waves). If we define the e-fold ionospheric damping time as τ_I, then these values correspond to $\tau_I = 32 - 53$ Alfvén wave periods. With $\tau_A \sim 100s$, this gives $\tau_I \sim 0.9 - 1.5$ hours. This is much more than the previously estimated poloidal lifetime. Consequently, depending on the ratio τ_I/τ, magnetospheric poloidal waves could experience a polarisation rotation from $\xi_x \rightarrow \xi_y$, within their ionospheric lifetimes.

In a realistic kinetic plasma, after a time τ_k the phase mixing will reach a radial length scale $L_k = 2\pi/\omega'_A\tau_k$, such as the ion Larmor radius. At this point, the phase mixing may saturate at radial scales $\sim L_k$ (e.g., Rankin et al. (1993)), and hence the MHD results will require revision. However, if $\tau < \tau_k$, then we can predict that waves which are observed to have a dominant poloidal polarisation will have been driven a time less than τ ago.

Local plasma conditions may be critical in determining when high m second harmonic poloidal waves are excited. Engebretson et al. (1992) found using AMPTE-CCE data that Pc4 waves of this type are preferentially excited during quiet geomagnetic conditions, and are perhaps associated with plasmaspheric re-filling which creates conditions favourable for wave excitation. Singer et al. (1982) also observed Pc4 waves of this type which were correlated with plasmapause density gradients. They also saw a wave gap in their data between regions supporting pulsations, associated with a plasma density depletion, which suggests that the ambient plasma density might be critical in determining where waves are driven. If local plasma conditions are important, then these same local conditions could determine the speed with which the polarisation rotation occurs. In regions where ω'_A is large, the poloidal Alfvén wave lifetime will be small and thus these waves are less likely to be observed in these locations.

Our simulations have considered the solution to an initial value problem: the boundary conditions correspond to the initial bounce resonance driven fields. In that sense, our results may be more applicable to situations where the waves are no longer being driven. Where a continuous energy source is present, and the wave particle interactions remain active, a summation over repeatedly driven evolving wave solutions may be a more accurate representation of the behaviour which would be observed.

We should also note that in a dipole magnetic field, the eigenfrequencies of the undriven, decoupled poloidal and toroidal wave operators are different because of the different functional variation of the scale factors in each of the operators. The frequency variation we have used above strictly applies to toroidal rather than poloidal waves. However, since the difference between the two eigenfrequencies is typically small (e.g., Wright and Smith (1990) found a $< 1\%$ difference between the poloidal and toroidal eigenfrequencies for second and higher harmonics in a study of Alfvén waves in the Jovian magnetosphere), their variation with L should be similar, and the above estimate of τ should be a reasonable approximation.

The fact that the eigenfrequencies of the two operators are different on a given field line makes it technically impossible to synthesise a purely torsional Alfvén wave in a geometry such as a dipole (Cross, 1988). In fact, only very specific geometries (such as the box model) allow purely torsional waves to be generated (Wright, 1990). This is a point to which we return later.

iii) Hodograms of Poloidal MHD Alfvén Wave Fields.

In addition to considering simply the polarisation rotation experienced by evolving poloidal waves, we can also examine the evolution which would be observed by satellites crossing them. In Figure (5.10) we plot hodograms showing the evolution of the physical displacements ξ_x^P and ξ_y^P, each panel showing a time interval of $3\tau_A$ (we choose $\lambda = 50$ so that $\tau \sim 77\tau_A$). The columns show the fields at the centre and on either side of the initial disturbance profile (at $x = 0.7, 0.75, 0.8$), whilst the rows show the waves at different times during the simulation.

We can clearly see at $t = 0$ that ξ_x^P dominates ξ_y^P, and initially these disturbances oscillate in phase (or anti-phase depending on their position relative to $x = 0.75$), representing torsional Alfvén waves having field guided Poynting flux. However, by $t = \tau$, the

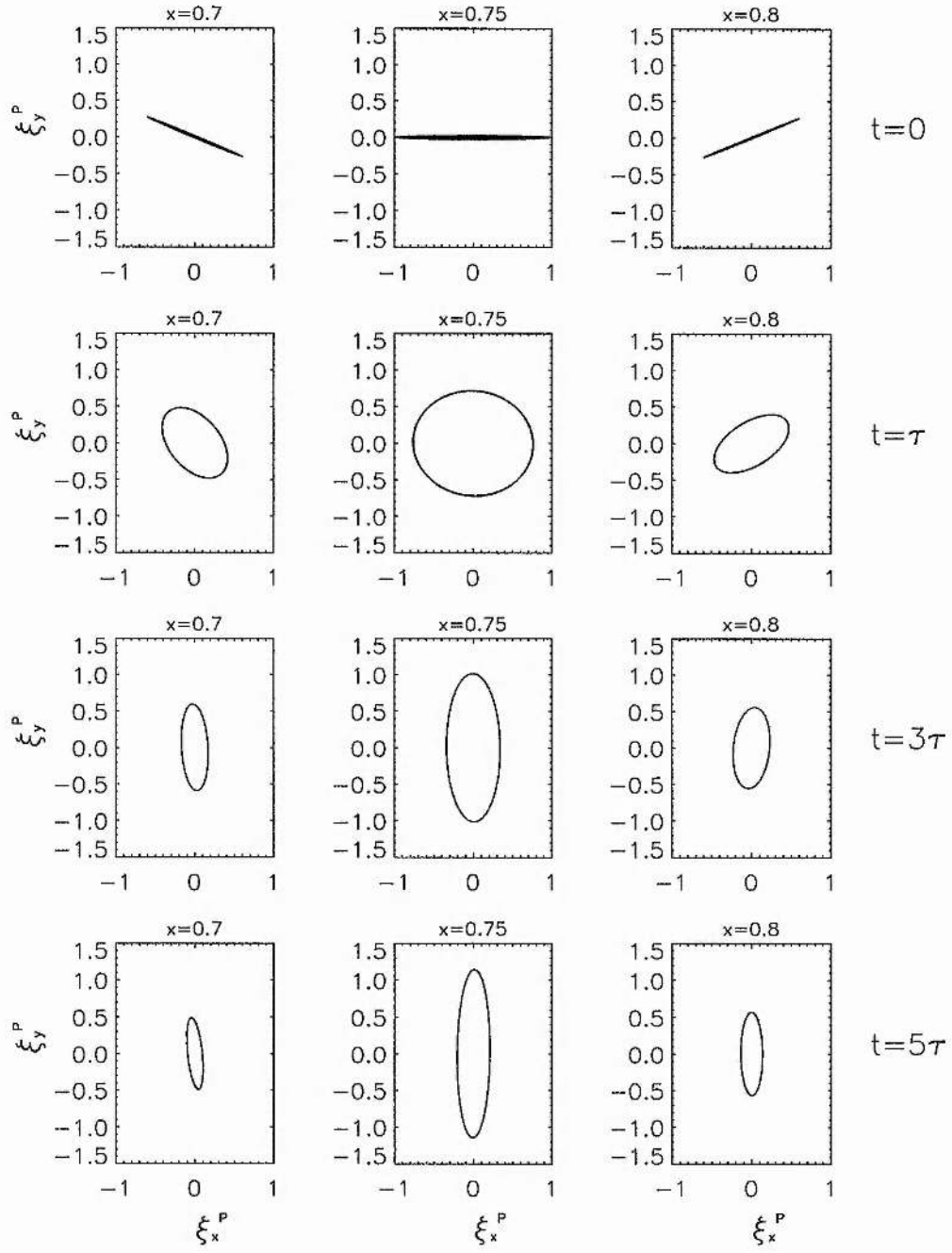

Figure 5.10: Hodograms showing the evolution of the plasma displacements ξ_y^P verses ξ_x^P. Each panel shows three Alfvén periods of poloidal wave evolution. Columns depict the wave variation in L at $x = 0.7$, $x = 0.75$ (at the centre of the initial disturbance), $x = 0.8$; Rows show the fields at times $t = 0$, $t = \tau$, $t = 3\tau$, and $t = 5\tau$.

amplitude $\xi_x^P \approx \xi_y^P$. At this time, we can see that the component of ξ_y^P which has been driven by phase mixing, is now $\pi/2$ out of phase with ξ_x^P (this is particularly clear in the central panel). This is to be expected from the analysis in section 4.1, since the driven component of $\xi_y^P = -ik_x\xi_x^P/\lambda$, with k_x as given in equation (5.7). Rather than being linearly polarised, the waves have become circularly polarised at $t = \tau$. As t increases further ξ_x^P continues to decrease in amplitude and the waves develop an elliptical polarisation. At $x = 0.7, 0.8$, the polarisation ellipses are slightly skewed, due to the initial ξ_y^P which was imposed to ensure $b_z(x, t = 0) = 0$.

Azimuthally travelling solutions may be found by summing two standing wave solutions, of which one has been presented here. The change from poloidal to toroidal polarisation is preserved, however, at $t = \tau$ the travelling waves are more linearly rather than circularly polarised.

Hughes and Grard (1984), used data from GEOS1, ISEE1 and ISEE2 to study second harmonic geomagnetic pulsations which were observed at the inner boundary of the plasma sheet. These waves were dominantly radially polarised, and were believed to have been driven by bounce resonance with energetic ($\sim$ 5 keV) ions. The polarisations of the waves observed by the ISEE satellites were unusual. In Figure (8) of Hughes and Grard, both ISEE1 and ISEE2 saw elliptically polarised waves whose transverse field amplitudes varied with UT. However, the polarisation changes seen by the two satellites could not be explained simply in terms of just static LT or co-incident UT descriptions. We do not attempt to re-analyse the data of Hughes and Grard (1984) here, but believe that the polarisation rotation we have discussed could be important in the evolution of waves such as those which they observed. If poloidal waves do experience a polarisation rotation in time, then the ellipticity and the skewed angle of the polarisation ellipse at any time will be determined both by the details of the drift-bounce resonance excitation mechanism (which will govern the initial wave configuration) and by the evolution of the wave fields in the inhomogeneous magnetospheric plasma. Consequently, the time at which a satellite such as ISEE crosses a pulsation (which will be localised in L-shell) may be critical in determining the wave fields which are observed.

In addition, poloidal Alfvén waves are often observed (Takahashi et al., 1990) to have phase velocities in the azimuthal direction (a requirement if they are driven by a drift or drift-bounce resonance mechanism (Southwood and Kivelson, 1981; Southwood and Kivelson, 1982)). Hence, the evolving poloidal wave fields can also be moving with respect

to an observing satellite. In the ISEE1 and ISEE2 observations of Hughes and Grard (1984) (at $L \sim 7-8$), the two satellites observed poloidal waves with opposite polarisations for $t \sim 30$ minutes, although they were only separated by ~ 9 minutes in their orbits. This was interpreted as possibly indicating that the poloidal waves disturbances were following the orbiting ISEE satellites. Our estimate of τ, for similar L-shells, from the previous section was only 13 minutes. Consequently, in analyses of data from poloidal Alfvén waves, we believe that the polarisation rotation we have discussed should be included as it constitutes an important feature of high m poloidal wave evolution in the magnetosphere.

iv) Dipolar Poloidal Alfvén Wave Studies.

Recently, Ding et al. (1995) considered the temporal evolution of poloidal Alfvén waves in a dipole geometry. Some of their results were quite different in character from those found by Radoski (1974) and our present study. At early times the results of Ding et al. (1995) (their Figure 2 - reproduced as our Figure (5.11)) agree with previous work, and show a switch from poloidal to toroidal perturbations. However, at later times the polarisation changes from being toroidal to poloidal to toroidal in a cyclic pattern. This behaviour is at odds with the irreversible transition from poloidal to toroidal motions discussed in other studies.

Why does this discrepancy arise? Could it be a result of working in a dipole geometry? We find that this is not the case, and favour the following explanation in terms of phase mixing and numerical resolution: Given the grid resolution and other quantities from Ding et al.'s paper, we anticipate that the phase mixing length will equal the numerical grid resolution size after a finite time, which is less than their simulation duration.

To excite guided poloidal waves, Ding et al. (1995) imposed a radially localised poloidal disturbance, chose $\lambda \gg 1$, and added a small toroidal wave component to ensure a field aligned Poynting flux at $t = 0$ (N.B. a poloidal wave has a radial ξ and b (i.e. ξ_L, b_L), and an azimuthal E (i.e., E_ϕ), whilst a toroidal wave has an azimuthal ξ and b (i.e., ξ_ϕ, b_ϕ) and a radial E (i.e., E_L)).

The poloidal component which they impose takes the form

$$E_{1\phi} = E_{pert} f(q) \cos(m\phi) \exp\left[-(L-7)^2/L_W^2\right] \tag{5.22}$$

where q is a field aligned co-ordinate which varies $-1 \leq q \leq +1$ between the endpoints of

the field lines ($f(q) = \sin(\pi q)$),$m(= 100)$ is the azimuthal wavenumber of the waves (which are standing in azimuth) and $L_W(= 0.3)$ is the radial width of the waves centred on $L = 7$. The initial toroidal component is

$$E_{1L} = \frac{\sin(m\phi)}{mh_L \cos(m\phi)} \frac{\partial}{\partial L}(h_\phi E_{1\phi}) \tag{5.23}$$

where h_L, h_ϕ and h_q are the scale factors of the dipole field.

Ding et al. (1995) found that in their simulation the poloidal component of their waves oscillates with a period $T_P \sim 6.99t_A$, whilst their toroidal components oscillate with a "fast" period of $T_{fast} \sim 6.97t_A$, t_A being a normalising Alfvén period. In their Figure (2) (reproduced here as our Figure (5.11) - which shows the temporal evolution of the velocities and fields in the centre of their initial disturbance at $L = 7$), the toroidal component initially increases (from its small initial value) whilst the poloidal component can be seen to decrease. However, at $t \sim 25t_A$, the toroidal component reaches a maximum, its amplitude stops increasing, and then decreases until its amplitude is zero at $t \sim 50t_A$. This oscillation cycle repeats itself so that the toroidal component has another node at $t \sim 100t_A$. Ding et al. (1995) call this second toroidal period T_{slow}.

By completing a Fourier transform of the time series of the wave magnetic fields b_L and b_ϕ at $L = 7$, Ding et al. found a single poloidal frequency $f_P \sim 0.143t_A^{-1}$ and two toroidal frequencies $f_{T1} \sim 0.153t_A^{-1}$ and $f_{T2} \sim 0.134t_A^{-1}$. These correspond to periods of $6.99t_A$, $6.54t_A$ and $7.46t_A$ respectively. They interpret the periods T_{fast} and T_{slow} to be the result of beating between the frequencies f_{T1} and f_{T2}, as this gives resulting beat periods of $\sim 6.97t_A$ and $\sim 109.29t_A$.

A crucial point in Ding et al.'s paper is that in their discussion, they mention that increasing their models radial resolution significantly increases the value of T_{slow}. They go on to suggest that the double toroidal frequency is a general characteristic of magnetospheric poloidal Alfvén waves, and that the beating between these two frequencies could possibly explain the long period polarisation reversals such as those seen by Hughes and Grard (1984). Further unpublished results (R.E. Denton, *Personal Communication*) also show the beat period to be dependent on the grid resolution. Hence, we can identify the beats as a finite grid resolution effect in the following way.

We would expect Ding et al. (1995) to observe phase mixing of their poloidal disturbance in the radial direction. Inspection of their Figure (3) (reproduced as our Figures

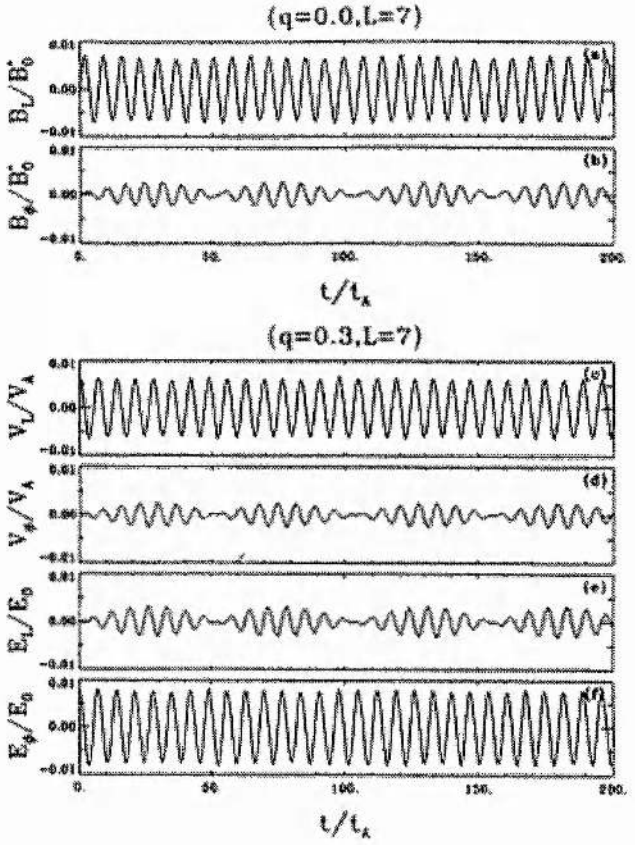

Figure 5.11: Temporal variations of the perturbed magnetic field, plasma flow, and electric field associated with the poloidal waves - reproduced from Ding et al. (1995), Figure (2). The subscripts L and ϕ indicate the radial azimuthal components respectively.

(5.12) and (5.13)) shows that their waves initially oscillate as torsional Alfvén waves, and generate phase mixing fine scales in time (see the panels $t = 52.5t_A$ and $t = 56.0t_A$). By $t = 105.0t_A$ however, this phase mixing structure is no longer apparent. We believe that this is because by $t = 25t_A$, their model is failing to resolve the MHD wave fields which it is attempting to describe.

We believe the two toroidal frequencies f_{T1} and f_{T2} seen in the Fourier transform of the b_ϕ time series taken at $L = 7$ correspond to the oscillation frequencies of the adjacent two grid cells at $L = 7 \pm 0.2$. In Figure (5.14) we plot the functions $E_{1\phi}(t = 0)$ and $\partial E_{1\phi}(t = 0)/\partial L$ (which is $\propto E_{1L}(t = 0)$ for $L \gg 1$), and over-plot the values of the

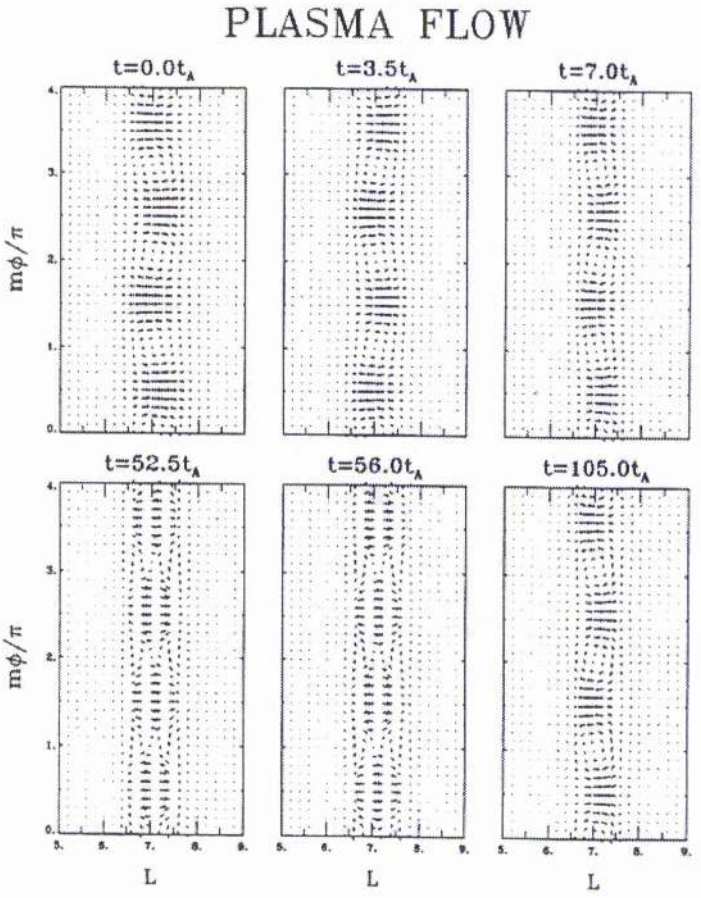

Figure 5.12: Snapshots of plasma flow (v_L, v_ϕ) for the poloidal waves, shown at $q = 0.3$ where the radial plasma flow perturbation has a maximum. Reproduced from Ding et al. (1995), Figure (3a).

functions at the finite grid points as asterisks. This shows that $\partial E_{1\phi}(t = 0)/\partial L$ peaks at the grid-points $L = 7 \pm 0.2$. Hence it seems likely that the Fourier analysis of b_ϕ at early times will be dominated by frequencies from the adjacent grid cells. Indeed, with a standard finite differencing scheme then at grid point n, we would expect

$$b_{\phi n} \propto \frac{\partial E_{1\phi}}{\partial L} = \frac{1}{2\Delta L}(E_{1\phi(n+1)} - E_{1\phi(n-1)}). \tag{5.24}$$

Further evidence comes from the fact that when ΔL is decreased (more radial grid cells), we would expect the adjacent grid cell frequencies f_{T1} and f_{T2} to be closer to each other, and hence we would expect T_{slow} to increase. This is in accord with the discussion

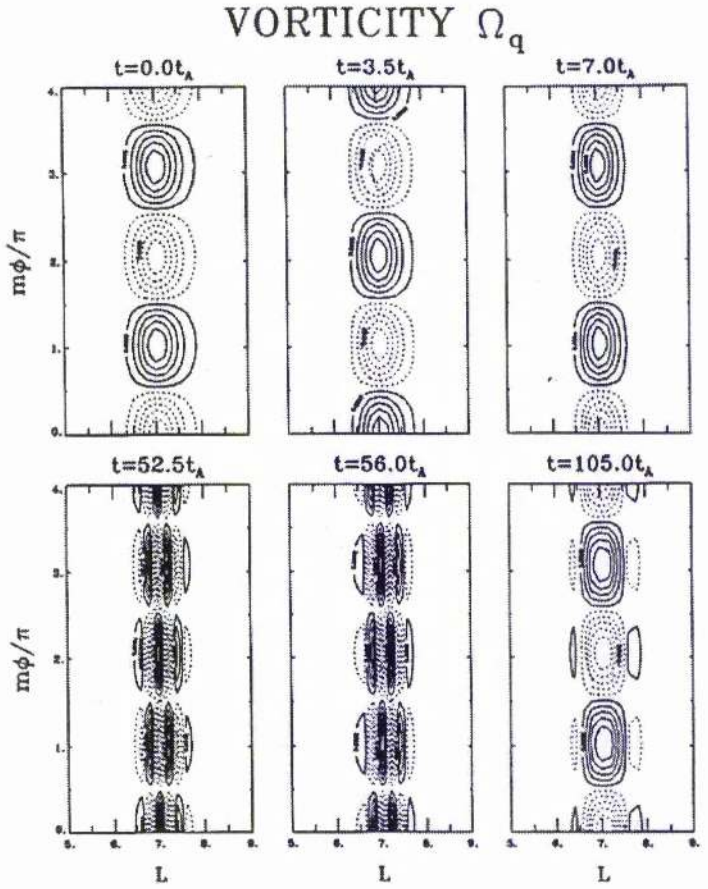

Figure 5.13: Snapshots of the corresponding contours of vorticity Ω_q for the poloidal waves, again at $q = 0.3$. Reproduced from Ding et al. (1995), Figure (3b).

of Ding et al. (1995), and the results from other unpublished runs (R. E. Denton, *Personal Communication*). Indeed, Denton says that $T_{slow} \propto 1/\Delta L$.

We can calculate the time taken in the simulations of Ding et al. (1995) for the phase mixing length to reach their radial grid scale. Assuming that to resolve a radial oscillation requires 3 nodes and 2 anti-nodes, then the finest resolvable waves will have a width of $\Delta X = 4\Delta L = 0.8$. Hence using the dipole geometry, we find at $L = 7$

$$t_{grid} \sim \frac{m}{L\Delta X \frac{\partial \omega_A(L)}{\partial L}} \sim 25 t_A. \tag{5.25}$$

Similarly, we can calculate the poloidal lifetime at the equator at $L = 7$, and predict $\tau \sim 285 t_A$. This is longer than t_{grid}, and hence the simulations do not have the resolution

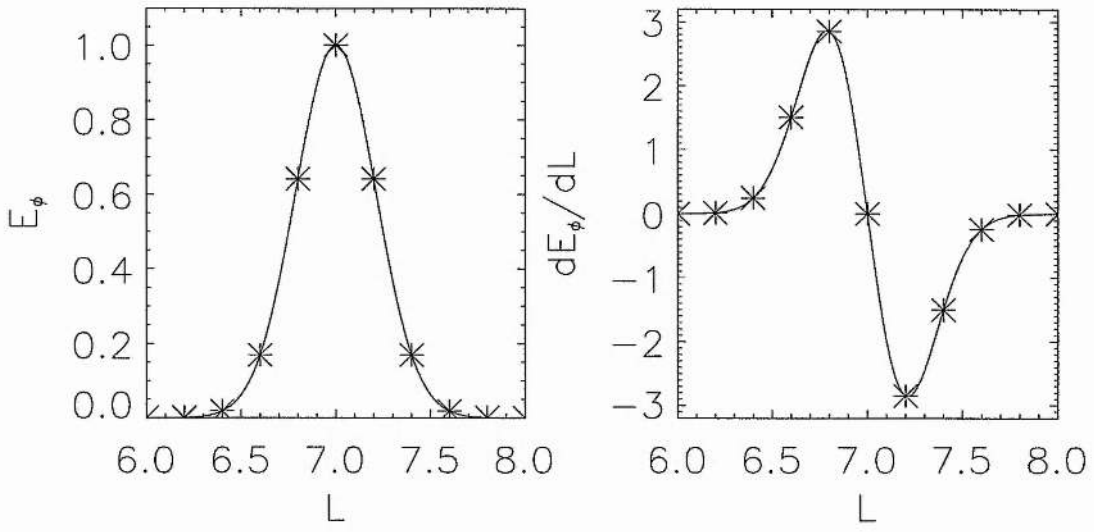

Figure 5.14: The functions $E_{1\phi}(t=0)$ and $\partial E_{1\phi}(t=0)/\partial L$ used in the study by Ding et al., (1995). The asterisks show the grid resolution of $\Delta L = 0.2R_E$ they used.

to reveal the full polarisation reversal from poloidal to toroidal. For $t > 25$, the phase mixing scale of the waves can not be resolved by the grid, and this is the reason for the unusual (and unphysical) polarisation behaviour observed in this interval. For $t < 25$ the scheme should resolve the wave fields, and the results reported for $0 < t < 25$ are in agreement with Radoski (1974) and our solutions.

The point of completing this re-analysis of Ding et al. (1995)'s results is to stress that high m poloidal Alfvén waves (even in a dipole geometry) can be expected to evolve in time due to the individual field lines within a spatially localised disturbance each oscillating at their own natural frequencies. Hence phase mixing in the L-shell direction will generate fine scales in E_ϕ, and drive a polarisation rotation from poloidal to toroidal.

In a realistic kinetic plasma, once the phase mixing reaches a radial length scale L_k, such as the ion Larmor radius, then the phase mixing may saturate with radial scales $\sim L_k$ (e.g., (Rankin et al., 1993)), and hence the MHD results will require revision. In contrast to the conclusions of Ding et al. (1995), we believe that MHD can be used to describe the early time evolution of poloidal waves, and only at later times will non-MHD effects become important.

Ding et al. (1995) argue that their results are valid, even though they have collapsed to "grid scale singular eigenfunctions", because of the impossibility of finding well behaved wave normal mode solutions in an inhomogeneous plasma without dissipation (Barston, 1964; Sedláček, 1971a; Uberoi, 1972; Southwood, 1974; Chen and Hasegawa, 1974a). As we have discussed in section (3.5), it is certainly true that a normal mode analysis, seeking to find $\exp i\omega t$ solutions to the coupled wave problem, will produce eigenfunctions which are singular where $\omega = \omega_A(r)$. However, as Barston (1964) points out, although the eigenfunctions are singular in ω, a well behaved solution can be constructed from a summation over the governing singular eigenfunctions (see Chapter 3).

In particular, in this thesis we have used this result to employ Fourier series expansions to study the temporal evolution of waves in compressible inhomogeneous plasmas. In the studies of Cally and Sedláček (1994), and Mann et al. (1995), it was found that the wave behaviour in incompressible and compressible inhomogeneous plasmas was dominated by the decoupled toroidal oscillation of field lines at their local natural Alfvén frequencies. Consequently, for numerical studies to produce results which are meaningful, they must fully resolve the phase mixing fine scales which will develop in time. We believe this is why Ding et al. fail to observe the "development of phase mixing to the extent predicted by ideal MHD".

With the above provisos it appears that the switch from poloidal to toroidal polarisation of poloidal ($k_z \ll \lambda$) Alfvén waves is observed in box (present study), hemi-cylindrical (Radoski, 1974), and even dipole (Ding et al., 1995) geometries. Thus it is likely that this behaviour will be observed in real magnetospheric geometries.

5.3 Evolution of $k_z \gtrsim \lambda$ Azimuthally Small Scale Waves.

In this section, we relax the condition $k_z \ll \lambda$ (which is applicable to waves in the terrestrial magnetosphere) and consider the numerical evolution of waves having $k_z \gtrsim \lambda$, both being large compared to $k_x(x, t = 0)$. With this ordering, clearly k_z is no longer $O(1)$ and hence equation (5.5) is no longer valid. Thus we might expect some different wave features to be revealed. We examine these here.

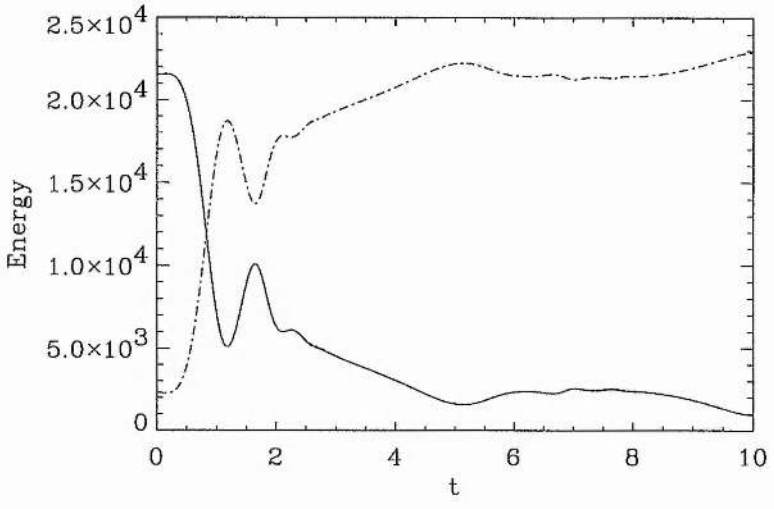

Figure 5.15: Time evolution of the $\hat{\mathbf{x}}$ integrated energy densities $E_p = \int_0^1 e_p dx$ and $E_t = \int_0^1 e_t dx$. The polarisation rotation from poloidal to toroidal is apparent, as is extra oscillations occuring as a result of the propagation of a fast wave.

5.3.1 Numerical $k_z \gtrsim \lambda$ Results.

In Figure (5.15), we plot the amplitude of E_p and E_t verses time, generated by the incompressible localised initial conditions described in equation (5.12), for $A^2 = 1.0$, $B^2 = 0.1$, $\lambda = 50$, $k_z = 500$, and $N = 100$. A similar overall asymptotic polarisation from poloidal to toroidal is apparent (c.f. Figure (5.8)), however extra oscillations in the energy transfer are also present (Note that the maximum value of E_c is still small and $\sim E_p(t = 0)/200$.) These extra features occur during the process of the polarisation rotation, because a fast mode of significant amplitude is driven, which subsequently propagates away from the initial disturbance across the background magnetic field.

In Figures (5.16), (5.17) and (5.18), we plot the poloidal, toroidal, and total energy densities e_p, e_t and e_T $(= e_p + e_t + e_c)$ as a function of x and t, for the same parameters. Several interesting features are revealed.

Firstly, the initially incompressible poloidal wave begins to asymptote towards a toroidal polarisation (as in section (5.2.3)). Secondly however, after a time $t \sim \tau$ $(= 1$ at $x = 0.75)$, a fast wave pulse can be seen to propagate towards large x. This wave reflects at $x = 1$ (at $t \approx 2.5$), and travels back towards the initial disturbance. The fast

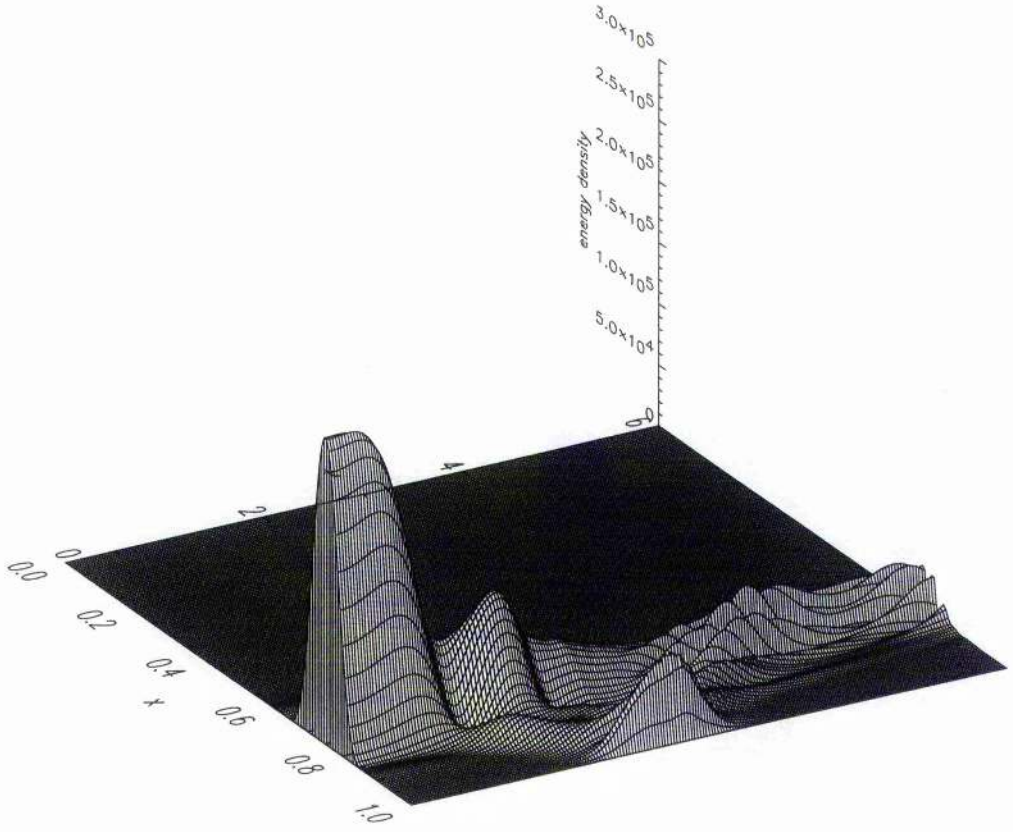

Figure 5.16: Time evolution of the poloidal energy density e_p as a function of x and t, for $A^2 = 1.0$, $B^2 = 0.1$, $k_z = 500.0$ and $\lambda = 50$. These values give $\tau \sim 1$ (at $x = 0.75$).

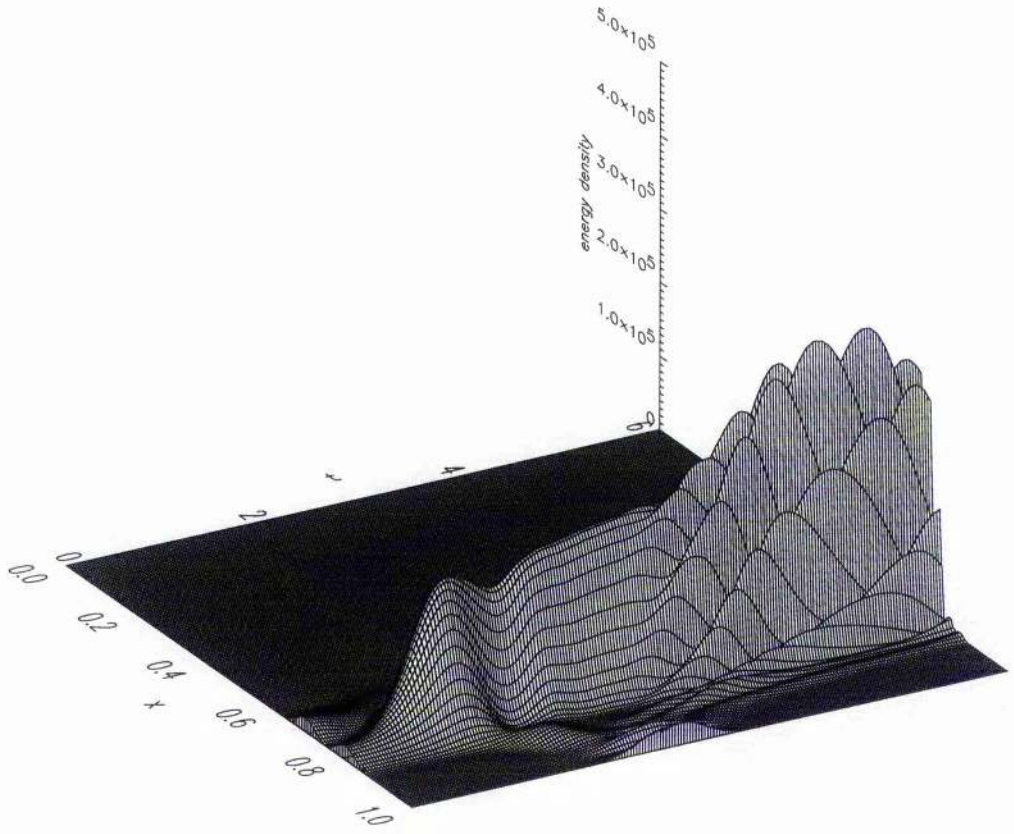

Figure 5.17: Time evolution of the toroidal energy density e_t as a function of x and t, for $A^2 = 1.0$, $B^2 = 0.1$, $k_z = 1.0$ and $\lambda = 50$.

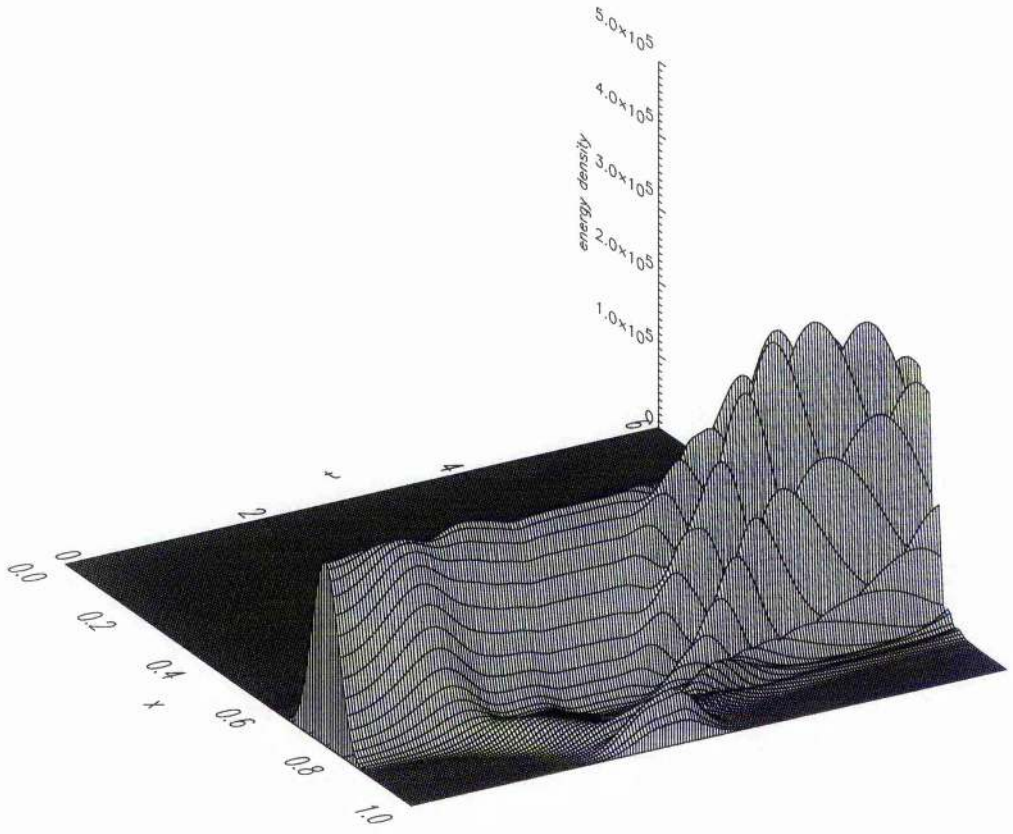

Figure 5.18: Time evolution of the total energy density e_T $(= e_p + e_t + e_c)$ as a function of x and t, for $A^2 = 1.0$, $B^2 = 0.1$, $k_z = 1.0$ and $\lambda = 50$.

waves are refracted in the inhomogeneous media, as is clearly demonstrated by the waves curved trajectory. The waves appear to have a turning point around $x \approx 0.75$. Longer time evolution results depict the fast waves repeatedly refracting towards $x = 1$, reflecting, and then returning to $x \approx 0.75$ in a periodic fashion.

This refraction is similar to that studied by Wright (1994a), in the context of waves in a magnetospheric waveguide. In his study, Wright excited low λ waves which repeatedly refracted in x (the radial direction) between a turning point (inside the magnetosphere) and a reflection at the simulation boundary (assumed to be the magnetopause). Whilst refracting in x, the waves propagated (in y) downtail. We discuss the refraction of high λ waves in section (5.3.2).

The third striking feature in these figures is the generation of fine scale large amplitude features at $t \sim 5$, $x \approx 0.75$. These apparently bizarre structures disappear once the fast wave has refracted away from the initial disturbance location, to leave again smooth energy density surfaces.

To further illustrate these features, we plot contours of constant e_p as a function of x and t in Figure (5.19), and schematically illustrate the fast wave propagation (depicted as contours in Figure (5.19)) in Figure (5.20). The decay of the initially poloidal wave, the propagation of the fast wave, and the energy density fine structure at $t \sim 5$ and $t \sim 10$ are all clearly shown. This generation of fine structure can be explained by considering summations of linear wave amplitudes. Whilst both (linearised) fast and Alfvén waves separately possess smoothly varying energy densities (quadratics of separate wave field amplitudes), when both of these field amplitudes are algebraically summed, quadratics of the combined wave fields need not necessarily be smooth.

This occurs because taking a quadratic of combined linearised wave amplitudes (e.g. $(\xi_{\alpha 1} + \xi_{\alpha 2})^2$ $(\alpha = x, y)$) produces a different result to summing the individual wave energy densities separately (e.g. $\xi_{\alpha 1}^2 + \xi_{\alpha 2}^2$). The Alfvén wave field ($\xi_{\alpha 1}$) has fine spatial scales ($\sim L_{ph}$) but a smooth energy density. The fast mode ($\xi_{\alpha 2}$) has a spatially smooth e_p. However, the sum $(\xi_{\alpha 1} + \xi_{\alpha 2})^2$ (generated where the waves trajectories cross at $t \sim 5, 10$) reveals the fine structures associated with the combination of $\xi_{\alpha 1}$ and $\xi_{\alpha 2}$.

In Figure (5.21), we plot expanded contours of the total energy density e_T around $x = 0.75$, as a function of x and t. The fine scale features around $t \approx 5$ and 10 are clearly shown (having spatial scales which decrease in time), as is the smooth total energy density when the fast and Alfvén waves are not superimposed (note that the amplitude of the lowest

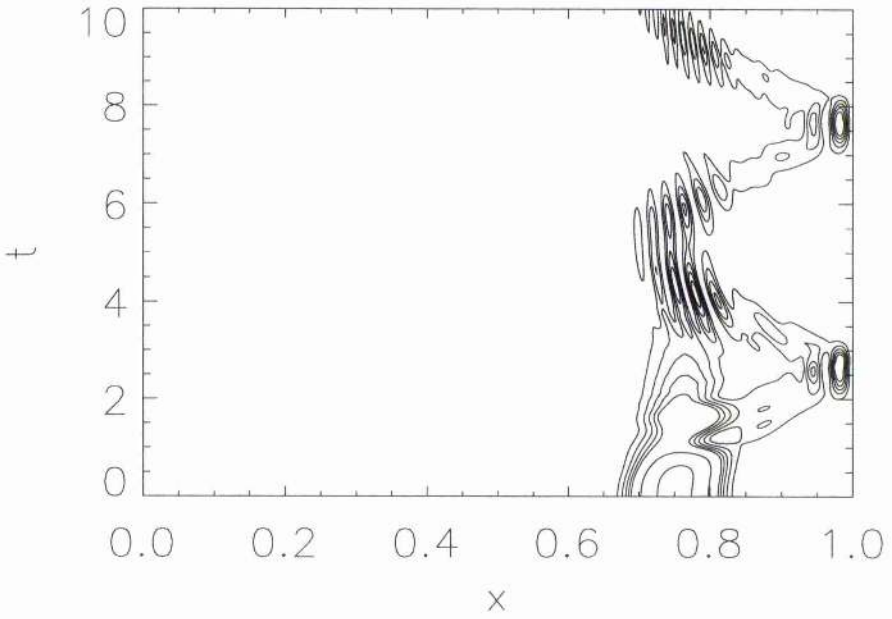

Figure 5.19: A contour plot of the poloidal energy density e_p as a function of x and t, for $A^2 = 1.0$, $B^2 = 0.1$, $k_z = 500.0$ and $\lambda = 50$. The levels plotted are $1 - 5 \times 10^4, 1 - 3 \times 10^5$)

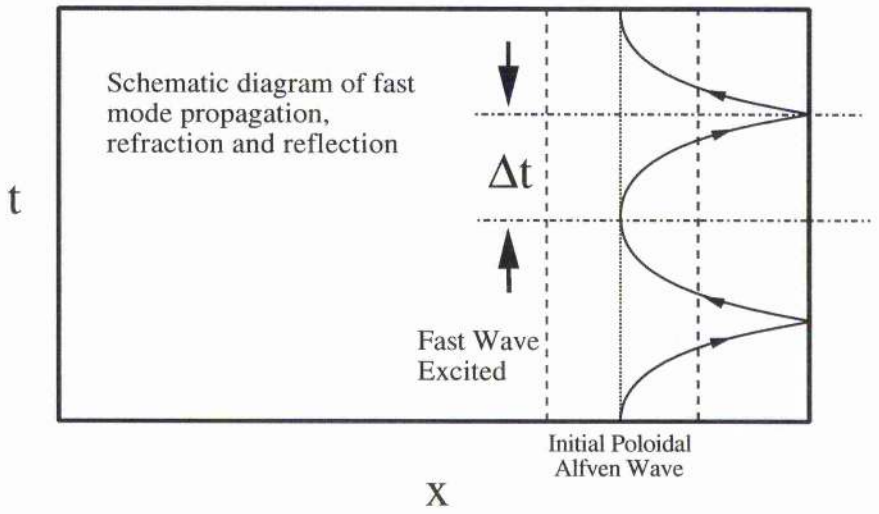

Figure 5.20: Schematic diagram of the propagation path of the fast wave, driven during the evolution of the initially poloidal Alfvén wave.

contour in this Figure is too high to show the fast waves refraction).

In Figure (5.22), we plot e_T as a function of x, at $t = 5$. At this time, the phase mixing length is 0.025. This is in excellent agreement with the observed length scale of ~ 0.024 shown in Figure (5.22), and with the displacement scales of the waves at $t = 5$ (not shown). In this instance, the dominant length scales of e_T (or e_p, e_t) are $\sim L_{ph}$, rather than $L_{ph}/2$. Which of these two scalings results, depends upon the relative phase and amplitudes of the constituent fast and Alfvén wave components. In this case, the fast wave shifts the majority of the fine scale Alfvén wave phase mixing perturbations so that they no longer oscillate about zero. Once this profile is squared, the perturbation scaling of L_{ph} is maintained by the energy densities.

5.3.2 Fast Wave Refraction Bounce Period.

The fast waves driven during the evolution of the initially Alfvénic poloidal waves, contain contributions from both e_p and e_t (i.e., both $\dot{\xi}_x$ and b_x; and $\dot{\xi}_y$ and b_y). The large amplitude of fast wave e_p and e_t, when $k_z \gtrsim \lambda$ (c.f. figures (5.6) and (5.7) when $k_z \ll \lambda$), can be understood by noting that $b_x \propto k_z \xi_x$ and $b_y \propto k_z \xi_y$. Hence, increasing k_z increases the magnitude of b_x and b_y (i.e. e_p and e_t), so that the fast wave becomes clearly visible in Figures (5.16) - (5.18). We now turn our attention to a calculation of the fast wave refraction bounce period.

Following Wright (1994a), we calculate the speed of propagation of the fast wave packet by ray tracing the path of its wavefronts in 3-D space. To calculate the time taken for a fast wavepacket to travel from the centre of the initial disturbance to the boundary of the box at $x = 1$, Δt (see Figure (5.20)), we must determine the variation of the fast waves k_x with x. Recalling the expression for the evolution of b_z in an inhomogeneous plasma discussed in Chapter 3 (equation (3.42)), then we know that the fast waves have a WKB turning point determined by $k_x(x_t) = 0$, i.e.,

$$\omega^2 = (k_y^2 + k_z^2) v_A^2(x_t) \tag{5.26}$$

where x_t is the turning point. Since the fast waves are being driven by evolving poloidal Alfvén waves, it is reasonable to assume that the resultant fast waves will have a frequency given by $\omega_f \sim \omega_A(x = 0.75)$.

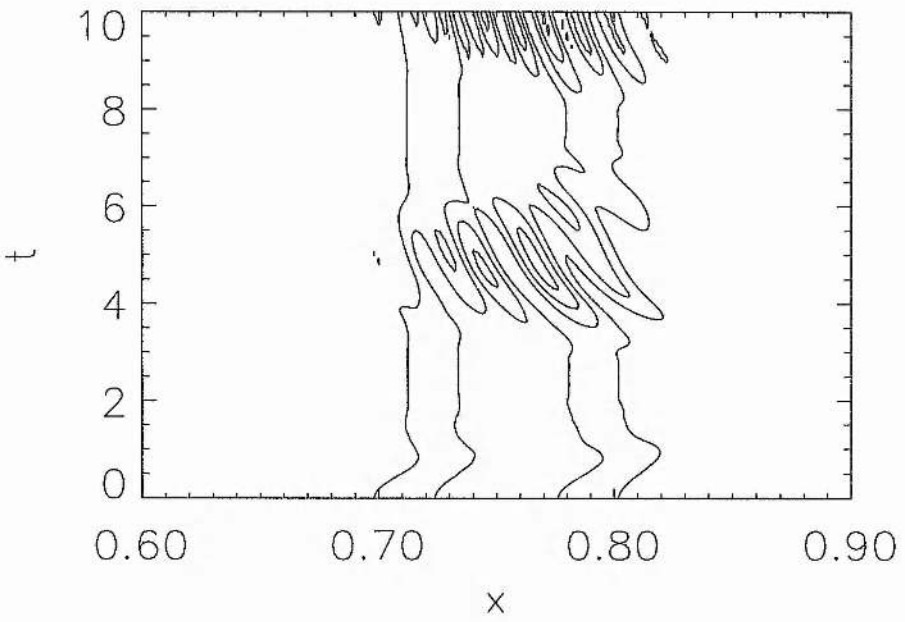

Figure 5.21: A contour plot of the total energy density e_T as a function of x and t, for $A^2 = 1.0$, $B^2 = 0.1$, $k_z = 500.0$ and $\lambda = 50$.

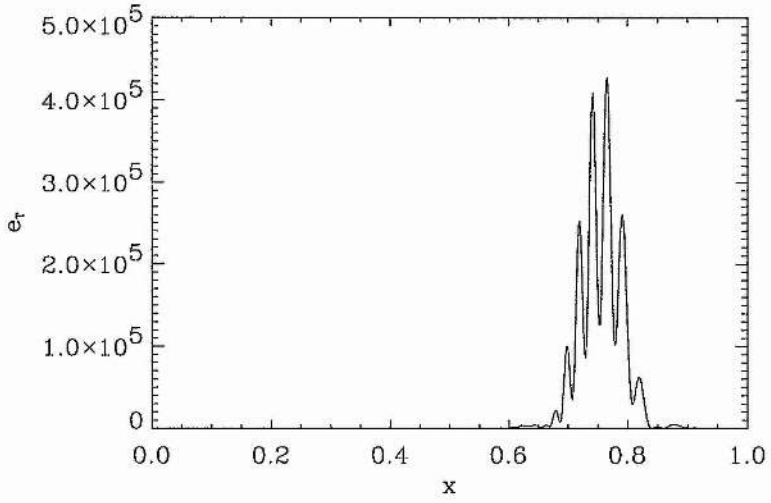

Figure 5.22: e_T verses x at $t = 5$. Again for $A^2 = 1.0$, $B^2 = 0.1$, $k_z = 500.0$ and $\lambda = 50$.

Since $k_z^2 \gg k_y^2$ (both large), we expect the turning point of the fast waves to be very close to the position of the initial poloidal Alfvén wave disturbance - i.e. $x_t \sim 0.75$. This proposition is supported by the numerical results.

Since the Alfvén speed decreases with x, the fast waves should be propagating (rather than evanescent) in the region $x > x_t$ - as is observed (see also Chapter 4, where the small λ fast cavity modes appeared ducted at large x, whilst they resonantly drove FLR's beyond the turning point). To calculate the form of $k_x(x)$, we again use the WKB form of equation (3.42) (where the second term has been neglected because of the WKB assumption of a large wavenumber in x) to obtain

$$\frac{d^2 b_z}{dx^2} + \left(\frac{\omega^2}{v_A^2(x)} - k_y^2 - k_z^2 \right) b_z = 0, \tag{5.27}$$

which should be applicable to waves in the propagation region (Inhester, 1987; Wright, 1994a). This allows the definition of a local wavenumber in x

$$k_x^2(x,\omega) = \frac{\omega^2}{v_A^2(x)} - k_y^2 - k_z^2 \tag{5.28}$$

(Wright, 1994a).

The fast wave phase fronts travel at the local Alfvén speed, in a direction governed by

$$\frac{dx}{k_x(x)} = \frac{dy}{k_y} = \frac{dz}{k_z} \tag{5.29}$$

where $k_y(=\lambda)$ and k_z are fixed. The velocity of a fast wavepacket in the x direction is given by

$$\frac{v_A(x)k_x(x)}{k} = \frac{v_A^2(x)k_x(x)}{\omega} \tag{5.30}$$

where the total wavenumber k is given by $k^2 = k_x^2 + k_y^2 + k_z^2$, and satisfies the local fast mode dispersion relation $\omega^2 = k^2(x)v_A^2(x)$. Hence, we can calculate Δt by evaluating the following integral

$$\Delta t = \int_{x_t}^{1} \frac{\omega dx}{v_A^2(x)k_x(x)} \tag{5.31}$$

where k_x is a function of x. Consequently, we are left with the equation for the refraction bounce time

$$\Delta t = \int_{x_t}^{1} \frac{\omega dx}{v_A^2(x)\sqrt{\frac{\omega^2}{v_A^2(x)} - k_y^2 - k_z^2}}. \tag{5.32}$$

With v_A^2 as defined in equation (2.11), setting $C^2 = A^2 - (k_y^2 + k_z^2)/\omega^2$, and defining a new variable X so that $x = 1 - X/\pi$ ($dx = -dX/\pi$), then this integral can be written as

$$\Delta t = \frac{A^2}{\pi}\int_0^{X_t} \frac{dX}{C^2 + B^2\cos X} + \frac{B^2}{\pi}\int_0^{X_t} \frac{\cos X dX}{C^2 + B^2\cos X} \tag{5.33}$$

where $x_t = 1 - X_t/\pi$. The required solution for Δt has hence been expressed in terms of elliptic integrals.

Knowing

$$\int \frac{dx}{\sqrt{a + b\cos x}} = \sqrt{\frac{2}{b}} F(\gamma, \frac{1}{r}) + C \tag{5.34}$$

and

$$\int \frac{\cos x dx}{\sqrt{a + b\cos x}} = \sqrt{\frac{2}{b}}\left[2E(\gamma, \frac{1}{r}) - F(\gamma, \frac{1}{r})\right] + C \tag{5.35}$$

when $b \geq |a| > 0$, and $0 \leq \pi x \leq \cos^{-1}(-a/b)$ (Gradshteyn and Ryzhik, 1965) (as is the case when $A^2 = 1.0$, $B^2 = 0.1$, $k_z = 500$, and $\lambda = 50$); and where $F(\gamma, \frac{1}{r})$ and $E(\gamma, \frac{1}{r})$ are elliptic integrals of the first and second kinds; and

$$\gamma = \sin^{-1}\left(\sqrt{\frac{b(1 - \cos x)}{a + b}}\right) \tag{5.36}$$

and

$$r = \sqrt{\frac{2b}{a + b}}; \tag{5.37}$$

then we can calculate Δt. At $X = 0$, $\gamma = 0^o$, and at $X = X_t$, $\gamma = 90^o$. With the above parameters we find that $1/r = 22^o$ and $\gamma = 90^o$, and using tabulated values (Abramowitz and Stegun, 1972) we find $E(90^o, \frac{1}{r}) = 1.51414$, and $F(90^o, \frac{1}{r}) = 1.63072$ with $E(0^o, \frac{1}{r}) = F(0^o, \frac{1}{r}) = 0$. Hence $\Delta t = 2.52033$. This is in excellent agreement with the observed refraction bounce time of ~ 2.5.

5.4 Conclusions.

In section (5.2), we presented the results from the temporal evolution of magnetospheric ($k_z \ll \lambda$) poloidal Alfvén waves in an inhomogeneous plasma. We numerically

investigated the evolution of the coupled poloidal (ξ_x) and toroidal (ξ_y) plasma displacements of these waves for large (but non-infinite) azimuthal wavenumbers (λ). We found that initially poloidally polarised waves, with a field guided Poynting flux, evolve so as to remain essentially incompressible. We observe that their polarisation rotates from a poloidal configuration to asymptotically approach a purely toroidal polarisation. We suggest that this is a result of the phase mixing of the initial poloidal disturbances in meridian planes. On this basis, we define a poloidal lifetime $\tau \sim \lambda/\omega_A'(x)$, where $' = d/dx$. This implies that satellites crossing high m poloidal Alfvén waves (often observed as Pc4 waves in the afternoon) will see a different polarisation depending on the time since the waves were excited. Moreover, if m and $\omega_A(L)$ are known, it enables us to put limits upon how recently the poloidal Alfvén wave was excited.

Consequently, high m magnetospheric poloidal Alfvén waves (with $k_z \ll \lambda$) will initially evolve as decoupled field line oscillations which phase mix in meridian planes. Asymptotically in time, their poloidal polarisation will become toroidal, as first envisaged by Radoski (1974), and the waves will become decoupled toroidal field line oscillations. The dominance of decoupled field line oscillations in the evolution of waves in inhomogeneous plasmas has been previously discussed in the literature (Cally, 1991; Cally and Sedláček, 1994; Mann et al., 1995) and in Chapter 4, and we believe that initially field guided magnetospheric ($k_z \ll \lambda$) poloidal Alfvén waves also reveal this dominant behaviour as they evolve in time.

In section (5.3), we relaxed the condition $k_z \ll \lambda$ (which resulted in field guided waves) and considered the numerical evolution of initially incompressible poloidal waves having $k_z \gtrsim \lambda$. The overall polarisation rotation of the localised Alfvén waves is maintained, however during the energy transfer from poloidal to toroidal polarisation, fast mode waves of sizeable amplitude are excited. These subsequently propagate across the background magnetic field, are refracted towards large x, and repeatedly reflect at the simulation boundary before refracting back to the wave turning point near the initial disturbance location. This interpretation is supported by an analysis in terms of the ray trajectories of fast wavepackets in which we calculated the fast wave propagation speed and determined the fast wave refraction time between the edge of the simulation domain and the turning point.

Chapter 6

Asymptotic Poloidal Alfvén Wave Solutions.

6.1 Introduction.

In the previous chapter, section (5.2.3), we presented numerical results showing how large "azimuthal" wavenumber magnetospheric ($k_z \ll \lambda$) poloidal Alfvén waves oscillate at the local Alfvén frequency, and asymptotically in time approach a purely toroidal polarisation state (see also Mann and Wright (1995)). This polarisation rotation was seen to occur on a timescale much longer than the local Alfvén period. Consequently, in this chapter we undertake a multiple timescales asymptotic analysis of the evolution of the poloidal Alfvén waves in an inhomogeneous plasma.

We adopt the same 1-D model as in previous chapters, and consider the equations initially presented in Chapter 2. We compare our analytical results with those calculated using the numerical matrix eigenvalue code.

6.2 Multiple Time-Scales Analysis.

We consider the solutions to the following equations (which were previously presented as equations (5.1), (5.2) and (5.3)).

$$\frac{1}{\omega_A^2(x)}\frac{\partial^2 \xi_x}{\partial t^2} + \xi_x = -\frac{1}{k_z^2}\frac{\partial b_z}{\partial x} \tag{6.1}$$

$$\frac{1}{\omega_A^2(x)}\frac{\partial^2 \xi_y}{\partial t^2} + \xi_y = -\frac{i}{k_z^2}\lambda b_z \tag{6.2}$$

$$b_z = -\frac{\partial \xi_x}{\partial x} - i\lambda \xi_y \tag{6.3}$$

Each of the equations (6.1) and (6.2) can be considered to describe decoupled ξ_x and ξ_y Alfvén oscillations, coupled via the compressional magnetic field perturbation b_z. We can combine these two equations into a single equation by equating b_z to give

$$\frac{1}{\omega_A^2(x)}\frac{\partial^2 \xi_x}{\partial t^2} + \xi_x = \frac{1}{i\lambda}\frac{\partial}{\partial x}\left(\frac{1}{\omega_A^2(x)}\frac{\partial^2 \xi_y}{\partial t^2} + \xi_y\right). \tag{6.4}$$

As we considered in Chapter 5, section (5.2.2), equation (6.2) implies that $b_z \sim \xi_y/\lambda$, equation (6.1) that $\xi_y \sim \xi_x/\lambda$ and hence we have $b_z \sim \xi_x/\lambda^2 \sim \xi_y/\lambda$. Knowing that to leading order $b_z \sim \xi_y/\lambda$, we have the relation

$$\frac{\partial \xi_x}{\partial x} + i\lambda \xi_y \sim \frac{\xi_y}{\lambda}. \tag{6.5}$$

If we expand out the components of ξ_x and ξ_y in a power series in the small parameter ϵ, so that

$$\xi_x = \xi_{x0} + \epsilon\xi_{x1} + \epsilon^2\xi_{x2} + \cdots \tag{6.6}$$

and

$$\xi_y = \xi_{y0} + \epsilon\xi_{y1} + \epsilon^2\xi_{y2} + \cdots \tag{6.7}$$

(where $\xi_{\alpha n} \sim O(1), \alpha = x, y$), then we find that $\xi_{y0} = 0$. Hence we find that to leading order

$$\frac{\partial \xi_{x0}}{\partial x} + i\lambda\epsilon\xi_{y1} = 0. \tag{6.8}$$

This suggests the ordering of the parameters ϵ and λ so that

$$\epsilon = 1/\lambda. \tag{6.9}$$

We can substitute the expansions (6.6) and (6.7) into equation (6.4), and use the relationship in equation (6.5) to gain

$$\frac{1}{\omega_A^2(x)}\frac{\partial^2}{\partial t^2}\left(\xi_{x0}+\epsilon\xi_{x1}+\ldots\right)+\xi_{x0}+\epsilon\xi_{x1}+\ldots=$$
$$\frac{1}{i\lambda}\left\{\frac{\partial}{\partial x}\left[\frac{1}{\omega_A^2(x)}\frac{\partial^2}{\partial t^2}\left(\frac{1}{-i\lambda}\frac{\partial\xi_{x0}}{\partial x}+\epsilon^2\xi_{y2}+\epsilon^3\xi_{y3}+\ldots\right)+\right.\right.$$
$$\left.\left.\frac{1}{-i\lambda}\frac{\partial\xi_{x0}}{\partial x}+\epsilon^2\xi_{y2}+\epsilon^3\xi_{y3}+\ldots\right]\right\}. \tag{6.10}$$

Now, if we undertake a standard multiple time scales analysis (Bender and Orszag, 1978), we can define a long timescale τ given by

$$\tau=\epsilon t \tag{6.11}$$

where $\epsilon=1/\lambda$, as suggested by equation (6.8). To complete the multiple scales analysis, we treat the variables t and τ as independent (even though they are related by $\tau=\epsilon t$). We will re-write the expansion in equation (6.6) in terms of a multiple scales variable Φ so that

$$\xi_x(x,t)=\Phi_0(x,t,\tau)+\epsilon\Phi_1(x,t,\tau)+\cdots \tag{6.12}$$

Using the chain rule, then we find that

$$\frac{\partial\xi_x}{\partial t}=\left(\frac{\partial\Phi_0}{\partial t}+\frac{\partial\Phi_0}{\partial\tau}\frac{d\tau}{dt}\right)+\epsilon\left(\frac{\partial\Phi_1}{\partial t}+\frac{\partial\Phi_1}{\partial\tau}\frac{d\tau}{\partial t}\right)+\ldots \tag{6.13}$$

i.e.,

$$\frac{\partial\xi_x}{\partial t}=\frac{\partial\Phi_0}{\partial t}+\epsilon\left(\frac{\partial\Phi_0}{\partial\tau}+\frac{\partial\Phi_1}{\partial t}\right)+O(\epsilon^2). \tag{6.14}$$

Similarly,

$$\frac{\partial^2\xi_x}{\partial t^2}=\frac{\partial^2\Phi_0}{\partial t^2}+\epsilon\left(2\frac{\partial^2\Phi_0}{\partial t\partial\tau}+\frac{\partial^2\Phi_1}{\partial t^2}\right)+O(\epsilon^2). \tag{6.15}$$

In this way, the left hand side (LHS) of equation (6.10) becomes

$$\frac{1}{\omega_A^2(x)}\frac{\partial^2\Phi_0}{\partial t^2}+\Phi_0+\epsilon\left(\frac{2}{\omega_A^2(x)}\frac{\partial^2\Phi_0}{\partial t\partial\tau}+\frac{1}{\omega_A^2(x)}\frac{\partial^2\Phi_1}{\partial t^2}+\Phi_1\right)+O(\epsilon^2). \tag{6.16}$$

To calculate the right hand side (RHS) of equation (6.10), we need to evaluate the derivatives with respect to x.

6.2.1 Zeroth Order Solution.

To leading order, we simply have the equation

$$\frac{1}{\omega_A^2(x)}\frac{\partial^2\Phi_0}{\partial t^2} + \Phi_0 = 0 \tag{6.17}$$

which has the solution

$$\Phi_0(x,t,\tau) = H(x,\tau)\exp i\omega_A(x)t. \tag{6.18}$$

6.2.2 First Order Solution.

In accord with the standard multiple scales analysis, we seek to find the τ dependence of H so that the oscillations at first order in ϵ (i.e., Φ_1), whose undriven natural frequencies are also $\omega_A(x)$ (see equation (6.10)), are not secularly driven by Φ_0. This ensures that the asymptotic expansion orderings of Φ_0, Φ_1 etc with ϵ remain valid over the long timescale τ, rather than just the short timescale t.

Neglecting the high order terms $\epsilon^n\xi_{yn}$ $(n \geq 2)$ in the RHS of equation (6.10), this simply becomes

$$\frac{1}{\lambda^2}\left\{\frac{\partial}{\partial x}\left[\frac{1}{\omega_A^2(x)}\frac{\partial^2}{\partial t^2}\left(\frac{\partial\Phi_0}{\partial x}\right) + \frac{\partial\Phi_0}{\partial x}\right]\right\}. \tag{6.19}$$

With the solution for Φ_0 given in equation (6.18), then we find that

$$\frac{\partial\Phi_0}{\partial x} = H(x,\tau)i\omega_A'(x)t\exp i\omega_A(x)t + H'(x,\tau)\exp i\omega_A(x)t \tag{6.20}$$

where $a' = \partial a/\partial x$.

To determine the τ dependence of $H(x,\tau)$, we need to calculate the full expansion of equation (6.19) on the basis of equation (6.18). The expanded solution to this is given in Appendix B. It is interesting to note that the variation of H with x only enters the equations at order ϵ^2, and hence to order ϵ (i.e., $1/\lambda$) the form of $H(x)$ is un-important.

To order ϵ, we have the equation

$$\frac{1}{\omega_A^2(x)}\frac{\partial^2\Phi_1}{\partial t^2} + \Phi_1 = -\frac{2}{\omega_A^2(x)}\frac{\partial^2\Phi_0}{\partial t\partial\tau} - 2\frac{i\omega_A'^2(x)}{\omega_A(x)}\tau\Phi_0 - 2\frac{i\omega_A'^2(x)}{\omega_A(x)}\tau^2\frac{\partial\Phi_0}{\partial\tau}. \tag{6.21}$$

Since we want to avoid Φ_1 being secularly driven by Φ_0, then we require that the RHS =0 (i.e., so that the first order oscillator is not resonantly driven at $\omega_A(x)$ - the frequency of the zeroth order solution). This gives the relation

$$\frac{\partial H}{\partial \tau} + \tau \omega_A'^2(x) H + \tau^2 \omega_A'^2(x) \frac{\partial H}{\partial \tau} = 0 \tag{6.22}$$

so that

$$\frac{\partial H}{\partial \tau} = -\frac{\tau \omega_A'^2(x)}{(1 + \omega_A'^2(x)\tau^2)} H \tag{6.23}$$

and hence

$$\ln H = -\frac{1}{2} \ln(1 + \omega_A'^2(x)\tau^2) + \ln C(x). \tag{6.24}$$

The constant of integration is determined by boundary conditions, e.g., $C(x) = H(x, \tau = 0)$, so that

$$H(x, \tau) = \frac{H(x, \tau = 0)}{(1 + \omega_A'^2(x)\tau^2)^{\frac{1}{2}}}. \tag{6.25}$$

Reverting to the notation of (5.4), we see that $H(x, \tau = 0) = G(x)$, and so the leading order solution for ξ_x is given by

$$\xi_x = \frac{G(x) \exp i\omega_A(x)t}{(1 + \omega_A'^2(x)\tau^2)^{\frac{1}{2}}}. \tag{6.26}$$

Similarly, to order ϵ (i.e., $1/\lambda$) from equation (6.8), we have the ξ_y solution

$$i\xi_y = -\frac{1}{\lambda} \frac{\partial \xi_x}{\partial x} = -i\omega_A'(x)\tau H(x, \tau) \exp i\omega_A(x)t - \frac{H'(x, \tau)}{\lambda} \exp i\omega_A(x)t + O(\epsilon^2). \tag{6.27}$$

At the centre of the initial disturbance $H'(x, \tau) = 0$, so the required solution becomes

$$i\xi_y = -i\omega_A'(x)\tau H(x, \tau) \exp i\omega_A(x)t. \tag{6.28}$$

If at $t = 0$ we have initial conditions whereby ξ_x has a maximum amplitude, we have the leading order solutions (in the centre of a symmetric initial disturbance)

$$\xi_x = H(x, \tau) \cos \omega_A(x)t \tag{6.29}$$

and

$$i\xi_y = \tau\omega_A'(x)H(x,\tau)\sin\omega_A(x)t. \tag{6.30}$$

6.2.3 Second and Higher Order Solutions.

In order to calculate how the variation of H with x affects the rate of polarisation rotation from poloidal to toroidal, it is necessary to determine the solutions to order ϵ^2. In principle, this should not be difficult (although algebraically tedious), since the multiple scales analysis on the LHS of equation (6.10) can be easily extended to higher orders. Unfortunately, however, since higher order b_z is no longer negligible, there is not a simple way to relate ξ_{x1} to ξ_{y2}. This is because at this order they are not related in the same way as ξ_{x0} and ξ_{y1} in equation (6.8). However, it is gratifying to note that the form of $H'(x)$ only becomes important at the order of ϵ^2, and hence that the polarisation rotation which was demonstrated numerically in section (5.2.3) in the previous chapter (even with a strongly localised $G(x)$ chosen to match magnetospheric observations) can be expected to be a robust feature of ideal poloidal Alfvén wave evolution, regardless of their envelope in x.

6.3 Comparison of Asymptotic and Numerical Results.

In this section, we consider a comparison between the asymptotic solutions derived in the previous section, and numerical time evolution results determined using the eigenvalue method described in Chapter 2.

The first case which we consider is one where the function $H(x)$ has only a small gradient $H'(x)$. To remove any fast mode components from the initial conditions, we impose $b_z(x, t = 0) = 0$ and hence choose

$$\xi_x(x, t = 0) = \sin\pi x \tag{6.31}$$

$$i\xi_y(x, t = 0) = -\frac{\pi}{\lambda}\cos\pi x. \tag{6.32}$$

Since $i\xi_y(x, t = 0)$ has a node at $x = 0.5$, we follow the evolution of the displacements at this position. This ensures that $i\xi_y$ grows monotonically from zero. We select $A^2 = 1.0$, $B^2 = 0.1$, $k_z = 1.0$ and $\lambda = 50$, and consequently the initial amplitude of $i\xi_y$ is small, and $H(x)$ is given by $\sin\pi x$.

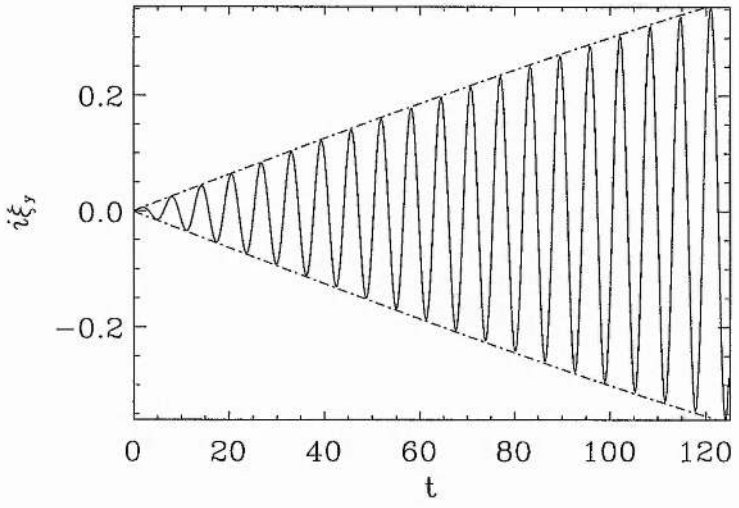

Figure 6.1: Growth of toroidal ($i\xi_y$) displacements at $x = 0.5$, as a function of t, for $\xi_x(x, t = 0) = \sin \pi x$. The solid line represents numerical results, whilst the dot-dash line is the multiple scales derived envelope.

In Figure (6.1) we plot the evolution of $i\xi_y$ at $x = 0.5$. The solid line shows the numerical results, whilst the dot-dashed line represents the envelope $\tau\omega'_A(x)H(x,\tau)$ predicted by equation (6.30). The agreement between the numerical and the multiple time scales results is excellent, with equation (6.30) correctly predicting the sinusoidal time dependence of the $i\xi_y$ response.

We further examine the long timescales (τ) evolution in Figures (6.2) and (6.3). Figure (6.2) shows the oscillating (the Alfvén period $\tau_A(x = 0.5) = 6.28$) and decaying numerical poloidal displacement amplitude, again at $x = 0.5$ ($\tau(x = 0.5) = 318.3$). The multiple scales envelope predicted by equation (6.29) is over-plotted, and agrees excellently with the numerics. Similarly, in Figure (6.3) we plot the numerical oscillation and growth of the toroidal ($i\xi_y$) oscillations, along with the envelope from equation (6.30). Again, excellent agreement is observed.

We now turn to a brief examination of the effects of the x dependence of $H(x)$. In Chapter 5, section (5.2.3), we observed that even for x localised poloidal Alfvén waves (as observed in the Earth's magnetosphere) the polarisation rotation from poloidal to toroidal was still active. To examine the validity of the multiple scales analysis in the presence of strong gradients $H'(x)$, we now impose the same initial conditions as section (5.2.3)

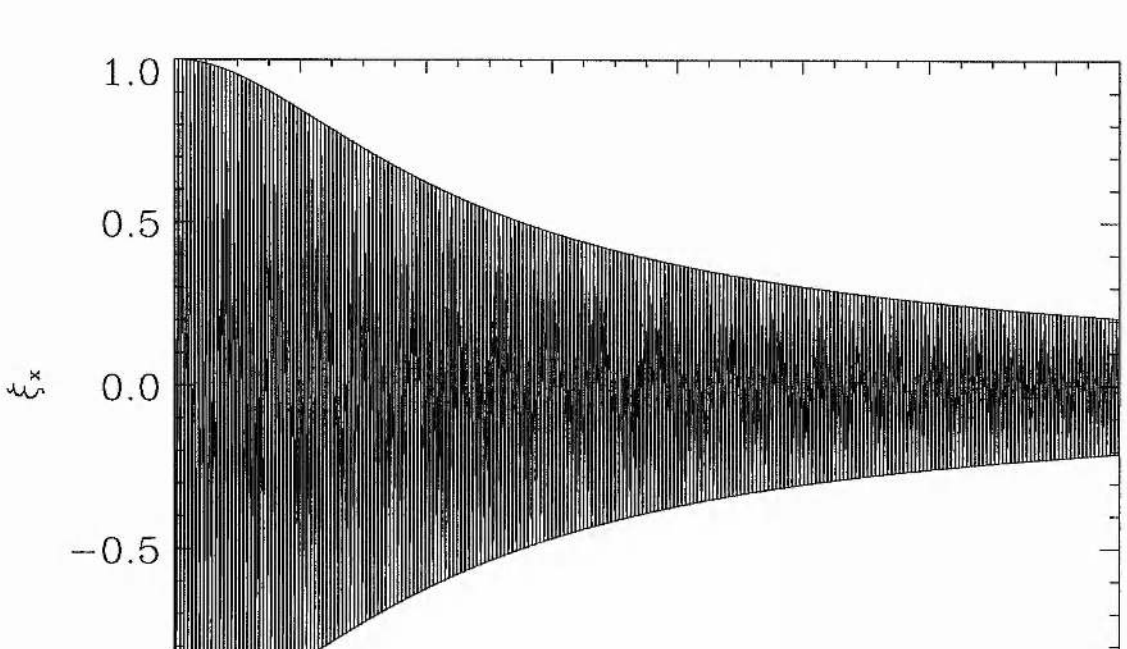

Figure 6.2: Oscillating decay of numerical poloidal (ξ_x) displacements at $x = 0.5$, as a function of t, for $\xi_x(x, t = 0) = \sin \pi x$. Over-plotted is the leading order multiple scales derived envelope.

(equation (5.12)), namely

$$\xi_x(x, t = 0) = \begin{cases} 0 & 0 \leq x < 0.65 \\ 1 - \sin(10\pi x) & 0.65 \leq x \leq 0.85 \\ 0 & 0.85 < x \leq 1.0 \end{cases} \tag{6.33}$$

with

$$i\xi_y(x, t = 0) = -\frac{1}{\lambda}\frac{\partial \xi_x}{\partial x}(x, t = 0). \tag{6.34}$$

In Figures (6.4) and (6.5) we again plot the numerical evolution, and the predicted multiple scales envelopes (equations (6.29) and (6.30)), for ξ_x and $i\xi_y$ respectively. We follow the evolution of the displacements at $x = 0.75$, (i.e., in the middle of the disturbance, where ξ_y has a node) with the same parameters as earlier.

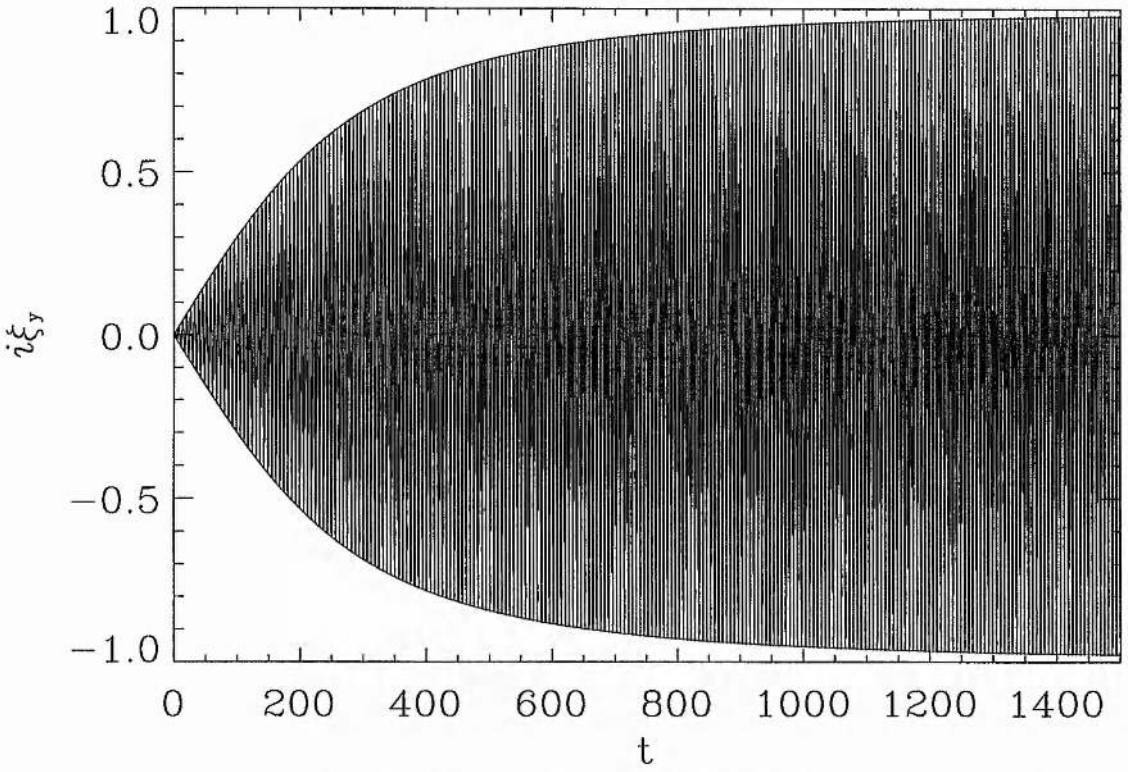

Figure 6.3: Oscillating growth of numerical toroidal ($i\xi_y$) displacements at $x = 0.5$, as a function of t, for $\xi_x(x, t = 0) = \sin \pi x$. Over-plotted is the leading order multiple scales derived envelope.

The global polarisation rotation is again clearly shown, however the dependence $H(x)$ introduces a small higher order correction to the leading order multiple scales solution. This occurs despite the fact that $H'(x = 0.75) = 0$, and is probably a result of the interaction between adjacent field lines (oscillating with different amplitudes) which exist when λ is finite. However, even for the strongly localised function imposed, the correction is small (see also Figures (5.5) - (5.8) which show details of the same wave evolution in terms of the energy density of the waves, and also the x dependence of their displacements).

We briefly note here that relaxing the condition $b_z(x, t = 0) = 0$, by for example setting $i\xi_y(x, t = 0) = 0$, has only a small effect on the global pattern of polarisation rotation observed, so long as $k_z \ll \lambda$. The initial conditions may drive a fast mode, in addition to the dominant poloidal Alfvénic motions; however it's amplitude is usually small. These fast waves do introduce some extra oscillations, at a frequency different from ω_A, and hence

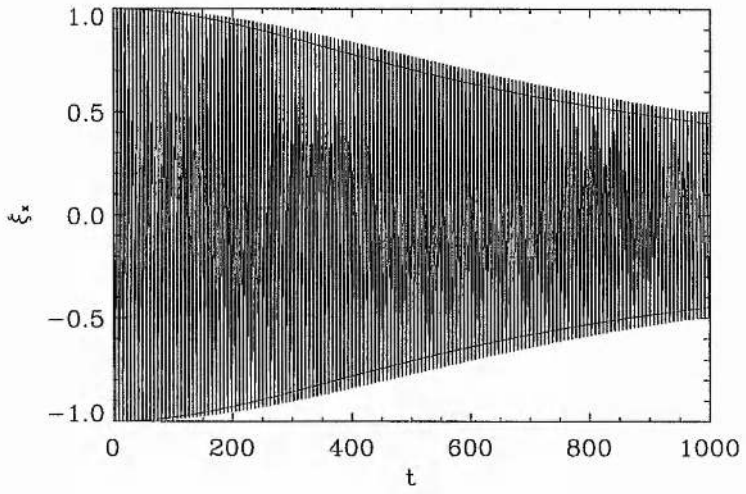

Figure 6.4: Oscillating decay of numerical poloidal (ξ_x) displacements at $x = 0.75$, as a function of t, for the initially localised disturbance. Over-plotted is the leading order multiple scales predicted envelope, which has a small higher order departure from the numerics.

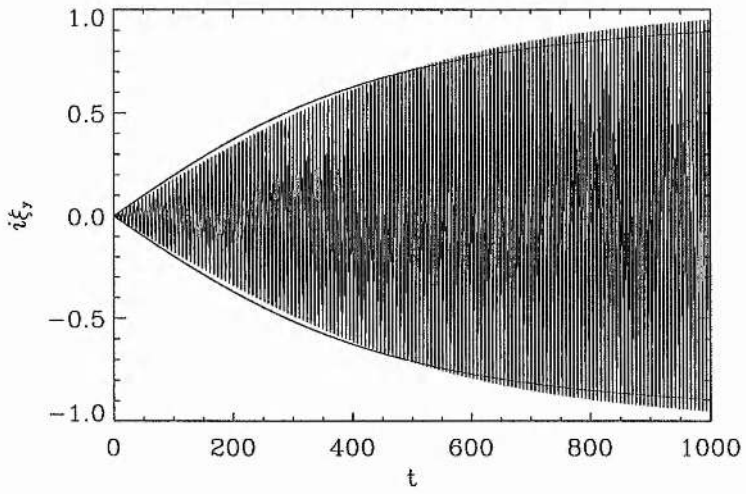

Figure 6.5: Oscillating growth of numerical toroidal ($i\xi_y$) displacements at $x = 0.75$, as a function of t, again for the localised initial conditions. Over-plotted is the leading order multiple scales derived envelope, which departs slightly from the numerics.

at short times they can distort slightly the purely sinusoidal ξ_y oscillation pattern which occurs when $b_z(t = 0) = 0$ (Figure (6.1)). However, the dominant behaviour remains that of a polarisation rotation from poloidal to toroidal, and the effect of introducing a small b_z component into the initial conditions does little to change the overall picture.

6.4 Conclusions.

In this Chapter, we have utilised the method of multiple time scales analysis to obtain an analytical asymptotic expansion solution for the ideal poloidal Alfvén wave lifetimes discussed in Chapter 5 (for $k_z \ll \lambda$). The multiple scales analysis, on the basis of an assumption about the ordering $b_z \sim \xi_y/\lambda$, correctly predicts the numerically observed polarisation rotation. We also determine that for large λ poloidal Alfvén waves, the localised envelope of displacement amplitudes (of magnetospheric poloidal Alfvén waves) has only a second order effect on the ideal poloidal MHD Alfvén wave lifetime. Consequently, the polarisation rotation observed is a robust feature of poloidal Alfvén wave evolution, and can be expected to occur regardless of the form of the x (radial or L-shell) envelope of the initial poloidal wave.

Chapter 7

Summary and Suggestions for Future Work.

7.1 Thesis Summary.

In this thesis, we have considered the temporal evolution of ideal MHD waves in non-uniform media and their application to pulsations in the Earth's magnetosphere. We employed a 1-D box model (e.g. Southwood (1974)) and concentrated upon understanding the important underlying physics of the problem. Assuming that the background plasma was cold, we investigated the coupling between fast and Alfvén wave modes. High resolution (in both x and t) simulations were presented and these allowed the accurate determination of the fine spatial scales developed by the coupled waves, especially over very long times.

Chapter 2 outlined the details of the model magnetosphere, explained the details of the method of numerical solution, and the checks used to ensure the codes convergence and accuracy. In Chapter 3, our attention turned to the normal eigenmodes of the inhomogeneous system. We examined the details of the governing eigenmodes in both uniform and non-uniform background plasmas, and derived analytic results where possible. We investigated the form of the eigenmodes when $\lambda = 0$ (decoupled waves), when λ was small (applicable to resonant Alfvén wave excitation), and when λ was large (poloidal Alfvén waves). Within an ideal MHD formulation, it is possible for these eigenmodes to be singular (c.f. the Barston (1964) modes). The singular modes are responsible for the excitation of field line resonances, and can result in phase mixing. We examined the details of these

singularities, compared the numerical results to analytical solutions, and discussed their implications for time dependent studies. As $\lambda \rightarrow \infty$, the wave modes approach the limit of decoupled poloidal Alfvén waves (Dungey, 1967). At the end of Chapter 3, we examined the features of these large λ eigenmodes.

Chapters 4 and 5 considered the numerical solution of the initial value problem, i.e., solving for the temporal evolution of coupled wave modes. Chapter 4 tackled the resonant excitation of FLRs, whilst Chapter 5 concentrated upon the evolution of large (but not infinite) λ Alfvén waves.

Chapter 4 looked at the temporal development of resonance fine scales, as driven by compressional cavity eigenmodes. We found at early times the resonances were broad, and later approach a width determined by the imaginary part of the cavity modes eigenfrequency (c.f. the quasi-modes, see e.g., Sedláček (1971a)). Within their overall widths, pulsations can continue to develop fine displacement scales via phase mixing. We defined a *phase mixing length* (L_{ph}) based upon undriven toroidal field line oscillations, $L_{ph} = 2\pi/\omega'_A t$, where $\omega'_A = d\omega_A/dx$. We hence determined the finest (ideal) length scales developed at any time and verified the result numerically. We also briefly discussed how the ideal results may be modified by both ionospheric dissipation, and kinetic effects. Finally, we compared our results to detailed FLR observations reported in the literature.

In Chapter 5, we first considered cases where $\lambda \gg k_x(x, t = 0), k_z$ (where k_x, k_z are the wavenumbers in x and z) and found the well known $\lambda \rightarrow \infty$ poloidal Alfvén solution (Dungey, 1967) to be modified when λ is finite. In time, the initially poloidal waves approach an asymptotic toroidal polarisation, comprising decoupled oscillations at the local Alfvén frequency. We determined the ideal poloidal Alfvén wave lifetime τ (defined as the time taken for toroidal and poloidal amplitudes to become equal) evaluated numerically. We showed that the lifetime could be reliably estimated as the time for the phase mixing length to become equal to $2\pi/\lambda$, i.e., $\tau = \lambda/\omega'_A$. We compared our results to satellite data, and to other inhomogeneous poloidal Alfvén wave studies, notably those of Ding et al. (1995). We suggest that the unphysical results of Ding et al. arise from a lack of spatial resolution in their study.

We continued the numerical analysis in Chapter 5 by considering the evolution of waves where $k_z \gtrsim \lambda$, both much greater than k_x at $t = 0$. A similar polarisation rotation results, however during the energy transfer the initially incompressible perturbation drives a compressional component. When $k_z \gtrsim \lambda$ this component results in a fast wave of significant

amplitude. The fast wave propagates away from the initial disturbance and experiences multiple reflections and refractions between the edge of the simulation domain and its turning point. We verified the observed numerical fast wave propagation (and refraction) by ray tracing the path of the fast wavefronts in space.

Finally, in Chapter 6, we considered an asymptotic analysis of the magnetospheric poloidal Alfvén wave. We used the method of multiple time scales, derived the leading order displacement solutions and found them to be in excellent agreement with our numerical results.

One of the central results of the work presented in this thesis is the importance of decoupled toroidal field line oscillations, and hence the phase mixing length, in determining the time-dependent behaviour of coupled MHD wave modes in cold, but fully compressible, non-uniform plasmas. (The importance of the decoupled toroidal eigenmodes has been discussed in the context of incompressible plasmas by Uberoi and Sedláček (1992) - see also Cally and Sedláček (1994)). In the studies presented in Chapter 4, we reported how the finest spatial scales developed at the resonance could be predicted by the use of the phase mixing length, defined using considerations of undriven toroidal Alfvén waves. This time dependent resonant absorption occurs when λ is small. However, when λ is large (Chapter 5 and 6), our results demonstrate a similar important dependence on the phase mixing length. In particular, we were able to understand the finite poloidal Alfvén wave lifetime by considering the time taken for the initial poloidal disturbance to phase mix to the spatial scale $2\pi/\lambda$. Consequently, the phase mixing length is a useful and important parameter which can be used to understand the evolution of coupled fast and Alfvén waves in non-uniform compressible plasmas, regardless of their azimuthal variation.

7.2 Possible Future Work.

7.2.1 Further Analysis of ULF Wave Satellite Data.

The time dependent results which we presented in Chapter 4 predicted the possible existence of fine spatial scales inside the overall envelope of FLRs. It was argued that these ideal fine scales would become limited by either ionospheric dissipation, or by kinetic effects. If these fine scales exist within magnetospheric FLRs, then satellites crossing them should observe systematic frequency shifts due to spatial as well as temporal oscillations.

Inbound and outbound satellites would be expected to see shifts with opposite sign. Systematic frequency differences of this kind were observed by Anderson et al. (1989) with AMPTE/CCE (see their Figure (6)), and it would be interesting to apply the results from Chapter 4 to a prediction of the frequency shift which AMPTE would be expected to see. This could yield information about ω'_A.

7.2.2 Inclusion of Ionospheric Conductivity in FLR Studies.

The dominant dissipation mechanism of FLR Alfvén wave fields at the resonance is believed to be ionospheric. Hence relaxing the assumption of a perfectly conducting ionosphere would provide an interesting area for future work. In particular, since the ionospheric dissipation of dominantly fast (small field aligned currents) and dominantly Alfvénic (strong field aligned currents) waves are very different (Kivelson and Southwood, 1988), a single complex k_z cannot be imposed for both fast and Alfvén waves - as is often the practice in the literature. Since in non-uniform media the fast and Alfvén waves are coupled together, there will be a continual change in k_{zi} (the imaginary part of k_z) from one suitable for fast waves far from the resonance, to one more suited to Alfvén waves at the resonant field line. It is clearly possible to assume different values of k_{zi} on and off resonance (e.g. McDiarmid and Allan (1990)), however this is just an approximation and is not rigorous mathematically. Time dependent studies of the evolution of FLR's driven in a non-uniform medium with conducting boundaries is at least a two dimensional problem and would be an interesting future research topic.

Moreover, toroidal magnetospheric signals with fine (x) scales (large k_x) experience an exponential damping between the ionosphere and the ground (Southwood and Hughes (1983), equation (6.9)). Significant ionospheric shielding of toroidal magnetic signals from the ground can occur when $1/k_x \lesssim h$, where h is the height of the ionospheric E-region ($\sim$ 120km)(Southwood and Hughes (1983) and references therein). (The ionosphere also introduces a polarisation rotation of 90^o between the magnetosphere and the ground (Hughes and Southwood, 1976; Southwood and Hughes, 1983)). On the basis of Chapter 4, we expect FLR widths to narrow in time. Hence models including a realistic ionosphere would make it possible to determine how long it takes before the resonance narrows so that the magnetospheric toroidal magnetic signals are no longer detectable on the ground.

Similarly, since it is likely that resonantly driven FLRs experience the effects of

both the monochromatic cavity driver (a transient response) and a local latitude dependent frequency response, it would be interesting to examine the effect of the resonant fields decaying more quickly than the cavity mode. Previous studies of the combined response of these two frequency components concluded that ground based magnetometers could record signatures which are more monochromatic than those recorded *in situ* on satellites (e.g., McDiarmid and Nielsen (1987) and McDiarmid and Allan (1990)). It may be possible that the slower cavity mode ionospheric damping could enhance this effect, especially since ground based magnetometers spatially integrate magnetic signals (Poulter and Allan, 1985) and hence further mask latitude dependent frequencies. This might help to reconcile some of the differences between ground and satellite magnetometer observations.

7.2.3 Reflectivity of Radial Magnetospheric Boundaries.

In Chapter 4, we considered global compressional disturbances perfectly reflected at the radial boundaries. To set up radially standing cavity eigenmodes in a realistic magnetosphere requires strong reflection to be maintained, so that the necessary constructive and destructive interference can occur. Whilst the plasmasphere should be a strong reflector of waves incident from within, the near perfect reflection at the magnetopause is far from certain. If the cavity boundaries are not sufficiently reflecting, it is unlikely that radially standing magnetospheric cavity waves will develop.

With a radially leaky waveguide model, the combined effects of imperfect radial reflection and wave propagation downtail could be investigated (c.f. the perfectly reflecting waveguide models of Wright (1994a), Rickard and Wright (1994) and Rickard and Wright (1995)). The answers to several important questions could be sought with this model. Firstly, how much wave trapping is required to produce radially standing cavity modes in the near Earth magnetosphere? How will imperfect reflection modify the slowly azimuthally propagating waveguide modes? (i.e. those modes which will drive FLRs (Wright, 1994a)) Secondly, the time over which resonances are driven for determines whether they exhibit dominantly broadband latitude dependent frequency oscillations, or produce the localised amplitude peak which is characteristic of the resonance (Wright, 1992b). Wright's time dependent study predicts that resonances must be driven for at least $\sim 1.5 - 2$ periods in order to reveal resonant behaviour. It would be interesting to investigate the likely FLR response of pulsations driven by leaky waveguide modes. It may be possible that

the amplitude decay of waveguide modes, through both rapid absorption at the resonance (which may occur over only a few wave periods, e.g. Mann et al. (1995)) and transmission through the leaky boundaries produces compressional amplitudes which are often too small to be detected by satellites.

7.2.4 Non-Monotonic Radial Alfvén Speed Studies.

Chapter 4 assumed a monotonic radial variation in Alfvén speed. However, as we discussed in Chapter 1, the existence of the plasmapause means that the whole magnetosphere may be better approximated by two coupled cavities. Zhu and Kivelson (1989) considered the normal modes of this system, and found cavity modes which could exist in either of these two cavities, or tunnel through the plasmapause boundary to exist in both. Similarly, Allan et al. (1986a) considered a time dependent solution in a hemi-cylindrical geometry with a plasmapause, and again found characteristics of tunnelling. They found that a coincidence of the plasmapause with a cavity wave node enhanced plasmaspheric tunnelling.

Recent observational studies show low-latitude pulsations to be possibly driven by both cavity mode type waves (e.g. Ziesolleck et al. (1993)), or by sub-storms in the form of Pi2 pulsations (e.g. Yumoto et al. (1994)). It would be interesting to modify our assumed density profile to include more Fourier harmonics and introduce a plasmapause. This would allow a time dependent investigation of the tunnelling of incident propagating fast waves, and an examination of the creation of trapped plasmaspheric cavity eigenmodes. With a numerical model of this kind, better analytic scaling laws could be developed, which could subsequently be used to interpret low-latitude data.

7.2.5 Poloidal Alfvén Waves in a Dipole Geometry.

In Chapters 5 and 6 we discussed the poloidal to toroidal polarisation rotation experienced by large (not infinite) λ poloidal Alfvén waves. It would be interesting to attempt the multiple scales analysis presented in Chapter 6 in geometries other than a box - notably in a dipole. In a dipole, the ordering $b_{\|} \sim \xi_y/\lambda$ should still be applicable. One complication however is that since dipole poloidal and toroidal eigenfrequencies differ, the resonant transfer of energy into toroidal oscillations will be slightly altered, especially over very long timescales. It may be possible to perturb the toroidal eigenfrequency about the

poloidal one, and obtain analytic solutions involving scalings with both λ and the frequency mismatch.

7.2.6 Kinetic and Electron Inertia Effects at Alfvén Resonances.

A final and more speculative suggestion for future work centres around the modification of fine scale MHD wave modes by kinetic and electron inertia effects. It has been suggested that the fine scales which develop at FLRs (with equatorial scales $\sim 0.1R_E$) can excite kinetic Alfvén waves near the equator, and electron inertia waves near the ionosphere. These waves are excited when pulsation length scales reach the order of the ion Larmor radius (r_L) or the electron inertia length ($\lambda_e = c/\omega_{pe}$, where ω_{pe} is the electron plasma frequency) respectively (Streltsov and Lotko, 1994). This mode conversion introduces wave dispersion, and can broaden the FLR.

Moreover, the eigenfunctions of these dispersive Alfvén waves have fine scale radially aligned structures in their propagation regions. Since these kinetic/two fluid waves can generate field aligned electric fields (Kletzing, 1994; Rankin et al., 1993), it has been suggested that they could be responsible for generating the banded auroral structures, having scales $\sim 1-10$km, which are often observed. Auroral observations of sub-storm related arcs have shown modulation at the frequency of a co-existing FLR (Samson et al., 1991b; Xu et al., 1993) which may link FLRs to auroral electron acceleration. Moreover, observations of field aligned electron fluxes by Kremser et al. (1987) show them to be consistent with acceleration by kinetic Alfvén waves. The previously generally accepted auroral acceleration mechanism, namely electro-static double layers, has been recently criticised since it relies upon the conservative electrostatic force (Bryant, 1992; Bryant et al., 1992). Particle acceleration by these waves offers an alternative mechanism.

Modelling of these kinetic/two fluid effects is beginning to be attempted, although the models used have so far been in box geometries (Rankin et al., 1993; Kletzing, 1994; Wei et al., 1994), and to date the effects of ionospheric conductivity have not been included. Since these may be critical in determining whether the necessary lengths (λ_e, r_L) are reached, future models should attempt to incorporate them.

In Chapter 4, we discussed the possibility of generating pulsation fine scales internally via phase mixing. Their internal radial structure is very similar to the observed auroral bands, and it would be interesting to investigate the effects of kinetic/two fluid

mode coupling on these features. Extensions to include a dipole geometry, and a conducting ionosphere would also ultimately be desirable.

Finally, we note that surface waves propagating on the inhomogeneous boundary between open and closed magnetic field lines (threading the near Earth edge of the plasmasheet) could also mode convert to kinetic/two fluid waves (Streltsov and Lotko, 1994). Within the inhomogeneous layer, the surface wave can resonantly couple to even more localised Alfvénic oscillations within the inhomogeneity (see Hollweg (1987) for an interesting discussion of the physics involved), and then mode convert to kinetic/two fluid waves. In the model of Streltsov and Lotko (1994), a perfectly conducting ionosphere is assumed, as are several orderings of the governing parameters. Extensions to their work, by the inclusion of ionospheric conductivity and the use of a more realistic geometry would be interesting. This would allow the self-consistent inclusion of field aligned variations in $\mathbf{B}$ and ρ, for example in a dipole, and would provide the opportunity for challenging research.

Mode conversion studies of the kinds described above, would begin to put the relationship between aurora and ULF pulsations on a firmer theoretical footing.

Appendix A

Mathieu Function Fast Eigenmode Solutions.

In this Appendix, we describe how to generate the Mathieu function solution fast eigenmodes from the integral order Mathieu functions of the first kind, se_{2n+2} (After McLachlan (1947)).

A.1 Recursion Relations Necessary to Calculate se_{2n+2}.

Substituting the expansion for se_{2n+2} into Mathieu's equation (3.22), differentiating the $\sin(2r+2)z$ terms in the summation explicitly and using the trigonometric identity $\sin(2r+2)z\cos 2z = \frac{1}{2}(\sin 2(r+2)z + \sin 2rz)$, we find that for $r = 0$ (dropping the superscript $(2n+2)$ on $B_{2r+2}^{(2n+2)}$ for brevity)

$$(a-4)B_2 - qB_4 = 0, \tag{A.1}$$

where a represents a characteristic number. Similarly, for $r \geq 1$ we find the recursion relation

$$\left[a-(2r+2)^2\right]B_{2r+2} - q\left(B_{2r+4} + B_{2r}\right) = 0, \tag{A.2}$$

where a represents a characteristic number. Now, we can use equation (A.2) to define the ratio between increasing adjacent expansion coefficients so that

$$v_{2r} = \frac{B_{2r+2}}{B_{2r}} \tag{A.3}$$

and so on. Rewriting equation (A.2) gives

$$\left[a - (2r+2)^2\right] v_{2r} - q\left(1 + v_{2r+2}v_{2r}\right) = 0 \tag{A.4}$$

where we have used the fact that

$$\frac{B_{2r+4}}{B_{2r}} = \frac{B_{2r+4}}{B_{2r+2}} \cdot \frac{B_{2r+2}}{B_{2r}} = v_{2r+2}v_{2r}. \tag{A.5}$$

We can hence write

$$v_{2r} = \frac{q}{(a - (2r+2)^2 - qv_{2r+2})}. \tag{A.6}$$

Using equation (A.1) gives the result that

$$v_2 = (a-4)/q \tag{A.7}$$

and hence also

$$a = 4 + v_2 q. \tag{A.8}$$

(Note that when $q = 0$, then $a = 4$ - see Figure (3.5)).

We can define an infinite continued fraction in terms of v_{2r}, which converges as $r \to \infty$, by dividing the denominator and the numerator by $(2r+2)^2$. This gives

$$v_{2r} = \frac{q}{(2r+2)^2} \Big/ \left(\frac{a}{(2r+2)^2} - 1 - \frac{qv_{2r+2}}{(2r+2)^2}\right). \tag{A.9}$$

and hence the infinite continued fraction

$$E_{2r} = \frac{q/(2r+2)^2}{(a/(2r+2)^2 - 1-)} \cdot \frac{q^2/(2r+2)^2(2r+4)^2}{(a/(2r+4)^2 - 1-)} \cdot \frac{q^2/(2r+4)^2(2r+6)^2}{(a/(2r+6)^2 - 1-)} \cdots \tag{A.10}$$

This converges as $r \to \infty$ because the numerator of this continued fraction $\to 0$ whilst the denominator $\to -1$. Combining equation (A.10) and (A.8) gives a transcendental expression for all the characteristic numbers a given by

$$a = 4 + v_2 q = 4 + \frac{q^2/(4)^2}{(a/(4)^2 - 1-)} \cdot \frac{q^2/(4)^2(6)^2}{(a/(6)^2 - 1-)} \cdot \frac{q^2/(6)^2(8)^2}{(a/(8)^2 - 1-)} \cdots \tag{A.11}$$

The roots of this equation are the (infinite) set of values of a (in this case b_{2n+2}) which correspond to the functions se_{2n+2}. However, numerical iteration can only be used on this series to converge on the solution b_2. To find the other solutions b_{2n+2} $(n > 0)$ a method involving the matching of an infinite continued fraction with a terminating one must be employed. These solution methods are discussed in the following two sections.

We should also stress here that the standard trigonometric solution of Mathieu's equation discussed in these sections strictly only applies to solutions corresponding to positive values of q. However, when comparing the standard form of Mathieu's equation to the decoupled fast eigenmode equation, we found that $q = -2\omega^2 B^2/\pi^2$, which is negative. In this case the characteristic numbers (or eigenvalues) stay the same (since the q verses a stability diagram (Figure (3.5)) is symmetric about $q = 0$), however the eigenfunctions are different.

Introducing the transform of variables $z \to \pm(\pi/2 \pm z)$ has the same effect as changing the sign of q in Mathieu's equation. Hence we can write the solutions for the fast eigenmodes which we require as

$$se_{2n+2}(z, -q) = (-1)^n se_{2n+2}(\pi/2 - z, q) \tag{A.12}$$

$$= (-1)^n \sum_{r=0}^{\infty} (-1)^r B_{2r+2}^{(2n+2)} \sin(2r+2)z. \tag{A.13}$$

Consequently, to find the fast eigenmode solution, we need to introduce the modification of sign $(-1)^r$ into the expression for the coefficients $B_{2r+2}^{(2n+2)}$. (Note that the sign $(-1)^n$ is just a convention to ensure that the series $\sin mz$ (which is the $q = 0$ solution) has positive coefficients, and hence is unimportant in completing the calculation of particular Mathieu functions and comparing them to the numerically determined fast eigenmodes).

A.2 Calculation of Fundamental Fast Eigenmode.

Despite the fact that equation (A.11) defines all the (infinite) values of a (in this case b_{2n+2}), for the purposes of calculation, it can only be used to determine the value of the fundamental characteristic number b_2. We can calculate that particular value of the characteristic number, which we will denote here as simply a, as follows.

First of all, we need an estimate of a. Neglecting all but the first term in the continued fraction, then equation (A.11) can be written as

$$a = 4 + \frac{q^2/(4)^2}{a/(4)^2 - 1 - 0}. \tag{A.14}$$

This gives the following quadratic for a

$$a^2 - 20a + (64 - q^2) = 0 \tag{A.15}$$

with the solution

$$a = 10 \pm \sqrt{36 + q^2}. \tag{A.16}$$

Using values of $A^2 = 1.0$ and $B^2 = 0.9$, and the first (Runge-Kutta calculated) decoupled fast eigenfrequency ω then we find that the parameter $q = 2.33$. With this value of q, equation (A.16) gives values of $a = 3.56$ or 16.44. The values of these two initial approximations to the value of a can then be used in the expression (A.11) (where higher order terms have now been included in the continued fraction) to obtain a next order iteration value for a, and hence to investigate which of the quadratic solutions is nearest to the correct characteristic number which the full continued fraction expression will converge to. In this case it was the smaller root which corresponded to the correct value of a. Once we know an input value for a, equation (A.11) can be used to iterate to obtain a more accurate value. Only a few terms in this equation are required, since the convergence of the series is very quick. For example, when $r = 6$, then the modification $qv_{12}/(2r + 2)^2 \sim 2.3 \times 10^{-6}$. This is $\ll |-1|$, and hence only a few terms are required to calculate a to many decimal places. In fact, the choice of where to truncate the series in r will determine the accuracy with which you can determine the value of a.

Once the value of the characteristic number a has been calculated, this can be substituted into the expression for the terminated continued fraction (terminated at $r = r^*$) expression for v_{2r}, i.e., equation (A.10) for E_{2r}. This allows the calculation of E_{2r} for each value of r, up to $r = r^*$. In this way, the values of all the coefficients B_{2r+2} from $r^* \leq r \leq 1$ (i.e., $B_{2r^*+2} \rightarrow B_4$) can be calculated in terms of B_2 (i.e., $r = 0$) by using the relations in equation (A.5). Then using the normalisation of section (3.4.3), the values for B_{2r+2} (with $n = 0$) can be used to construct the fundamental decoupled fast eigenfunction.

A.3 Calculation of Higher Harmonic Fast Eigenmodes.

In addition to the infinite continued fraction in equation (A.10), we can also derive a terminating continued fraction which involves decreasing powers of r. By matching these series together, we can iterate to find the higher harmonic characteristic numbers b_{2n+2} $(n > 0)$, and hence their Mathieu function expansion coefficients $B_{2r+2}^{(2n+2)}$ $(n > 0)$.

From equation (A.2) we can define the following expression

$$u_{2r+4} = \frac{q}{a - (2r+2)^2 - q u_{2r+2}} \tag{A.17}$$

where $u_{2r+2} = B_{2r}/B_{2r+2}$ (clearly $u_{2r+2} = v_{2r}^{-1}$). Subsequent substitution for decreasing r, and noting that equation (A.1) gives the expression $u_4 = q/(a-4)$, gives the terminating continued fraction

$$F_{2r+4} = \frac{q}{[a-(2r+2)^2-]} \cdot \frac{q^2}{[a-(2r)^2-]} \cdot \frac{q^2}{[a-(2r-2)^2-]} \cdots \\ \cdots \frac{q^2}{[a-(4)^2-]} \cdot \frac{q^2}{[a-4]}. \tag{A.18}$$

Now, to find the characteristic number a of a particular harmonic (n) (i.e., b_{2n+2}) we divide equation (A.2) by $B_{2r+2}^{(2n+2)}$ to get the equation

$$-q u_{2r+2} + \left[a - (2r+2)^2\right] - q v_{2r+2} = 0. \tag{A.19}$$

Using the infinite continued fraction E_{2r+2} (terminated at some $r = r^*$) and the terminating continued fraction F_{2r+2}, then we can write

$$-q F_{2r+2} + \left[a - (2r+2)^2\right] - q E_{2r+2} = G_{2r+2} \tag{A.20}$$

where G_{2r+2} is a numerical remainder determined by the accuracy of the characteristic number a. We can use this equation to interpolate about $G_{2r+2} = 0$ to find a particular value of a in the following way.

First, we need an estimate of the particular harmonic (n) characteristic number a, i.e., b_{2n+2} (which can preferably be got from tables - or by trial and error). We then use F_{2r+2} (the terminating continued fraction calculated with $r = n$) and E_{2r+2} (the infinite continued fraction terminated at $r = r^*$, with $r = n$) to get a value of G_{2r+2}. Seeking the

solution $G_{2r+2} = 0$, we can interpolate in the subsequent calculations of a. This iteration converges towards the required value of b_{2n+2} (i.e, using $r = 2$ results in the calculation of b_6), its accuracy being determined by the choice of r^*.

Once b_{2n+2} has been found we use equation (A.17) to find the values of u_{2r} ($r = n+1, n, n-1, \cdots, 1$) and equation (A.6) to find the values of v_{2r+2} ($r = n+1, n+2, n+3, \cdots, r^*$). These can then be used to find the values of $B_{2r+2}^{(2n+2)}$ ($r \neq n$) in terms of $B_{2r+2}^{(2n+2)}$ ($r = n$). Again, using the normalisation which we have previously described in section (3.4.3) all the coefficients $B_{2r+2}^{(2n+2)}$ can be found, and hence the solution for the higher harmonic integral Mathieu functions of first order (i.e., the harmonic fast eigenmodes) can be calculated.

Appendix B

Poloidal Alfvén Wave Multiple Scales Equation.

In this Appendix, we consider the multiple scales expansion of the RHS of equation (6.10) given in Chapter 6. For clarity, we re-state that equation here, i.e.,

$$\frac{1}{\lambda^2}\left\{\frac{\partial}{\partial x}\left[\frac{1}{\omega_A^2(x)}\frac{\partial^2}{\partial t^2}\left(\frac{\partial \xi_{x0}}{\partial x}\right)+\frac{\partial \xi_{x0}}{\partial x}\right]\right\} + \frac{1}{i\lambda}\left\{\frac{\partial}{\partial x}\left[\frac{1}{\omega_A^2(x)}\frac{\partial^2}{\partial t^2}\left(\epsilon^2\xi_{y2}+\epsilon^3\xi_{y3}+\cdots\right)+\epsilon^2\xi_{y2}+\epsilon^3\xi_{y3}+\cdots\right]\right\}. \quad \text{(B.1)}$$

If we consider the terms arising from the leading order (i.e., $\partial\xi_{x0}/\partial x$) part then we can determine the leading order behaviour of ξ_x.

With $\xi_{x0} = \Phi_0(x,t,\tau) = H(x,\tau)\exp i\omega_A(x)t$, then the second $\partial\xi_{x0}/\partial x$ term (i.e., $\lambda^{-2}\partial^2\xi_{x0}/\partial x^2$) gives

$$\frac{\Phi_0}{\lambda^2}\left[-\omega_A'^2(x)t^2+2i\omega_A'(x)t\frac{H'}{H}+i\omega_A''(x)t+\left(\frac{H'}{H}\right)^2+\left(\frac{H'}{H}\right)'\right] \quad \text{(B.2)}$$

i.e.,

$$\Phi_0\left\{-\omega_A'^2(x)\tau^2+\frac{1}{\lambda}\left(2i\omega_A'(x)\tau\frac{H'}{H}+i\omega_A''(x)\tau\right)+\frac{1}{\lambda^2}\left[\left(\frac{H'}{H}\right)^2+\left(\frac{H'}{H}\right)'\right]\right\}. \quad \text{(B.3)}$$

Similarly, the first term in $\partial\xi_{x0}/\partial x$ gives

$$\frac{1}{\lambda^2}\left\{\frac{\partial}{\partial x}\left[-i\omega_A'(x)t\Phi_0 - 2\frac{\omega_A'(x)}{\omega_A(x)}\Phi_0 - H'e^{i\omega_A(x)t} - 2\frac{\omega_A'(x)}{\omega_A(x)}\tau\frac{\partial H}{\partial\tau}e^{i\omega_A(x)t}\right.\right.$$
$$+\frac{1}{\lambda}\left(2i\omega_A'(x)\frac{\partial H}{\partial\tau}e^{i\omega_A(x)t} + 2i\omega_A(x)\frac{\partial H'}{\partial\tau}e^{i\omega_A(x)t}\right)$$
$$\left.\left.+\frac{1}{\lambda^2}\left(i\omega_A'(x)t\frac{\partial^2 H}{\partial\tau^2}e^{i\omega_A(x)t} + \frac{\partial^2 H'}{\partial\tau^2}e^{i\omega_A(x)t}\right)\right]\right\} \tag{B.4}$$

which expands out to give

$$\frac{1}{\lambda^2}\left\{\omega_A'^2t^2\Phi_0 - i\omega_A'tH'e^{i\omega_A(x)t} - i\omega_A''t\Phi_0 - 2i\frac{\omega_A'^2}{\omega_A}t\Phi_0 - 2\frac{\omega_A'}{\omega_A}H'e^{i\omega_A(x)t} - 2\left(\frac{\omega_A'}{\omega_A}\right)'\Phi_0\right.$$
$$-i\omega_A'tH'e^{i\omega_A(x)t} - H''e^{i\omega_A(x)t} - 2i\frac{\omega_A'^2}{\omega_A}\tau t\frac{\partial H}{\partial\tau}e^{i\omega_A(x)t}$$
$$\left.-2\frac{\omega_A'}{\omega_A}\tau\frac{\partial H'}{\partial\tau}e^{i\omega_A(x)t} - 2\left(\frac{\omega_A'}{\omega_A}\right)'\tau\frac{\partial H}{\partial\tau}e^{i\omega_A(x)t}\right\}$$
$$+\frac{e^{i\omega_A(x)t}}{\lambda^3}\left\{-2\left(\frac{\omega_A'}{\omega_A}\right)^2\frac{\partial H}{\partial\tau}t + 2i\frac{\omega_A'}{\omega_A^2}\frac{\partial H'}{\partial\tau} + 2i\left(\frac{\omega_A'}{\omega_A^2}\right)'\frac{\partial H}{\partial\tau}\right.$$
$$\left.-2\frac{\omega_A'}{\omega_A}\frac{\partial H'}{\partial\tau}t + 2i\frac{1}{\omega_A}\frac{\partial H''}{\partial\tau} + 2i\left(\frac{1}{\omega_A}\right)'\frac{\partial H'}{\partial\tau}\right\}$$
$$+\frac{e^{i\omega_A(x)t}}{\lambda^4}\left\{-\left(\frac{\omega_A'}{\omega_A}\right)^2\frac{\partial^2 H}{\partial\tau^2}t + i\frac{\omega_A'}{\omega_A^2}\frac{\partial^2 H'}{\partial\tau^2}t + i\left(\frac{\omega_A'}{\omega_A^2}\right)'\frac{\partial^2 H}{\partial\tau^2}t\right.$$
$$\left.+i\omega_A'\frac{\partial^2 H'}{\partial\tau^2}t + \frac{\partial^2 H''}{\partial\tau^2}\right\}. \tag{B.5}$$

So, to order $1/\lambda$, the second term in $\partial\xi_{x0}/\partial x$ results in

$$\Phi_0\left\{\omega_A'^2\tau^2 - \frac{1}{\lambda}\left[i\omega_A''\tau + 2i\omega_A'\tau\frac{H'}{H} - 2i\frac{\omega_A'^2}{\omega_A}\tau - 2i\frac{\omega_A'^2}{\omega_A}\tau^2\frac{\partial H}{\partial\tau}\frac{1}{H}\right] + O(\lambda^{-2})\right\}. \tag{B.6}$$

Consequently, combining both the terms from $\partial\xi_{x0}/\partial x$ to order $1/\lambda$, we find that the terms $\omega_A'^2\tau^2$, $i\omega_A''\tau/\lambda$, and $2i\omega_A'\tau H'/H\lambda$ all cancel. This leaves the RHS of equation (6.10), to order ϵ, given by

$$-\frac{2i}{\lambda}\frac{\omega_A'^2}{\omega_A}e^{i\omega_A(x)t}\left(\tau H + \tau^2\frac{\partial H}{\partial\tau}\right). \tag{B.7}$$

Bibliography

Abramowitz, M. and Stegun, A. (1972). *Handbook of Mathematical Functions*, Dover Publications, New York.

Adam, J. A. (1986). Critical layer singularities and complex eigenvalues in some differential equations of mathematical physics, *Phys. Rep.* **142**: 263.

Allan, W. (1983). Quarter-wave ULF pulsations, *Planet. Space Sci* **31**: 323.

Allan, W. and Knox, F. B. (1979). The effect of finite ionospheric conductivities on axisymmetric toroidal Alfvén wave resonances, *Planet. Space Sci.* **27**: 939.

Allan, W. and Poulter, E. M. (1989). Damping of magnetospheric cavity modes: A discussion, *J. Geophys. Res.* **94**: 11,843.

Allan, W., Poulter, E. M. and White, S. P. (1986a). Hydromagnetic wave coupling in the magnetosphere - Plasmapause effects on impulse-excited resonances, *Planet. Space Sci.*, **34**: 1189.

Allan, W., White, S. P. and Poulter, E. M. (1986b). Impulse-excited hydromagnetic cavity and field-line resonances in the magnetosphere, *Planet. Space Sci.*, **34**: 371.

Anderson, B. J., Engebretson, M. J. and Zanetti, L. J. (1989). Distortion effects in spacecraft observations of MHD toroidal standing waves: Theory and observations, *J. Geophys. Res.* **94**: 13,425.

Anderson, B. J., Engebretson, M. J., Rounds, S. P., Zanetti, L. J. and Potemra, T. A. (1990). A statistical study of pulsations observed by the AMPTE/CCE magnetic fields experiment, 1, Occurrence distributions, *J. Geophys. Res.* **95**: 10,495.

Arfken, G. (1985). *Mathematical Methods for Physicists*, Academic Press, San Diego.

Arscott, F. M. (1964). *Periodic Differential Equations*, Pergamon Press, Oxford.

Axford, W. I. and Hines, C. O. (1961). A unifying theory of high-latitude geophysical phenomena and geomagnetic storms, *Can. J. Phys.* **39**: 1433.

Barston, E. M. (1964). Electrostatic oscillations in inhomogeneous cold plasmas, *Ann. Phys. (N.Y.)* **29**: 282.

Bender, C. M. and Orszag, S. A. (1978). *Advanced Mathematical Methods for Scientists and Engineers*, McGraw-Hill, New York.

Boyd, J. P. (1981). Sturm-Liouville eigenproblems with an interior pole, *J. Math. Phys.* **22**: 1575.

Boyd, T. J. N. and Sanderson, J. J. (1969). *Plasma Dynamics*, Nelson, London.

Bracewell, R. N. (1986). *The Fourier Transform and its Applications*, McGraw-Hill, New York.

Bray, R. J. and Loughhead, R. E. (1974). *The Solar Chromosphere*, Chapman and Hall, London.

Browning, P. K. and Priest, E. R. (1984). Kelvin-Helmholtz instability of a phase-mixed Alfvén wave, *Astron. Astrophys.* **131**: 283.

Bryant, D. A. (1992). Electron acceleration in space plasmas, *Ann Geophysicae* **10**: 333.

Bryant, D. A., Bingham, R. and de Angelis, U. (1992). Double layers are not particle accelerators, *Phys. Rev. Lett.* **68**: 37.

Budden, K. G. (1961). *Radio Waves in the Ionosphere*, C.U.P., London.

Burghes, D. N., Kendall, P. C. and Sweet, P. A. (1969). A physical explanation of the difficulties appearing in the theory of toroidal magnetohydrodynamic oscillations, *Mon. Not. R. Astr. Soc.* **143**: 9.

Cally, P. S. (1991). Phase mixing and surface waves: A new interpretation, *J. Plasma Phys.* **45**: 453.

Cally, P. S. and Sedláček, Z. (1994). A Fourier-space description of oscillations in an inhomogeneous plasma, II, Discrete approach, *J. Plasma Phys.* **52**: 265.

Cao, M., McPherron, R. L. and Russell, C. T. (1994). Statistical study of ULF wave occurrence in the dayside magnetosphere, *J. Geophys. Res.* **99**: 8731.

Chan, A. C., Mengfen, X. and Chen, L. (1994). Anisotropic Alfvén ballooning modes in Earth's magnetosphere, *J. Geophys. Res.* **99**: 17,351.

Chapman, S. (1970). Auroral physics, *Ann. Rev. Ast. Astrophys.* **8**: 61.

Chapman, S. and Ferraro, V. C. A. (1930). A new theory of magnetic storms, *Nature* **126**: 129.

Chen, L. and Hasegawa, A. (1974a). A theory of long-period magnetic pulsations 1. Steady state excitation of field line resonance, *J. Geophys. Res.*, **79**: 1024.

Chen, L. and Hasegawa, A. (1974b). A theory of long-period magnetic pulsations 2. Impulsive excitation of surface eigenmode, *J. Geophys. Res.*, **79**: 1033.

Chen, L. and Hasegawa, A. (1974c). Plasma heating by spatial resonance of Alfvén wave, *Phys. Fluids* **17**: 1399.

Chen, L. and Hasegawa, A. (1988). On magnetospheric hydromagnetic waves excited by energetic ring current particles, *J. Geophys. Res.* **93**: 8763.

Chen, L. and Hasegawa, A. (1991). Kinetic theory of geomagnetic pulsations, 1, Internal excitations by energetic particles, *J. Geophys. Res.* **96**: 1503.

Cowley, S. W. H. (1982). The causes of convection in the Earth's magnetosphere: A review of developments during the IMS, *Rev. Geophys. Space Phys.* **20**: 531.

Cowling, T. (1976). *Magnetohydrodynamics*, Adam Hilger, Bristol.

Cross, R. C. (1988). Torsional Alfvén modes in dipole and toroidal magnetospheres, *Planet. Space Sci.* **92**: 12,233.

Crowley, G., Hughes, W. J. and Jones, T. B. (1987). Observational evidence for cavity modes in the Earth's magnetosphere, *J. Geophys. Res.* **92**: 12,233.

Crowley, G., Hughes, W. J. and Jones, T. B. (1989). Correction to "Observational evidence for cavity modes in the Earth's magnetosphere", *J. Geophys. Res.* **94**: 1555.

Ding, D. Q., Denton, R. E., Hudson, M. K. and Lysak, R. L. (1995). An MHD simulation study of the poloidal mode field line resonance in the Earth's dipole magnetosphere, *J. Geophys. Res.* **100**: 63.

Dungey, J. W. (1954). Electrodynamics of the outer atmosphere, *Technical Report Sci. Rep. 69*, Penn. State Univ., University Park.

Dungey, J. W. (1961). Interplanetary magnetic field and the auroral zones, *Phys. Rev. Lett.* **6**: 47.

Dungey, J. W. (1967). Hydromagnetic waves, *in* S. Matsushita and W. H. Campbell (eds), *Physics of Geomagnetic Phenomena*, Vol. 2, Academic, San Diego, Calif., pp. 913–934.

Ellis, P. and Southwood, D. J. (1983). Reflection of Alfvén waves by non-uniform ionospheres, *Planet. Space Sci.,* **31**: 107.

Engebretson, M. J. and Anderson, B. J. (1995). A search for global mode ULF waves in the AMPTE CCE data set, *J. Geophys. Res.* . Submitted.

Engebretson, M. J., Murr, D. L., Erickson, K. N., Strangeway, R. J., Klumpar, D. M., Fuselier, S. A., Zanetti, L. J. and Potemra, T. A. (1992). The spatial extent of radial magnetic pulsation events observed in the dayside near synchronous orbit, *J. Geophys. Res.* **97**: 13,741.

Federov, E. N., Mazur, N. G., Pilipenko, V. A. and Yumoto, K. (1995). On the theory of field line resonances in plasma configurations, *Phys. Plasmas* **2**: 527.

Forslund, D., Kindel, J. M., Lee, K., Lindman, E. L. and Morse, R. L. (1975). Theory and simulation of absorption in a hot plasma, *Phys. Rev. A* **11**: 679.

Fujita, S. and Patel, V. L. (1992). Eigenmode analysis of coupled magnetohydrodynamic oscillations in the magnetosphere, *J. Geophys. Res.* **97**: 13,777.

Goedbloed, J. P. (1983). Lecture notes on ideal magnetohydrodynamics, *Technical Report 83-145*, Rijnhuizen.

Gold, T. (1959). Motions in the magnetosphere of the Earth, *J. Geophys. Res.* **64**: 1219.

Gradshteyn, I. S. and Ryzhik, I. M. (1965). *Table of Integrals Series and Products*, Academic Press, London.

Graham, G. (1724). An account of observations made of the variation of the horizontal needle at London, in the latter part of year 1722, and beginning of 1723, *Phil. Trans. Roy. Soc.* **33**: 96.

Hansen, P. J. and Goertz, C. K. (1992). Validity of the field line resonance expansion, *Phys. Fluids B* 4: 2713.

Harrold, B. G. and Samson, J. C. (1992). Standing ULF modes of the magnetosphere: A theory, *Geophys. Res. Lett.*, **19**: 1811.

Hasegawa, A. and Chen, L. (1974). Plasma heating by Alfvén wave phase mixing, *Phys. Rev. Lett.* **32**: 454.

Hasegawa, A. and Chen, L. (1976). Kinetic processes in plasma heating by resonant mode conversion of Alfvén wave, *Phys. Fluids* **19**: 1924.

Hasegawa, A. and Uberoi, C. (1982). *The Alfvén Wave*, Technical Information Center, U.S. Department of Energy, Virginia.

Heyvaerts, J. and Priest, E. R. (1983). Coronal heating by phase mixed shear Alfvén waves, *Astron. Astrophys.*, **117**: 220.

Hollweg, J. V. (1987). Resonance absorption of magnetohydrodynamic surface waves: A physical discussion, *Ap. J.* **312**: 880.

Hollweg, J. V. and Yang, G. (1988). Resonance absorption of compressible magnetohydrodynamic waves at thin "surfaces", *J. Geophys. Res.* **93**: 5423.

Hughes, W. J. (1974). The effect of the atmosphere and ionosphere on magnetospheric micropulsation signals, *Nature* **249**: 493.

Hughes, W. J. (1980). Multi-satellite observations of geomagnetic pulsations, *J. Geomag. Geoelectr.* **32**(Suppl. II): 41.

Hughes, W. J. (1983). Hydromagnetic waves in the magnetosphere, *in* R. L. Carvillano and J. M. Forbes (eds), *Solar Terrestrial Physics - Principles and Theoretical Foundations*, D. Reidel, Dordrecht.

Hughes, W. J. (1994). Magnetospheric ULF waves: A tutorial with a historical perspective, *in* M. J. Engebretson, K. Takahashi and M. Scholer (eds), *Solar Wind Sources of Magnetospheric Ultra-Low-Frequency Waves*, Geophysical monograph; 81, A.G.U., Washington.

Hughes, W. J. and Grard, D. J. L. (1984). A second harmonic geomagnetic field line resonance at the inner edge of the plasma sheet: GEOS 1, ISEE 1, and ISEE 3 observations, *J. Geophys. Res.* **89**: 2755.

Hughes, W. J. and Southwood, D. J. (1976). An illustration of modification of geomagnetic pulsation structure by the ionosphere, *J. Geophys. Res.* **81**: 3241.

Hughes, W. J., McPherron, R. L. and Russell, C. T. (1977). Multiple satellite observations of pulsation resonance structure in the magnetosphere, *J. Geophys. Res.* **82**: 492.

Hughes, W. J., Southwood, D. J., Mauk, B., McPherron, R. L. and Barfield, J. N. (1978). Alfvén waves generated by an inverted plasma energy distribution, *Nature* **275**: 43.

Inhester, B. (1987). Numerical modelling of hydromagnetic wave coupling in the magnetosphere, *J. Geophys. Res.* **92**: 4751.

Kivelson, M. G. and Southwood, D. J. (1985). Resonant ULF waves: A new interpretation, *Geophys. Res. Lett.* **12**: 49.

Kivelson, M. G. and Southwood, D. J. (1986). Coupling of global magnetospheric MHD eigenmodes to field line resonances, *J. Geophys. Res.*, **91**: 4345.

Kivelson, M. G. and Southwood, D. J. (1988). Hydromagnetic waves and the ionosphere, *Geophys. Res. Lett.* **15**: 1271.

Kivelson, M. G., Etcheto, J. and Trotignon, J. G. (1984). Global compressional oscillations of the terrestrial magnetosphere: The evidence and a model, *J. Geophys. Res.* **89**: 9851.

Kletzing, C. A. (1994). Electron acceleration by kinetic Alfvén waves, *J. Geophys. Res.* **99**: 11095.

Kokubun, S., Erickson, K. N., Fritz, T. A. and McPherron, R. L. (1989). Local time asymmetry of Pc4-5 pulsations and associated particle modulations at synchronous orbit, *J. Geophys. Res.* **94**: 6607.

Krauss-Varban, D. and Patel, V. L. (1988). Numerical analysis of the coupled hydromagnetic wave equations in the magnetosphere, *J. Geophys. Res.* **93**: 9721.

Kremser, G., Korth, A., Ullaland, S. L., Roux, A., Perraut, S., Pedersen, A., Schmidt, R. and Tankanen, P. (1987). Field-aligned fluxes of energetic electrons related to the onset of magnetospheric substorms, *Proceedings of 21st ESLAB Symposium (Small Scale Plasma Processes)*, number 275 in *ESA-SP*, Eur. Space Agency, p. 83.

Lee, D. H. and Lysak, R. L. (1989). Magnetospheric ULF wave coupling in the dipole model: The impulsive excitation, *J. Geophys. Res.* **94**: 17,097.

Lee, D. H. and Lysak, R. L. (1991). Impulsive excitation of ULF waves in the three-dimensional dipole model: The initial results, *J. Geophys. Res.* **96**: 3479.

Lee, M. A. (1980). Comments on the dissipation of hydromagnetic surface waves, *Ap. J.* **240**: 693.

Lighthill, M. J. (1958). *Introduction to Fourier analysis and generalised functions.*, C.U.P., Cambridge.

Lighthill, M. J. (1960). Studies on magneto-hydrodynamic waves and other anisotropic wave motions, *Phil. Trans. Roy. Soc.* **A252**: 397.

Lin, N., Engebretson, M. J., Reinleitner, L. A., Olson, J. V., Gallagher, D. L., Cahill, Jr., L. J., Slavin, J. A. and Persoon, A. M. (1992). Field and thermal plasma observations of ULF pulsations during a magnetically disturbed interval, *J. Geophys. Res.* **97**: 14,859.

Mann, I. R. and Wright, A. N. (1995). Finite lifetimes of ideal poloidal Alfvén waves, *J. Geophys. Res.* in press.

Mann, I. R., Wright, A. N. and Cally, P. S. (1995). Coupling of magnetospheric cavity modes to field line resonances : A study of resonance widths, *J. Geophys. Res.* in press.

McDiarmid, D. R. and Allan, W. (1990). Simulation and analysis of auroral radar signatures generated by a magnetospheric cavity mode, *J. Geophys. Res.* **95**: 20,911.

McDiarmid, D. R. and Nielsen, E. (1987). Simultaneous observation of monochromatic and variable period geomagnetic pulsations, *J. Geophys. Res.* **92**: 4449.

McLachlan, N. W. (1947). *Theory and Application of Mathieu Functions*, Oxford University Press, London.

Mitchell, D. G., Engebretson, M. J., Williams, D. J., Cattell, C. A. and Lundin, R. (1990). Pc5 pulsations in the outer dawn magnetosphere seen by ISEE 1 and 2, *J. Geophys. Res.* **95**: 967.

Newton, R. S., Southwood, D. J. and Hughes, W. J. (1978). Damping of geomagnetic pulsations by the ionosphere, *Planet. Space Sci.* **26**: 201.

Parker, E. N. (1958). Dynamics of the interplanetary gas and magnetic fields, *Ap. J.* **128**: 664.

Poedts, S., Goossens, M. and Kerner, W. (1990). Temporal evolution of resonant absorption in solar coronal loops, *Comp. Phys. Comm.* **59**: 95.

Poulter, E. M. and Allan, W. (1985). Transient ULF pulsation decay rates observed by ground based magnetometers: The contribution of spatial integration, *Planet. Space Sci.* **33**: 607.

Radoski, H. R. (1967). Highly asymmetric MHD resonances: The guided poloidal mode, *J. Geophys. Res.*, **72**: 4026.

Radoski, H. R. (1974). A theory of latitude dependent geomagnetic micropulsations: The asymptotic fields, *J. Geophys. Res.*, **79**: 595.

Radoski, H. R. (1976). Hydromagnetic waves: Temporal development of coupled modes, *Environ. Res. Pap. 559*, Air Force Geophys. Lab., Hanscom Air Force Base, Mass.

Rae, I. C. and Roberts, B. (1981). Surface waves and the heating of the corona, *Geophys. Astrophys. Fluid Dynamics* **18**: 197.

Rankin, R., Samson, J. C. and Frycz, P. (1993). Simulations of driven field line resonances in the Earth's magnetosphere, *J. Geophys. Res.*, **98**: 21,341.

Rickard, G. J. and Wright, A. N. (1994). Alfvén resonance excitation and fast wave propagation in magnetospheric waveguides, *J. Geophys. Res.* **99**: 13,455.

Rickard, G. J. and Wright, A. N. (1995). ULF pulsations in a magnetospheric waveguide: Comparison of real and simulated satellite data, *J. Geophys. Res.* **100**: 3531.

Roberts, B. (1985). Magnetohydrodynamic waves, *in* E. R. Priest (ed.), *Solar System Magnetic Fields*, D. Riedel, Dordrecht, chapter 3.

Roberts, B. (1991). Magnetohydrodynamic waves in the Sun, *in* E. R. Priest and A. W. Hood (eds), *Advances in Solar System Magnetohydrodynamics*, C.U.P., chapter 6, p. 105.

Ruohoniemi, J. M., Greenwald, R. A., Baker, K. B. and Samson, J. C. (1991). HF radar observations of field line resonances in the midnight/early morning sector, *J. Geophys. Res.* **96**: 15,697.

Samson, J. C., Greenwald, R. A., Ruohoniemi, J. M., Hughes, T. J. and Wallis, D. D. (1991a). Magnetometer and radar observations of magnetohydrodynamic cavity modes in the Earth's magnetosphere, *Can. J. Phys.* **69**: 929.

Samson, J. C., Harrold, B. G., Ruohoniemi, J. M. and Walker, A. D. M. (1992a). Field line resonances associated with MHD waveguides in the magnetosphere, *Geophys. Res. Lett.* **19**: 441.

Samson, J. C., Hughes, T. J., Creutzberg, F., Wallis, D. D., Greenwald, R. A. and Ruohoniemi, J. M. (1991b). Observations of a detached, discrete arc in association with field line resonances, *J. Geophys. Res.* **96**: 15,683.

Samson, J. C., Jacobs, J. A. and Rostoker, G. (1971). Latitude-dependent characteristics of long period geomagnetic pulsations, *J. Geophys. Res.* **76**: 3675.

Samson, J. C., Wallis, D. D., Hughes, T. J., Creutzberg, F., Ruohoniemi, J. M. and Greenwald, R. A. (1992b). Substorm intensifications and field line resonances in the nightside magnetosphere, *J. Geophys. Res.* **97**: 8495.

Samson, J. C., Waters, C. L., Menk, F. W. and Fraser, B. J. (1995). Fine structure in the spectra of low latitude field line resonances, *Geophys. Res. Lett.* . in press.

Sedláček, Z. (1971a). Electrostatic oscillations in a cold inhomogeneous plasma, 1, Differential equation approach, *J. Plasma Phys.*, **5**: 239.

Sedláček, Z. (1971b). Electrostatic oscillations in cold inhomogeneous plasma, 2. Integral equation approach, *J. Plasma Phys.*, **6**: 187.

Singer, H. J., Hughes, W. J. and Russell, C. T. (1982). Standing hydromagnetic waves observed by ISEE1 and 2: Radial extent and harmonic, *J. Geophys. Res.* **87**: 3519.

Siscoe, G. L. (1983). Solar system magnetohydrodynamics, *in* R. L. Carvillano and J. M. Forbes (eds), *Solar Terrestrial Physics - Principles and Theoretical Foundations*, D. Reidel, Dordrecht.

Smith, G. D. (1985). *Numerical Solution of Partial Differential Equations*, Oxford University Press, Oxford.

Southwood, D. J. (1974). Some features of field line resonances in the magnetosphere, *Planet. Space Sci.*, **22**: 483.

Southwood, D. J. (1976). A general approach to low-frequency instability in the ring current plasma, *J. Geophys. Res.* **81**: 3340.

Southwood, D. J. (1985). An introduction to magnetospheric MHD, *in* E. R. Priest (ed.), *Solar System Magnetic Fields*, D. Riedel, Dordrecht, chapter 2.

Southwood, D. J. and Allan, W. (1987). Hydromagnetic cavity eigenmodes in a non-uniform plasma, *Proceedings of 21st ESLAB Symposium (Small Scale Plasma Processes)*, number 275 in *ESA-SP*, Eur. Space Agency, p. 179.

Southwood, D. J. and Hughes, W. J. (1983). Theory of hydromagnetic waves in the magnetosphere, *Space Sci. Rev.* **35**: 301.

Southwood, D. J. and Kivelson, M. G. (1981). Charged particle behaviour in low-frequency geomagnetic pulsations, 1, Transverse waves, *J. Geophys. Res.* **86**: 5643.

Southwood, D. J. and Kivelson, M. G. (1982). Charged particle behaviour in low-frequency geomagnetic pulsations, 2, Graphical approach, *J. Geophys. Res.* **87**: 1707.

Speziale, T. and Catto, P. J. (1977). Linear wave conversion in an unmagnetised, collisionless plasma, *Phys. Fluids* **20**: 990.

Steinolfson, R. S. and Davila, J. M. (1993). Coronal heating by resonant absorption of Alfvén waves: The importance of the global mode and scaling laws, *Ap. J.* **415**: 354.

Stewart, B. (1861). On the great magnetic disturbance which extended from August 2 - September 7, 1859, as recorded by photography at the Kew observatory, *Phil. Trans. Roy. Soc. Lond.* **11**: 407.

Stoer, J. and Bulirsch, R. (1980). *Introduction to numerical analysis*, Springer-Verlag, New York.

Streltsov, A. V. and Lotko, W. (1994). Dispersive field line resonances on auroral field lines, *J. Geophys. Res.* . Submitted.

Takahashi, K. and Anderson, B. J. (1992). Distribution of ULF energy ($f < 80$mHz) in the inner magnetosphere: A statistical analysis of AMPTE CCE magnetic field data, *J. Geophys. Res.* **97**: 10,751.

Takahashi, K., McEntire, R. W., Lui, A. T. Y. and Potemra, T. A. (1990). Ion flux oscillations with a radially polarised transverse Pc5 magnetic pulsation, *J. Geophys. Res.* **95**: 3717.

Takahashi, K., McPherron, R. L. and Hughes, W. J. (1984). Multi-spacecraft observations of the harmonic structure of Pc3-4 magnetic pulsations, *J. Geophys. Res.* **89**: 6758.

Thompson, M. J. and Wright, A. N. (1994). Comment on "Validity of the field line resonance expansion", *[Phys. Fluids B 4, 2713 (1992)] Phys. Plasmas* **1**: 1092.

Uberoi, C. (1972). Alfvén waves in inhomogeneous magnetic fields, *Phys. Fluids* **15**: 1673.

Uberoi, C. (1995). Surface wave excitation of local field line oscillations, *J. Geophys. Res.* **100**: 12,127.

Uberoi, C. and Sedláček, Z. (1992). Alfvén waves in inhomogeneous magnetic fields: An integro-differential equation formulation, *Phys. Fluids B* **4**: 6.

Van Allen, J. A. and Frank, L. A. (1959). Radiation around the Earth at a radial distance of 107,400 km, *Nature* **183**: 430.

Vasyliunas, V. M. (1983). Large-scale morphology of the magnetosphere, *in* R. L. Carovillano and J. M. Forbes (eds), *Solar-Terrestrial Physics, Principles and Theoretical Foundations*, Vol. 104, D. Reidel, Dordrecht, p. 243.

Walker, A. D. M., Greenwald, R. A., Stewart, W. F. and Green, C. A. (1979). Stare auroral radar observations of Pc 5 geomagnetic pulsations, *J. Geophys. Res.* **84**: 3373.

Walker, A. D. M., Ruohoniemi, J. M., Baker, K. B. and Greenwald, R. A. (1992). Spatial and temporal behaviour of ULF pulsations observed by the Goose Bay HF radar, *J. Geophys. Res.* **97**: 12,187.

Wei, C. Q., Samson, J. C., Rankin, R. and Frycz, P. (1994). Electron inertial effects on geomagnetic field line resonances, *J. Geophys. Res.* **99**: 11,265.

Wentzel, D. G. (1979). The dissipation of hydromagnetic surface waves, *Ap. J.* **233**: 756.

Wright, A. N. (1990). On the existence of transverse MHD oscillations in an inhomogeneous magnetoplasma, *J. Plasma Phys.* **43**: 83.

Wright, A. N. (1992a). Coupling of fast and Alfvén modes in realistic magnetospheric geometries, *J. Geophys. Res.* **97**: 6429.

Wright, A. N. (1992b). Asymptotic and time-dependent solutions of magnetic pulsations in realistic magnetic field geometries, *J. Geophys. Res.* **97**: 6439.

Wright, A. N. (1994a). Dispersion and wave coupling in inhomogeneous MHD waveguides, *J. Geophys. Res.* **99**: 159.

Wright, A. N. (1994b). MHD theory of magnetic pulsations, *in* J. A. Holtet and A. Egeland (eds), *Physical Signatures of Magnetospheric Boundary Layer Processes*, Kluwer Academic, Norwell Mass., p. 329.

Wright, A. N. and Rickard, G. J. (1995). A numerical study of resonant absorption in a magnetohydrodynamic cavity driven by a broadband spectrum, *Ap. J.* 444: 458.

Wright, A. N. and Smith, P. R. (1990). Periodic features in the Alfvén wave wake of Io, *J. Geophys. Res.* **95**: 3745.

Wright, A. N. and Thompson, M. J. (1994). Analytical treatment of Alfvén resonances and singularities in non-uniform magnetoplasmas, *Phys. Plasmas* **1**: 691.

Wylie, Jr., C. R. (1960). *Advanced Engineering Mathematics*, McGraw-Hill, New York.

Xu, B. L., Samson, J. C., Liu, W. W., Creutzberg, F. and Hughes, T. J. (1993). Observations of optical aurora modulated by resonant Alfvén waves, *J. Geophys. Res.* **98**: 11,531.

Yumoto, K., Isono, A., Shiokawa, K., Matsuoka, H., Tanaka, Y., Menk, F. W. and Fraser, B. J. (1994). Global cavity mode-like and localised field line Pc3-4 oscillations stimulated by interplanetary impulses (Si/Sc): Initial results from the 210° MM magnetic observations, *in* M. J. Engebretson, K. Takahashi and M. Scholer (eds), *Solar Wind Sources of Magnetospheric Ultra-Low-Frequency Waves*, Geophysical Monograph; 81, A.G.U., Washington.

Zhu, X. and Kivelson, M. G. (1988). Analytic formulation and quantitative solutions of the coupled ULF wave problem, *J. Geophys. Res.* **94**: 8602.

Zhu, X. and Kivelson, M. G. (1989). Global mode pulsations in a magnetosphere with a non-monotonic Alfvén velocity profile, *J. Geophys. Res.* **94**: 1479.

Ziesolleck, C. W. S., Fraser, B. J., Menk, F. W. and McNabb, P. W. (1993). Spatial characteristics of low-latitude Pc3-4 geomagnetic pulsations, *J. Geophys. Res.* **98**: 197.